THE UNIVERSITY OF SHEFFIELD

FACULTY OF ENGINEERING

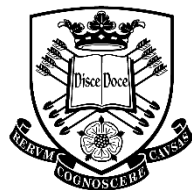## DEPARTMENT OF MATERIALS SCIENCE AND ENGINEERING

Manufacture and Characterisation of *in situ* Titanium Carbide Reinforced Ti6Al4V Composites by Selective Laser Melting

A thesis submitted in fulfilment of the requirements for the degree of Doctor of Philosophy

by

İDRİS TUĞRUL GÜLENÇ

NOVEMBER 2021

The
University
Of
Sheffield.

Abstract

Metal matrix composites (MMCs) offer various advantages over metallic alloys due to their low density, high strength, and tailorable properties. However, their manufacture with conventional methods is challenging due to the presence of hard particles. Selective laser melting (SLM) is a promising method for manufacturing MMCs, but the preparation of homogeneous powder feedstocks is a challenge for its widespread adaptation. This study examines the manufacture and characterisation of *in situ* TiC reinforced Ti6Al4V matrix composites using carbon-coated near-spherical Ti6Al4V powder feedstock via SLM. Spherical homogeneously coated carbon-Ti6Al4V composite powders were prepared by direct mixing to retain the flowability of particles. *In situ* TiC-Ti6Al4V composites were manufactured using this powder feedstock. TiC-Ti6Al4V composites' microstructure was examined using optical microscopy, X-ray diffraction, X-ray computed tomography, scanning electron microscopy, and electron backscatter diffraction. Microhardness tests, dry reciprocating wear tests and *in situ* SEM scratch tests were employed to assess the performance of Ti6Al4V-TiC composites. Nearly fully dense parts with homogeneously distributed TiC nanoparticles smaller than 500 nm size was achieved with optimum processing parameters. Lower SLM energy density led to lack of fusion defects, while high energy

density resulted in keyhole pores. TiC presence induced parent β grain and martensite lath refinement. Grain boundary length increased more than twice with TiC particle formation, and martensite lath size was reduced ~ 30%. The hardness of TiC-Ti6Al4V composites was measured as ~100 HV higher than their unreinforced equivalents. The wear rate of Ti6Al4V-TiC composites was measured as higher than unreinforced Ti6Al4V parts. *In situ* SEM scratch tests were showed that TiC particles may come off from the Ti6Al4V matrix under frictional forces, and third body abrasion may cause the higher wear rate. This study showed that nearly fully dense *in situ* TiC-Ti6Al4V composites can be manufactured using directly mixed composite powder feedstock.

Acknowledgements

I would like to thank my friends for enjoying life together with me.

I have to enormously thank my parents for their endless support, backing me whenever I need them and encouraging me for my PhD research all the time.

The biggest thanks go to my love, Elif, for coming with me to the UK without a second thought, for being there whenever I needed, for making life meaningful, colourful and enjoyable for all these years.

Table of Contents

List of Figures

List of Tables

List of Abbreviations

AM   Additive Manufacturing

CAD   Computer-aided design

DED   Direct energy deposition

EBM   Electron beam melting

MMCs   Metal matrix composites

PBF   Powder bed fusion

SLM   Selective laser melting

SLMed   Selective laser melted

SEM   Scanning electron microscopy

α   Hexagonal close-packed (HCP) alpha titanium phase

α′   Hexagonal close-packed (HCP) martensitic titanium phase

β   Body-centred cubic (BCC) beta titanium phase

OM   Optical microscopy

XRD   X-ray diffraction

XCT	X-ray computer tomography
CT	Computer tomography
EBSD	Electron backscatter diffraction
TiC	Titanium carbide
EDS	Energy-dispersive X-ray spectroscopy
IPF	Inverse pole figure
SE	Secondary electron
VED	Volumetric energy density
LED	Linear energy density
HAZ	Heat affected zone
CTE	Coefficient of thermal expansion
COF	Coefficient of friction
EDS	Energy-dispersive X-ray spectroscopy
PDF	Powder diffraction file
CCD	Central composite design
RSM	Response surface method
Sa	Areal surface roughness

Chapter 1: Introduction

Alloys have found a predominant use in many engineering applications due to their distinctive properties. However, evolving technology introduces more complex requirements from materials to keep up its development. Composite materials are remarkable candidates to meet these requirements due to their tailorable properties. They possess combination of properties of the matrix and the reinforced materials that can be altered by changing the composition and the processing route. Among the composite materials, metal matrix composites (MMCs) are promising materials for high performance applications. [1], [2].

MMCs include a metallic matrix containing one or more fibre, whisker, or particle reinforcement addition. They offer the flexibility of design for the demand [3]. Size, shape, distribution and chemical composition of the reinforcement phase, choice of the matrix alloy, chosen manufacturing method yield different end products [3], [4]. In particular, in situ reinforcement particles offer good matrix-reinforcement bonding and possess a higher thermodynamic stability compared to *ex situ* reinforcements [5]. However, MMCs' manufacture is not a straightforward process. The advantages they

have can only be exploited if end-products can be manufactured at a reasonable cost [1].

MMCs' manufacturing has been carried through various methods such as arc melting [6], induction melting [7], powder metallurgy [8] and spark plasma sintering [9]. These methods have certain issues such as clustering and wetting of reinforcement particles, gas entrapment within the matrix and particle-matrix interface. [10]. Additionally, substantial machining is required after these methods to achieve acceptable quality. Machining of MMCs is a complex process due to the presence of hard particles [11]. Titanium matrix composites (TMCs), as a popular class of MMCs, have even more difficulties during machining arising from titanium's low thermal conductivity, high chemical reactivity and low modulus [12], [13].

Selective laser melting (SLM) is an additive manufacturing (AM) method allowing near-net shape manufacturing of metallic components [14]. Like most additive manufacturing methods, it reduces the production stages significantly by providing the opportunity to form parts directly from powder feedstock. Although it is a relatively new method, extensive research has been conducted on the processing of metals through SLM. Particularly, hard to machine metals, such as titanium alloys, nickel superalloys, have taken great attention.

Among other metal AM methods, SLM offers the best feature size resolution [15], [16]. Parts have a different microstructure than their conventionally processed equivalents when processed by SLM due to the rapid heating and cooling cycles [17], [18]. Even though rapid cooling and heating cycles are problematic for some metal alloys, they can provide outstanding advantages for nanoparticle reinforced composites. Particle agglomeration is a significant problem, particularly for nanosized reinforcements [19], [20]. Limited solidification duration and extensive mixing of the melt pool during the SLM process can provide direct manufacturing of nanoparticle reinforced TMCs.

Some attempts have been made to manufacture TiC [21]–[23] and TiB [24]–[26] reinforced TMCs by SLM. TiC, particularly, is one of the best candidates as a reinforcement phase due to its chemical stability and similar density and coefficient of

thermal expansion to titanium [9]. However, powder feedstock preparation remains as an issue [27]. Nanosized feedstock particles are needed to achieve finely dispersed reinforcements; however, they are expensive due to their fine size and introduce health and safety risks [5], [27]. Additionally, reinforcement powders should be evenly dispersed on the matrix particles to achieve homogeneous distribution after the SLM. Direct mixing of particles fails to distribute reinforcement homogeneously. On the other hand, ball milling provides homogeneous distribution and mixing but causes particle damage and reduces the flowability of feedstock [27].

Considering previous studies and current state of the art methods, there is a need to produce TMCs via SLM using a cost-effective powder feedstock that meets the requirements of the SLM process.

1.1. Project aim and objectives

This project aims to manufacture and characterise evenly dispersed, nanosized *in situ* TiC reinforced titanium matrix composites from undeformed and homogeneously mixed composite powder feedstock by selective laser melting. The following objectives are identified to achieve this aim:

- Reviewing effects of selective laser melting processing parameters on unreinforced Ti6Al4V alloy and having a benchmark for TiC reinforced composites,
- Investigating direct mixing method to achieve homogeneously mixed graphite flake – Ti6Al4V composite powder feedstock to produce *in situ* TiC reinforced titanium matrix composites by selective laser melting,
- Studying effects of processing parameters on the relative porosity of TiC reinforced titanium matrix composites and understanding the mechanism behind porosity formation,
- Characterisation of TiC reinforced and unreinforced Ti6Al4V parts using optical and electron microscopy, electron backscatter diffraction and X-Ray diffraction and correlating microstructure with processing parameters,

- Examining *in situ* TiC formation process and effects of TiC presence on the microstructure of Ti6Al4v alloy,
- Identifying mechanical and tribological properties of TiC reinforced and unreinforced Ti6Al4V parts using microhardness, wear, and *in situ* scratch tests.

1.2. Thesis outline

This thesis consists of 8 chapters. The contents of the chapters are briefly listed below.

Chapter 2 gives the literature review on additive manufacturing with a focus on selective laser melting, heating, and cooling cycles during selective laser melting, microstructure of selective laser melted Ti6Al4V alloys and previous studies on titanium carbide reinforced titanium matrix composites manufactured by selective laser melting.

Chapter 3 presents the materials, followed by experimental procedures and a detailed explanation of the specific techniques.

Chapter 4 investigates feasibility of directly mixed graphite flake and Ti6Al4V powder feedstock for selective laser melting process. A pulsed wave selective laser melting system is used in this chapter. Effects of processing parameters on porosity formation, *in situ* reinforced composites' microstructure and mechanical properties are examined. Additionally, the formation mechanism of titanium carbide is discussed. A relatively low energy density window is examined in this chapter.

Chapter 5 explores the processing of unreinforced Ti6Al4V using a continuous wave selective laser melting system. Various processing parameters are used, and the effect of parameters on material's properties and microstructure is examined. Large area electron backscatter diffraction is performed to create a benchmark microstructure for titanium carbide reinforced samples processed in Chapter 6.

Chapter 6 examines the manufacture of *in situ* titanium carbide reinforced composites using a continuous wave selective laser melting system. A higher energy

density window than Chapter 4 is used in this chapter. The effect of powder mixing durations on the composite powder's homogeneity is examined. Microstructural and mechanical property changes for different processing parameters are discussed, and large area EBSD maps are taken to reveal the effect of *in situ* titanium carbide formation on the microstructure. Change of TiC particle size depending on processing parameters is evaluated.

Chapter 7 studies tribological and wear properties of unreinforced and TiC reinforced Ti6Al4V parts. Dry sliding reciprocating tests are performed, and friction and wear behaviours are examined. *In situ* scratch tests in an SEM environment are performed to reveal the effect of titanium carbide presence on the wear and friction response.

Chapter 8 documents the key findings of this study and suggests future studies to explore the area further.

Chapter 2: Literature Review

2.1. Additive Manufacturing

The concept of manufacturing evolves in parallel with developments in other technologies. Revealing an engineering product traditionally consists of many successive steps. All these steps are connected to each other, and any modification in one of these results in a change in the whole chain. A typical manufacturing journey of a metallic part starts with the raw material, and after that, plastic deformation, heating, cooling, joining, and machining is followed for the desired form [28]–[30]. Some or all these steps are included depending on the requested material properties.

Manufacturing by subtracting reveals scrap material [31]. During the whole process, most of the material from the initial form is removed, so a lot of scrap material shows up. Additive manufacturing (AM) has an entirely different approach to the manufacturing process. Its main principle is adding parts instead of subtracting them as its very name signifies [28], [30], [32]. Therefore, the scrap produced by the subtractive manufacturing procedures is being reduced significantly. Additionally,

there are notably fewer steps during the production chain of AM [30]. Hence, AM offers various advantages over subtractive manufacturing.

The reverse approach of AM also enables complex geometries that cannot be achieved with conventional machining [33], [34]. Complex shapes are provided by removing material using cutting tools in machining. However, there is a limit to what a cutting tool can reach. Therefore, it limits the part's maximum complexity [30]. AM, on the other hand, needs no or limited machining to achieve complex shapes. This also reduces the cost of cutting tools and the machining process. This is particularly significant for hard-to-machine metals such as titanium, superalloys and metal matrix composites (MMCs) [11], [35].

There are different metal AM methods. These can be divided into various groups based on different approaches. One approach is classifying into two groups as *direct to metal* methods and *indirect* processes [36]. Direct energy deposition (DED) and powder bed fusion (PBF) methods require less or no post-processing and can be classified as *direct to metal* methods. In contrast, ultrasonic additive manufacturing can be classified as an indirect method due to mandatory machining to achieve end-shape [36], [37]. Hence, DED and PBF methods have more opportunities to exploit the advantages of AM. Additional classifications can be made considering feedstock material (powder, wire) and energy source (laser, electron beam, arc, ultrasonic vibration).

DED and PBF methods may only be classified as actual metal AM methods due to the aforementioned less or no need for post-processing. There are different DED methods using laser, electron beam or arc as the energy source [14], [36]. These energy sources may use powder or wire feedstock as the raw material[14]. PBF, on the other hand, only uses powder as the raw material, as is evident from its name. A thin layer of powder is laid down in PBF methods and fused by an energy source [15]. The energy source is the main difference between PBF methods. Electron beam melting (EBM) uses an electron beam as the energy source, while selective laser melting (SLM) uses a laser beam to fuse powders [38].

The energy source, the electron beam or the laser beam, affects the melting behaviour of powders and end-part properties differently [38]. There are several reasons behind these differences. When the energy source hits the powder layer, it only melts a small volume of it, resulting in rapid solidification of molten volume [39]. In EBM, the energy of electrons is used for melting the powder layer [40], [41], whereas photon energy is used for SLM [27]. The electron beam additionally charges powder particles negatively, so they repel each other [15]. This causes the formation of a powder cloud due to overcoming gravitational forces. Moreover, particles charged negatively repel incoming electrons, so the melt track and the heat-affected zone (HAZ) becomes wider [42]. These effects cause the requirement of coarser powder feedstock, worse surface finish, larger layer thickness and larger minimum feature size for EBM compared with SLM [15].

On the other hand, residual stress of metal parts produced by SLM remains higher than EBM equivalents [38]. Rapid heating and cooling cycles during SLM cause high residual stresses through the part [43]. Residual stress generates a reduction of ductility and fatigue strength in the end product [44]. Preheating of powder bed can be provided to reduce heating and cooling speed [43], [45]. Resistive heaters are needed in SLM equipment if residual stress reduction is desired [15]. However, this requires an extra rig in the equipment and makes the process more complicated and expensive. By contrast, there is no need for additional equipment in the EBM. The powder bed can be heated by defocussing the electron beam and quickly scanning the layer [15], [41]. Besides, the temperature can be reached by resistive heaters of the SLM is lower than defocussed electron beam heating [15], [41]. Hence, aimed temperatures may not be achieved with the SLM. This difference causes different microstructures at the end of these two processes. EBM products generally have lower residual stress, crack and distortion tendency than SLM ones [41].

The smaller melt pool of the SLM process enables more precise control and finer feature resolution among all metal AM methods [15], [16]. Therefore, it offers the best opportunity to research new alloys and metal matrix composite (MMC) systems.

2.1.1. Selective Laser Melting

Selective laser melting (SLM) is a powder bed fusion (PBF) method. The requested part's computer aided design (CAD) file is sliced for desired layer thickness before the SLM process. A thin layer of powder having the same thickness as the sliced data is laid down onto the substrate plate before melting. After that, this layer is melted by a laser beam according to the sliced CAD data. Melting of each layer is repeated until the requested dimensions are reached. This process is explained in more detail below.

2.1.1.a. Principles of selective laser melting

The essential parts of an SLM equipment are illustrated in Figure 2.1. SLM parts are manufactured on a base plate to avoid damage due to residual stresses [15]. The base plate is lowered down for the layer thickness required as the first step of the process. Then, the powder feeder raises its level to release enough powder to cover the base plate. The recoater blade moves over the raised powder feeder and covers the base plate with the powder. The excessive powder is collected in the overflow container to be used later. After the baseplate is covered with powder, the laser beam scans the base plate for the required area of the current layer. The recoater blade moves back to the original position, and this process is repeated until all layers are processed. At the end of the process, the end-part embedded in an unprocessed powder bed is achieved.
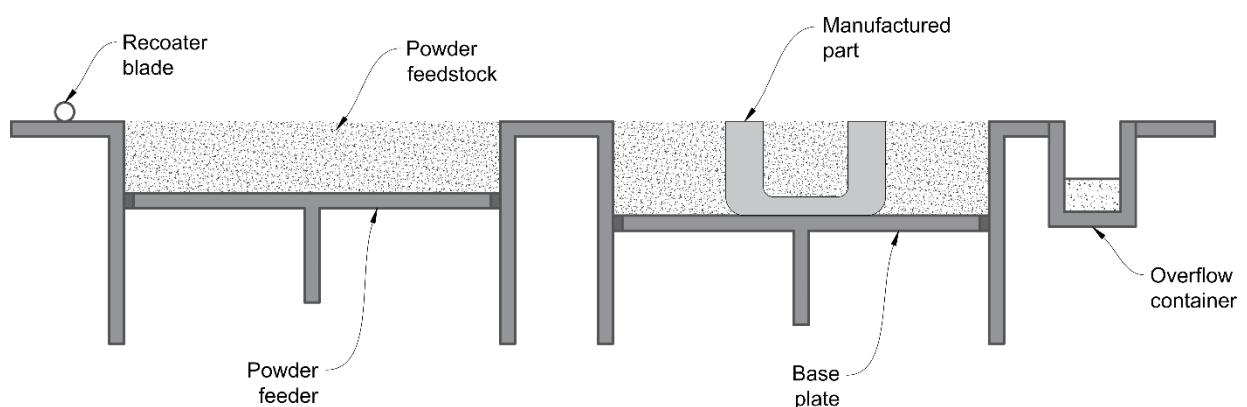
Figure 2.1. A general overview of a typical selective laser melting equipment.

Powder flowability is a significant aspect of the SLM process. The powder is laid down onto the base plate from the powder feeder by the recoater blade (Figure 2.1). During this process, powder particles are moved within the base plate. A good flowability of

powder particles is essential for even coating of the base plate [32], [46]. Additionally, particle shape and size distribution are also important for powder bed density and its optical and thermal properties [19], [27]. Powder characteristics affect laser absorption of the powder layer [47]. Powder properties become particularly important when different powder feedstocks are mixed for new combinations [27]. However, processing parameters have the most significant impact on the manufactured part's properties [48].

Parameters of SLM processing affects the properties of the end product [49]. There are four main processing parameters for SLM when a continuous wave laser is used [50]. These are laser scan speed, laser power, hatch distance and layer thickness. During SLM, laser scans the powder bed using linear scan patterns. The travel speed of the laser during this linear scan is called the laser scan speed or laser speed. The laser power term defines the power level of the laser during processing. The distance between linear laser scans is named the hatch space or hatch distance. Finally, the thickness of a layer spread on the base plate before processing is called layer thickness.

The four parameters listed above are the most effective ones on a part's quality and the most intensively varied ones during the investigation for optimum parameters [51], [52]. However, over 45 parameters affect the end product's quality [48]. Some of these are related to powder feedstock, such as particle size distribution, some related to building environment, such as oxygen level, some related to the equipment itself, such as equipping with continuous or pulsed lasers, and some are related to the melt pool, such as melt pool viscosity [48], [50], [52]. Nevertheless, predominantly the four parameters explained in the previous paragraph is used due to their significant effect on the part properties and simplicity [48], [53]−[55].

Volumetric and linear energy densities are common terms to evaluate the SLM processing parameters. Volumetric energy density (VED) for continuous-wave lasers is expressed as followed [49], [50], [56]:

$$E_v = \frac{P}{h \times t \times v} \tag{2.1}$$

In addition to VED, linear energy density (LED) is also used to examine effects of the laser travel. Equation (2) shows (LED) [57]:

$$E_l = \frac{P}{v} \tag{2.2}$$

P is the laser power, h is the hatch distance, t is the layer thickness, and v is the laser scan speed in these equations. Even though ranges of other parameters should be evaluated alongside VED [58], it gives a simple overview of the effective processing parameters [59].

When a pulsed-wave laser is used, different parameters are effective on the end part properties. Unlike continuous-wave lasers, pulsed lasers do not remain active all the time during the linear travel of the laser [60]. They are fired for a defined duration, move to the next pulse point, and fired again. This loop is repeated until the laser's linear scan is completed. The distance between laser pulses is named point distance (x_{pd}), and the duration laser activated at each pulse point is called exposure time (t_{exp}) [60], [61]. The speed laser moves between individual pulses is also affects the energy input to the system. This is generally a constant value for the equipment but useful to transform the movement of the pulsed laser to continuous laser's laser scan speed. This term is named laser jump speed (C) [61], [62].

Volumetric energy density for the pulsed lasers is defined as followed [62], [63]:

$$E_v = \frac{P \times t_{exp}}{x_{pd} \times h \times l} \tag{2.3}$$

The equation below defines linear energy density for the pulsed laser systems [64]:

$$E_l = \frac{P \times t_{exp}}{x_{pd}}$$

(2.4)

Average travel speed formulation is used to transform pulsed laser's movement to the continuous laser's scan speed [61]:

$$v = \frac{x_{pd}}{t_{exp} + (\frac{x_{pd}}{c})}$$

(2.5)

All these formulations give a simple but informative overview of the energy input to the system. Particularly, VED involves all the significant processing parameters. However, it should be noted that the same energy density acquired from different parameter combinations may give different outcomes [58], [59], [65], [66]. Therefore, processing parameters should also be evaluated independently alongside energy density.

2.1.1.b. Properties of selective laser melted alloys

When the laser moves over the powder layer, it creates a small volume of molten material. The solid base plate underneath the powder layer and surrounding powder has an enormous size compared with the melt pool. This provides a massive heat sink for the molten material [67]. Therefore, rapid heating and cooling cycles are typical for the SLM process [68]. This type of thermal cycle is undesirable for some materials, especially when the crack susceptibility is high [64]. The heating of the base plate and surrounding powders can be applied to reduce the thermal gradient if needed [43].

Rapid cooling of SLM results in different microstructures and properties than conventional processes [17], [18]. The strength of selective laser melted (SLMed) materials in the as-built condition is usually superior to their conventionally processed counterparts [27], [32], [69]; however, this generally comes at the expense of ductility

[45]. Rapid cooling through the base plate also causes anisotropic properties for SLMed parts [70], [71]. Their properties are different when tests are performed parallel and perpendicular to the build direction [72]. Various types of materials exhibit different resultant microstructures.

A wide range of alloys is examined for metal AM [37], [73]. Ferrous alloys, nickel alloys, aluminium alloys, titanium alloys and superalloys are some examples of them. Every alloy that can be welded is considered suitable for AM [18], [74]. The main driving force for a material to be used in AM is the need for less or no machining during manufacturing [18], [32]. Relatively expensive alloys, such as Ti-based ones, cause expensive scrap chips during machining [18]. However, AM parts can be produced with quite less or no scrap [23]. This highlights some alloys for additive manufacturing. Titanium alloys, steel and nickel-based alloys are the most intensively studied alloy groups for SLM [75], [76].

Ti6Al4V, as the most commonly used Ti alloy [77], is the most comprehensively investigated material for metal AM [75]. Therefore, extensive research is performed on its properties after processing with various AM methods. The following section focuses on AM and SLM of Ti alloys with a focus on the Ti6Al4V alloy.

2.1.2. Titanium Alloys in Additive Manufacturing

2.1.2.a. The metallurgy of titanium

Titanium was discovered in 1791 by William Gregor but could not be refined until the beginning of the 20th century [78], [79]. Its widespread usage took 50 years more after its purification. Its lower density than steel and nickel-base superalloys, high specific strength, operating temperatures up to 538°C, good corrosion resistance, and the ability to be produced by conventional methods, such as forging, casting and welding, made it a significant alloy [79], [80]. The aerospace industry is the biggest consumer of titanium alloys [78]. In addition to this, titanium and its alloys are used in architecture, chemical processing, power generation, marine, sports and

transportation industries [78]. The biocompatibility and corrosion resistance of Ti enable it to be applied as a biomaterial [81], [82].

Titanium is an allotropic element, so it has different crystal structures at different temperatures [78], [83]. Pure Ti has a hexagonal close pack (HCP) structure at room temperature, and this phase is called the α titanium. It turns to the body-centred cubic structure (BCC) above 882°C, and this phase is known as the β titanium [83]. The allotropic transformation enables different heat treatments to tailor its properties [78].

The crystal structure is a determinant of the material's properties. Two different Ti phases have varying characteristics. For example, α titanium has less plastic deformation capacity due to reduced slip systems of the HCP structure, whilst β titanium has a better ductility thanks to its BCC structure [78], [83]. Therefore, different titanium alloys with different phases and phase combinations have separate properties.

Titanium alloys are classified as α, β and $\alpha+\beta$ alloys [78]. α stabiliser and β stabiliser elements are used to tailor the microstructure [83]. α alloys have better welding properties while having poor forging capabilities [78], [83]. They are also insensitive to heat treatments [84]. $\alpha+\beta$ titanium alloys' properties are a mixture of α and β alloys, and their microstructure can be tailored in a broad diversity [83]. On the other hand, β alloys have the best formability among Ti alloys [85]. However, their density is higher, and modulus is lower than the other titanium alloy [83], [86].

Conventionally, titanium parts are made using casting, forging, welding, machining and powder metallurgy [12]. Forging and machining give good mechanical properties and surface finish combination; however, most Ti alloys are hard to forge due to the HCP structure [85]. Additionally, their machining is a complex process. Their low thermal conductivity and high chemical reactivity reduce the tool life, and the lower modulus causes more spring effect and deflection of the part during machining [12], [13]. Hence, the production of titanium alloys can be described as expensive. These difficulties in the production of Ti alloys make them a potential research subject for

AM methods. AM promises near-net shape products, which means less machining, less scrap, and no need for forging tools. This potential makes Ti alloys the most studied alloy group for AM [75]. As the most widely used Ti alloy [77], Ti6Al4V is studied intensively for additive manufacturing. The typical chemical composition of Ti6Al4V is given in Table 2.1 [87].

Table 2.1. Typical composition of Ti6Al4V alloy (wt.%) [87].

Ti	Al	V	Fe	O	C	N	H
Balance	5.5-6.75	3.5-4.5	Max. 0.30	Max. 0.20	Max. 0.10	Max. 0.05	Max. 0.015

2.1.2.b. Selective laser melting of Ti6Al4V alloy

The as-built microstructure of the SLM Ti-6Al-4V consists of martensitic phase (α') [38], [88], [89]. The reason behind this crystal structure is rapid heating and cooling cycles during the SLM process [88]. The molten material starts to cool down after the laser passes over it. When Ti6Al4V cools down, the solid β phase is formed from the liquid [90]. The heat is transferred mostly through the solid base plate [68], [90]. The β grains elongated through the vertical heat transfer direction [39]. As a result, columnar β grains through the build direction are formed [67].

During melting a layer, the melt pool reaches the previous layer to provide total bonding between them. This overlap between layers allows the growth of beta grains alongside more than one layer [90]. Further rapid heat transfer results in diffusionless martensitic transformation within the prior beta grains [50], [91]. Figure 2.2(a) shows the martensitic structure of the Ti6Al4V in the as-built condition and Figure 2.2(b) shows reconstructed prior β grains from Figure 2.2(a). Boundaries of the parent β grains can be seen even before the reconstruction process (Figure 2.2(a)). Additionally, several layer long parent β grains can be noticed from the reconstructed image (Figure 2.2(b)).

The anisotropic solidification leads to a preferred grain growth direction. β phase has the BCC crystal structure. The preferred growth direction for cubic crystals is <100>

direction [67]. Hence, the β phase solidifies along this preferred direction [39], [67]. The laser's scan direction is rotated for each layer to distribute residual stresses uniformly [50], [92]. Parent β grains' <100> growth direction may slightly skew from the build line for some cases [67], [72], [88]. Simonelli et al. [67] proposed that this skewness may arise from local thermal gradients arising from laser scan direction rotation between layers.
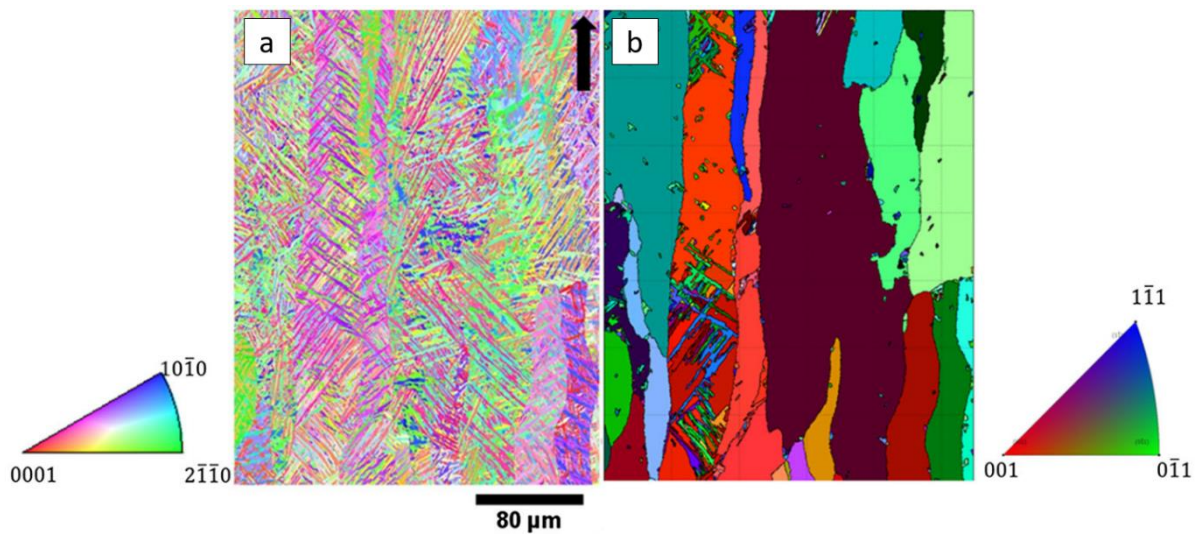
Figure 2.2. (a) Inverse pole figure (IPF) orientation map of the Ti6Al4V alloy's as-built microstructure after the SLM process, (b) reconstructed parent β phase's IPF map. The black arrow on (a) represents the build direction [67].

SLMed Ti-6Al-4V shows higher tensile strength than their forged and cast counterparts in as-built condition [89], [93]. On the other hand, its elongation is lower than these. The martensite phase is the reason behind the high strength and low ductility of as-built SLM material [38], [70]. The hardness of the as-built structure is also higher than the wrought state [94] [35].

The martensitic structure formed during SLM differs from the martensite achieved by quenching the wrought Ti6Al4V [95]. The primary mechanism behind this behaviour is the cyclic thermal history of the SLM process [68]. Figure 2.3 shows the thermal history of a point (P) during the processing of a single layer. Subsequent laser lines scan the surface during the processing of the same layer. Predecessor laser scans (n-4, n-3, n-2 and n-1) preheat the location P prior to melting down (Figure 2.3). After the location P is melted and solidified, following laser scans (n+1, n+2, n+3, n+4) causes

cyclic heating events at this location. These could be effective up to four cycles (~500 μm). The temperature for the $(n+1)^{th}$ scan reaches well above the β-transus temperature of the Ti6Al4V phase. Therefore, intrinsic heat treatments take place during the scan of the same layer.

Subsequent layers cause even a higher heat treatment effect [68]. Figure 2.4 gives the thermal history of a point (P) due to successive layers. When the laser beam melts the powder layer, it penetrates some of the previous layer to provide a total binding between them. Therefore, the $(l+1)^{th}$ layer heats the lth layer to above the solidus temperature. Following layer $((l+2)^{th})$ causes heating of the lth layer above the β-transus temperature. This cycle heats the location P multiple times, affecting the microstructure of the end part [95], [96].
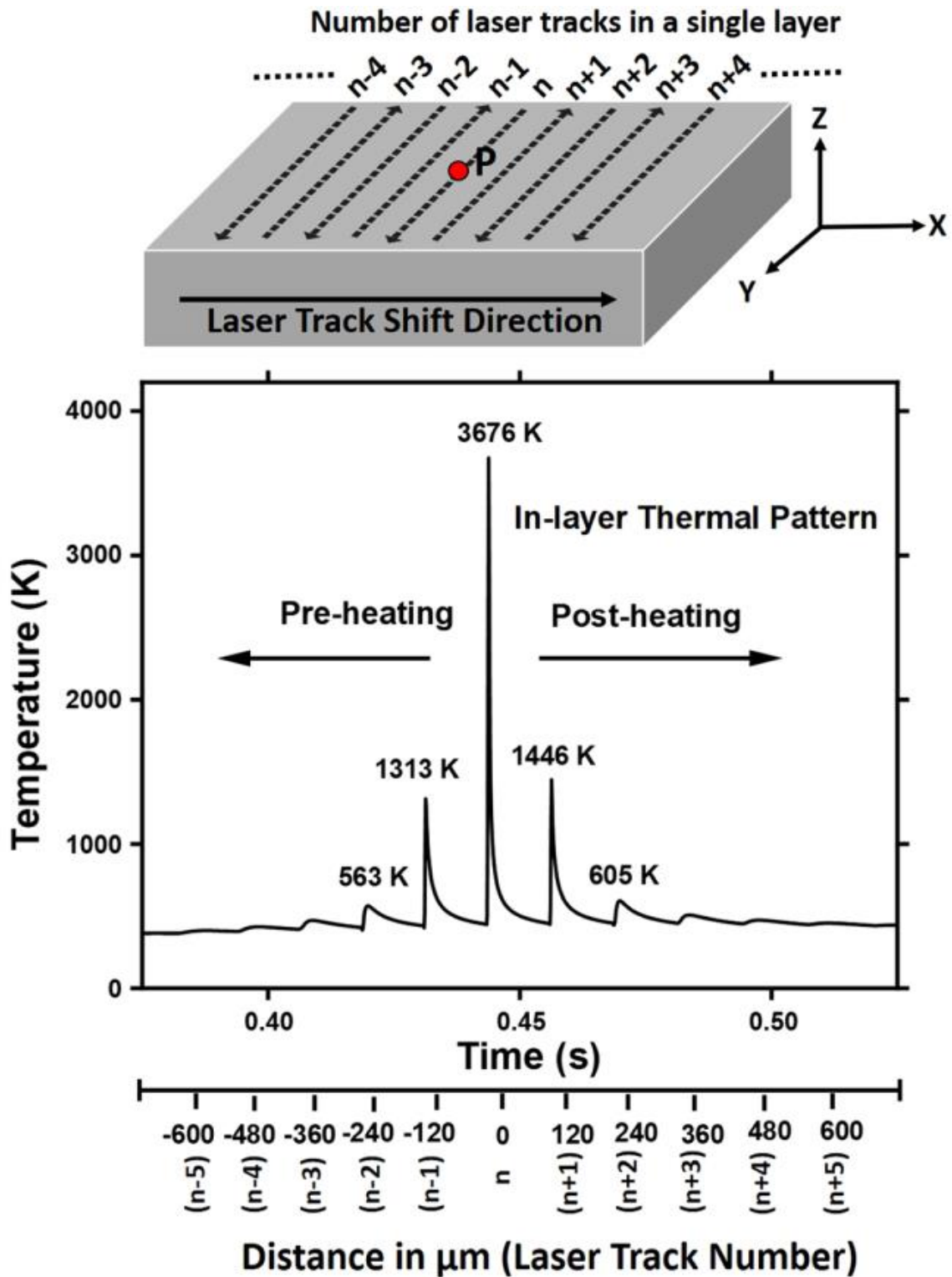
Figure 2.3. Thermal history of a location (P) during the processing of a single layer [68].
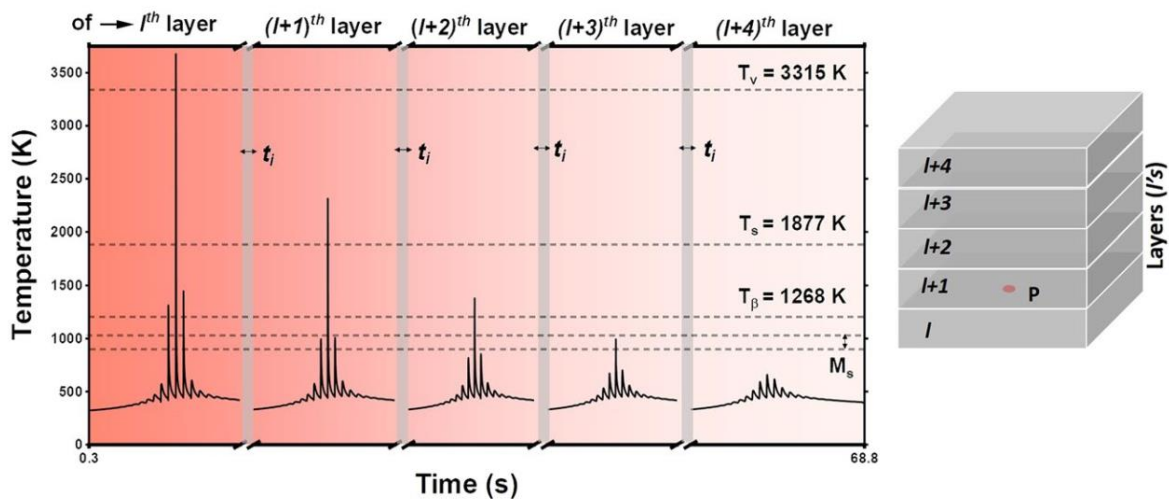
Figure 2.4. Thermal cycles point P undergoes due to subsequent layers [68].

The cyclic load mentioned above results in a hierarchical martensitic structure [96]. When the lth layer is scanned, primary martensites are formed upon cooling. During the $(l+1)^{th}$ layer's production, all of the lth layer is heated above the β-transus temperature. However, the rapid heating and cooling result in residue dislocations within the structure after the *β* transformation. These act as nucleation sites for the martensitic transformation, and smaller secondary martensites are formed. Partial transformation of the lth layer during the $(l+2)^{th}$ and $(l+3)^{th}$ layers and a martensitic structure containing primary, secondary, tertiary and quartic martensites is formed.

Jang et al. [96] proposed a martensite size range for primary, secondary, tertiary and quartic martensites. They classified primary, secondary, tertiary and quartic martensites according to the major axes lengths of >20 μm, 10-20 μm, 1-10 μm and <1 μm, respectively. On the other hand, the martensite structure formed during SLM is different from the one formed on wrought Ti6Al4V parts after water quenching [95]. The thermal history of SLM results in a unique microstructure for SLM Ti6Al4V parts.

SLMed part's porosity and selected processing parameters are related to each other for powder bed fusion processes. Figure 2.5 illustrates porosity change for different laser powers, scan speeds [97]. The lower and higher energy densities cause porosity, and parameters should be chosen in an optimum processing zone. The lack of fusion type defects is formed when a lower energy density is chosen [98]. These defects are

identified with irregular defect borders and partially molten particles. The main reason behind this defect is the insufficient energy of the laser beam to penetrate the entire layer.
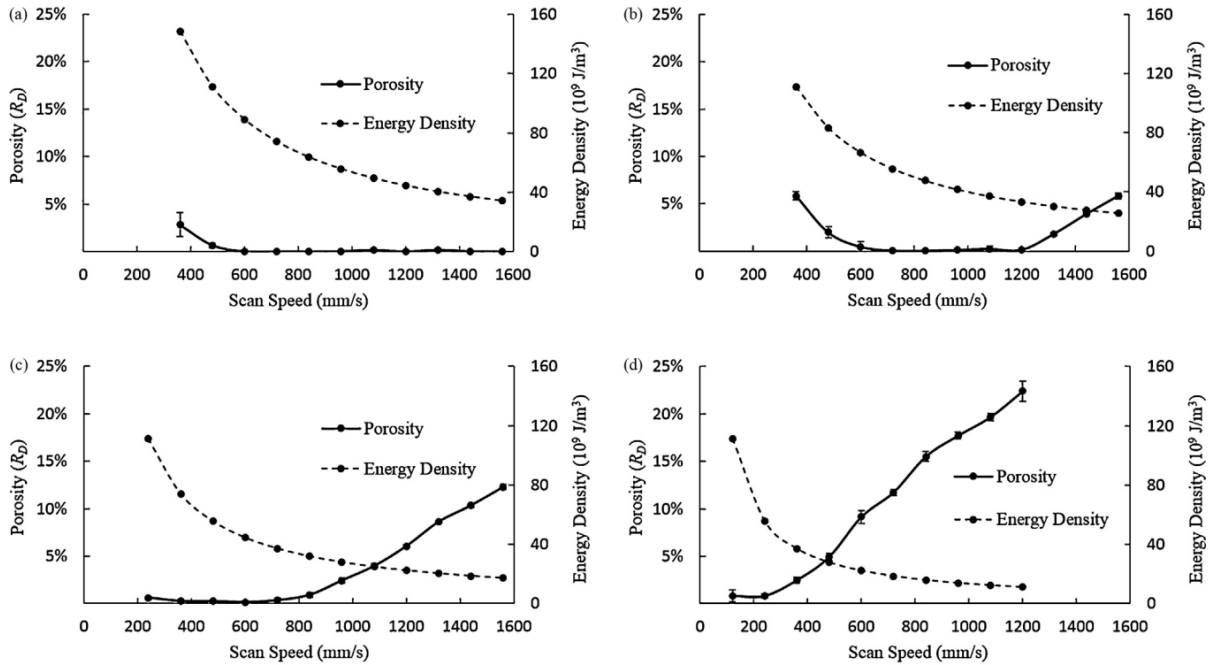
Figure 2.5. Porosity change against energy density and speed for different laser powers (a) P=160W, (b) P=120W, (c) P=80W, (d) P=40W [97].

The keyhole pores are formed when the excessive energy density is used during the SLM processing [98]–[100]. Keyhole pores mostly have spherical shapes (Figure 2.6). When the excessive energy density is chosen, it causes evaporation in the melt pool. Evaporated metal creates a recoil pressure on the molten metal underneath [100], [101]. The recoil pressure increases exponentially, whereas surface tension drops linearly with increasing temperature [100], [102].

Increasing recoil pressure overcomes surface tension and pushes molten metal to a deeper position. After a certain depth, a local cold zone in the above regions of the molten metal cools down, and increasing surface tension creates a pore [100]. The hydrostatic pressure of the molten metal leads to spheroidization of the pore. This pore may leave the melt pool through the surface of it. If it is trapped by the solidification front, a keyhole pore is formed [100], [103]. This mechanism takes place if a threshold value is passed [99]–[101]. The average keyhole pore size is smaller if the difference

between energy density and the keyhole threshold value is low. In contrast, higher differences create larger pores due to exponentially increasing recoil pressure [100].
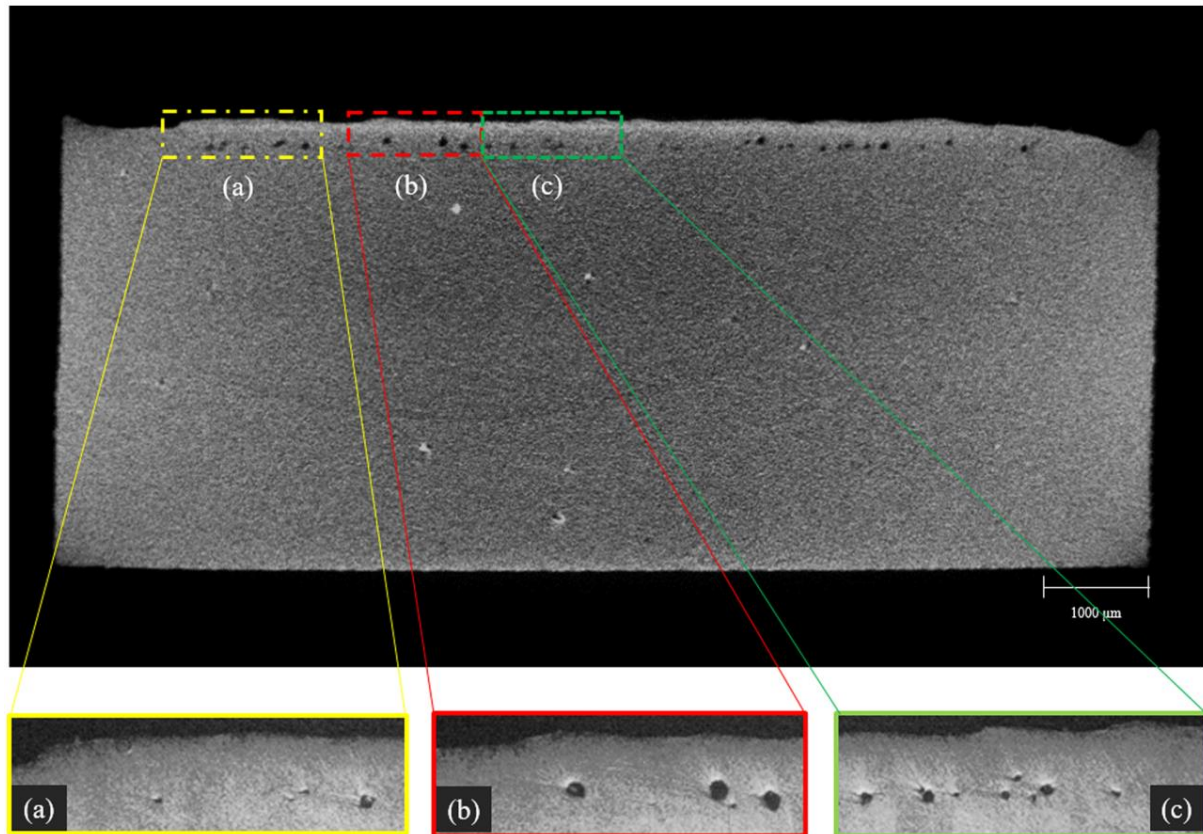
Figure 2.6. X-ray tomography image of spherical keyhole pores (top) and their confirmations with optical images [100].

2.2. Metal Matrix Composites

Composite materials have covered our everyday life for a long time. Examples of composite materials can be found in nature as coconut palm or as simply wood in the fibre reinforced composite form[104]. Composites are defined as the mix of two or more different materials to combine their desired properties [2]. A variety of reinforcement particles and matrix phases have been used to meet requirements [105], [106]. Metal matrix composites (MMCs) offer several advantages such as high specific strength, elevated service temperature and increased wear resistance over metallic alloys [2].

MMC term is mainly used to refer to light metal matrix composites, and research is focussed on this class [1]. Titanium is a promising matrix material due to its excellent corrosion resistance, excellent biocompatibility and high specific strength [107]. The addition of ceramic particles to the Ti matrix can increase the service temperature of the material up to 200°C and can improve its poor wear resistance [108]. They could also offer better materials for biomedical applications due to the opportunity to tailor their modulus for the bone [53]. The objectives of the MMCs development can be summarized as follows [1], [2], [109]:

- Increasing specific strength,
- Combining increase of the strength and toughness,
- Advancing high temperature creep performance,
- Enhancing high-temperature fatigue strength,
- Increasing thermal shock resistance,
- Achieving better corrosion resistance,
- Raising modulus of elasticity,
- Decreasing thermal expansion.

One or more of these objectives may be aimed at the development of MMCs; however, these are only rough guidance. Depending on the function of the material, more specific objectives, such as improving the wear behaviour against sliding contact, can be aimed [1].

Different reinforcements have been used for MMCs. The reinforcements can be in the particle, short fibre, whisker or continuous fibre forms [110], [111]. Additionally, layered composites can also be manufactured by bringing different material layers together [112]. Figure 2.7 represents particle, whisker, and continuous fibre reinforced composite's structures. Particle reinforced and whisker reinforced composites are a very similar class of materials to each other [111]. They provide isotropic material properties if the reinforcement's even dispersion and the whisker orientation's random distribution can be provided [106], [111]. Continuous fibre reinforced composites, on the other hand, shows anisotropic properties. Mechanical properties, for instance, is

higher if the load is applied parallel to the reinforcement fibres but weaker in the transverse direction due to limited matrix strength. Additionally, their cost is high due to complex processing steps and expensive fibre reinforcements [107], [111]. Therefore, particle reinforced composites are a better option when isotropic properties are required.
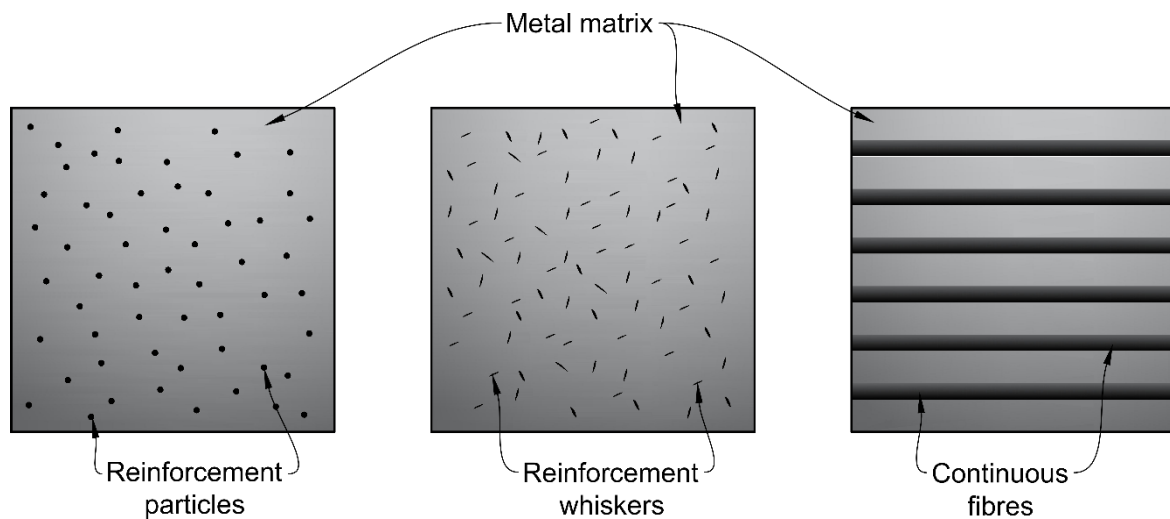
Figure 2.7. Illustration of different metal matrix composite reinforcements: particle reinforced (left), whisker reinforced (middle), and continuous fibres (right).

Nanosized reinforcement particles are preferred for particle or whisker reinforced materials [27]. These particles can provide strength to the system in various ways. They limit the movement of dislocation by pinning them and cause dislocation bowing around and between particles [27], [113], [114]. This effect is called Orowan strengthening and becomes particularly significant when the reinforcement size is in the submicron scale [114]. In addition to this, coefficient of thermal expansion (CTE) mismatch between reinforcement particles and matrix material causes increased strength. When the MMC part cools down, CTE mismatch between reinforcement particles and matrix creates stresses around particles [27], [114]. This stress generates defects, such as dislocations, around particles and increased dislocation density leads better strength.

In addition to Orowan and CTE mismatch strengthening mechanisms, grain refinement further develops MMC's strength [27], [53], [115], [116]. Addition of nanoparticles to the liquid metal provides heterogeneous nucleation zones to the

system [108], [115], [116]. Additionally, the presence of these particles limits the grain growth [27]. As a result, matrix material with more grain boundaries than unreinforced counterpart becomes stronger.

Particle and whisker reinforced MMCs can be manufactured as *ex situ* and *in situ* methods [2], [27], [107], [108], [113]. *Ex situ* processing involves the addition of stable reinforcement particles at the beginning of the process [5], whereas *in situ* reinforcement refers to a process in which reinforcement particles formed through a reaction during the manufacturing [5], [27], [115]. *In situ* methods have a variety of advantages over the *ex situ* ones [5], [115].

In situ reinforcement particles have a cleaner particle-matrix interface than *ex situ* ones which is preferred for better bonding between matrix and reinforcement [5]. Additionally, *in situ* particles have a better dispersion within the matrix [27]. This is particularly significant for nanosized particles due to their high surface area and surface energy [2], [27]. Another advantage of the *in situ* particles is their better chemical stability than *ex situ* counterparts [27]. Nanosized particles are required to have a good distribution of the reinforcement within the matrix [19], [117]. However, the small size of these particles makes them more expensive and introduces health and safety issues. The combination of all these effects brings *in situ* methods forward.

The manufacture of *in situ* TMCs has been performed using various methods. Vacuum arc melting [6], powder metallurgy [8], vacuum hot-press sintering [118], vacuum induction melting [7] and spark plasma sintering (SPS) [9], [119], [120] has been utilised for *in situ* TMC production. Despite their favourable characteristics, there are still critical challenges in the manufacture of MMCs. Their manufacturing is considered as a costly process when they are produced with the conventional methods [5]. Reinforcement agglomeration, gas entrapment and reinforcement wetting are some of the main issues [121]. When it comes to the titanium matrix composites (TMCs), cost even becomes a more severe issue [116]. Machining and forging of titanium parts are already complex without the addition of reinforcement parts [12], [13]. The addition of the hard particles makes the process even harder, more complex and more expensive

[11], [107], [109]. These are the main reasons limiting widespread usage of TMCs [1], [107].

The selective laser melting (SLM) process have unique characteristics to overcome the difficulties of TMC manufacturing. SLM parts need less or even no machining [18], [32], and the cost of expensive plastic deformation dies is not present. Additionally, its unique heating and cooling regime makes it a significant candidate for MMC production.

2.2.1. Processing of *in situ* Titanium Matrix Composites via Selective Laser Melting

Additive manufacturing methods have been adopted for *in situ* TMC manufacturing, including laser deposition [122], [123], wire-arc [124] and SLM [21]–[24]. Using SLM, *in situ* growth of TiC [21]–[23], [125], [126] and TiB [24]–[26], [127], [128] have been investigated. *In situ* TiC synthesis has been used with Ti [22], Ti-Al [21], [125] and Ti-Mo [23], [126] matrices. Depending on the TMC manufacturing method, processing parameters, the feedstock material chemistry and morphology need to be carefully optimised.

SLM processing parameters are significant to determine the reinforcement phase's properties. Gu et al. [21], [125] examined SLM of *in situ* TiC reinforced titanium aluminide. They used a ball-milled powder feedstock containing 50 at.% Ti, 25 at.% Al and 25 at.% C. The main motivation of the study was developing a TiC reinforced titanium aluminide for high-temperature applications. They have found that SLM processing parameters are effective on TiC morphology and size. The higher laser energy input resulted in more spherical TiC particles. On the other hand, no information regarding the relative porosity of the structure has been reported.

The addition of reinforcements may deteriorate the properties of TMCs for certain conditions. Manufacture of *ex situ* TiC reinforced TMCs have been performed in a study using nanosized TiC and conventional SLM Ti powders [129]. Four different compositions, 7.5, 12.5, 17.5, 22.5 wt.% TiC, have been examined. A maximum relative

density of 98.3% has been achieved. Figure 2.8 shows the microstructure of the four different TiC additions. Morphology of TiC particles transformed from nanosized plates to dendritic particles. Average TiC particle thickness was reported as ~77 nm for the 12.5 wt.% TiC addition (Figure 2.10(b)). The wear resistance of TMC is increased when the TiC addition increases from 7.5 wt.% to 12.5 wt.%. However, a decrease of the wear resistance is reported for composites containing more than 12.5 wt.% TiC.

Powder processing prior to composite part's manufacturing is determinative of the flowability of feedstock. Kühnle et al. [128] examined *in situ* TiC and TiB_2 reinforced TMCs using 72 wt. %Ti + 28 wt. % B_4C powder feedstock. In this study, a planetary ball mill is used to mix the powders. They only conducted single-line laser track experiments to examine the *in situ* reaction. TiC and TiB_2 phases are formed in the microstructure; however, a high powder layer thickness of 100 μm must be used due to the agglomeration and irregular morphology of the powder particles.
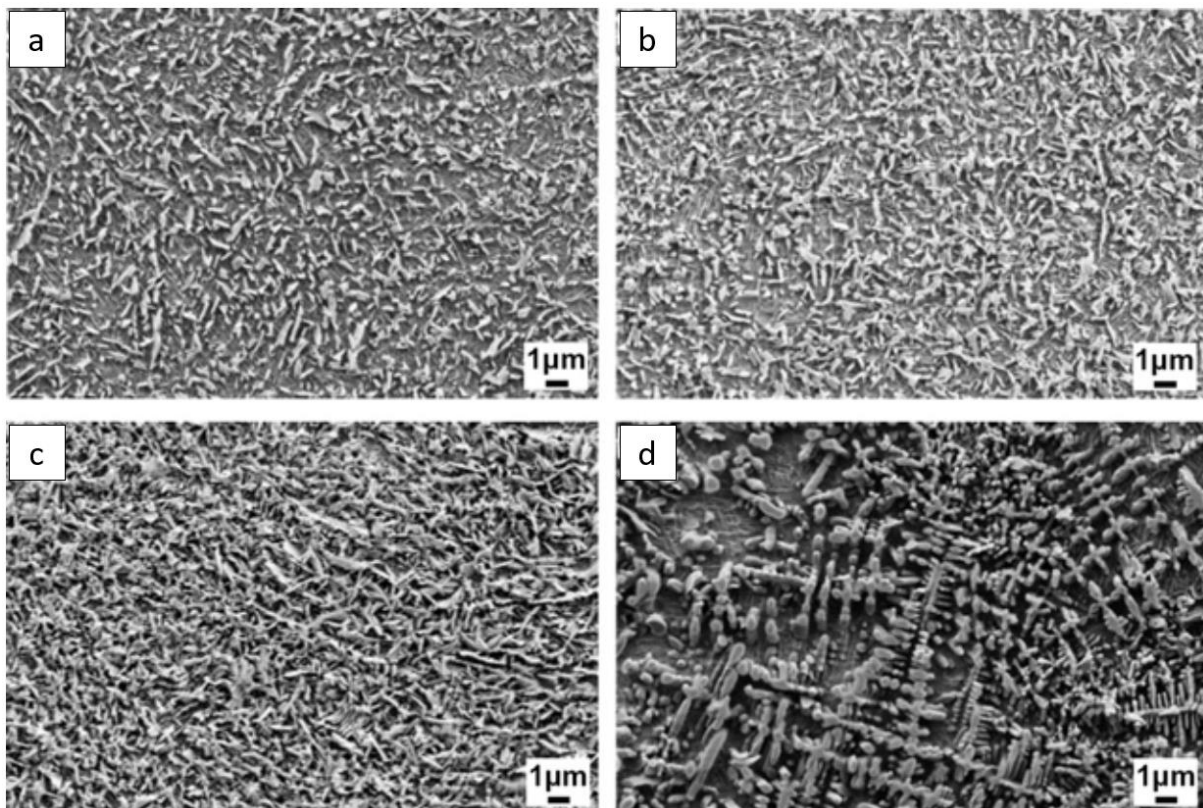
Figure 2.8. Secondary electron SEM images of Ti/TiC composites containing (a) 7.5 wt.%, (b) 12.5 wt.%, (c) 17.5 wt.%, (d) 22.5 wt.% TiC [129].

The same composition of powder feedstock can be prepared using different mixing methods and initial powders. For example, Gu et al. [19] studied the densification behaviour of two different powder feedstocks. The first powder feedstock is prepared by ball milling and using micron-sized TiC and Ti powders. Ti powders of the first batch had a 45 μm average particle diameter. The second feedstock is prepared using nanosized TiC particles and a smaller Ti powder batch. Ti particles chosen for the second type of powder batch had an average particle diameter of 22.5 μm. Figure 2.9 shows two different feedstock powders prepared by ball milling and direct mixing. The directly mixed second batch powder had an inhomogeneous coverage of TiC particles on it. This is probably due to the lack of adhesion between TiC and Ti particles. On the other hand, ball-milled powders significantly deformed, and their morphology is totally changed. Therefore, powder flowability and chemistry homogeneity issues are present for ball milled and directly mixed particles, respectively.
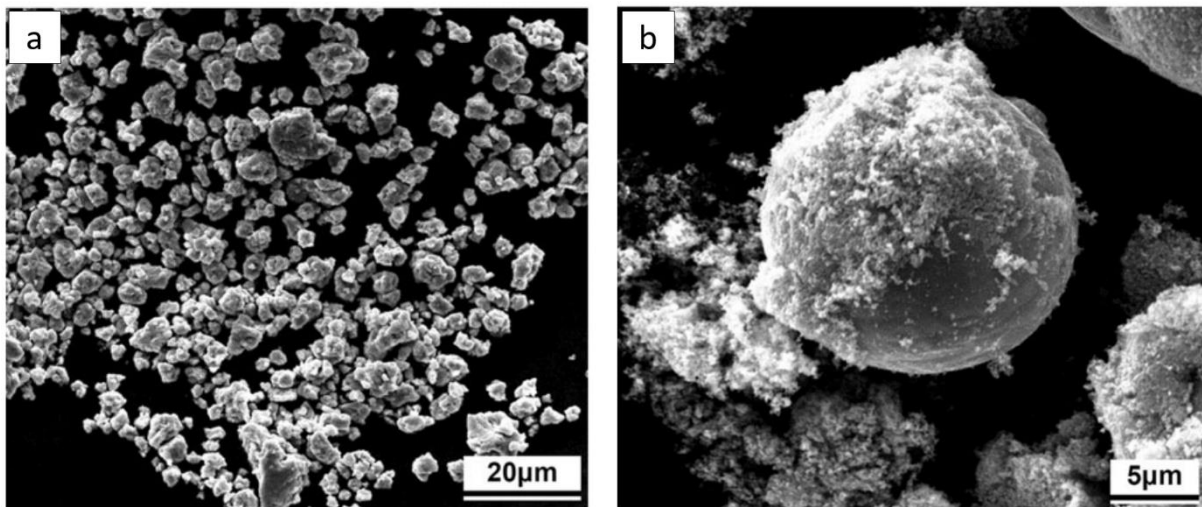
Figure 2.9. (a) Ball milled and (b) directly mixed titanium - titanium carbide powder feedstocks [19].

Several studies argued that TiC is formed through the dissolution-precipitation mechanism during SLM process [19], [21], [22], [129]–[131]. This formation theory can be explained as follows: TiC particles dissolve into the liquid titanium due to the high energy of the laser beam. Upon cooling, TiC nuclei form from the liquid metal. These nuclei grow with dropping temperature, and finally, TiC particles dispersed within the matrix are achieved. Rapid cooling and resultant insufficient time for grain growth enable finely dispersed TiC particles within the structure [19], [125]. However, fine TiC

particles are necessary if TiC is used as the reinforcement source for this mechanism; otherwise, undissolved coarse TiC is reported with the structure [117], [132].

The addition of Mo and Mo_2C particles into the Ti powder matrix is studied to achieve *in situ* TiC reinforced β phase TMCs [23], [126]. Decomposition of Mo_2C particles into Mo and C took place during laser melting. Decomposed Mo dissolved into the Ti matrix. The whisker shaped TiC particles dispersed homogeneously within the matrix is achieved. The authors claimed a different TiC formation mechanism than previous studies proposed. According to their hypothesis, decomposed C from Mo_2C directly reacts with Ti rather than dissolving in it. They claimed that if the molten material temperature remains below 2483°C, Ti directly reacts with Ti with the combustion mechanism. On the other hand, when a parameter set resulting in higher energy density is used, the melt pool temperature increases, and C dissolves in liquid Ti. Finer TiC particles were observed when higher energy densities were used. They argue that the dissolution-precipitation formation of TiC at higher energy density resulted in finer TiC particles, whereas the direct reaction of Ti and C resulted in coarser particles. Microstructures of two different energy density levels are given in Figure 2.10.
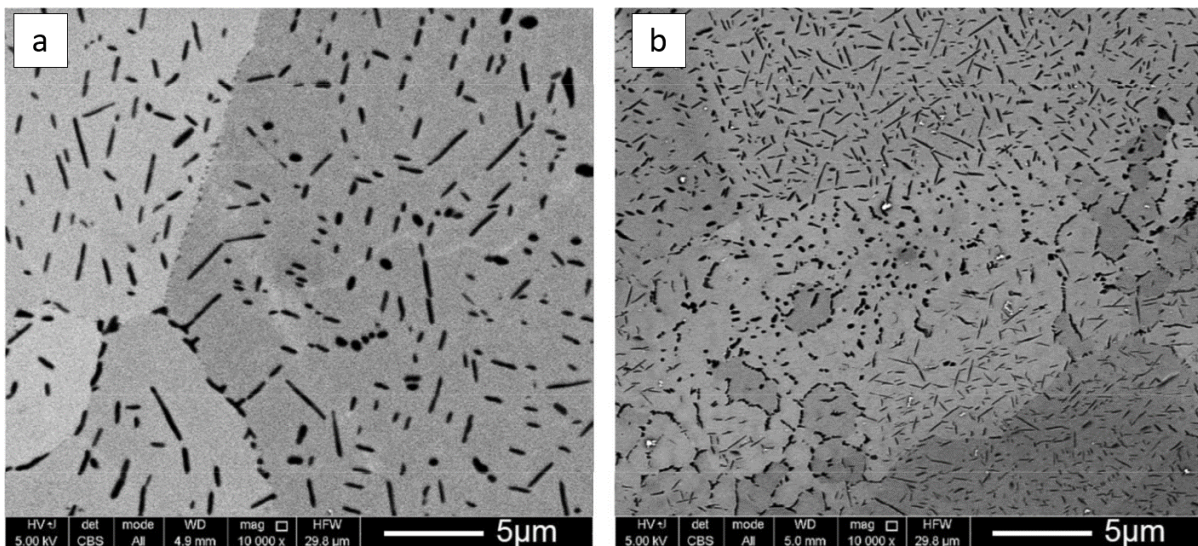
Figure 2.10. Microstructure of TiC reinforced TMC composites at two different energy input levels (a) low energy density, (b) high energy density [23].

Marangoni convection has a significant function for the fine particle distribution of SLMed MMCs. High heat gradient within the melt pool results in surface tension

differences. These differences cause the Marangoni convection within the melt pool and provide its mixture [27], [133]. This convection helps homogeneous distribution of the reinforcement particles within the matrix [19], [20], [129], [131]. The rapid nature of the SLM process and Marangoni convection creates a unique combination for the manufacture of MMCs. One of the biggest issues for SLMed composites is the preparation of the powder feedstock. A homogeneous feedstock with spherical morphology and optimum particle size distribution is the key to good part quality.

Methods for TMC powder mixing are typically direct mixing and ball milling [27]. Although ball milling provides a good particle intermixing, even to nanoscale particle dispersion, processed powder's flowability can reduce due to the high deformation of particles [128], [134], [135]. In comparison, the direct powder mixing method results in a more limited intermixing but reduced mechanical damage/particle shape change [27]. Feedstock particles should have an acceptable flowability to cover all the layer uniformly during SLM [27], [32], [136]. The morphology of the starting powder is the key to its flowability and packing capabilities [53], [136]. To manufacture MMCs with SLM, therefore, requires an efficient methodology for the production of spherical powder of mixed chemistry, which will generate the desired MMC microstructure upon laser processing. Direct mixing is a suitable candidate for SLM feedstock preparation, with the additional flexibility of enabling standard Ti-based feedstock powder to be readily mixed with a range of secondary phase chemistries/ratios.

Chapter 3: Materials and Methodology

3.1. Materials

3.1.1. Ti6Al4V Alloy Powder

Gas atomised Ti6Al4V (grade 23) powder supplied from Carpenter Additive was used as the feedstock material. The composition of the powder provided by the manufacturer is given in Table 3.1.

Table 3.1. Chemical composition (wt.%) of Ti6Al4V powder provided by the manufacturer.

Ti	Al	V	Fe	O	C	N	H
Balance	5.5-6.50	3.50-4.50	0.25	0.13	0.08	0.03	0.0125

Y	Other, each		Other, total				
0.005	<0.10		<0.40				

Malvern Mastersizer 3000 laser diffraction particle size analyser was used to measure the particle size in the wet measurement mode. Figure 3.1 shows the particle size

distribution. Ten individual measurements are displayed in the graph. A perfect overlap between repeating measurements confirms homogeneous particle size distribution. D10, D50 and D90 were measured as 21.7 µm, 31.6 µm and 45.3 µm, respectively. SEM images of the particles are given in Figure 3.2. Most of the particles are spherical, with some irregularities, which are typical for gas atomised powder [137]. Particle size distribution and morphology are suitable for use in selective laser melting [36].
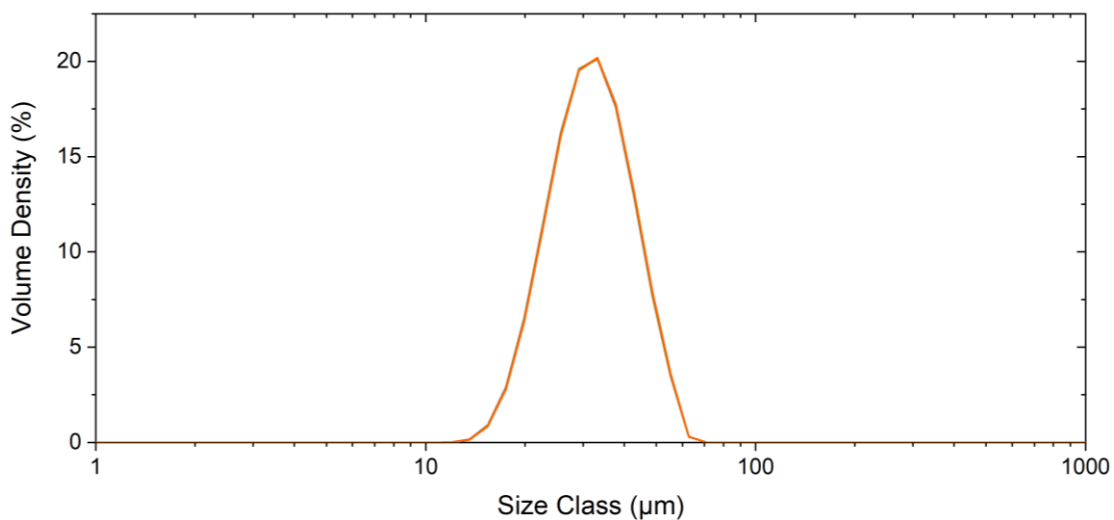
Figure 3.1. Particle size distribution of Ti6Al4V powder.
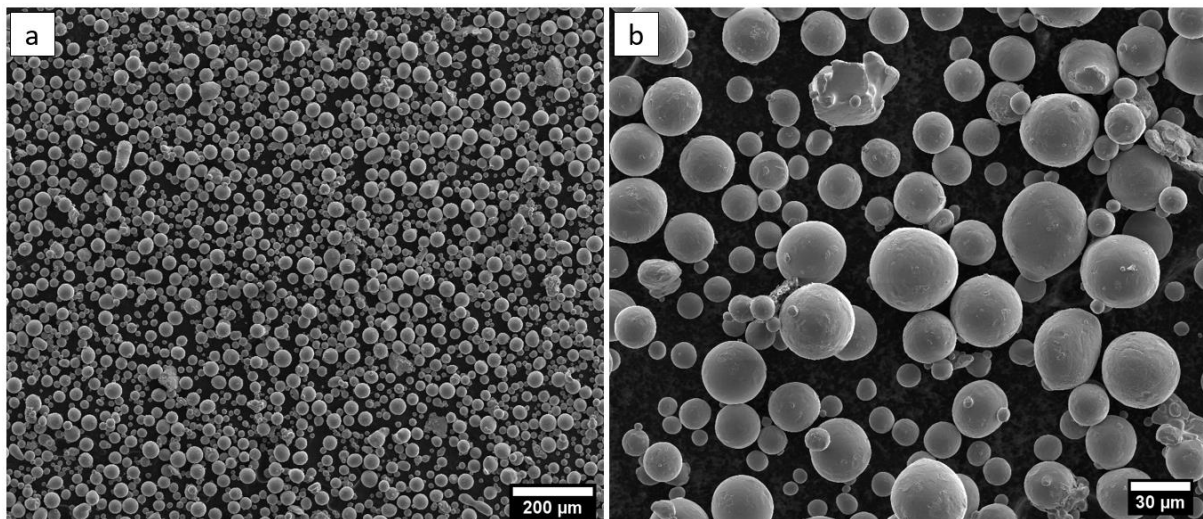
Figure 3.2. Secondary electron SEM images of Ti6Al4V powder at (a) low and (b) high magnifications.

3.1.2. Graphite Flake

Graphite flakes (99%, metals basis) sourced from Alfa Aesar were used as the carbon source. The median flake size was reported between 7.00-11.00 μm by the manufacturer. SEM images of flakes are shown in Figure 3.3. Graphite flakes had a plate-like morphology and lamellar shape.
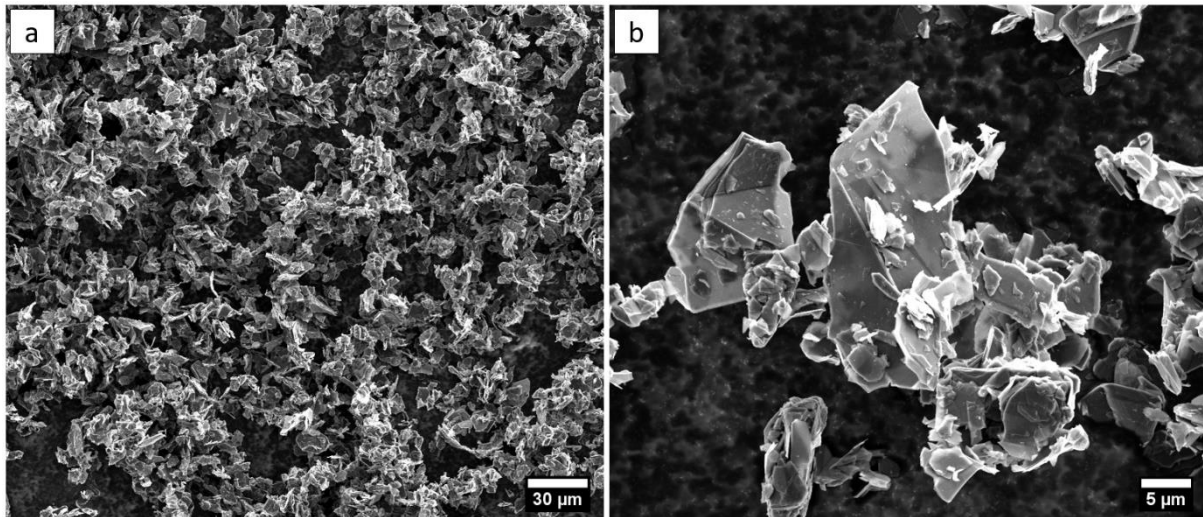
Figure 3.3. Secondary electron SEM images of graphite flakes at (a) low and (b) high magnifications.

3.1.3. Powder Processing

99 wt.% Ti6Al4V powder and 1 wt.% graphite flake were directly mixed in a planetary ball mill (PM 100, Retsch) to achieve composite powder feedstock. Grinding balls were not placed into the mixing jar to preserve the original morphology of the Ti6Al4V particles. PM 100 planetary ball mill has a large rotating sun wheel on the bottom. Over the sun wheel, the powder jar is eccentrically positioned (Figure 3.4). The sun wheel and powder jar rotate in opposite directions. The high energy created due to the speed difference between the sun wheel and the jar provides an efficient powder mix. Figure 3.4 shows the working principles of the PM 100 ball mill from the top view.
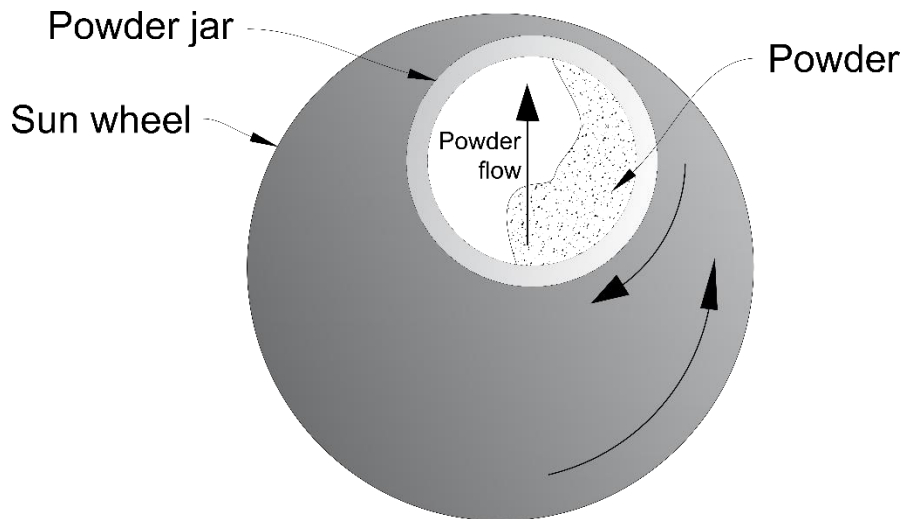
Figure 3.4. Working mechanism of the planetary ball mill.

3.2. Selective laser melting processing

Selective laser melting (SLM) is the direct manufacturing of components from the computer-aided design (CAD) files using a laser energy source in a layer by layer fashion. There are several steps of component manufacturing using SLM. First, the CAD data file, usually in .stl (stereolithography) format, needs to be sliced according to the equipment system and preferred layer thickness. There are several software packages capable of doing this process. Autodesk Netfabb Premium version 2019 and 2020 are used for all parameter assignment, part positioning, final data slicing and exporting processes in this study.

Two different pieces of equipment were used for selective laser melting (SLM) processing. Although both are SLM equipment, there are some differences between their working principles and energy sources.

3.2.1. Renishaw SLM 125 System

Renishaw SLM 125 is a selective laser melting machine equipped with a continuous wave laser controlled to create a pulsed regime effect. Therefore, this laser will be referred to as a pulsed wave laser within this document. It is a fibre laser with a maximum power of 200 W, 1070 nm wavelength and 70 μm spot size [61]. The laser in this system is fired for a defined duration (exposure time) and then shuts off. After

that, it moves for a specified distance (point distance) and fires during the exposure time again. This cycle is repeated until the liner scan of the laser is completed. The speed laser travels between individual laser exposures (jump speed) is fixed at 4.1 m/s for SLM 125 [61]. Following formulations were employed to calculate volumetric energy density (Equation 3.1), linear energy density (Equation 3.2) and average travel speed (Equation 3.3) when SLM 125 was used:

$$E_v = \frac{P \times t_{exp}}{x_{pd} \times h \times l} \tag{3.1}$$

$$E_l = \frac{P \times t_{exp}}{x_{pd}} \tag{3.2}$$

$$v = \frac{x_{pd}}{t_{exp} + (\frac{x_{pd}}{c})} \tag{3.3}$$

P is the laser power, t_{exp} is the exposure time, x_{pd} is the point distance, h is the hatch space, l is the layer thickness, and C is the jump speed in these equations.

SLM 125's outer view is given in Figure 3.5. The equipment is controlled through the touchscreen on the front face. The build is monitored from the viewing window against any failures during a build.

Figure 3.5. Renishaw SLM 125's outer view.

Interior parts of SLM 125 are illustrated in Figure 3.6. A powder hooper provides the powder feed. First, the required dosage of the powder is released from the powder hopper. After that, the recoater blade moves onto the base plate and creates an evenly coated powder layer on it. The excessive powder is fed into the overflow for reuse. After covering the base plate with powder, the pulsed laser processes the layer according to the corresponding slice data. The base plate is 125 mm $\times$ 125 mm square with approximately 10 mm thickness. It was made from commercially pure titanium alloy.
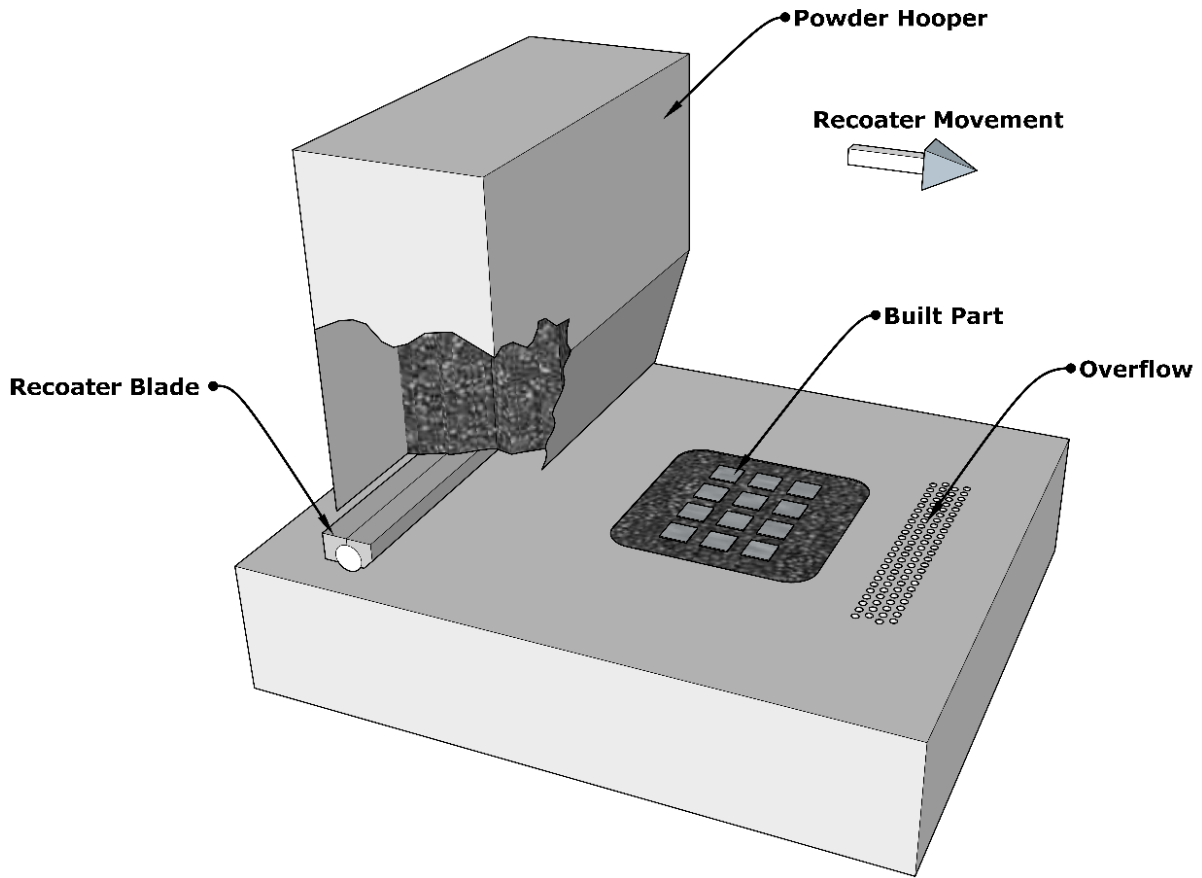
Figure 3.6. Renishaw SLM125's interior parts.

3.2.2. Aconity Mini System

Aconity Mini was the other SLM system used in this study. It is equipped with a 1070 nm wavelength, 200 W continuous-wave fibre laser having 80 μm spot size [138]. When Aconity Mini was used, the following equations were utilised for volumetric energy density (Equation 3.4) and linear energy density (Equation 3.5) calculations:

$$E_v = \frac{P}{v \times h \times l} \tag{3.4}$$

$$E_l = \frac{P}{v} \tag{3.5}$$

P is the laser power, v is the laser travel speed, h is the hatch distance, and l is the layer thickness in these equations.

The outer view of the Aconity Mini system is given in Figure 3.7. Aconity Mini is controlled by a process control computer, and the data input is performed through the conventional mice and keyboard. It has a separate build chamber and control unit and is a highly flexible system.

Figure 3.7. Outer view of the Aconity Mini system [138].

Interior parts of the Aconity Mini is represented in Figure 3.8. It has a cylindrical baseplate with ⌀140 mm diameter and approximately 10mm thickness. It has a different powder feed system than Renishaw AM 125. A powder feed plate with the same diameter as the build base plate is used rather than a powder hopper. The powder feed plate is raised to provide enough powder, and then the recoater blade moves over it and transports powder over the base plate. The excessive powder is collected in the overflow reservoir. The powder feed plate provides more efficiency in terms of powder consumption over the powder hopper. Some of the powder is lost due to minor leakages on the behind of Renishaw SLM 125's powder hopper. Aconity Mini's powder feed

system, on the other hand, provides a more efficient powder feed, and less amount of powder is needed for the exact build height.
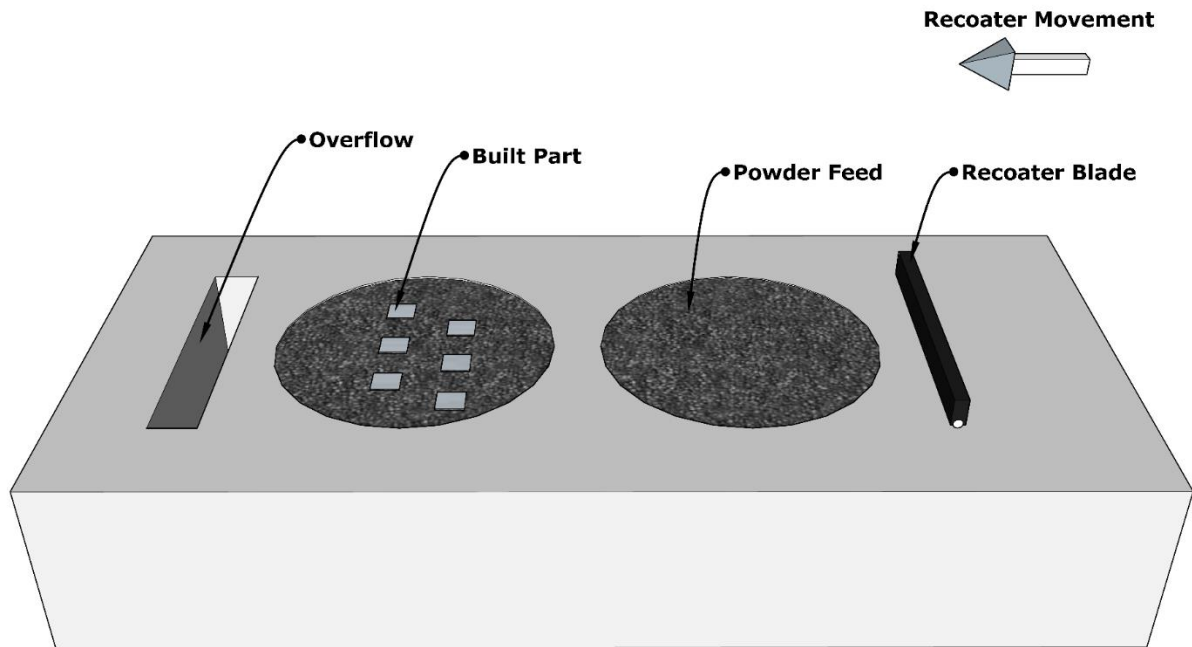
Figure 3.8. Aconity Mini system's interiors.

3.2.3. Experimental Design

Response surface methods (RSM) were used for SLM parameter generation and statistical analysis of the results in this study. RSM is an experimental design and analysis tool used to investigate the effects of experimental conditions on a response [139], [140], such as hardness. Two different response surface methods, Box-Behnken design and central composite design (CCD), were used. Box-Behnken design requires fewer experiments than CCD, and at least three different variables are needed. Therefore, it is a more suitable design to reduce the number of samples when three or more variables are included. Figure 3.9(a) shows parameter levels for a Box-Behnken design when three variables are used.

On the other hand, Central composite design requires more runs for the same amount of variables. However, more variable levels, including extremes, are also tested with CCD. Figure 3.9(b) shows parameter levels for CCD when two parameters are tested. Box-Behnken design was used to evaluate three different parameters (exposure time,

point distance, hatch distance) of a pulsed wave laser system with fewer runs, whereas CCD design was used to assess two different parameters (laser travel speed, hatch distance) of a continuous wave laser system with more precision and to see the effect of extremes. Minitab 18 software package was used for parameter generation and statistical analyses of both experimental designs. Samples were placed on the SLM baseplates in a random order provided by the software for each run.
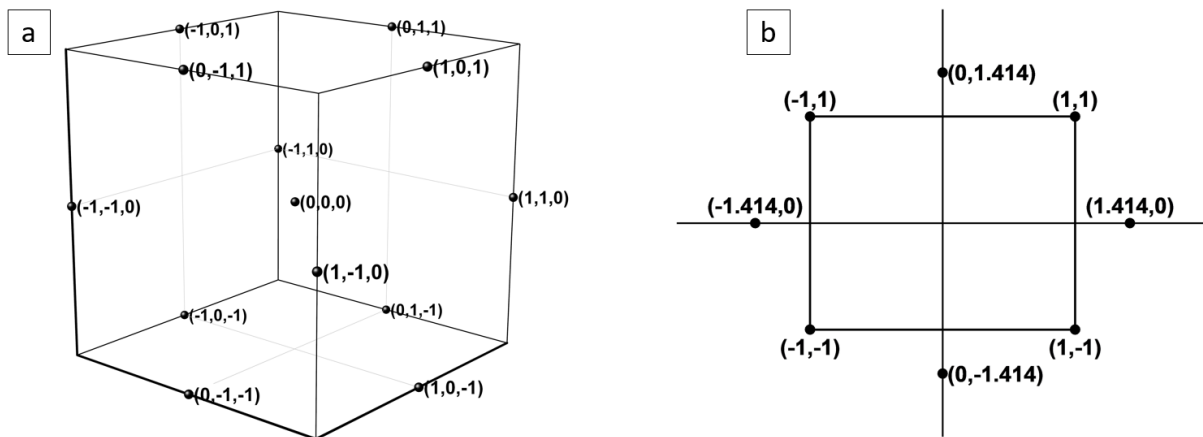
Figure 3.9. Levels of different variables in (a) Box-Behnken design, (b) central composite design (CCD).

3.3. Characterisation

3.3.1. Sample Preparation

Samples were cut using a Struers Secotom-50 precision cutting machine. Buehler SimpliMet hot mounting press was used to embed samples into conductive bakelite. Mounted samples were ground and polished using a Buehler AutoMet grinder-polisher. Respectively, P800, P1200, P2500 and P4000 grit papers were used for grinding. 150 rpm plate speed, 40 rpm head speed, complimentary head rotation direction and 5 N/sample force were applied for one minute for each grinding step. Next, ground samples were polished using colloidal silica suspension and MD-Chem polishing cloth supplied from Struers. 10 N/sample force was used for 20 minutes during polishing, whereas other parameters were kept the same with the grinding step. After that, samples were cleaned in isopropyl alcohol using an ultrasonic bath for 5 minutes. Lastly, samples were polished using a colloidal silica-free polishing cloth for

10 minutes to clean the surface from sticky colloidal silica. Before and after each step, samples were cleaned using isopropyl alcohol. Polished samples were etched in the boiling solution of 95 vol.% water, 4 vol.% HCl and 1 vol.% H_2SO_4 solution for 20 minutes.

3.3.2. Optical Microscopy

Nikon Eclipse ME600 Metallurgical Microscope was used for optical microscopy imaging. It was exploited for microstructural examination and porosity analysis. Different methods have been employed for the porosity evaluation of additively manufactured parts by researchers. Archimedes method and optical image analysis are two common methods. However, previous studies showed that the Archimedes method might not give repeatable and accurate results, particularly when the relative density of the parts is high [61], [141]. Additionally, optical measurement provides more opportunities to evaluate the morphology of the pores. Hence, porosity measurements were performed using optical image analysis in this study.

Images of polished but not yet etched samples were taken on the planes parallel to the build direction. These images were stitched and then cropped into the same size to obtain consistent results. Stitched images thresholded and converted to black and white images. The ratio of black pixels (pores) to the white ones (solid metal) is calculated as relative porosity. Morphology of pores is used to evaluate defect types. All steps, including stitching and morphology examination, were performed using the ImageJ software pack's FijiJ distribution [142].

3.3.3. X-ray Diffraction Analysis

The microstructure of powder materials and all samples with different compositions were checked through X-ray diffraction (XRD) analysis. Bruker D2 Phaser X-ray diffractometer was used with Cu-Kα radiation, 30kV acceleration voltage, 0.2s step time, 0.02° step size and 20°-90° scanning window for data acquisition. International Centre for Diffraction Data (ICDD)'s powder diffraction file (PDF) database is used for the reference patterns. Following PDF records were used to define phases: 00-044-

1294 for α-titanium, 04-003-7272 for β-titanium, 00-056-0153 for graphite and 00-031-1400 for titanium carbide.

3.3.4. Scanning Electron Microscopy

Scanning electron microscope (SEM) images of samples were taken using FEI Inspect F50 equipped with a field emission gun (FEG) and an Oxford Instruments X-Max 80 EDS detector. An acceleration voltage of 20kV and a working distance of ~10 mm is used for SEM data acquisition.

3.3.4.a. Electron backscatter diffraction analysis

Electron backscatter diffraction (EBSD) is a versatile tool to examine orientation changes alongside the crystal samples. High-resolution large area EBSD scans were performed to investigate grain orientations of the selective laser melted samples. JEOL 7900F field emission gun (FEG) SEM equipped with Oxford Instruments HKL Advanced Symmetry EBSD System was used for EBSD data acquisition. 0.06 μm (Chapter 4) and 0.1 μm (Chapter 5 and 6) step sizes were used during acquisition. Samples were tilted to 70°, and an accelerating voltage of 20kV was used. The working distance was ~13 mm during acquisition. Scans were performed in parallel and perpendicular planes relative to the build direction. Parent β grain reconstruction was performed according to the Burgers orientation relationship in which $\{0111\}_\alpha//\{110\}_\beta$ and $\langle11\bar{2}0\rangle_\alpha//\langle111\rangle_\beta$. All data analysis and parent β grain reconstruction were performed using Oxford Instruments' AZtecCrystal software package.

3.3.5. Hardness Test

Vickers microhardness (HV) of the samples were measured using an automated Struers Durascan Hardness Tester. All the tests were performed in compliance with the ASTM E384 standard [143]. 500g load (HV 0.5) was applied for each indent, and seven measurements were conducted for each sample. The mean of seven measurements was reported as the hardness. A distance at least five times larger than

the indent diagonal were placed between individual measurements. Pores were avoided during measurements to rule out their effect.

3.3.6. X-ray Computed Tomography

X-ray computer tomography (XCT) analysis were performed to evaluate morphology and distribution of pores in 3D. XCT scans were carried out using a Zeiss Xradia 620 Versa X-ray CT scanner. Scanning parameters were set as follows: 4X lens, 110 kV acceleration voltage, 141 µA filament current. A voxel size of 0.85 µm was used to precisely image pores. Dragonfly version 2020.2 software was used for analysing and 3D reconstruction. Pores smaller than 50 voxels in size was removed to reduce the noise.

3.3.7. Wear Test

The tribological properties of selective laser melted parts were evaluated using dry sliding reciprocating wear test. Tests were performed using Bruker UMT-2 TriboLab in ball on plate configuration, according to ASTM G133-05 standard [144]. 0.5 N normal load, 2.5mm stroke distance, 1Hz frequency resulting in a total sliding distance of 54 m were used as testing parameters. Three different balls, AISI 52100 hardened bearing steel (grade 10), Si_3N_4 (grade 5) and Al_2O_3 (grade 5) ceramics, were used as counterpart materials. Composition of AISI 52100 bearing steel is given in Table 3.2. A conventionally processed Ti6Al4V (grade 23) plate sourced from William Gregor Ltd. was also used for wear tests to compare frictional properties of SLMed and conventional Ti6Al4V.

Table 3.2. Chemical composition of AISI 52100 hardened bearing steel (wt.%) [145].

Fe	C	Cr	Mn	Si	P	S
Balance	0.95-1.10	1.30-1.60	Max 0.25	0.15-0.30	Max 0.03	Max 0.025

3.3.8. Optical profilometry

Optical profilometry was used to evaluate the as-built surface texture of selective laser melted parts. Additionally, it was utilised to calculate the wear volume of the base

materials and counterpart balls. A common approach to measure wear volume is estimating it by extracting its linear depth profile from multiple positions through its width. Another alternative is measuring weight loss after the wear test. Even though these methods have been useful for evaluating the volume loss, they cannot precisely detect wear rate. This is particularly important for dry tests because the stick-slip mechanism may cause irregular wear track boundaries, and linear profile measurement may give wrong estimations. Therefore, a different approach is used in this study to measure wear volume correctly.

A stitched optical profilometry image showing the whole wear track was taken to measure the wear volume. After that, four different corners of the undamaged surface were used to perfectly level the surface as parallel to the imaging plane (Figure 3.10(a)). Then, using the volume calculation option in the Bruker's Vision 64 software, the total volume of the wear track was calculated (Figure 3.10(b)). This option gives the volume by placing a plane at a given height and calculating the volume below this plane. By adjusting the plane height at the undamaged surface level, a reliable wear volume was calculated. Not only for the wear volume loss but also wear track morphology were also evaluated by means of optical profilometry.
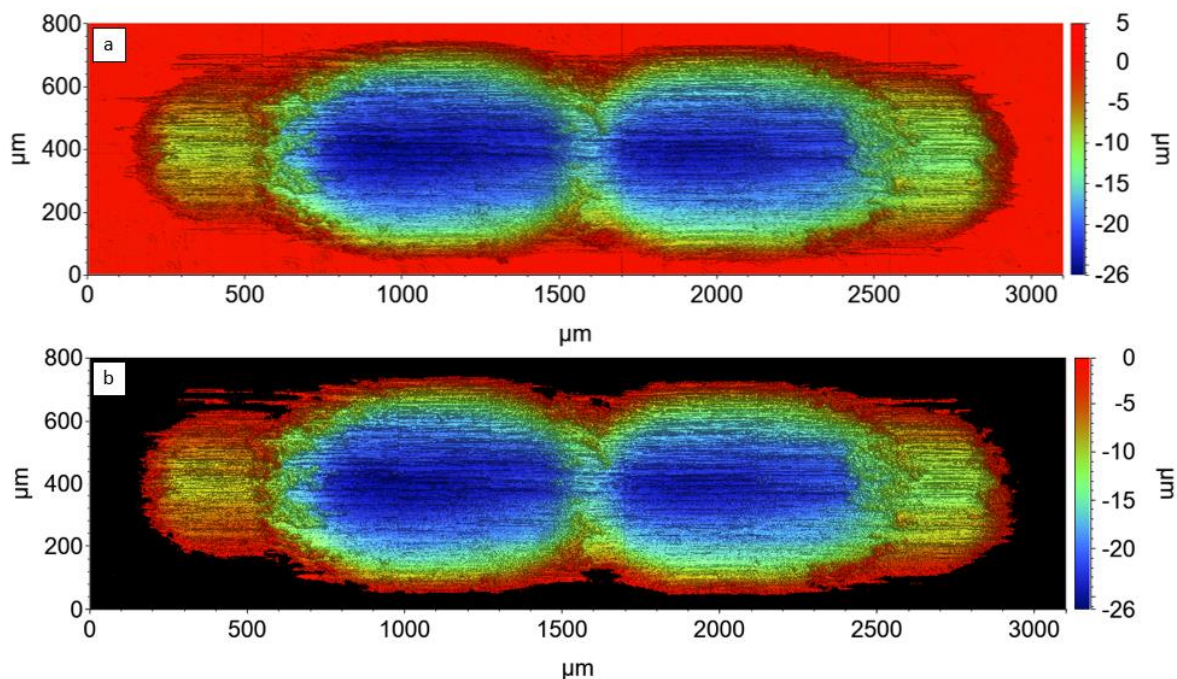
Figure 3.10. An example showing the steps followed for wear volume calculation: (a) perfectly levelled image and (b) following wear volume calculation.

When the wear rate of the counterpart ball was calculated, a slightly different route was followed. Similar to the base material, a stitched image of the wear scar on the ball was taken using optical profilometry. Then, an additional spherical shape removal tool is used to flatten the spherical surface. Lastly, the same wear volume calculation method with the base material was followed.

Specific wear rate was used to evaluate the wear performance of base materials and counterpart balls in this study. Specific wear rate was calculated using the following formulation:

$$Specific\ wear\ rate = \frac{Volume\ loss\ (mm^3)}{Sliding\ distance\ (m) \times Normal force\ (N)} \tag{3.6}$$

3.3.9. *In situ* SEM Scratch Test

In situ SEM scratch tests were performed to evaluate behaviours of different materials against frictional forces. Alemnis *in situ* nano indenter system installed within a FEI Nova NanoSEM 450 were utilised for these tests. A piezoelectric actuator is employed to push the indenter tip towards the material surface in this system. A conical diamond tip with a radius of 0.7 μm was used for tests. 25 mN normal load was applied with 5mN/s ramp-up speed. After 25mN load was reached, tests were performed for 100 μm length with a speed of 1 μm/s. *In situ* and post-mortem imaging were carried out for the examination.

Chapter 4: Assessing Feasibility of Directly Mixed Ti6Al4V and Carbon Feedstocks for Selective Laser Melting

4.1. Introduction

This chapter investigates the manufacture of *in situ* titanium carbide (TiC) reinforced Ti6Al4V composites using Renishaw SLM125 selective laser melting (SLM) machine equipped with a pulsed wave laser. The aim is to evaluate the feasibility of selective laser melting (SLM) of directly mixed carbon-Ti6Al4V composite powder feedstock. Mixed powders are examined using X-ray diffraction (XRD) and scanning electron microscope (SEM) analysis. During SLM manufacture of composite parts, exposure time, point distance and hatch distance are varied as processing parameters, and porosity of composites was evaluated using 2D optical images and 3D X-ray computer tomography (XCT) data. TiC presence in manufactured samples is verified with SEM images and XRD data. Finally, the hardness of composites is measured and compared with a plain sample. This chapter proved that directly mixed carbon-Ti6Al4V

composite powder feedstock can be used to manufacture *in situ* Ti6Al4V-TiC composites.

4.2. Experimental

Pre-alloyed Ti6Al4V powder and graphite flakes were mixed in the planetary ball mill for 60mins at 500rpm speed. Mixed powders were processed with Renishaw SLM125 system, which has a pulsed wave laser. A range of point distance, exposure time and hatch distance were used, and Box-Behnken response surface methodology is used for statistical analysis. Table 4.1 shows processing parameters for Ti6Al4V-TiC composites and plain Ti6Al4V samples. Laser power and layer thickness were kept constant at 200W and 30 μm, respectively, for all parameters. Samples had a dimension of 15mm × 15mm × 2mm and were cut parallel to the build direction for examination (Figure 4.1). An area of 6200μm × 600μm was examined for porosity calculations for all samples. 20 kV accelerating voltage and 0.06 μm step size are used for EBSD analysis. XCT scan was performed using 0.85 μm voxel size, 100 kV acceleration voltage, 141 μA filament current and 4× magnification lens.

Table 4.1. Processing parameters used with Renishaw SLM125.

Sample Number	Hatch Space (μm)	Exposure Time (μs)	Point Distance (μm)	Volumetric Energy Density (J/mm³)	Linear Energy Density (J/mm)	Average Travel Speed (mm/s)
1	90	60	63.5	70	0.189	841
2	110	60	63.5	57.3	0.189	841
3	90	74	63.5	86.3	0.233	710
4	110	74	63.5	70.6	0.233	710
5	90	67	57	87.1	0.235	705
6	110	67	57	71.2	0.235	705
7	90	67	70	70.9	0.191	833
8	110	70	67	63.3	0.209	776
9	100	60	57	70.2	0.211	771
10	100	74	57	86.5	0.26	648
11	100	60	70	57.1	0.171	908
12	100	74	70	70.5	0.211	769
13	100	67	63.5	70.3	0.211	770
14	100	67	63.5	70.3	0.211	770
15	100	67	63.5	70.3	0.211	770
Plain Ti6Al4V	95	70	60	81.9	0.23	709
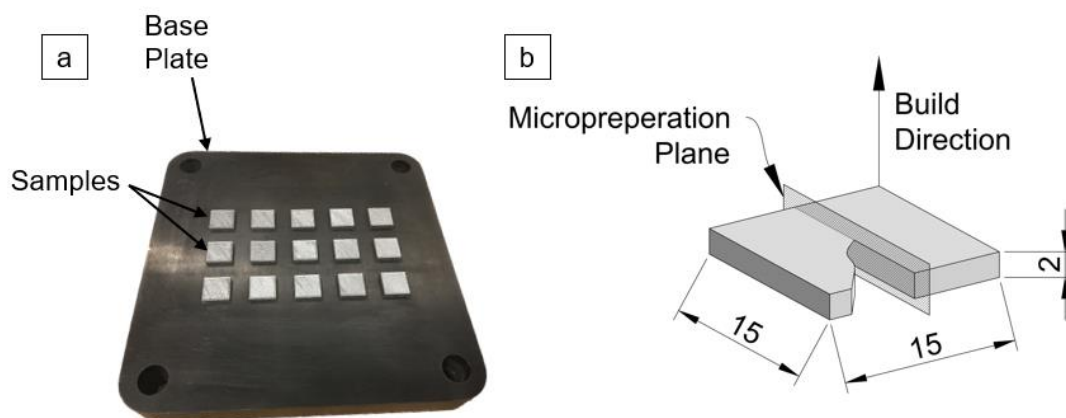
Figure 4.1. (a) processed parts on baseplate, (b) sample dimensions (in mm) and examination plane.

4.3. Feedstock Powder

The morphologies of the parent Ti6Al4V particles and graphite flakes were evaluated by SEM (Figure 4.2). The Ti6Al4V powders, fabricated by atomisation, are 0-53 μm size, with predominantly near-spherical morphology. Some irregular shaped Ti6Al4V particles are observed (Figure 4.2 (a)), together with small satellite particles adhering to bigger particles (Figure 4.2(a,c)), which both arise from the atomisation manufacturing process [137]. Most satellite particles are <10 μm in size and spherical in shape (Figure 4.2(a,c), white arrows), with some irregular adhered particles also present. Graphite particles exhibit a typical plate-like form (Figure 4.2(d)).

After 1h of mixing in the planetary mill, the surfaces of Ti6Al4V particles are coated by carbon (Figure 4.3). After 1h, a near-continuous carbon coverage of the surface was observed. The carbon coating has visibly varying thickness, which gives rise to a distinctive mottled pattern (Figure 4.3(b)) where the thicker carbon regions emit fewer secondary electrons (dark grey SE contrast), than adjacent regions with a thinner carbon layer overlaying the Ti6Al4V (light grey SE contrast). At higher magnification it can be seen that the graphite has been highly deformed by the milling process, producing an adhered film of agglomerated nanoparticles (Figure 4.3(d)).

At the junctions of big satellite particles with their parent particle, bands of reduced/minimal carbon coverage were observed due to the shielding of the junction region from direct mechanical compression during milling impacts (Figure 4.3(a,c), white arrows). Smaller satellite/adhered particles generally did not exhibit carbon-free contact areas (red arrows in Figure 4.3(a,c)) due to either the lack of shielding effect or because they are mobile. It is likely that mixing impacts will break off small and poorly bonded satellite particles, which can then adhere elsewhere to the large Ti6Al4V particles during the subsequent mixing process.

Some independent carbon particles were observed in the powder after 1h mixing. These residual particles had a different disc-like morphology (Figure 4.3(a), yellow arrow) compared to the original graphite flakes (Figure 4.2(d)), as a result of repeated

compressive impacts and fracture events due to the interaction with the larger, harder Ti6Al4V particles during mixing.
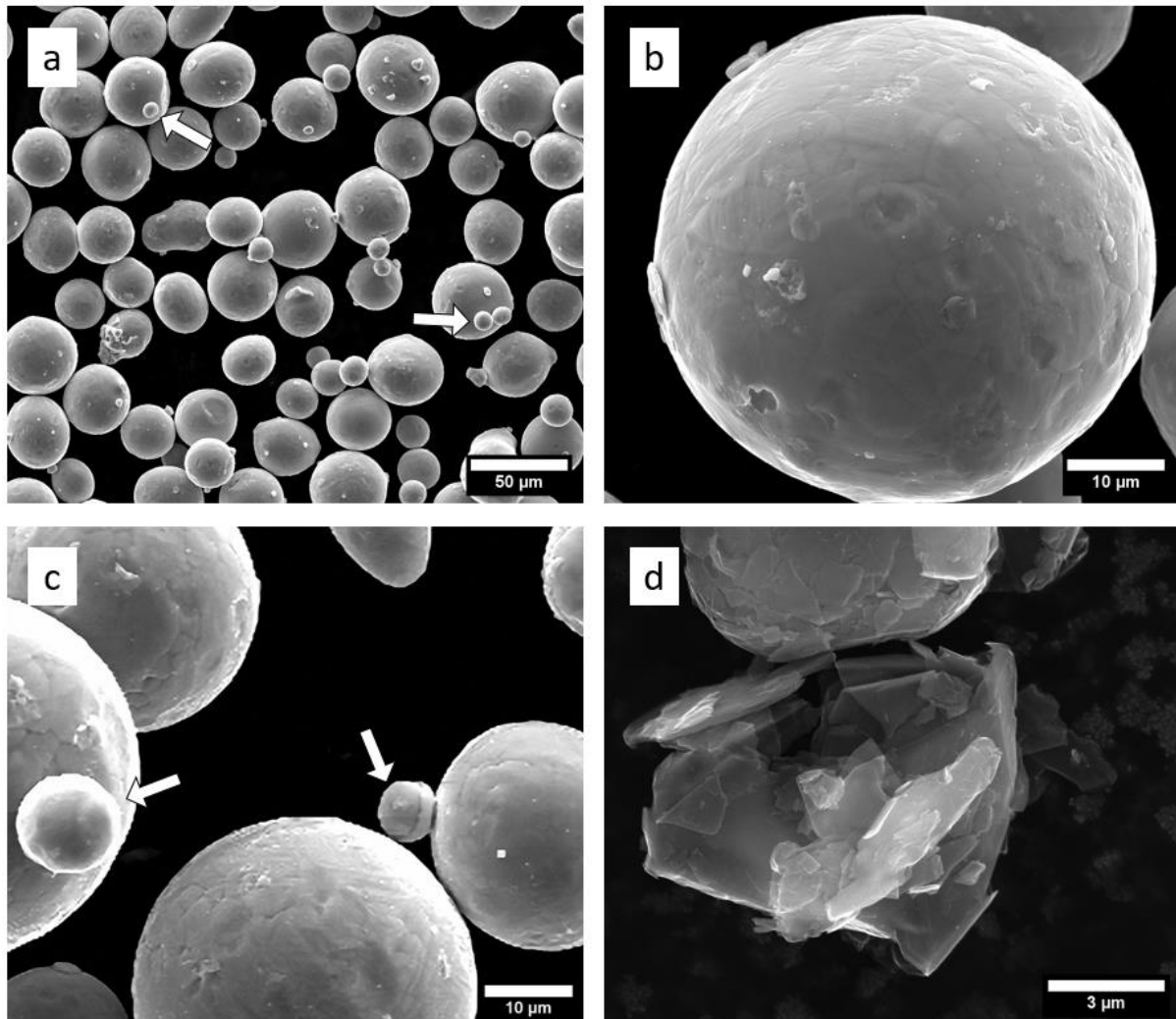
Figure 4.2. Secondary electron (SE) SEM images of (a,b) parent Ti6Al4V particles, (c) satellite particles on Ti6Al4V powder, and (d) graphite flake particles. Examples of satellite particles are indicated by white arrows.

The modification of the graphite during the mixing process was investigated by X-ray diffraction. Figure 4.4 shows representative XRD patterns of the graphite flakes, parent Ti6Al4V powder and mixed Ti6Al4V–carbon composite powder. For the composite, there are no diffraction peaks that indicate any chemical reaction during mixing, such as crystalline TiC formation. After 1h of mixing, the (0002) graphite peak has effectively disappeared. This is consistent with the transformation of crystalline graphite to amorphous carbon-nanoparticles during mixing (Figure 4.3).

As expected, after mixing with the soft graphite, the Ti6Al4V particles still exhibit good crystallinity (Figure 4.4). Importantly, no visible deformation was observed of Ti6Al4V particles after 1h of mixing, and the Ti6Al4V-carbon composite particles were therefore suitable for subsequent SLM processing.
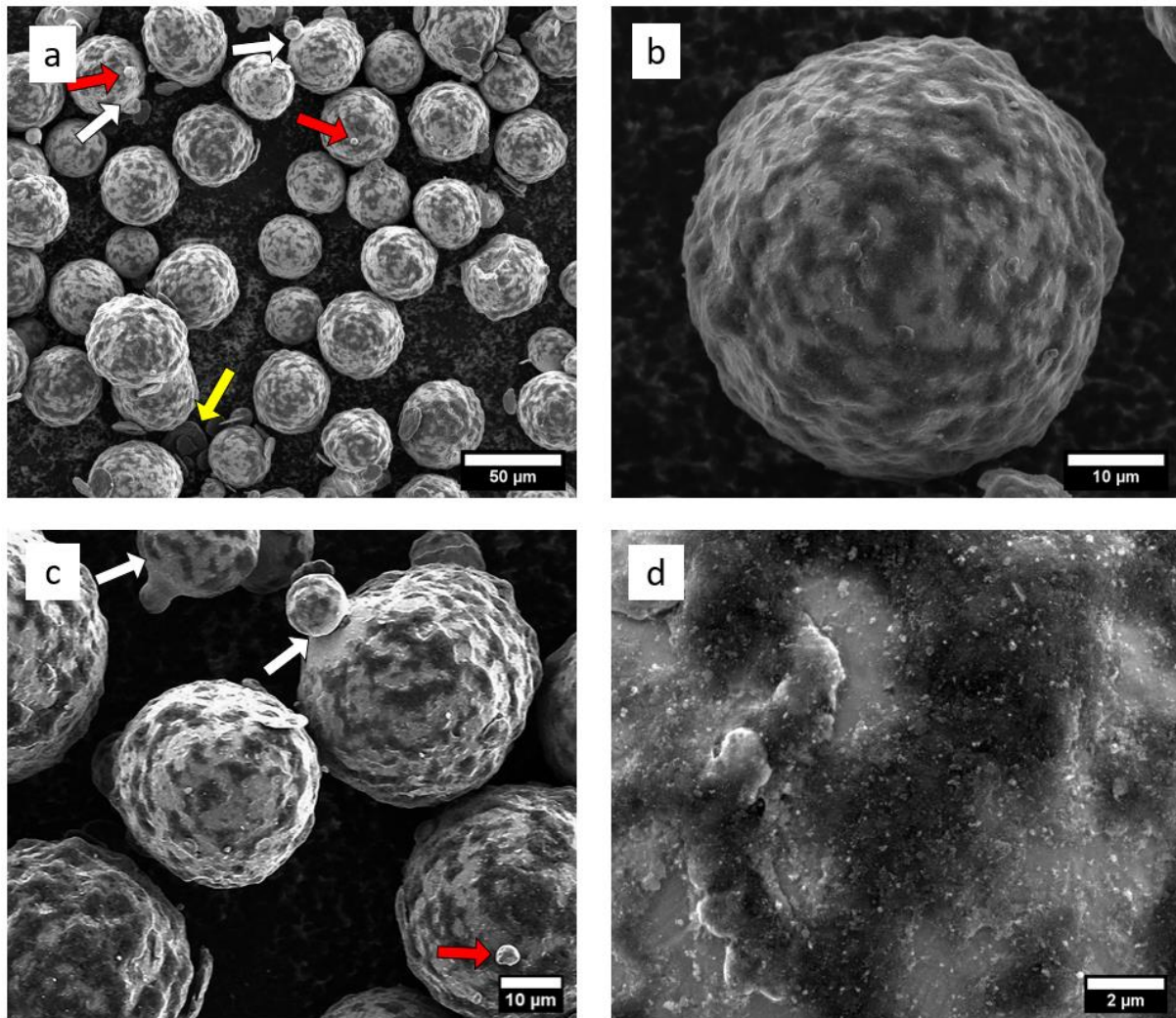
Figure 4.3. SE SEM images of mixed Ti6Al4V and graphite flake particles resulting in (a) composite Ti6Al4V-carbon particles and deformed carbon discs (yellow arrows). Larger (white arrows) and smaller (red arrows) satellite particles are still attached to the large Ti6Al4V particles; (b) carbon coated Ti6Al4V, with mottled contrast due to variable <2micron thickness of the carbon coating; (c) uncoated/carbon deficient regions around junctions of large satellite particles with supporting particle (white arrows); (d) carbon coated Ti6Al4V particle surface, exhibiting an adhered agglomeration of carbon nanoparticles.
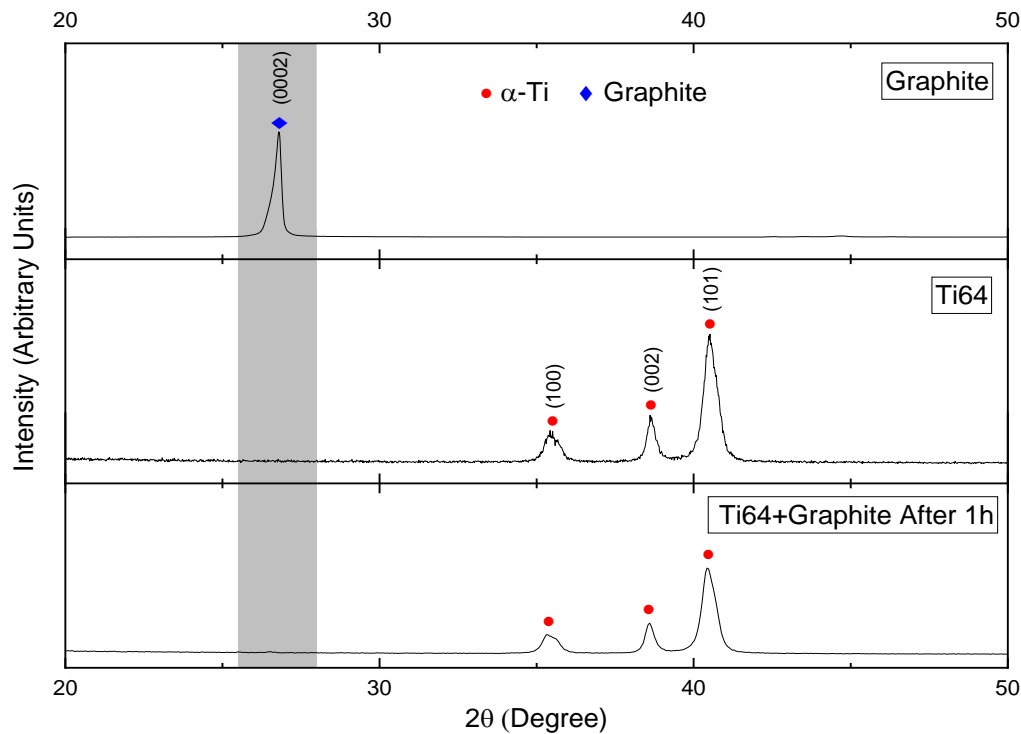
Figure 4.4. XRD patterns of graphite flakes, parent Ti6Al4V powder (Ti64), and the mixed Ti64+graphite powder after 1h of mixing.

4.4. SLM Processed Composites

The mixed Ti6Al4V–carbon composite powder was processed by SLM using 15 conditions listed in Table 4.1, and the cross-sectional microstructure parallel to the build direction analysed (Figure 4.1(b)).

4.4.1. Porosity of SLM Ti64 Composites

The porosity of the SLM Ti6Al4V–carbon samples varied from 3.6 – 0.5% (Figure 4.5(a), from optical measurements of areal porosity), giving corresponding material densities of between 96.4% and 99.5%. Response surface regression indicates that all three parameters used (hatch distance, exposure time, point distance) are significant for porosity when the confidence level is set to 95. p-values of hatch distance, exposure time and point distance are detected as 0.022, 0.046 and 0.035, respectively. Figure 4.5(a) shows how porosity of the SLM Ti6Al4V–carbon samples depend on energy density, with low energy densities causing higher porosity. Although the increase of energy density creates denser samples, the highest relative density is observed after

medium energy density processing (70.2 J/mm³ and 70.3 J/mm³). One sample processed with 70.6 J/mm³ had a higher porosity than expected.

Using areal porosity analysis, the number of pores in pore size ranges of 5-100 μm² up to 900-1000 μm² porosity area (100 μm² steps) was analysed for the samples processed with different energy density (Figure 4.5(b)). For a given cross-sectional area (6200μm × 600μm), lower energy density samples had the highest number of pores and number of large pores. The increasing SLM energy density creates a trend of pore count reduction. Figure 4.6 shows the change of porosity morphology in the Ti6Al4V−carbon composites depending on scanning parameters. The two lowest energy density samples (57.1 J/mm³ and 57.3 J/mm³) had more large irregular pores than others. This type of pore is associated with a lack of fusion of metal powders due to insufficient laser energy [39], [43], [98]. If the energy density is not high enough, it cannot melt particles completely, and the molten pool cannot reach the previous layer resulting in irregularly shaped big pores. Irregularity of pores reduces with increased energy density.
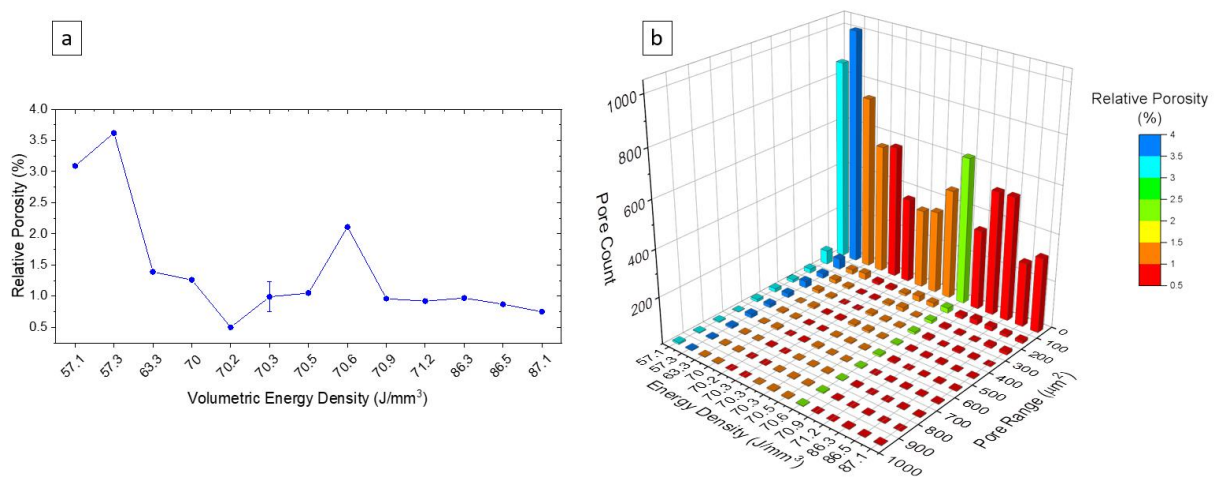
Figure 4.5. (a) Relative porosity of SLM Ti6Al4V−carbon composite with respect to a fully dense part for different SLM energy densities (error bar shows the standard error for multiple samples of the same energy density), (b) the number of pores for different pore size ranges and laser energy densities.

Figure 4.7 illustrates different porosity types resulting from different Ti6Al4V−carbon composite processing parameters. Irregularly shaped large pores in low energy density samples can be seen in Figure 4.7(a,b). Partially molten powder particles can be identified within the low and medium energy density samples (Figure 4.7(a,b,c)). At

high energy density the large lack of fusion defects disappear, with (most) defects smaller than the size of the original Ti6Al4V feedstock particles. These pores are still primarily irregular in shape and can have sharp edges (dashed square in Figure 4.7(d)). In addition to pores, there are also randomly distributed planar defects within the structure (Figure 4.7(c,d)) arising from unreacted carbon residue (Section 4.4.2).

To investigate the residual porosity in the Ti6Al4V–carbon composites in more detail, 3D volumetric porosities of low (57.3 J/mm^3) and medium (70.3 J/mm^3) energy density samples were analysed by X-ray computed tomography. Total volumetric porosities are calculated as 5.0% for the 57.3 J/mm^3 sample and 1.1% for the 70.3 J/mm^3 sample, a reduction of 78% with 57.3 J/mm$^3 \rightarrow$ 70.3 J/mm^3.

Figure 4.8(a,b) display the 3D distribution of pores reconstructed from the XCT analyses, with 0.85 μm voxel size and pores > 50 voxels plotted. Consistent with the 2D analysis, a significant reduction of both pore size and pore count is observed with increasing energy density 57.3 J/mm^3 (Figure 4.8 (a)) $\rightarrow$ 70.3 J/mm^3 (Figure 4.8 (b)).

Figure 4.8(e) compares the number of pores in different pore size ranges (individual pore volume) for the low (57.3 J/mm^3) and medium (70.3 J/mm^3) energy density samples. As the number of pores significantly reduces with increasing size, an incremental binning size is used to represent the data clearly. Pore binning size is chosen as 10 μm^3 between 30-100 μm^3, 100 μm^3 between 100-1000 μm^3, 1000 μm^3 between 1000-10,000 μm^3 and 10,000 μm^3 between 10,000-100,000 μm^3 pore volume ranges. For the same XCT analysed volume, total pore count is measured as 1350 for 57.3 J/mm^3 and 391 for 70.3 J/mm^3 energy density samples. Thus, by increasing the SLM processing energy density 57.3 J/mm$^3 \rightarrow$ 70.3 J/mm^3, the total number of pores has been reduced by 71% and this reduction has been observed for all pore size categories (Figure 4.8(e)).

Considering the pore morphologies within the Ti6Al4V–carbon composites, the 3D XCT analysis shows that there are complex pores significantly larger than the original particle sizes in the low energy density (57.3 J/mm^3) sample. These large pores are bound by partially molten particles due to poor fusion, as illustrated by the ~200 μm

diameter pore (~960,000 μm^3) in Figure 4.8(c)). Many large pores are aligned parallel to build direction because they continue through different layers (Figure 4.8(a)).

By comparison, the pores in the Ti6Al4V–carbon composite medium (70.3 J/mm³) energy density sample are predominantly smaller than the parent particle size (Figure 4.8 (b)). The pores are more spherical than at lower energy density (Figure 4.8 (d)); however, there is still a population of pores with concave inner surfaces (Figure 4.8(b), Figure 4.7(d)), which can be aligned perpendicular to the build direction. Such pores are indicative of insufficient energy density [98], with the concave pore surfaces originating from insufficient melting and cohesion between feedstock particles.

Hatch Distance \ Average Travel Speed	648 mm/s	705 mm/s	710 mm/s	769 mm/s	770 mm/s	771 mm/s	776 mm/s	833 mm/s	841 mm/s	908 mm/s
90µm		87.1 0.8%	86.3 1.0%					70.9 1.0%	70 1.3%	(arrow)
100µm	86.5 0.9%			70.5 1.1%	70.3 0.5%	70.2 0.5%				57.1 3.1%
110µm		71.2 0.9%	70.6 2.1%				63.3 1.4%		57.3 3.6%	(scale bar)
Exposure Time	74µs	67µs	74µs	74µs	67µs	60µs	70µs	67µs	60µs	60µs
Point Distance	57µm	57µm	63.5µm	70µm	63.5µm	57µm	67µm	70µm	63.5µm	70µm

Figure 4.6. Optical images of porosity of Ti6Al4V–carbon samples as a function of their SLM processing parameters average travel speed, hatch distance, point distance and exposure time (Lower right scale bar corresponds to 300 µm). Energy density (J/mm³) and relative porosity of individual images are given on the top left and right corners, respectively. Top right arrow shows SLM build direction).
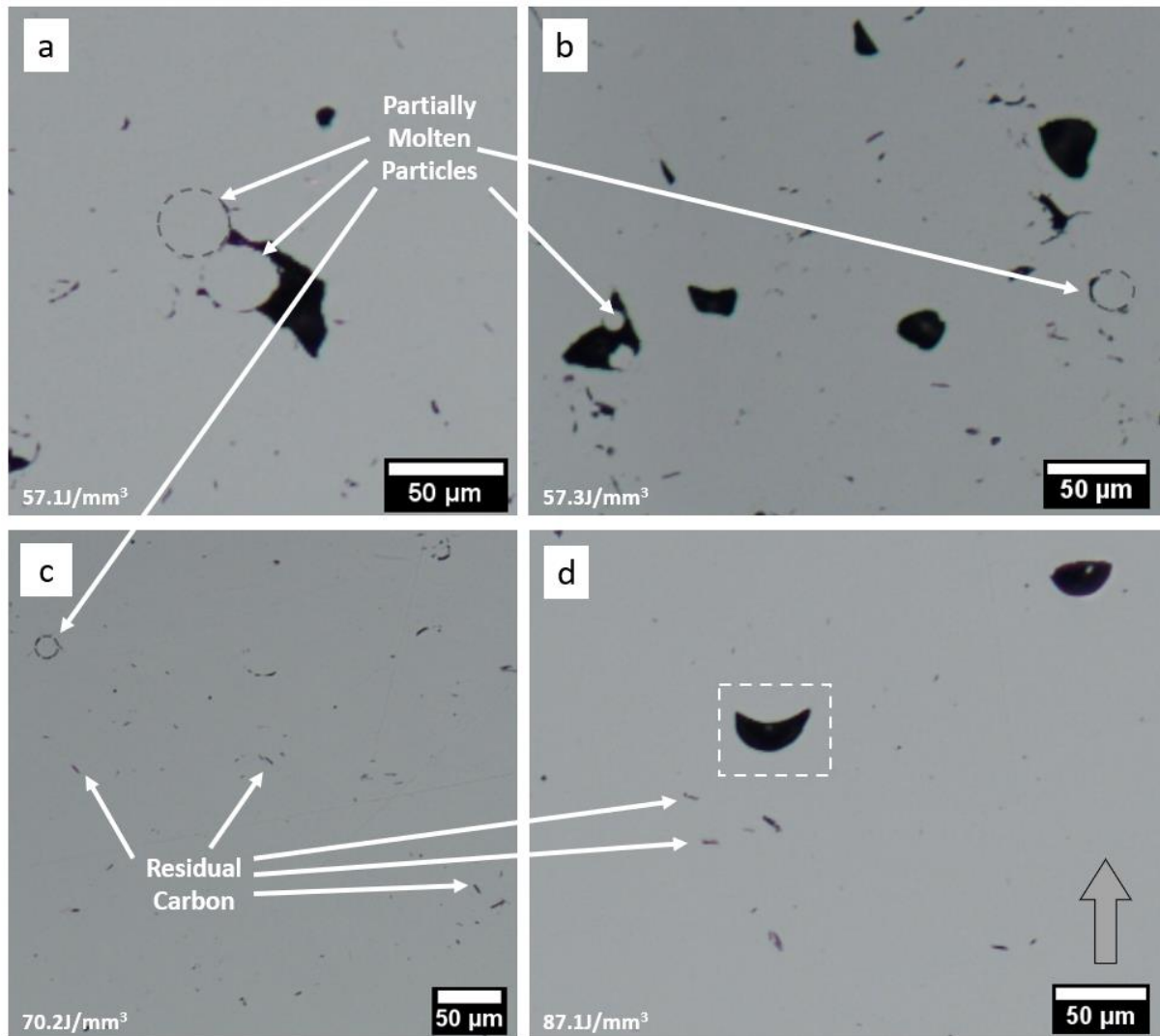
Figure 4.7. Representative optical images illustrating porosity defects in Ti6Al4V–carbon samples with different volumetric energy densities: a) 57.1 J/mm³, b) 57.3 J/mm³, c) 70.2 J/mm³, d) 87.1 J/ mm³. Examples of partially melted particles, microcracks and a crescent void are highlighted. The right-hand arrow represents the build direction for all images.
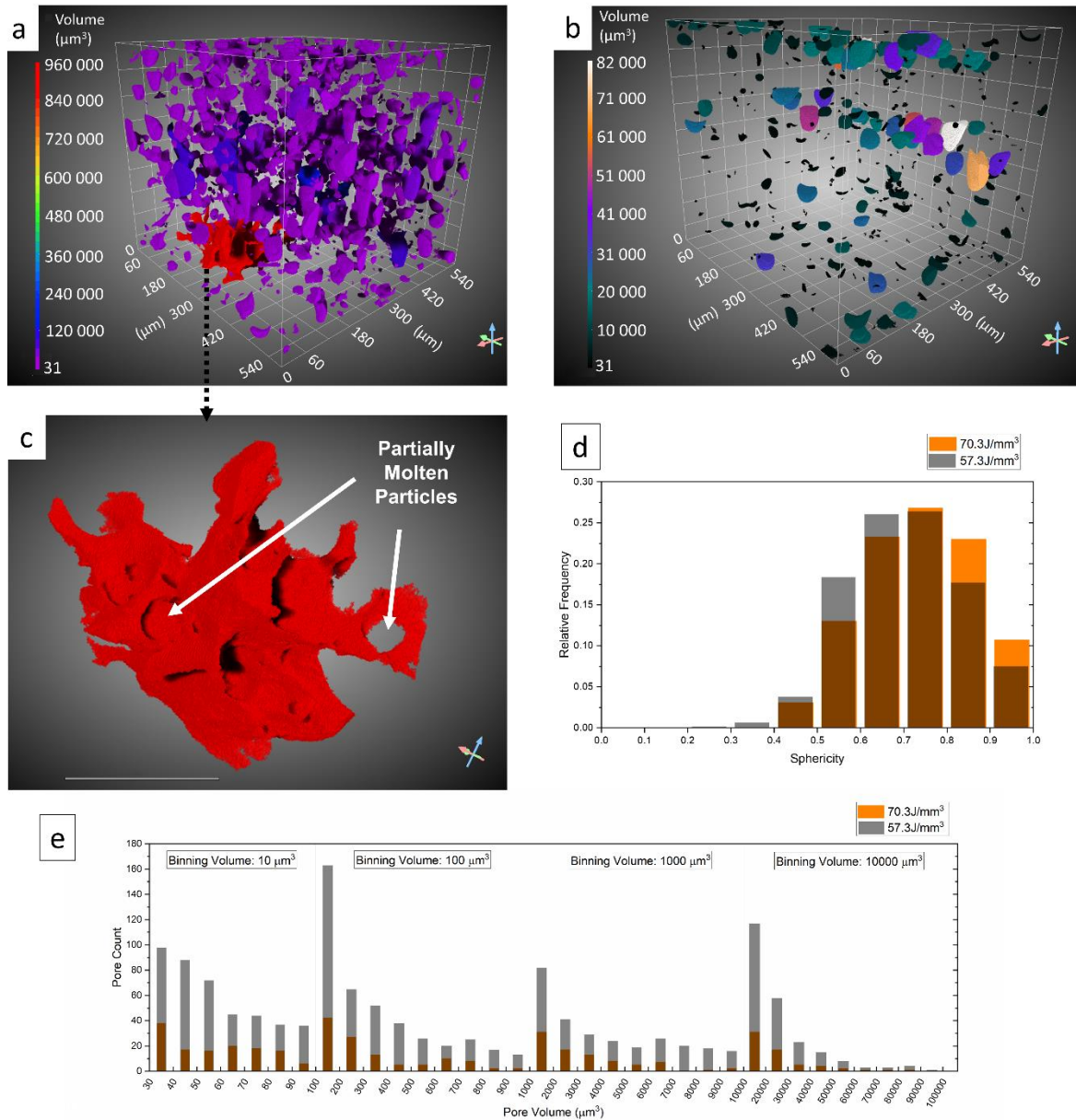
Figure 4.8. 3D porosity distribution in Ti6Al4V–carbon composites processed with different volumetric energy densities measured by XCT. (a) 57.3 J/mm³ (low energy density, largest pore highlighted in red), and (b) 70.3 J/mm³ (medium energy density). (c) Magnified view of the largest red pore within (a) (scalebar represents 100 µm), (d) pore sphericity distribution, and (e) pore count for different pore volumes generated from XCT scans (a) and (b). The light blue arrow indicates build direction in (a,b,c).

4.4.2. Composite Microstructure

The phases present within the SLM *in situ* Ti6Al4V-carbon composite were investigated by XRD and SEM. Figure 4.9 shows XRD patterns of a Ti6Al4V-carbon composite sample (70.3 J/mm³ energy density), a plain Ti6Al4V sample without any graphite addition, and the parent Ti6Al4V powder used for both composite and plain samples. The Ti6Al4V within the parent powder, plain Ti6Al4V, and Ti6Al4V-carbon

composite exhibited the α-Ti structure; no β-titanium peaks were identified by XRD. TiC diffraction peaks were observed in all composite samples, indicating that the Ti-C reaction occurred during SLM processing, and that crystalline TiC formed (cubic Fm-3m). TiC phase is stable in a range of C/Ti composition ratios from 0.5 to 1 [146]; therefore, TiC can take up theoretically within a range of 4.9-9.9wt.% carbon. The composite is hereafter referred to as a Ti6Al4V-TiC composite.

The microstructures of the Ti6Al4V-TiC composites were examined at higher magnification by SEM. A fine dispersion of ~0.1-1 µm TiC particles were observed dispersed throughout the α-Ti6Al4V matrix. (Figure 4.10). Chemical mapping of the particles by SEM-EDS confirms the local concentration of carbon within the dispersed TiC particles, and the associated lower local concentration of Al and V compared to the Ti6Al4V matrix (Figure 4.10((e):a-c)). In the region imaged in Figure 4.10(d), a continuous coating of TiC particles is observed to ring linear defects rich in carbon but devoid of Ti, Al, and V (Figure 4.10(e):d). Such a defect may arise from residual carbon platelets observed in the processed powder (Figure 4.3(a)), which are incompletely dissolved in the SLM processing and have reacted at their surface to form a sheath of TiC. Local concentrations of carbon may also potentially occur due to local displacement of carbon coating from the particles during the laying down of the powder layer onto the base plate prior to laser melting, or insufficient laser energy and resultant melting during the SLM process itself.
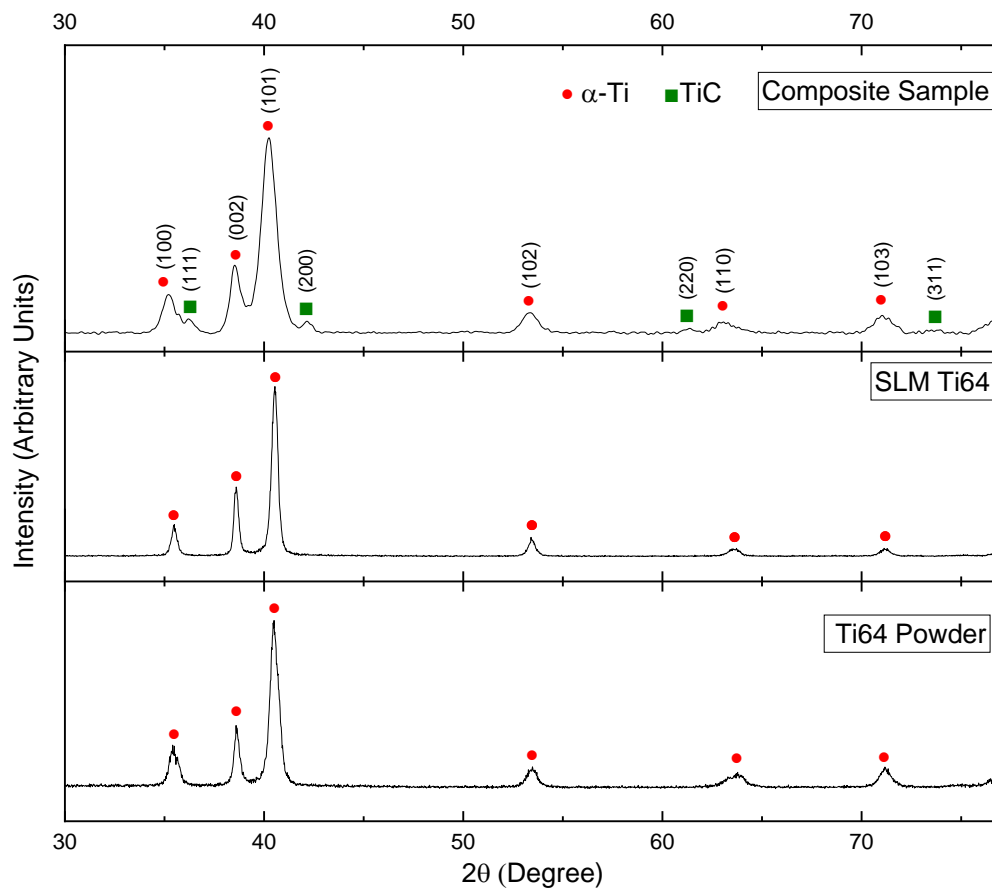
Figure 4.9. XRD patterns of an SLM Ti6Al4V-TiC composite (Composite Sample, 70.5 J/mm³ energy density), SLM processed Ti6Al4V (SLM Ti64), and parent Ti6Al4V powder.
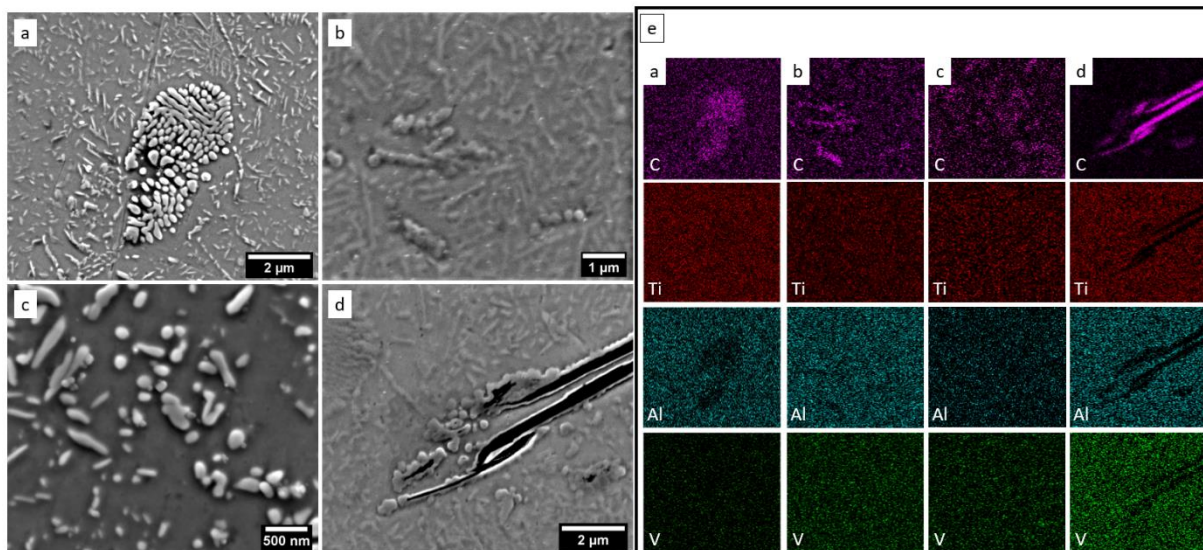
Figure 4.10. (a-d) TiC particles dispersed within the Ti6Al4V matrix in the SLM Ti6Al4V-TiC composite processed at 70.3 J/mm³ energy density. (e) EDS maps of C, Ti, Al and V distribution in the same sample regions of (a-d).

To examine the microstructure and texture of the α-Ti6Al4V matrix in more detail, EBSD analysis was carried out. Figure 4.11(a) shows a representative inverse pole figure (IPF) from EBSD analysis of a sample manufactured with medium energy density (70.3 J/mm³). Ti6Al4V processed by SLM typically has a martensitic microstructure (α') due to its rapidly cooled nature [67]. Similar to previous work, the microstructure consists of the martensite phase in this study, which occurred in distinct regions of crystallographically related grains due to the high temperature $\beta{\rightarrow}\alpha$ phase transition. Figure 4.11(b) shows reconstructed prior β grains from Figure 4.11(a) according to the $\beta{\leftrightarrow}\alpha$ orientation relationship of $\{0001\}_\alpha$ // $\{110\}_\beta$ and $\langle11\overline{20}\rangle_\alpha$ // $\langle111\rangle_\beta$. Columnar β grains elongated in the build direction are observed (Figure 4.11(b)), as previously reported for SLMed Ti6Al4V [67], [72]. However, the β–column width is significantly smaller than in previous studies, with maximum column width measured as 5 μm perpendicular to the build direction. Simonelli et al. [67] reported an average β–column width of 103±32 μm. There is a significant difference between prior β widths; however, the image in Figure 4.11 was taken in a quite smaller area than these two other studies. Therefore, the direct measure may not give precise results.
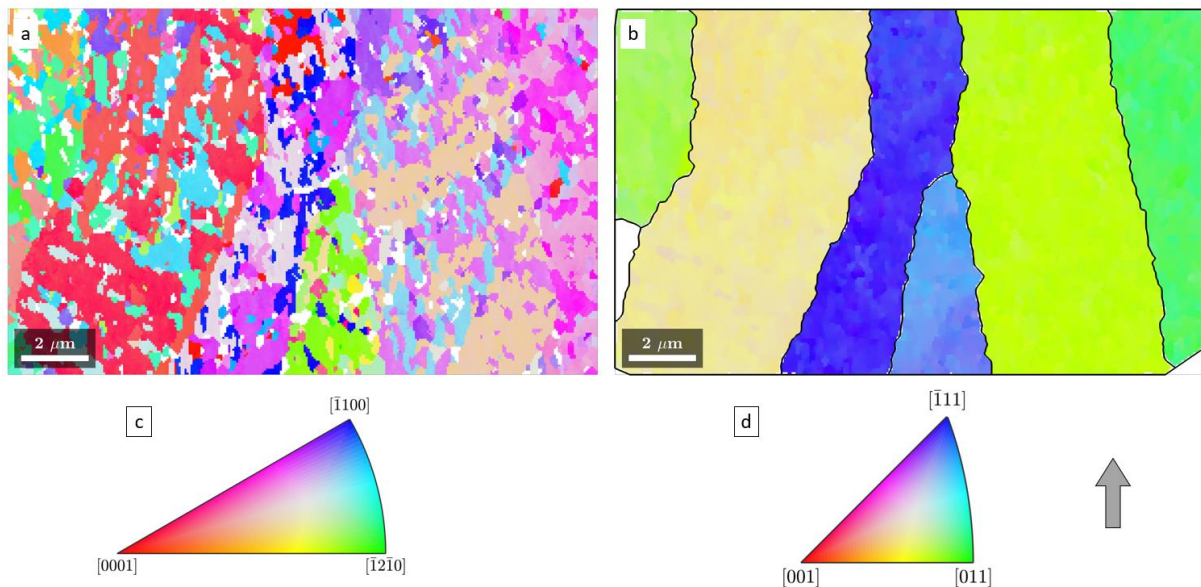
Figure 4.11. (a) EBSD IPF map of martensitic α-Ti64 phase matrix after medium energy density (70.3 J/mm³) SLM processing. (b) Reconstructed parent β grains calculated from EBSD map (a). (c) IPF colour key for orientation of α -HCP phase, d) IPF colour key for orientation of β - cubic phase. The SLM build direction is marked by the grey arrow on the right down.

4.4.3. Hardness

The hardness of the Ti6Al4V-TiC composites fabricated using different SLM processing parameters (Table 4.1) were measured parallel to the build direction using a 500g load. The average hardness of the SLM composite materials varied between 422 HV and 459 HV, compared to 420 HV for a plain SLM Ti6Al4V sample produced with the same equipment and alloy powder.

Figure 4.12 shows the variation in Ti6Al4V-TiC composite hardness as a result of processing parameters. Figure 4.12(a) shows change of hardness depending on different SLM exposure time and point distance values. Increasing exposure time and decreasing point distance, which result in higher linear energy density and decreased average travel speed, cause higher hardness. Response surface regression indicates that both exposure time and point distance are effective on hardness change, but hatch distance is defined as non-effective (0.298, 0.016, 0.030 are *p*-values at 95% confidence level for hatch distance, exposure time and point distance, respectively).

Figure 4.12(b) shows the change in Ti6Al4V-TiC composite hardness as a function of average laser travel speed. At high average laser travel speed (908 mm/s) the composite exhibits similar hardness to pure Ti6A4V (422 HV vs 420 HV). However, as the laser travel speed decreases, increasing the local energy input, the composite hardness increases indicating improved strength of the *in situ* composites. No significant relationship between porosity and hardness is observed.
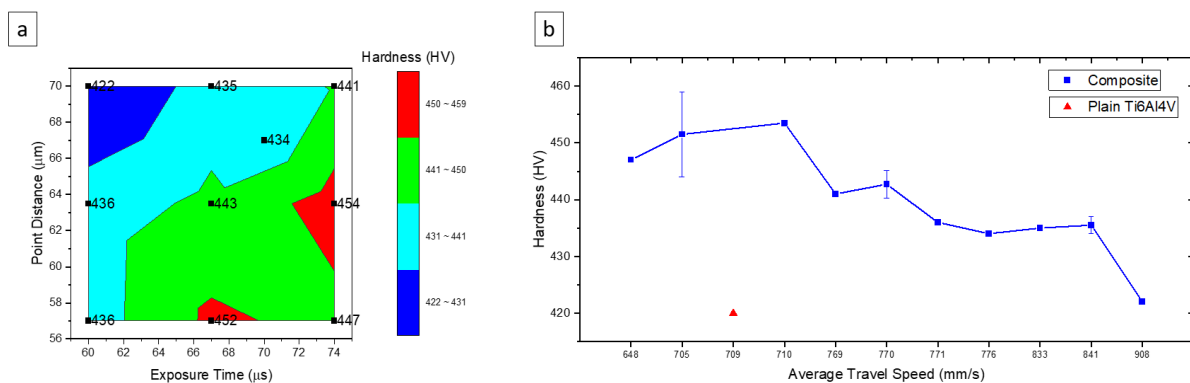
Figure 4.12. (a) Ti6Al4V-TiC hardness for different SLM exposure time and point distance parameters (points show individual average hardness measurements), (b) Ti6Al4V-TiC hardness as a function of average laser travel speed (error bars represent standard error for multiple samples of the same average travel speed).

4.5. Discussion

4.5.1. Powder Mixing

Powder flowability and morphology are significant aspects of SLM processing, important for even spread of powder in every layer and to achieve desired laser absorption. The particle coating method used in this study successfully generated a near-continuous coating of nanoparticle carbon on the pre-alloyed Ti6Al4V powders (Figure 4.3). Importantly, the direct mixing (rather than using ball milling) caused negligible deformation of the original Ti6Al4V particles, resulting in no adverse effects on flowability and laser absorption. Additionally, nanosized carbon particles may also aid rapid dissolution into the melt and may help to reduce interparticle friction during powder laying down.

Ex situ TiC particles have been commonly used as reinforcement for the additive manufacture of TiC reinforced TMCs and ball milling is typically used to prepare powder blends [27]. Wang et al. studied the effect of different TiC reinforcement particle sizes on the mechanical properties and reinforcement distribution within the matrix [117]. They found that the smaller the TiC particle size is, the better the mechanical properties and dispersion of the reinforcement within the matrix. Most of the studies using *ex situ* TiC reinforcement and SLM have used nanosized TiC particles due to their advantages [20], [129], [131]. However, the use of nanosized TiC particles significantly increases the cost of the raw material, and brings difficulties for handling and storage due to their high reactivity and potential toxicity. Production of composites by *in situ* particle nucleation and growth brings benefits such as cleaner particle-matrix interfaces and stronger bonding, more thermodynamically stable reinforcements and better particle distribution [5]. Therefore, the powder mixing route used in this study introduces significant advantages over *ex situ* methods.

4.5.2. SLM Processing

In situ Ti6Al4V-TiC composites were successfully fabricated, and a range of different SLM processing parameters used to optimise the process (Table 4.1).

4.5.3. Relative Porosity Change

The porosity of the SLM Ti6Al4V–TiC samples varied from 3.6 – 0.5% (Figure 4.5), measured from optical measurements of areal porosity. The lower energy density SLM samples had significantly higher porosity, and pores are large and irregular with associated partially molten particles (Figure 4.7(a,b), Figure 4.8(a)). These lack of fusion defects are typical for a low energy input of SLM [97], [98], [147]. Insufficient laser energy cannot melt the powder layer completely; therefore, particles are partially molten, and large sharp-edged porosities occur [147], Figure 4.8(c)). This type of defect is the most detrimental type for mechanical properties due to its sharp edges [98], [148] and should be avoided if possible because of causing stress concentrations.

In the SLM Ti6Al4V–TiC composites, with increasing energy density the pores become less frequent and smaller, being typically smaller than the size of the parent particles (Figure 4.5, Figure 4.6, Figure 4.7 and Figure 4.8). Pores becomes more spherical with increasing energy density due to disappearance of large lack of fusion defects (Figure 4.8(a,c,d)). Although pores become more spherical with raising energy density (Figure 4.8(d)), they are still not as spherical as observed for excessive SLM energy input [97], [98], which can causes spherical pores called keyhole pores. The maximum 87.1 J/mm energy input chosen in this study is not high enough to create spherical keyhole defects in Ti6Al4V [97], [98], [149]. For the lowest porosity composites manufactured, a population of irregular pores with concave inner surfaces were still observed (Figure 4.7(d)) probably due to some residual degree of partial melting and lack of fusion.

Increased melt viscosity due to the presence of ceramic particles has been proposed as the reason of the need for higher energy density to manufacture *ex situ* TMCs [20], [25]. Here TiC formation occurred *in situ* within the melt. The molten metal's viscosity will be affected by its modified chemistry containing carbon, and will increase once TiC particles start to form. Increased viscosity causes balling effect which is lack of wetting the previous layer by the molten material due to meltpool instability [20], [50]. A higher energy input is needed to provide enough wetting of the precedent layer [20].

The measured porosity of the Ti6Al4V–TiC TMCs in this study, down to 0.5% at the highest energy density investigated, is lower than related TMC studies. Material

densities of 98.2% [131], 97% [20] and 98.5% [19] have been reported for *ex situ* Ti/TiC reinforced TMC composites via SLM. TiC content used in these studies are 5 wt.% [131] and 15wt.% [19], [20]. Assuming consumption of all carbon during *in situ* reaction, TiC formation is expected within the range of 4.9%-9.9% depending on the Ti/C ratio of TiC particles in this study. Compared to *ex situ* TiC reinforced TMC composites, the 99.5% material density achieved in this *in situ* SLM TMC study is promising, and may improve further with increased energy density.

4.5.4. Microstructure and Hardness

The SLM Ti6Al4V and Ti6Al4V-carbon composites exhibited the martensitic α'-Ti structure due to the rapid cooling during SLM processing; no β-titanium peaks were identified by XRD. XRD analysis confirmed the formation of TiC (cubic Fm-3m) in all *in situ* composites processed (Figure 4.9). A fine dispersion of ~0.1-1 μm TiC nanoparticles are observed dispersed throughout the α'-Ti6Al4V matrix. The TiC morphologies are predominantly equiaxed, <5 particle clusters, or short platelets (Figure 4.10). The nanocarbon layer coated on the parent Ti6Al4V particles has clearly distributed well throughout the melt during SLM processing, with one defect associated with residual a carbon flake identified (Figure 4.10(d)).

EBSD analysis of α'-orientations after medium energy density (70.3 J/mm3) SLM processing identifies the prior β grains (Figure 4.11(b)) in the Ti6Al4V-TiC composite, which are elongated along the build direction, as typical for SLM processing of Ti6Al4V [67]. The <5 μm widths of the columnar β grains are finer than ~103±32 μm reported for previous SLM Ti6Al4V [67]. Smaller parent β grains, due to grain refinement by the TiC particles, will generate smaller and more orientations of daughter α'-grains (Figure 4.11(a)). Similar tendency on parent grain size refinement has been reported before for AM of TiC reinforced Ti6Al4V via laser direct energy deposition [150]; however, there are no studies on *in situ* TiC reinforced composites to the best of author's knowledge.

The *in situ* Ti6Al4V-TiC composites have improved hardness, 422 HV - 459 HV, compared to 420 HV for the plain SLM Ti6Al4V sample of this study, 391 HV [43] and

386 HV [92] from previous studies using the same alloy and SLM equipment [43]. A dispersion of TiC particles can improve hardness by mechanisms including grain refinement, limiting dislocation movement (Orowan strengthening) and increasing dislocation density [27], [115], [120], [151], [152].

The hardness of the Ti6Al4V-TiC composites varied with SLM processing parameters. Increasing exposure time and decreasing point distance, which result in higher linear energy density and decreased average travel speed, cause higher composite hardness (Figure 4.12).

Two different mechanisms for TiC formation were proposed by previous researchers. When high enough energy density values applied, TiC forms through dissolution-precipitation mechanism [19], [21], [22], [129]–[131]. In this mechanism, TiC nuclei form and grow from dissolved carbon within the liquid matrix. A different formation mechanism is proposed when the molten metal temperature remained below 2438°C, [23], [126], [153]. In this case, TiC directly formed rather than C dissolution in the liquid titanium. When a TiC layer formed around a carbon source below 2438 °C, further TiC formation requires diffusion of carbon through formed TiC shell in this mechanism [23]. Considering Ti6Al4V's optimum and lower than optimum energy density range used in this study, dominant meltpool temperature is expected as lower than 2438°C [23], [73], [154], [155]. Therefore, the dominant TiC formation process is direct carburisation rather than solution-precipitation mechanism. The carbon signal in Figure 4.10(d) indicates an undissolved carbon particle. A TiC may be formed around this particle by direct reaction of Ti and C and rapid solidification nature of SLM may not give enough time for diffusion of inner region carbons to form more TiC.

Temperature distribution of the molten metal during the SLM processing is not homogeneous [155], [156]. Centre of the meltpool reaches higher temperatures [156]. Therefore, a mix of both, dissolution-precipitation and direct reaction may take place at the same time due to temperature gradient within the melt pool. This may explain carbon particles with different sizes within the microstructure (Figure 4.10). Dissolution-precipitation particles are probably small particles nucleated from liquid

phase whereas relatively large particles probably arises from direct reaction mechanism [23]. Further optimisation of the SLM processing conditions e.g. using energy densities above 87 J/mm^3 may lead to fully dense Ti6Al4V-TiC composites with an optimised TiC content (eliminating residual carbon defects).

4.6. Conclusions

In this chapter, direct mixing of Ti6Al4V powders and graphite flakes and their processability via SLM to manufacture *in situ* TiC reinforced composites were examined. It was seen that Ti6Al4V powders were coated by graphite evenly, and the graphite flake was transformed to amorphous carbon after mixing for one hour. TiC formation took place after processing these samples via SLM using energy densities between 57.1 J/mm^3 and 87.1 J/mm^3. Optical porosity analysis revealed that increasing energy density resulted in higher relative density. Low energy densities resulted in large, irregular pores; however, they become smaller and more regular with energy density increase. Sphericity shifted to a higher level with increasing energy density, but partially molten particles are observed even with higher energy densities. Additionally, all samples had sharp-edged pores. Hatch distance, exposure time and point distance were effective on relative porosity according to statistical analysis. On the other hand, only exposure time and point distance were determined as effective on hardness. This chapter proved that the direct mixing concept is applicable for TMC manufacturing; however, higher energy density values should be tried for better porosity.

Chapter 5: Manufacture and Characterisation of Plain Ti6Al4V Alloy via Selective Laser Melting

5.1. Introduction

The previous chapter confirmed that the direct mixing method is suitable for the manufacture of TiC reinforced composites. In this chapter, plain Ti6Al4V samples are manufactured using a variety of processing parameters to understand the effects of processing parameters on unreinforced Ti6Al4V material properties, and to have a baseline to compare to composite parts' properties. Porosity of SLM parts was evaluated using optical microscopy (OM). The microstructure is examined using SEM, XRD, and EBSD. Samples' mechanical properties are assessed using hardness testing. The statistical importance of results were analysed using response surface methodology's central composite design, and porosity formation and hardness change were evaluated.

5.2. Experimental

Pre-alloyed Ti6Al4V powders were used for SLM processing. An Aconity Mini SLM system equipped with continuous fibre laser was used for sample processing. Laser speed and hatch space were varied, whereas laser power and layer thickness were set as 190W and 30 μm, respectively, for all parameters. Central composite design response surface methodology is used for parameter generation and statistical analysis. Table 5.1 lists the processing parameters used and the resultant volumetric and linear energy densities. Samples on the base plate after SLM processing are shown in Figure 5.1(a). Processed parts had the dimension of 10mm × 10mm × 5mm (Figure 5.1(b)). Porosity analyses were performed parallel to the build direction (YZ plane in Figure 5.1(b)). A total area of 5900μm × 1140μm was examined for porosity investigation of all samples. All SEM analyses were performed on the YZ plane, whereas EBSDs were performed both on parallel and perpendicular planes (YZ and XY planes in Figure 5.1). The SEM EBSD analyses used 20 kV accelerating voltage and 100 nm step size.

Table 5.1. Plain Ti6Al4V's SLM processing parameters.

Sample Number	Hatch Space (μm)	Laser Speed (mm/s)	Volumetric Energy Density (J/mm^3)	Linear Energy Density (J/mm)
1	64	960	103	0.198
2	96	960	69	0.198
3	64	1440	69	0.132
4	96	1440	46	0.132
5	57	1200	92	0.158
6	103	1200	51	0.158
7	80	861	92	0.221
8	80	1539	51	0.123
9	80	1200	66	0.158
10	80	1200	66	0.158
11	80	1200	66	0.158
12	80	1200	66	0.158
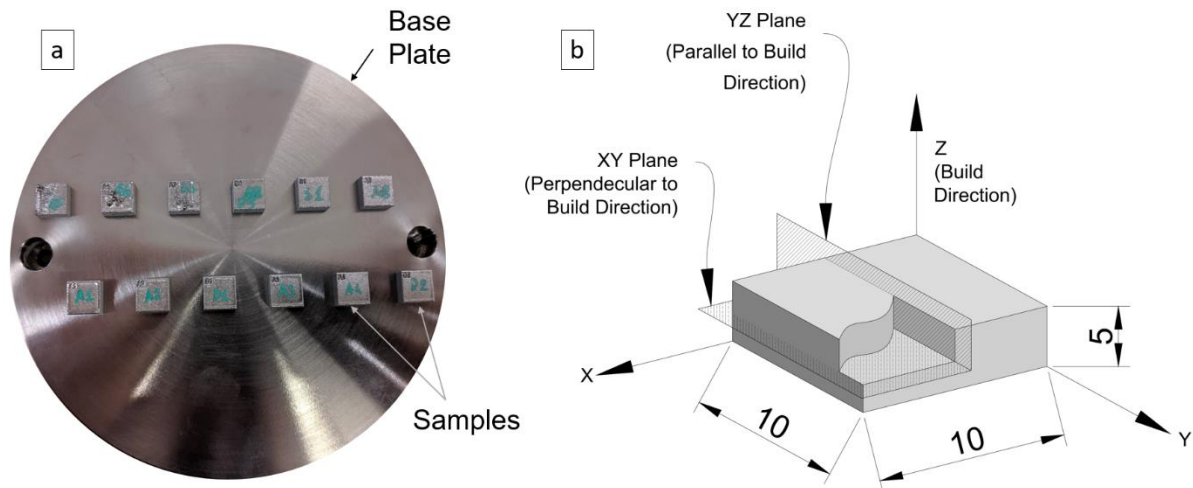
Figure 5.1. (a) Processed Ti6Al4V parts on the baseplate and (b) dimensions of the parts and examination planes for porosity, microstructure and EBSD analyses.

5.3. Selective Laser Melting Processing of Ti6Al4V

5.3.1. Relative Porosity

Figure 5.2(a) shows the change of relative porosity of SLM Ti6Al4V depending on laser speed and hatch space. Relative porosity varied from nearly fully dense (0.003%) parts to 0.43% porosity. For the sample with maximum 0.43% relative porosity, there were some localised pores on the right side of this sample (Figure 5.2(b), dashed rectangle). No statistically significant relationship was detected between processing parameters and porosity at 95% confidence level.

Spattering of molten material during powder melting is an inevitable part of the SLM process [157]. The large local pores seen in Figure 5.2(b) are likely to be related to spattered molten particles. The first reason is the highly localised presence of porosity within the whole cross-section in contrast to usual evenly distributed keyhole or lack of fusion pores. The laser energy may not be sufficient to melt large spatter particles solidified onto a specific layer, whereas powder particles and small spatter particles across the rest of the layer can be small enough to be completely molten.

Secondly, large spherical particles were seen on the top surface of some fabricated parts. Examples of parts with swelling defects on the top surface are highlighted in

Figure 5.3. This shows that spattered particles between different samples caused swelling defects only on some samples.

Processing parameters [157]–[159] and inert gas flow conditions affect spatter formation [158]. Significant spatter formation was observed on only some samples, so it is unlikely that its formation was related to inert gas flow. For the Aconity Mini system inert gas goes into the build chamber from the right side and goes out from the left side (Figure 5.3(a)). An unusual spatter particle formation from one of the parts on the right side of spatter detected parts (Figure 5.3(a)) resulted in swelling defects on the top surface of these parts. Inert gas flow moved these spatters downwind onto samples 3, 4 and 5, and spatter defect was seen on the top surfaces and resulted in high porosity for one of them (sample 3). There are three parts that may cause this, labelled as 8, 11 and 12 (Table 5.1). Samples 11 and 12 are manufactured using the same parameters as two others (9 and 10). However, such defect has not been seen in parts on the left of samples 9 and 10. Hence, sample 8 most likely caused spatter defect on samples 3, 4 and 5.

Qiu et al. [159], and Anwar and Pham [157] studied spatter evolution and resultant defect formation during SLM processing. Both studies reported that high scanning speed results in more spatter formation. Higher scan speed results in larger melt surface area and thermal gradient, and these cause melt pool instabilities; therefore, splashing velocity increases [159]. Sample 8 in this study has the highest laser scanning speed (1539 mm/s). This high speed might cause more spatter formation and higher spatter velocity. Argon flow carries spatter droplets over samples 11 and 12 with the help of increased splash velocity; hence, these are accumulated on parts 3, 4 and 5.
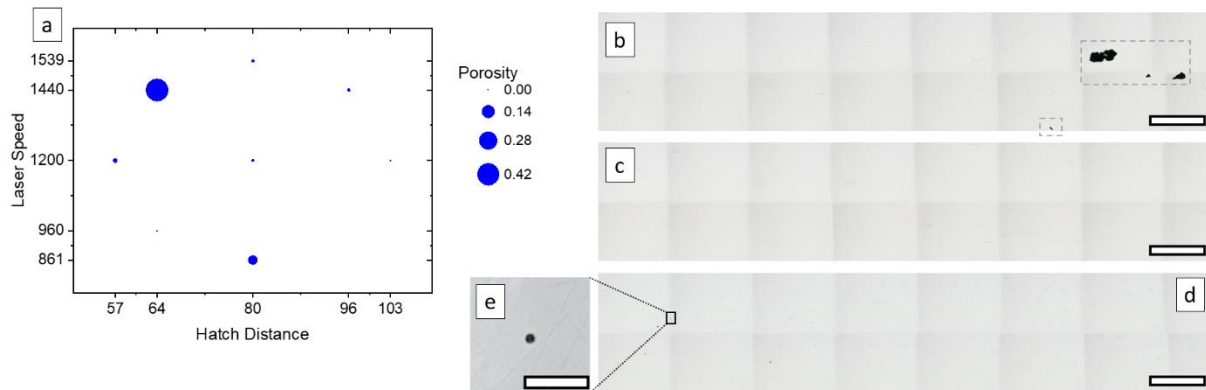
Figure 5.2. (a) Change of porosity depending on Ti6Al4V processing parameters. Optical images of samples which have (b) the highest relative porosity (sample 3), (c) the highest relative density (sample 9), (d) the highest energy density (sample 1) and (e) a spherical pore in the highest energy density. Scalebars in (b), (c), and (d) show 500 µm and the scalebar in (e) shows 50 µm. All images were taken from the YZ plane shown in Figure 5.1(b).

The second-highest Ti6Al4V relative porosity was measured as 0.072 with the sample manufactured using 861 mm/s laser scan speed and 80 µm hatch distance (sample 7 in Table 5.1). This is a significant reduction in porosity and can be defined as a nearly fully dense part. Overall, the processing parameters chosen in this study produced fully dense parts. Hatch distance and laser scan speed varied ±20% from manufacturer's recommended processing parameters, and this variation did not create a significant difference in parts' porosity.
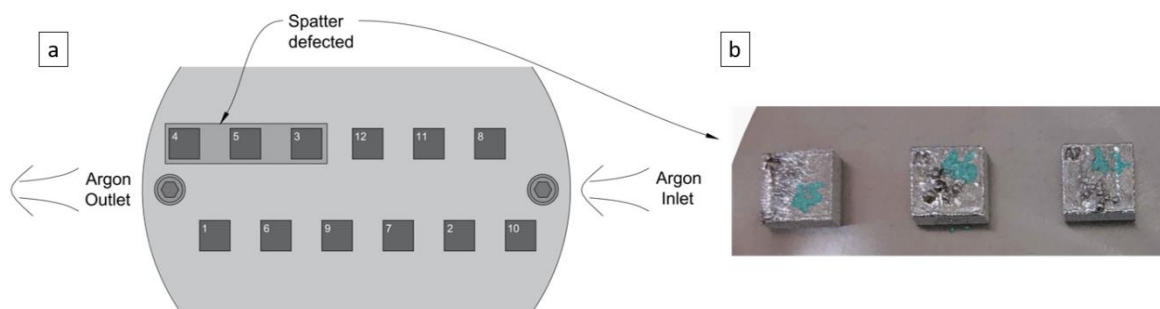
Figure 5.3. Ti6Al4V parts layout on the baseplate and parts 3-5 with visible spatter defect on their top surface, (b) photograph of parts 3-5 showing large spherical bumps on top surfaces. Numbers on parts show sample numbers in Table 5.1.

Even though relative porosity remains low, small spherical pores (<8 µm) can be detected within the highest energy density Ti6Al4V sample (Figure 5.2 (d,e), sample 1). Spherical pores in SLM are attributed to excessive energy density [100], [101], [103]. When the vaporisation of the molten metal takes place, recoil pressure causes depression of molten metal [101], [160]. Recoil pressure increases exponentially with

temperature, and this causes a deeper melt pool with more energy input [100], [102]. A local temperature drop in upper regions of the deep melt pool causes pore formation [100], and then this pore is trapped by the solidification track [100], [103].

The hydrostatic pressure of liquid metal and surface tension causes spherical pores in excessive energy density processing [100]. Keyhole formation takes place after passing a threshold energy density [99]–[101]. For the lower energy densities within the keyhole range, the average size of keyhole pores is lower, and pores are more spherical [100]. Spherical pores observed in the highest energy density Ti6Al4V sample (103 J/mm^3) (Figure 5.2(d,e)) were not identified in other samples. This shows that the highest energy density sample is just above the keyhole threshold energy density; hence, only small and spherical keyhole pores are observed.

5.3.2. Surface Structure

The top surface roughness (Sa) of Ti6Al4V parts diversifies between 4.5 µm and 73.9 µm. There was no statistically significant relationship between roughness and various processing parameters, when the confidence level was set as 95. The highest surface roughness was measured as 19.9 µm, 73.9 µm and 36.8 µm for samples 3, 4 and 5 in Table 5.1. These are samples on whose top surface swelling defects were observed (Figure 5.3). Top surface optical profilometry images of these samples, the highest energy density sample (sample 1 in Table 5.1) and a comparative medium energy density sample (sample 12 in Table 5.1) are given in Figure 5.4.

Swelling defects due to spattering liquid can be seen with optical profilometry images (Figure 5.4(a-f)). These defects are significantly larger than powder particle size and mostly irregular in shape; hence, they cannot be powder spatter particles. Large extended particles can be seen of sizes 278 µm (Figure 5.4(a)) and 360 µm (Figure 5.4(c)), with splash sizes being ~6 and ~8 times larger than maximum feedstock powder particle size (53 µm), respectively. Spherical defects on the surface (Figure 5.4(a,b)) are significantly larger than feedstock powder (80 µm).

Individual laser scan tracks cannot be seen on the Ti6Al4V sample with the highest roughness (sample 4), indicating significant spatter formation. This was the sample with the lowest energy density of 46 J/mm3. Limited energy density might not be able to melt large spatter particles completely; hence, roughness can be increased. The low relative porosity of this sample (0.009%) indicates that the energy density was high enough to create a fully dense part, but it was probably close to the threshold value for fully dense parts. On the other hand, spattering and rough surface were only seen on one half of the sample (Figure 5.3(b)) which may be due to the selective deposition of spatter particles moved by argon flow.

Ti6Al4V sample 3 has the highest porosity; however, its surface roughness (Sa=5.3 μm) is the lowest compared with the other two swelling defected samples (4 and 5). Even though the laser track lines are visible, some surface spattered large clusters can be seen in Figure 5.4((d), dashed circle). The large internal pore cluster (Figure 5.2(b)) may be the result of a large spatter particle that did not entirely melt due to its large size. However, this would have been an extraordinarily large particle, and such large spatter did not form again; hence, porosity is low in other regions.

The lowest Ti6Al4V roughness was seen on the sample with the highest energy density (Figure 5.4(g,h), sample 1). Only a limited number of spattered powder particles were identified on the top surface. A decrease of top surface roughness with rising energy density during SLM processing has been reported by other researchers [161]–[163]. High energy density results in a slower cooling rate [161], [162], lower viscosity [161], lower surface tension [100] and a larger melt pool [164]. A slower cooling rate gives more time to gravity to flatten the melt pool, and decreased viscosity and surface tension boost this process [161], [162]. Additionally, recoil pressure increases with rising temperature and flattens the molten metal's surface [165], [166]. All these effects result in a smoother top surface while using higher energy density.
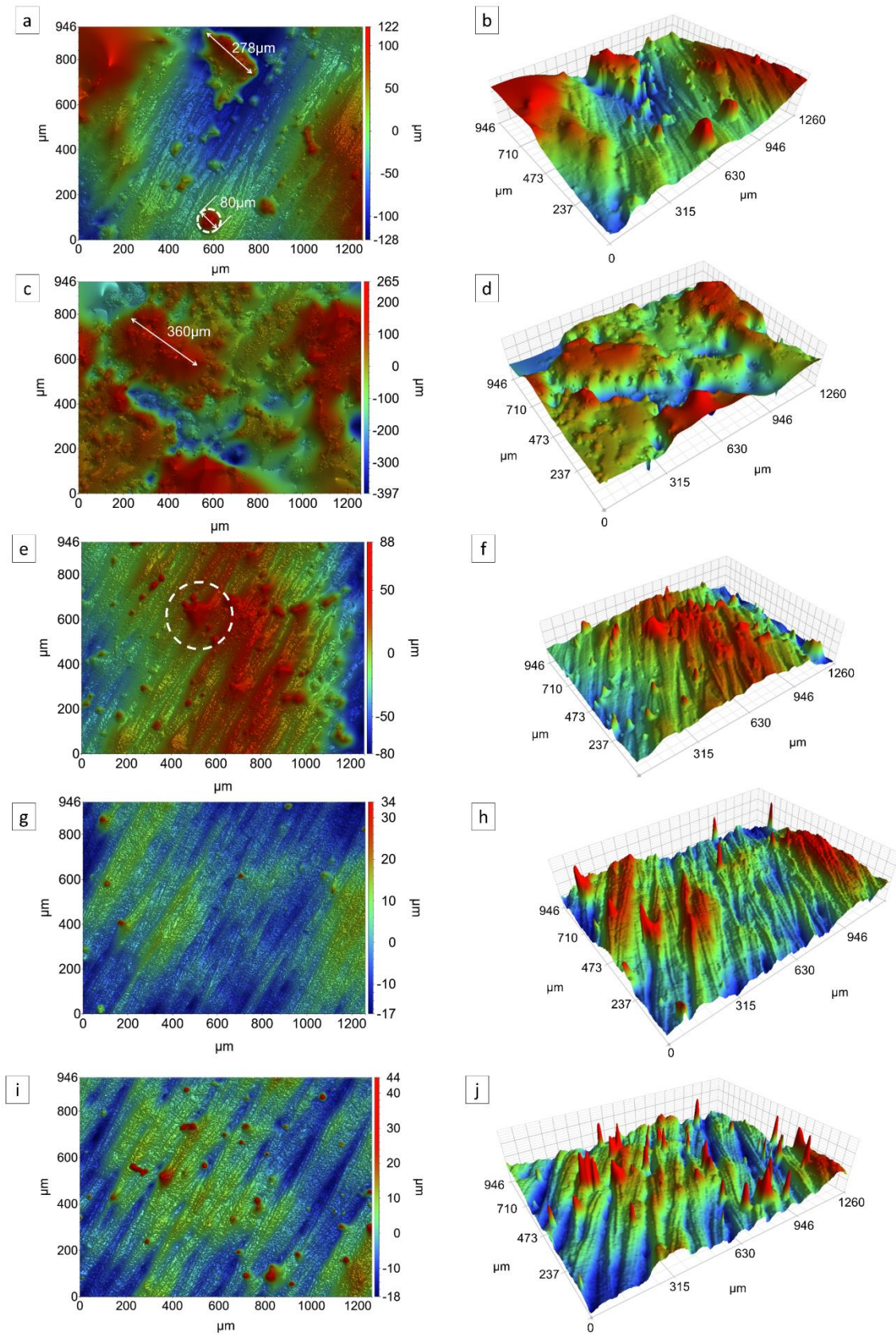
Figure 5.4. Optical profilometry images of Ti6Al4V samples (a) sample 5 top view, (b) 3D view, (c) sample 4 top view, (d) 3D view, (e) sample 3 top view, (f) 3D view, (g) sample 1 top view, (h) 3D view and (i) sample 12 top view, (j) 3D view.

Similar to the highest energy density Ti6Al4V sample (Figure 5.4(g,h)), the medium energy density samples' surface has some spattered powder particles (Figure 5.4(i,j), sample 12) and molten liquid splash particles. The number of spatter powder particles is more than for the highest energy density sample. Spattered particles having close dimensions to the original powder particle size are characterised as powder spatters, whereas large surface irregularities are associated with liquid splash [167]. Only powder spatters were observed with high energy density, whereas medium energy density also has liquid splash particles. Lower energy density causes a less stable melt pool and more spatter [159]; hence, increasing energy density resulted in less powder spatter, and disappearance of liquid spatter.

The side surface roughness of Ti6Al4V samples varied between Sa=14.1 µm and 17.1 µm. When the confidence interval was set at 95%, no statistically important relationship was found between surface roughness and processing parameters. Contour scanning is typically performed on SLMed parts to improve surface finish and dimensional accuracy [15], [168], and contour scan's laser parameters affects side surface structure [161]. However, no contour scan was applied in this study to rule out any potential modifications due to contour scanning. Unlike the top surface structure, no significant difference between the side surface microstructure of parts was observed. Partially molten particles were seen on all side surfaces (Figure 5.5(a,b)). This is the typical side surface structure for SLM parts [161], [168], [169]. Surrounding powders of melt pool are partially molten and solid particles adhere to molten side surfaces during the laser scan [161], [168].
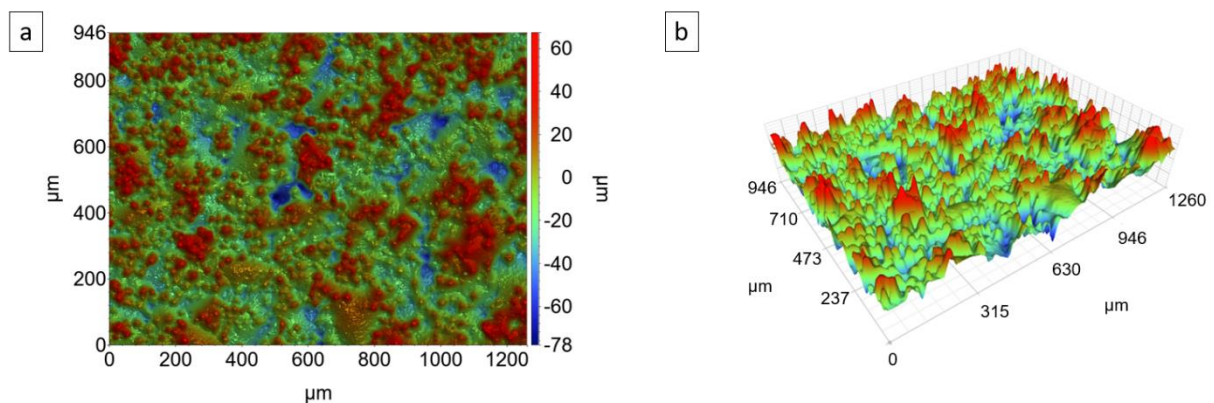
Figure 5.5. Optical profilometry images of Ti6Al4V sample 12 side surface (a) top view, (b) 3D view.

5.3.3. Microstructure

The crystallographic phases of the SLM processed Ti6Al4V were examined by XRD. The XRD diffraction pattern of sample 10 is given in Figure 5.6 as an example. Even though Ti6Al4V is typically an $\alpha+\beta$ alloy, only the α phase was detected by XRD here. The SLM process involves rapid heating and cooling cycles, and the cooling rate can reach 10^8 K/s [96]. Therefore, martensitic α' phase forms from the β phase during solidification [67]. Some retained β phase was reported by previous researchers [96]; however, no trace of β phase could be found by XRD or conventional SEM [17], [95], [96], [170], [171].
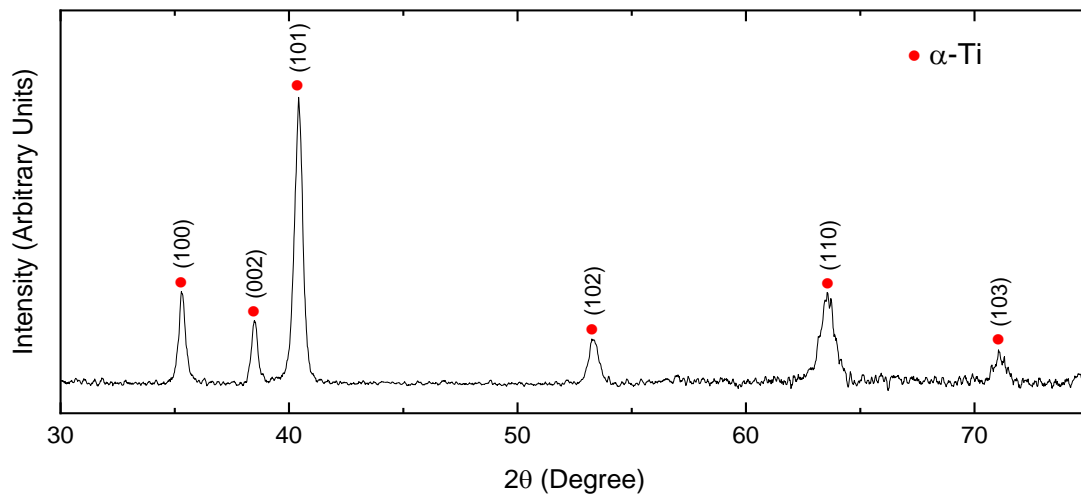
Figure 5.6. XRD profile of Ti6Al4V sample 10, identifying the α'-Ti phase.

SEM images of sample 12 are presented in Figure 5.7. Traces of columnar β grains can be seen in Figure 5.7(a,b). Hatch spacing is the determinant parameter on primary β column width [67], [89], [96]. Even though there is variation, the column width is correlated with the hatch spacing of 80 µm (Figure 5.7(a)). There is a variation of width and elongation direction of β grains through the build direction. The laser scan direction has been rotated by 67° (in the plane of layer) between adjacent layers to distribute thermal stresses randomly. This rotation results in β grain growth direction changes and column width variations [67]. More straight parent β grains and less variation of β grain width is observed when the rotation of the scan between layers was set to 90° [95], [96].

SEM images of the as-built Ti6Al4V martensitic microstructure are shown in Figure 5.7(b,c,d). The martensitic microstructure of SLM Ti6Al4V is different from conventional water quenching microstructure of wrought or cast materials [95], [96] and this results from the unique heating and cooling cycles of the SLM process [68], [95], [96], [172]. Water quenching results in continuous cooling of the material after solutioning in the complete β phase region [89], and the cooling takes place as one single event. In comparison, SLM has multiple heating and cooling cycles. Within a layer, adjacent laser tracks result in repeated heating and cooling cycles at a point within the structure [68], [95]. The heat created from neighbouring laser scans stimulates quick local heat treatments in the same layer, yet this is not the only heating, and cooling events take place.

Adjacent layers result in further heating and cooling cycles in addition to adjacent laser scans of the same layer [68], [95], [96]. The nth layer is affected by the thermal cycles of up to the $(n+4)^{th}$ layer [68], [95], [96]. The $(n+1)^{th}$ layer melts some part of the nth layer facilitating complete bonding between layers [68], and heats the remaining of nth layer above the β transus temperature [95], [96]. This creates a local heat treatment; however, some of the dislocations arrays remain in place in the β phase due to rapid heating [95], [96]. While the melted part of the nth layer transforms to the martensitic phase, the remaining segment heated above the β transus temperature goes through another martensitic transformation during rapid cooling. The remaining dislocations in the heated zone above β transus temperature work as nucleation sites for new martensites and secondary martensite forms alongside primary ones [68], [96]. This is the formation mechanism of the primary and secondary martensitic structure shown in Figure 5.7(b,c).

During the processing of the $(n+2)^{th}$ layer, the nth layer is heated above β transus temperature whereas no liquidation takes place in it [68], [96]. Similar to the mechanism that happened while processing $(n+1)^{th}$ layer, some dislocations remains again in n^{th} layer during the processing of $(n+2)^{th}$ layer due to the rapid heating regime [96]. The remaining dislocations accelerate the martensite nucleation and growth, and more secondary martensite formed in this cycle [96], [173], [174]. Similar to previous

layers, during the processing of the (n+3)th and (n+4)th layers, some of the martensite decompose to β in the nth layer, and this results in tertiary and quartic martensitic phases [96]. Tertiary and quartic martensite can be seen in Figure 5.7(d). Coarsening of primary, secondary and tertiary martensite takes place during processing of (n+2)th, (n+3)th and (n+4)th layers [95], [96]. As a result of these thermal cycles, a hierarchical martensitic structure forms with primary, secondary, tertiary and quartic martensites [68], [95], [96], [174], [175].

A martensite size range has been proposed by Yang et al. [96], [175] for primary, secondary, tertiary and quartic Ti6Al4V martensites. Major axis length is defined as >20 µm, 10-20 µm, 1-10 µm and <1 µm for primary, secondary, tertiary and quartic martensites, respectively. Martensite sizes in Figure 5.7(b,c,d) correlate well with these ranges.
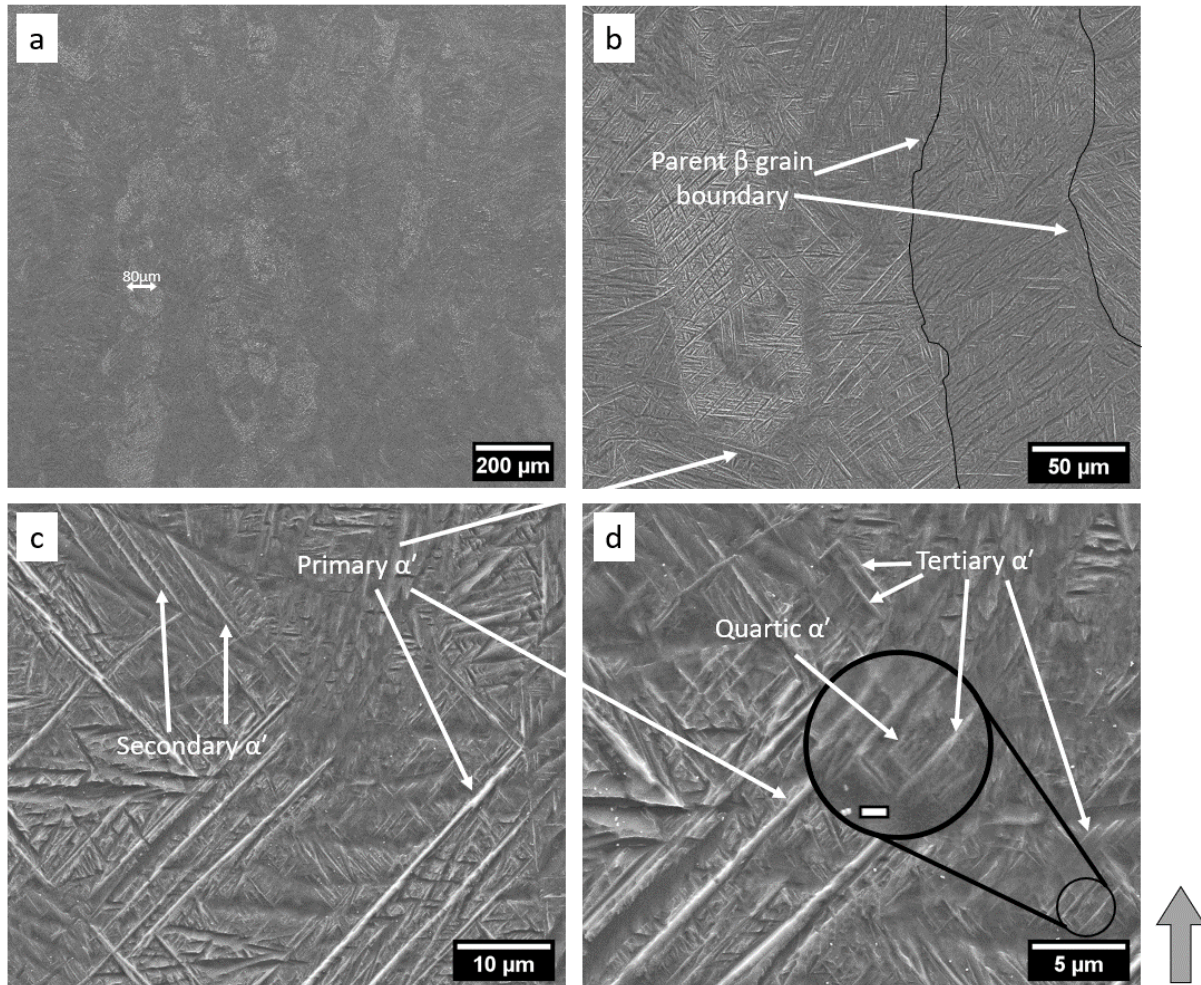
Figure 5.7. Secondary electron SEM images of Ti6Al4V sample 12 after etching, (a) overview of columnar parent β grains giving rise to α′ domains of different orientations, (b) parent β grain boundaries, (c,d) primary, secondary, tertiary and quartic α′ martensite structures. Scalebar in the magnified view in (d) corresponds to 500 nm. Bottom right arrow indicates SLM build direction.

Figure 5.8 shows secondary electron SEM images of etched samples 2 and 4. Both Ti6Al4V samples were processed using 190W laser power and 96 μm hatch spacing. The only difference between these two is the laser speed which was 960 mm/s for sample 2 and 1440 mm/s for sample 4. There is a microstructural difference between these two samples. Sample 2 (Figure 5.8(a,c)) has coarser martensite plates whereas sample 4 (Figure 5.8(b,d)) has finer ones. Change of as-built microstructure with processing parameters has been reported before by other researchers [49], [50], [96], [171], [176]. Yang et al. [96] and Han et al. [171] examined martensite plate size change for different hatch space and laser scan speed values. They both found that both hatch space and laser scan speed affect martensite plate size. Do et al. [49] examined martensite size change depending on different laser scan speed and reported similar

behaviour to this study. The mechanism of martensite change is discussed in more detail in section 5.3.4.
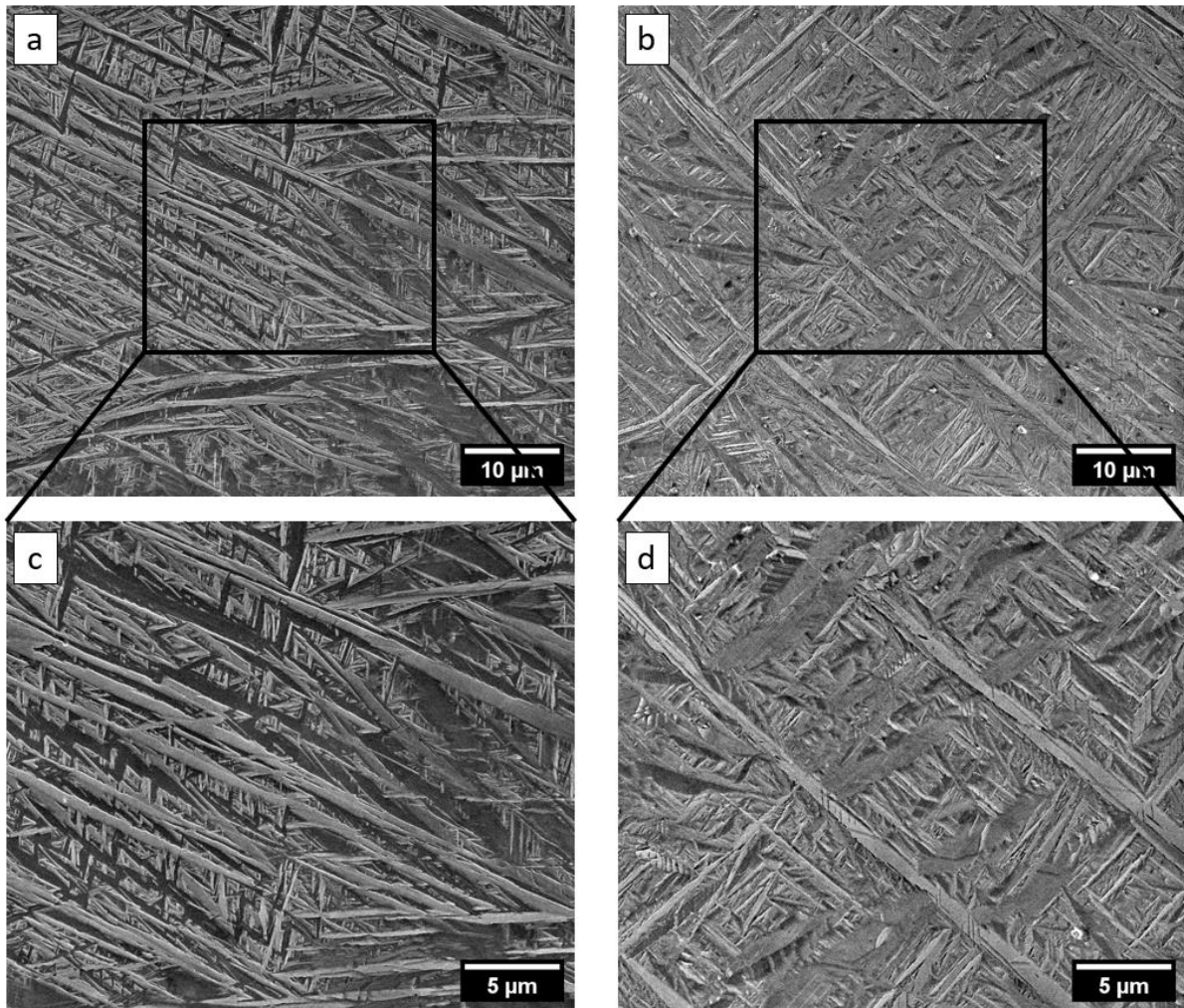
Figure 5.8. Secondary electron SEM images of Ti6Al4V martensitic α′ phase (a,c) sample 2, laser speed 960 mm/s, and (b,d) sample 4, laser speed 1440 mm/s, after etching. Both samples were processed with 190W laser power and 96 μm hatch spacing.

To examine in detail the crystallography of the martensitic α' phase, EBSD analysis was carried out on Sample 1, which is processed using 190 W laser powder, 960 mm/s laser scan speed and 64 μm hatch distance. Sample 1's inverse pole figure (IPF) map taken parallel to the build direction (YZ plane in Figure 5.1(b)) is shown in Figure 5.9(a,b,c). The α' phase hierarchical martensitic structure with different primary, secondary, tertiary and quartic α' phases platelet sizes crystallographic orientations can be seen throughout the structure. The martensite plate size distribution imaged by EBSD is further analysed a misorientation limit of 7° set to distinguish different martensite laths. Maximum Feret diameter is used to evaluate the martensite plate

length. The length range for primary, secondary, tertiary and quartic martensite phases are set as >20 μm, 10-20 μm, 1-10 μm and <1 μm, respectively [96], [175]. Martensite plates smaller than 0.5 μm are not taken into account, due to the 0.1 μm step size of the EBSD scan. For the area analysed, Figure 5.10(a) shows counts of martensite plates for different major axis lengths.

The number of smaller tertiary and quartic martensite platelets (less than 10 μm major axis length) detected by EBSD mapping is significantly higher than the larger primary and secondary ones. There is a sharp peak in the range of 1-2 μm length, which is the most abundant in terms of size distribution. For the region analysed by EBSD, the total number of different martensite types and the total area they cover in the specimen cross-section are presented in Figure 5.10(b). Despite being the second dominant martensite type, quartic martensite covers the least area. The total number of identified quartic martensite plates is ~24 times more than secondary plates and ~81 times more than primary martensite plates. However, the area covered by quartic martensite in the analysed cross-section is ~three times less than secondary and primary martensites. The smaller size of quartic martensite plates results in less area coverage despite a remarkable increase in total number. Tertiary martensite has a bigger plate size, and so it has the highest number of individual laths and highest coverage on the surface (Figure 5.10(b)).
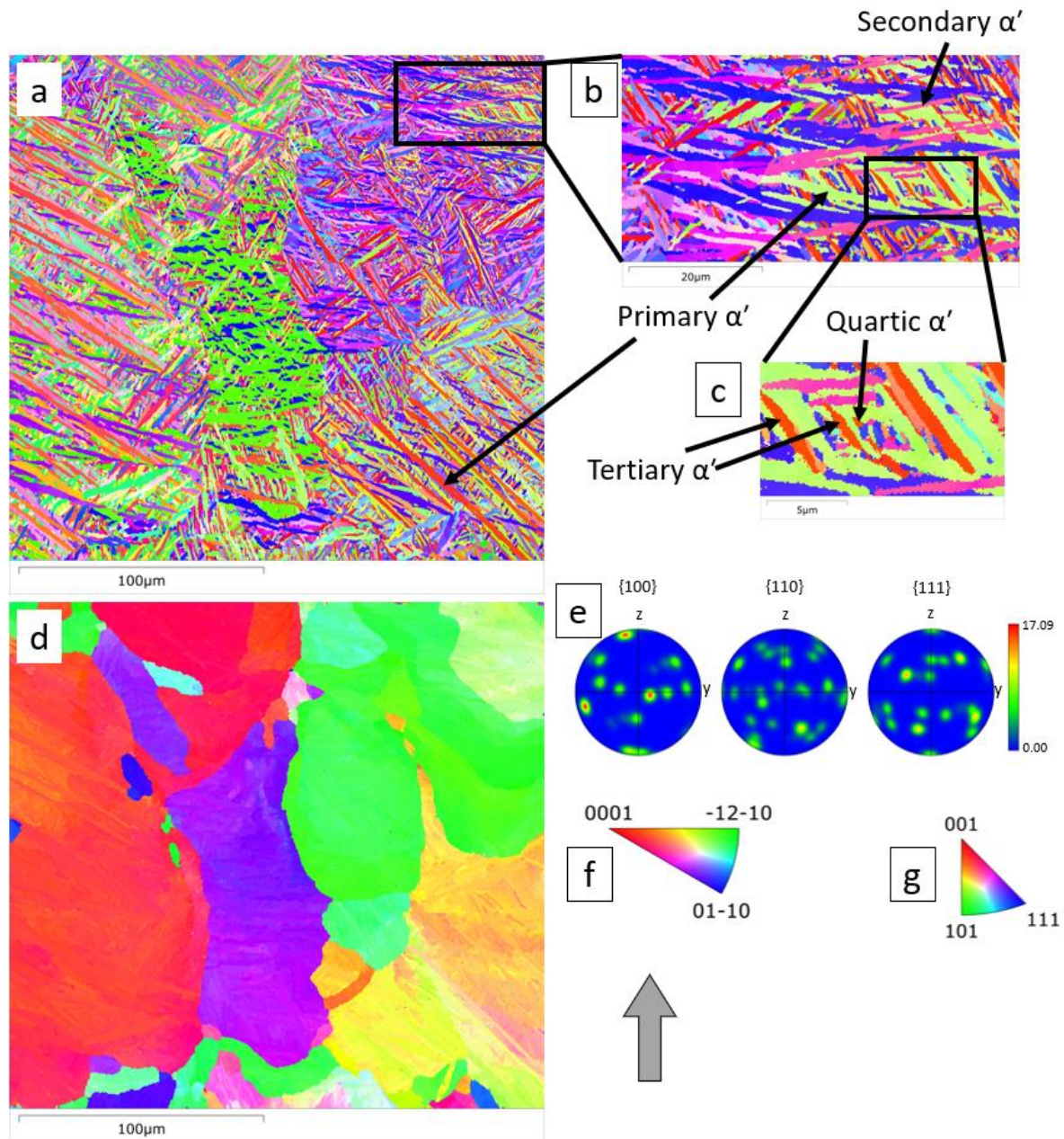
Figure 5.9. Ti6Al4V sample 1's (a) EBSD IPF image of α' phase; (b) magnified view of the rectangle region in (a) showing secondary α'; (c) magnified view of the rectangle in (b) showing tertiary and quartic α'; (d) reconstructed parent β phase's IPF map; (e) contour pole figures of {100}, {110} and {111} planes of reconstructed β phase; IPF colour key for (f) α' and (g) β phases. The bottom right arrow indicates SLM build direction (Z axis). IPF colours in (a) - (d) represented in the normal direction to image (X-axis).

The IPF map and pole figures of the reconstructed parent β phase determined from the EBSD α' phase mapping Figure 5.9(a) are shown in Figure 5.9(d) and Figure 5.9(e), respectively. Individual β grains grow through successive deposition layers. This sort of epitaxial growth through several SLM layers is typical for SLM of Ti6Al4V alloy [39], [67], [88], [177], [178]. Crystallographic texture is developed in $\langle 100 \rangle_\beta$ direction (Figure 5.9(e)). $\langle 100 \rangle_\beta$ direction is the preferred growth direction for cubic metals and

parent β grains grow in this direction [39], [89], [179]. The SLM heat is mostly transferred through the base plate, and this results in a heat gradient and columnar β grains parallel to the build direction [39], [67], [179]. There is a slight misorientation of β grains from the build direction (Z-axis) (Figure 5.9(d)). This slight shift is attributed to inhomogeneous local heat gradients due to the rotation of laser scans by 67° in each successive layer in this study [67], [88].

EBSD images taken from different planes and different materials had different imaging areas. This restrains the ability to compare results from different measurements. Parent β grain boundary length is the perfect measure to evaluate grain size effect; however, the different EBSD imaging areas preclude the comparison of different scans. To overcome this issue, the parent β grain boundary length is calculated from the reconstructed images, and then, this value is divided by the total area of this particular scan. Therefore, a number to assess grain size from different EBSD scans is achieved. The number calculated using this methodology will be named as parent β grain boundary length per unit area ($\mu m/\mu m^2$) after this point within this document. Parent β grain boundary length for per unit area from the reconstructed image of the EBSD scan acquired on the YZ plane when the grain boundary misorientation limit was set to 7° is 0.059 $\mu m/\mu m^2$.
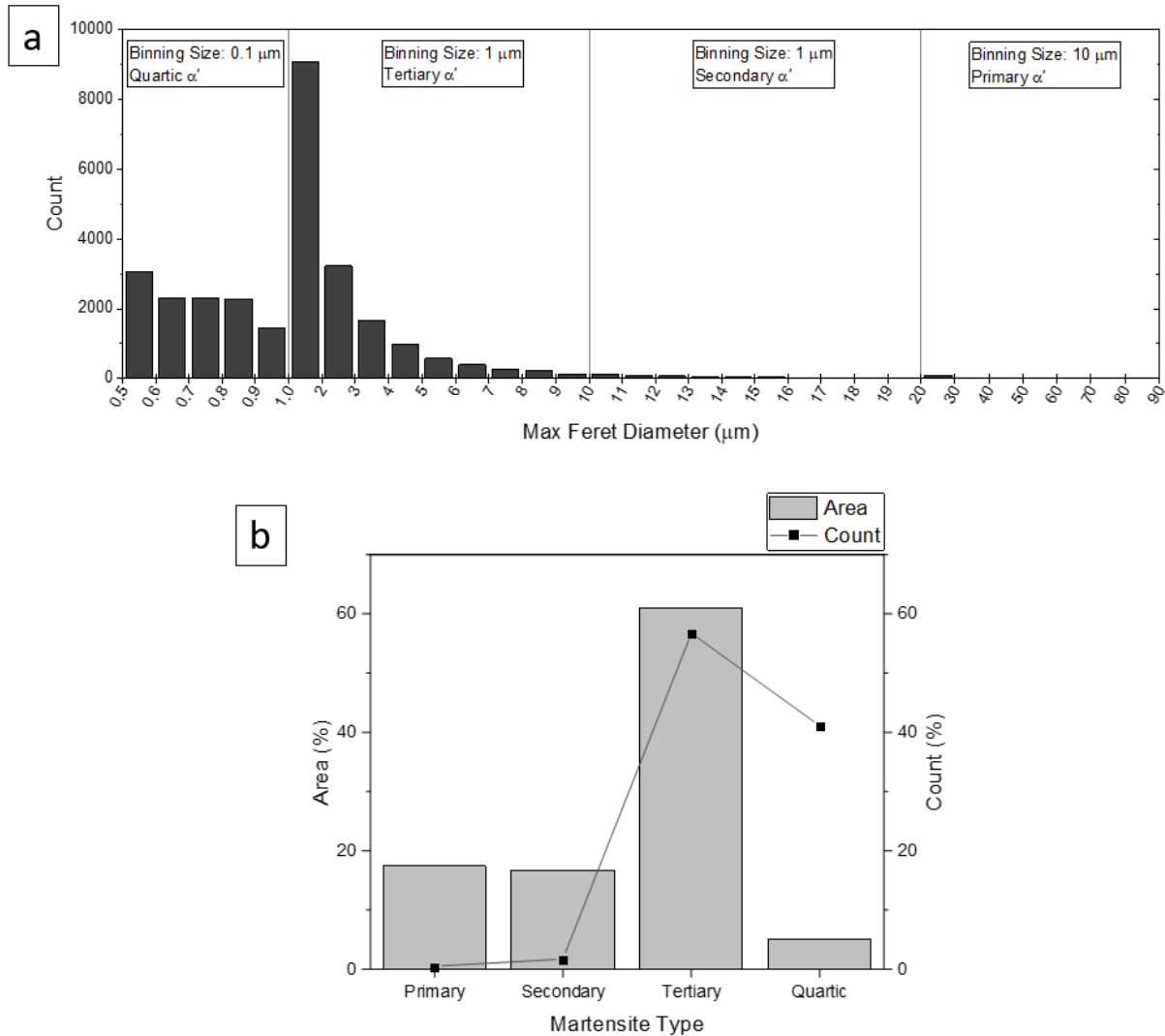
Figure 5.10. Martensite plate size analysis of Ti6Al4V Sample 1 EBSD scan in Figure 5.9: (a) Number of identified α′ martensite plates evaluated by their Maximum Feret diameter and, (b) area coverage fraction and total count fraction of different martensite types in the EBSD scan. Note different binning sizes for different martensite sizes in (a).

An IPF, taken perpendicular to the SLM build direction (XY plane in Figure 5.1(b)), of Ti6Al4V sample 1 is shown in Figure 5.11(a,b,c). As in the YZ plane (Figure 5.9(a,b,c)), four different martensite types are detected on the EBSD map of the XY plane cross-section parallel to the SLM layers. Figure 5.12(a) shows the α' martensite size distribution of Figure 5.11 which is comparable to the YZ plane (Figure 5.10(a)). The number of tertiary and quartic martensite plates outnumbers the primary and secondary martensite, whereas quartic martensite covers the least area despite being the second abundant type. There is a slight change in total numbers, but this arises statistically due to the two different total imaging frame sizes.
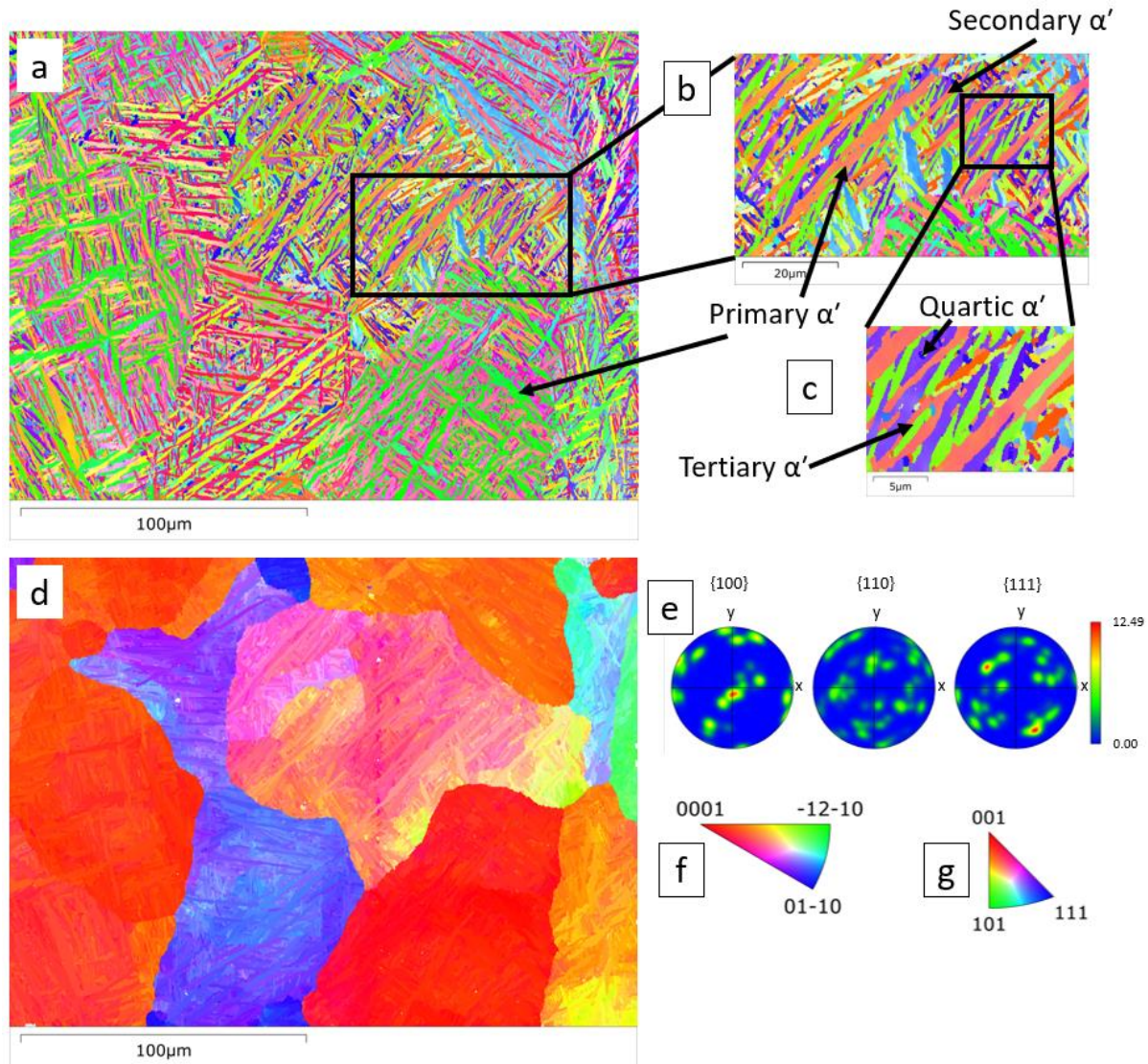
Figure 5.11 Ti6Al4V sample 1's (a) EBSD IPF image of α' phase, (b) magnified view of the rectangle region in (a) showing secondary α', (c) magnified view of the rectangle in (b) showing tertiary and quartic α', (d) reconstructed parent β phase's IPF map, (e) contour pole figures of {100}, {110} and {111} planes of reconstructed β phase, IPF colour key for (f) α' and (g) β phases. Acquisition was performed on XY plane perpendicular to the build direction, IPF colouring in (a) and (d) show orientations with respect to the paper surface normal (Z-axis).

The reconstructed parent β phase grains determined from the EBSD α' phase mapping in Figure 5.11(a) are shown in Figure 5.11(d). β grains does not have columnar morphology when imaged parallel to the build direction. This arises due to imaging through the transverse planes of the columnar grains. Significant {100} plane texture is seen perpendicular to the imaging plane (Figure 5.11(e)), which is also detected with YZ plane images (Figure 5.9(e)), consistent with preferential occurrence of grains with <100>$_\beta$ direction parallel to the build direction. Parent β grain boundary length for per unit area when the grain boundary misorientation was set to 7° is calculated as 0.064 $\mu m/\mu m^2$. This is quite close to the value measured for the YZ plane (0.059 $\mu m/\mu m^2$).
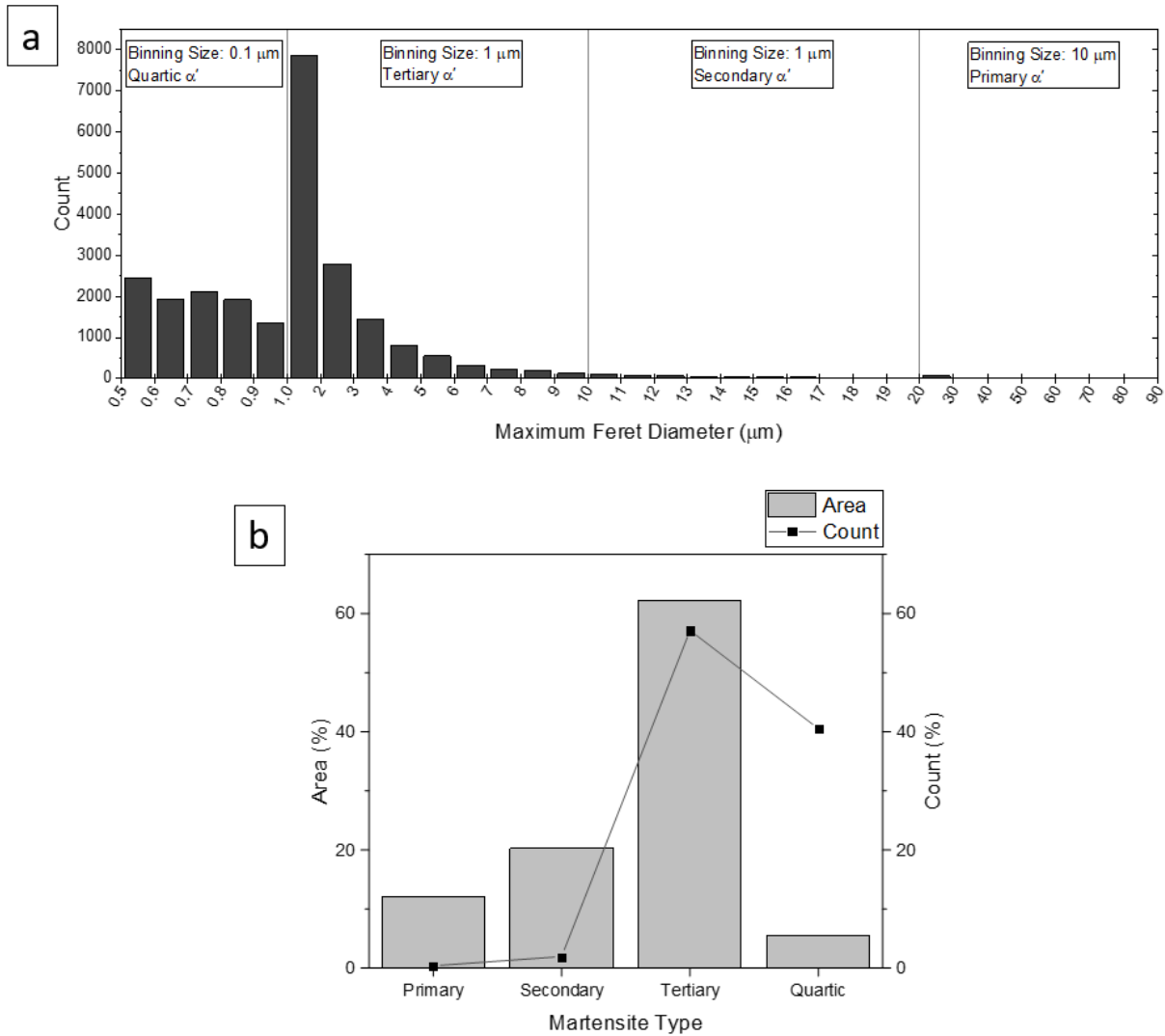
Figure 5.12. Martensite plate size analysis of Ti6Al4V sample 1 EBSD scan in Figure 5.11: (a) Number of identified α' martensite plates evaluated by their Maximum Feret diameter and, (b) area coverage fraction and total count fraction of different martensite types in the EBSD scan. Note different binning sizes for different martensite sizes in (a).

5.3.4. SLM Part Hardness

Hardness of Ti6Al4V parts processed with different processing parameters were analysed by microhardness measurements (HV0.5) on the parallel plane to the build direction (Figure 5.1(b)). Measured hardness values varied between 355 HV and 370 HV (Figure 5.13(a)). *p*-values of hatch distance, laser speed and 2-way interaction of laser speed and hatch distance are 0.505, 0.431 and 0.034, respectively. According to these results, the 2-way interaction of hatch space and laser speed is effective on hardness when the confidence interval is set at 95%. This means that their effect on

part hardness is dependant on each other. Therefore, the change of hardness should be examined while keeping the other value constant.

Figure 5.13(b) shows the change of hardness for different hatch spacing at three different laser scanning speed levels. High represents 1539 mm/s and 1440 mm/s, medium represents 1200 mm/s and low represents 960 mm/s and 860 mm/s laser scanning speeds. When laser scanning speed is set at a high or medium value, increasing hatch distance reduces the hardness. On the other hand, at low laser scan speeds, increasing hatch distance results in a hardness rise.

Figure 5.13(c) shows the change of hardness depending on the laser speed at different hatch distance levels. In Figure 5.13(c), high represents 103 µm and 96 µm hatch distances, medium represents 80 µm hatch distance, and low represents 64 µm and 57 µm hatch distances. Hardness increased with increasing laser speed, for hatch distances 57-80 µm. Conversely, laser speed increase resulted in hardness reduction if the hatch distance remains at a low value. The highest hardness is seen at 960 mm/s laser scan speed and 96 µm hatch distance combination.
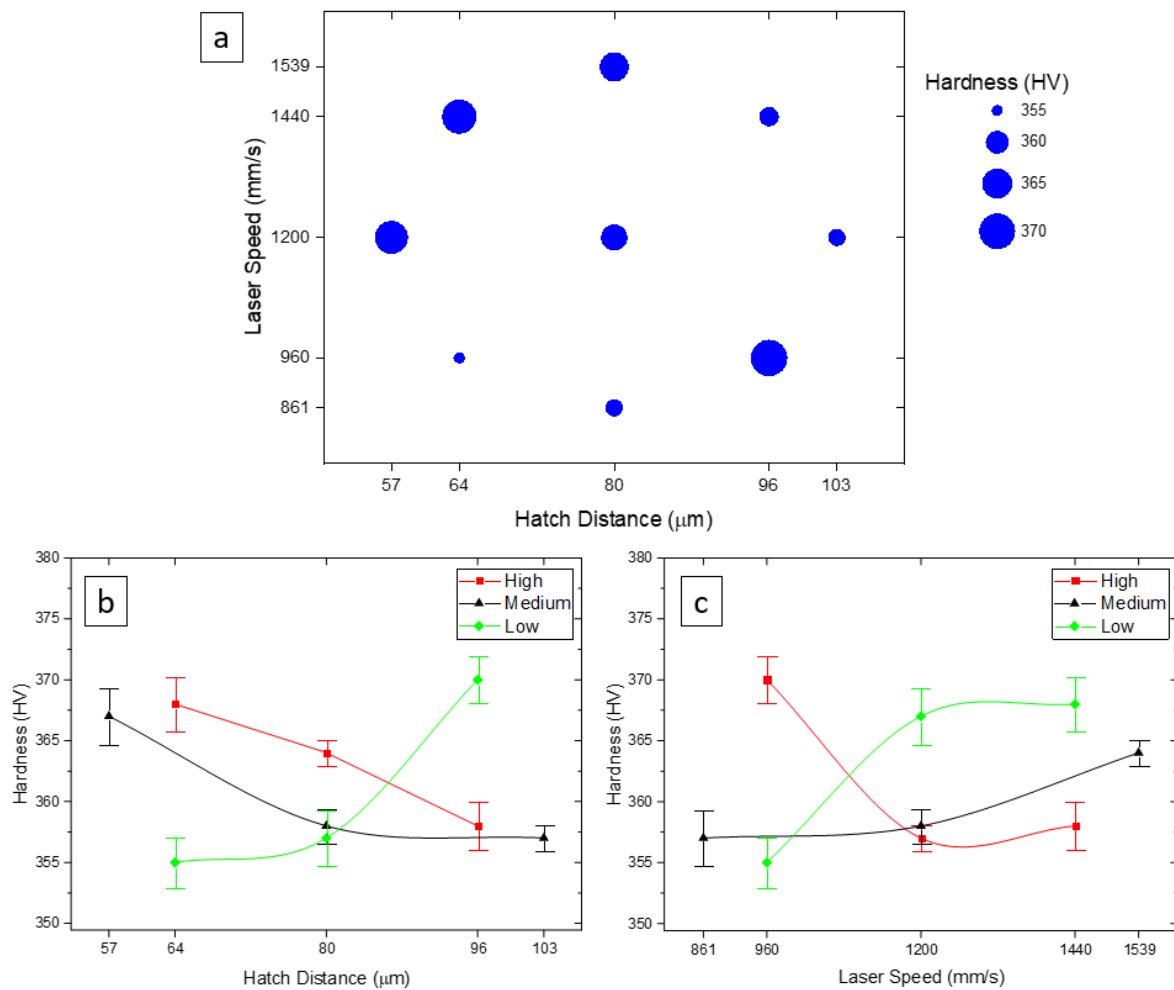
Figure 5.13. (a) Ti6Al4V hardness for different processing parameters, (b) Hardness dependence on hatch distance, with speeds High = 1539 mm/s and 1440 mm/s, Medium = 1200 mm/s, Low = 960 mm/s and 860 mm/s and (c) Hardness dependence on laser speed with hatch distances High = 103 µm and 96 µm, Medium = 80 µm, Low = 64 µm and 57 µm. Error bars (b,c) represent the standard error of mean.

There are several possible reasons behind the fairly modest 355 HV − 370 HV (4%) hardness changes observed with Ti6Al4V processing parameters. Spatter particles were observed on the top surface of some parts (samples 3, 4 and 5), and local porosity is observed in one of these parts (Figure 5.2, Figure 5.3 and Figure 5.4). Spatter particles are larger in size than original powder particles and probably travels from one part to another. Therefore, they may have a higher oxidation level or may have a different chemical balance than the original particles. Simonelli et al. [71] studied oxidation levels and alloying element segregation in spatter particles of AlSi10Mg, 316L and Ti6Al4V alloys. They found that there is chemical segregation and a thicker oxide layer on the surface in AlSi10Mg and 316L spatter particles. However, neither segregation, nor oxidation layer on the surface was observed in Ti6Al4V spatter

particles [71]. Additionally, if spatter particles are completely molten, there should be no residual porosity within the structure; hence the effect of spatter particles will probably be minimised due to mixing with original powder particles. Here, there is no trend observed between hardness and samples 3, 4 and 5, affected by spatter.

Porosity changes due to processing parameters can be a reason for hardness variation [51], [56], [173]. However, this is more prominent while using macrohardness measurements with high measurement loads [51], [56], [180], which can encompass significant number of pores within the hardness test volume. Javidrad et al. [56], Majumdar et al. [51], and Khorasani et al. [180] examined porosity and hardness of Ti6Al4V parts processed using different parameters, and identified the effect of porosity on hardness. All these studies performed macrohardness measurements; therefore, it is more likely that pores influenced hardness due to increased deformation volume during testing. In comparison, the HV0.5 microhardness measurement used in this study caused a reduced deformation volume and all Ti6Al4V samples had over 99.5% relative density according to optical image analysis (Figure 5.2). This porosity is too low to cause any measurable hardness differences compared with previous studies [56], [180].

A likely reason for Ti6Al4V hardness variation is varying microstructural properties due to different processing parameters. Change of Ti6Al4V microstructure with varying energy density is reported before by various researchers [49], [50], [88], [96], [171], [176]. Han et al. [171] investigated the change of hardness and α' martensite width for various energy densities. They stated that α' martensite size and alloy hardness is affected by processing parameters. Do et al. [49] and Zhao et al. [176] also investigated martensite size change and its effect on hardness and concluded different resultant martensite sizes and harnesses.

Similar to the previous studies, the mechanism behind Ti6Al4V hardness variation in this study likely arises from microstructural variations due to different SLM energy inputs. Figure 5.8 shows two different Ti6Al4V samples' microstructures whose processing parameters were the same except laser scanning speed (Hatch=High,

Figure 5.13(c)). Sample 2 was scanned with a slower laser speed (960 mm/s), whereas sample 4 was scanned with a faster one (1440 mm/s). Slower laser scan speed results in a lower cooling rate [181], and a lower cooling rate is likely to generate larger martensite plates [96], [171]. Here, sample 2 hardness was 370 HV, and sample 4 hardness was 358 HV. Do et al. [49] studied the change of martensite plate sizes and hardness depending on laser scan speed. They found that lower laser scan speed results in larger martensite plates and elevated hardness.

On the other hand, the trend of laser scan speed and hardness goes in totally the opposite direction while hatch distance set at medium and low values (Figure 5.13(c)). In this case, increasing laser scan speed results in higher hardness. SLM process has complex heating and cooling cycles due to subsequent laser scans and layers [68], [95], [182]. When the hatch distance becomes smaller, the reheating effect of consecutive laser scans becomes more dominant due to closer successive laser scans. The higher laser speed means the laser will scan neighbouring lines quicker, and this can result in a lower cooling rate, which can lead to larger martensite plates and higher hardness. This mechanism could be the reason behind the opposite behaviour at different hatch levels. However, it should be noted that the effect of processing parameters on martensite plate size requires deeper investigation and large area EBSD investigation on different energy densities would give more reliable data to reveal microstructural changes.

5.4. Conclusions

In this chapter, plain Ti6Al4V parts have been manufactured using various processing parameters. The microstructure, porosity, and hardness of these parts have been examined for different processing parameters. All parts have high relative density, and no relationship has been found between processing parameters and measured porosity. Some swelling due to spattering and consequent local porosity is observed on parts that were in a specific position in the buildplate. Signs of these spatter particles were observed on the top surface of these parts in optical profilometry images. Similar

to porosity, no relationship has been found between processing parameters and top and side surface roughness.

Hierarchical α' martensite structure is observed due to reheating effects of subsequent laser scans and layer during SLM, and the primary – quartic lath size distribution quantified using EBSD. Crystallographic texture with $\langle 100 \rangle_\beta$ aligned in the build direction is observed after parent β grain reconstruction. Hatch distance and laser scan speed are detected as effective on hardness change, and a 2-way interaction of these two is detected as statistically significant on hardness change. These results provide a benchmark for *in situ* TiC reinforced Ti6Al4V composites examined in the next chapter.

Chapter 6: Manufacture and Characterisation of *in situ* TiC Reinforced Ti6Al4V Matrix Composites via Selective Laser Melting

6.1. Introduction

In this chapter, the method used in Chapter 4 to prepare *in situ* Ti6Al4V-TiC composites is applied by means of an SLM machine equipped with a continuous wave laser. After proving the feasibility of the method, the effect of mixing time on the microstructure of the mixed powder is examined. The SLM energy density in Chapter 4 was evaluated as low for fully dense parts; hence, here a higher energy density window is used. The SLM *in situ* Ti6Al4V-TiC composites' relative porosity, microstructure, and hardness are investigated through optical microscopy, scanning electron microscopy, electron backscatter diffraction, X-ray diffraction, and micro-hardness.

6.2. Experimental

Graphite flakes and pre-alloyed Ti6Al4V powders are used to create feedstock powder. These powders were directly mixed in a planetary ball mill at 350rpm speed. Powders were mixed for eight hours, and powder samples were taken every hour to evaluate the effect of mixing duration on mixed powder. Composite powders mixed for eight hours were used for SLM processing with the Aconity Mini system equipped with a continuous wave laser. Table 6.1 shows the SLM processing parameters used. Laser power and layer thickness were kept constant at 190W and 30 µm, respectively, for all samples. Central composite design (CCD) response surface methodology is used for statistical analysis. Parts were manufactured on two baseplates, and their order on base plates was made randomly using CCD's run order (Figure 6.1(a)). Samples had dimensions of 10mm × 10mm × 3.5mm (Figure 6.1(b)). Stitched optical images taken in the YZ plane (Figure 6.1(b)) covering 6870µm × 640µm area are used for all samples' relative porosity analysis. SEM images were also taken on the YZ plane, whereas electron backscatter diffraction images (EBSD) were acquired on both YZ and XY planes (Figure 6.1 (b)). 20 kV accelerating voltage and 100nm step size were used for EBSD data collection.

Table 6.1. SLM processing parameters for composite Ti6Al4V-carbon powder.

Sample Number	Hatch Space (μm)	Laser Speed (mm/s)	Volumetric Energy Density (J/mm³)	Linear Energy Density (J/mm)
1	48	720	183	0.189
2	80	720	110	0.189
3	48	1200	110	0.233
4	80	1200	66	0.233
5	64	960	103	0.235
6	64	960	103	0.235
7	64	960	103	0.191
8	41	960	161	0.209
9	87	960	76	0.211
10	64	621	159	0.26
11	64	1300	76	0.171
12	64	960	103	0.211
13	64	960	103	0.211
14	64	960	103	0.211
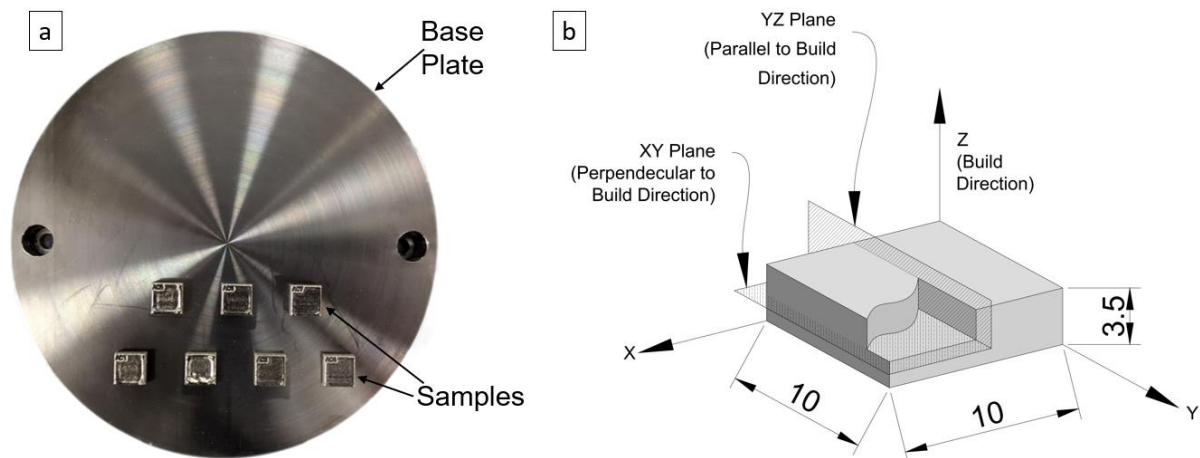
Figure 6.1. (a) SLM parts on the baseplate and (b) sample dimensions and examination planes.

6.3. Feedstock Powder

Secondary electron (SE) SEM images of the feedstock Ti6Al4V powder and graphite flakes are shown in Figure 6.2. Spherical Ti6Al4V particles are observed, with sizes mostly below ~50 μm, and some satellite particles also present (Figure 6.2(a,b), white

arrows). Additionally, a few irregularly shaped particles are also identified. This is a typical morphology for gas atomised powder feedstock [137]. Graphite flakes (Figure 6.2(c,d)) have a typical lamellar morphology [9].
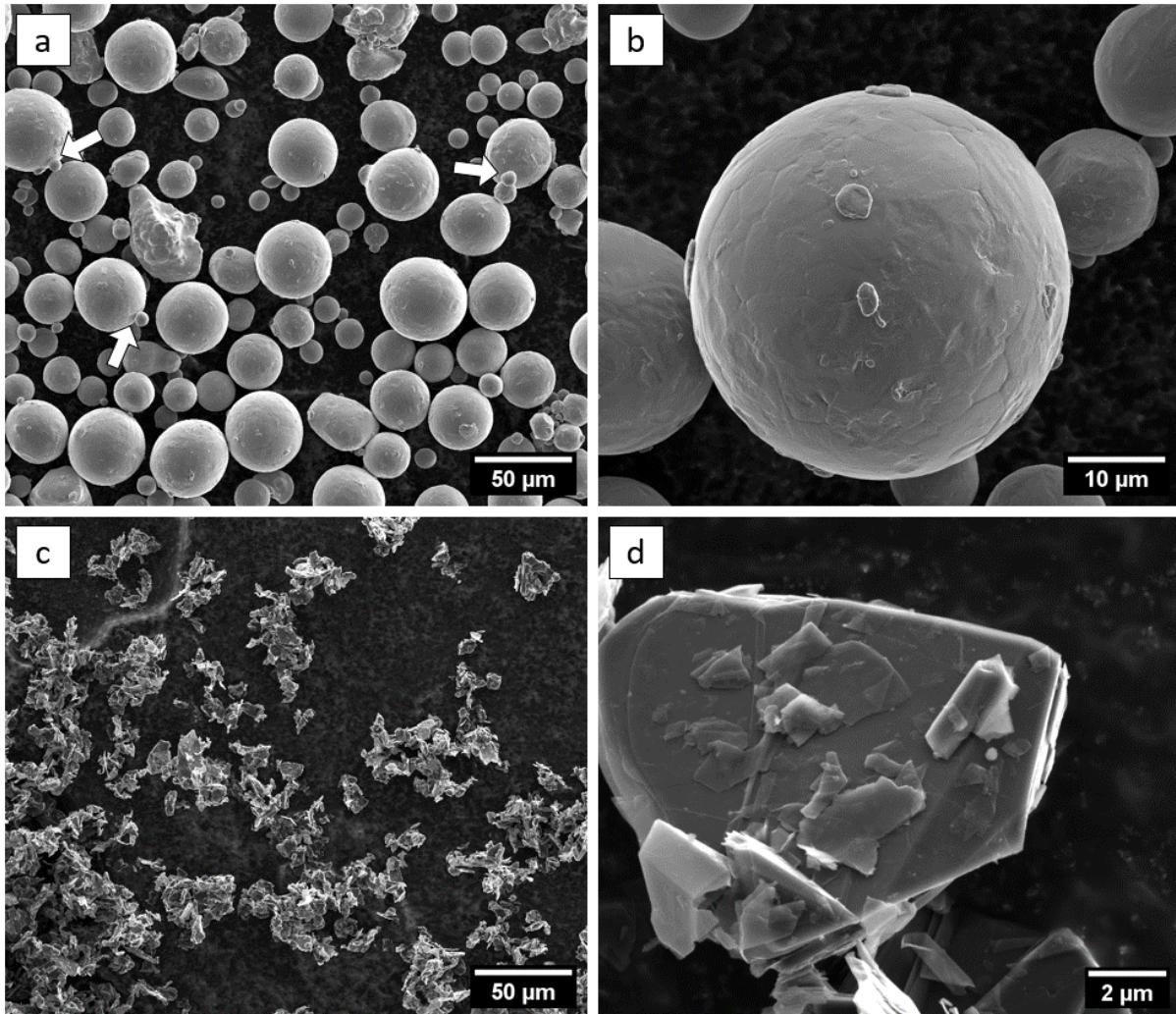
Figure 6.2. Feedstock (a,b) Ti6Al4V powder and (c,d) graphite flakes before direct mixing.

SEM images of mixed powders after one hour (1h), three hours (3h), four hours (4h), five hours (5h), seven hours (7h) and eight hours (8h) mixing are given in Figure 6.3. After 1h mixing, graphite flakes are broken into pieces, and some carbon is transferred onto the powder particles as small <5 μm irregular clumps (Figure 6.3(1h), Figure 6.4(1h)) separated by regions covered by just a sparse distribution of carbon nanoparticles. The red arrow in Figure 6.4(1h) shows a larger graphite flake particle attached onto the surface of a parent particle (Ti6Al4V). Some of the residual graphite flakes are shown with yellow arrows in Figure 6.3. The number of residual graphite

flakes is the highest after 1hour of mixing compared with the longer mixing durations where the carbon has been transferred onto the Ti6Al4V.

After 3h mixing, more carbon (darker SE contrast regions) is observed on the Ti6Al4V parent particles (Figure 6.3(3h)). More transferred carbon increases both the number of carbon clumps on the Ti6Al4V particles and their thickness. A slight reduction of remaining graphite flake particles is also seen due to more prolonged mixing and resultant carbon transfer onto parent particles. After 4h mixing, further coverage of irregular particles is observed (Figure 6.3(3h,4h), green arrows), and between the large carbon agglomerates a continuously rough surface is indicative of a very thin carbon coating even though it is insufficient to cause much reduction in SE signal due to SE emission from the underlying Ti6Al4V. Comparing 1h and 4h mixing, more transferred carbon particles can be seen on parent Ti6Al4V particles after 4h (Figure 6.4(1h,4h)).

A significant change of carbon coverage was seen after 5h mixing (Figure 6.3(5h)). Carbon covered area is increased, whilst the density of residual carbon flakes is reduced (yellow arrows). This trend continued for 7h, and 8h mixing durations and coverage of carbon continued to increase whereas residual flake lessened. After 8h, significantly higher carbon coverage than 1h and 4h can be seen in Figure 6.4. After 4h mixing, local carbon transfer onto particle surface produces a rough surface with large discrete carbon clumps (Figure 6.4(4h), red arrow). However, with further carbon transfer and impact damage, the surface becomes much smoother again after 8 hours with only discrete areas of low carbon coverage (Figure 6.4 (8h), light grey SE contrast).
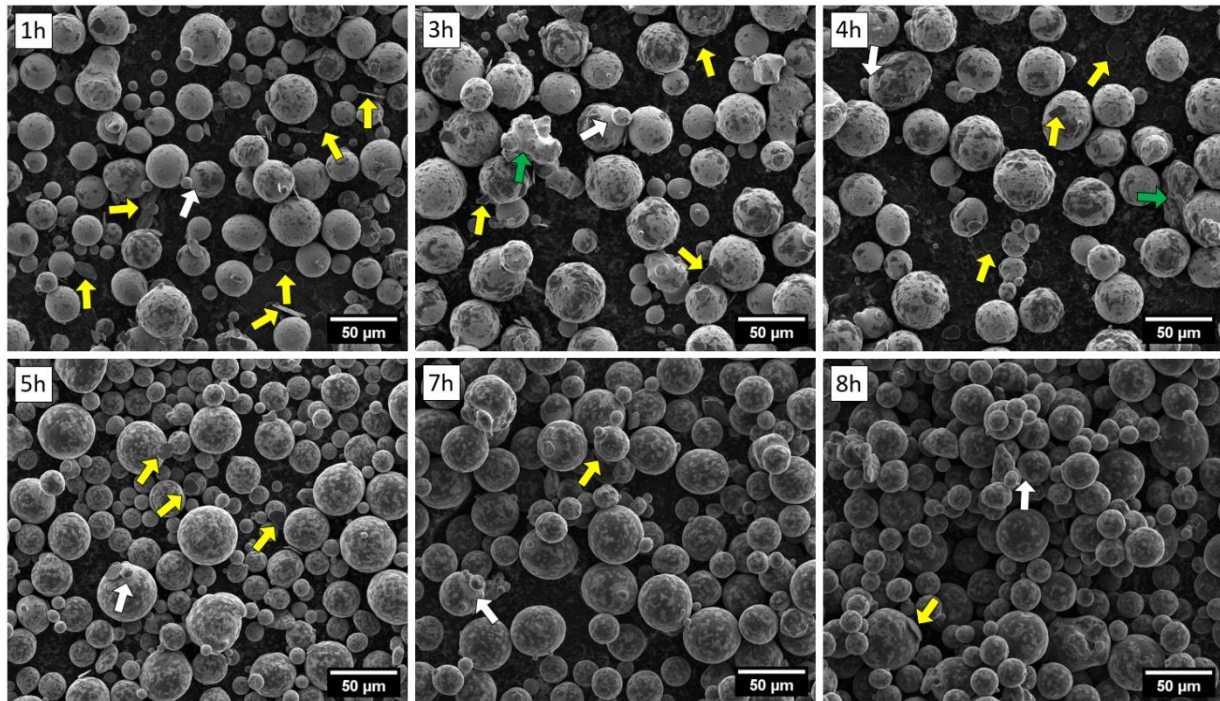
Figure 6.3. Secondary electron SEM images of composite powders after different mixing durations: (a) 1h, (b) 3h, (c) 4h, (d) 5h, (e) 7h, and (f) 8h.

Minimal carbon coverage regions around the Ti6Al4V parent and satellite particle junctions can be seen for all mixing durations (Figure 6.3, white arrows). This arises due to the shielding effect of satellite particles, so carbon particles find it difficult to reach these zones during impact events. However, the lack of carbon coverage zones get smaller with increasing time as multiple impact events and fracture of the carbon make it more likely that these regions are reached.
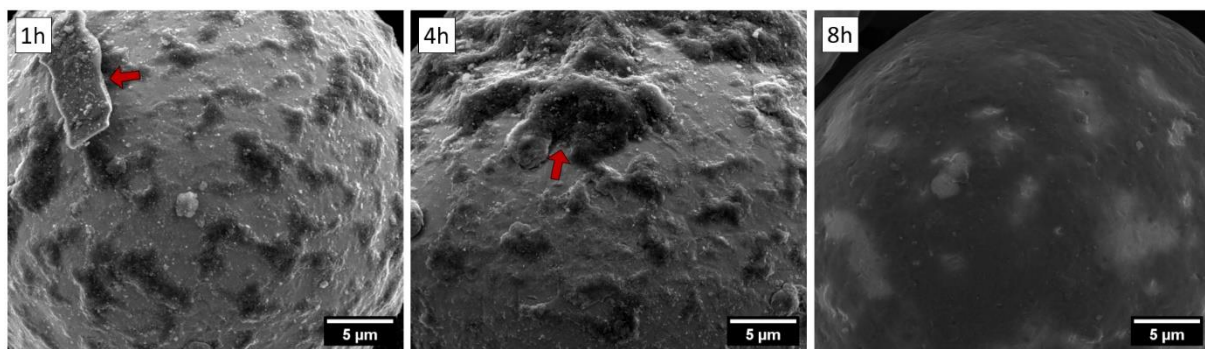
Figure 6.4. Secondary electron SEM images of composite Ti6Al4V-carcon powder particles mixed for (a) 1h, (b) 4h and (c) 8h.

Figure 6.5 shows XRD diffraction patterns of Ti6Al4V powder, graphite flakes, 1h, 4h and 8h mixed composite powders. The XRD of feedstock Ti6Al4V particles has only α' peaks due to rapid cooling. A distinctive peak at 26.5° belonging to graphite's (0002)

plane can be seen in the feedstock graphite flake's XRD pattern (shaded region in Figure 6.5). The (0002) peak of graphite flake is weakened dramatically after 1h mixing (magnified view in Figure 6.5(1h)) and can only be identified in a magnified view. This peak disappeared after 4h and 8h mixing. On the other hand, the presence residual parts of graphite flakes can be confirmed in the powder after 4h and 8h mixing from SEM analysis (Figure 6.3). However, their lower amount made them undetectable in the XRD after 4h and 8h mixing and is consistent with highly defective/amorphous carbon.

Increased mixing time resulted in more continuous carbon coverage around particles and a smoother coated particle surface. Increased mixing duration results in more impact events friction between parent, coated-parent, and carbon particles. Initially, graphite flake is transferred onto parent particles. However, friction, adhesion and wear processes from multiple impact events leads to breakup and damage of the graphite crystals into highly defective/amorphous carbon nanoparticles. The carbon disperses on the Ti6Al4V surface as aggregated clumps of carbon, that increase in depth and connectivity with increasing time. A homogeneous coating of parent particles is desirable for even distribution of subsequent reinforcement particles [5], [19], [183]. Additionally, a smoother particle surface and no/limited deformation of parent particles is beneficial for powder flowability [27], [32], [53], [128]. Therefore, the resultant powder after 8h mixing is desirable for better SLM end part properties.
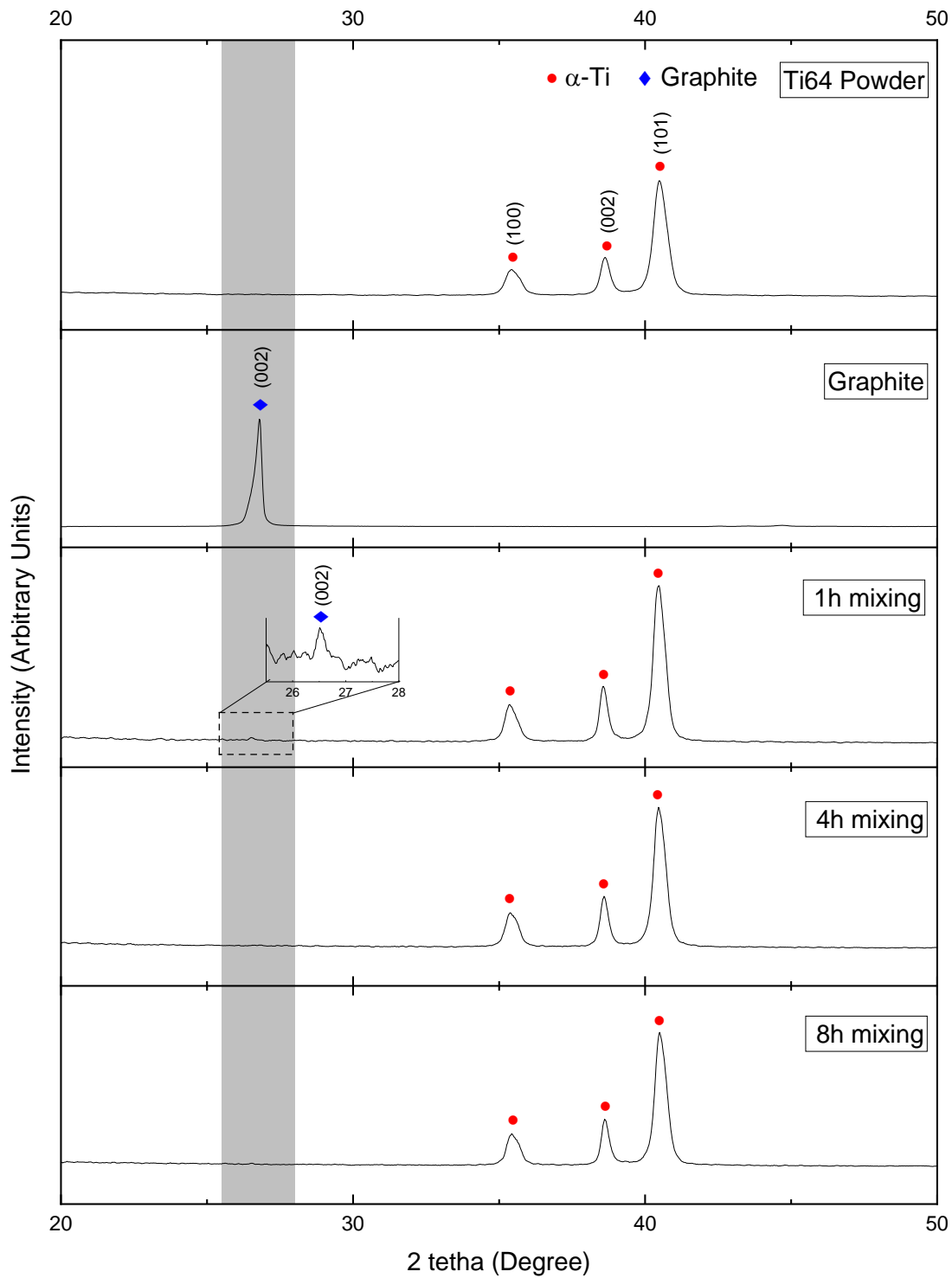
Figure 6.5. XRD profiles of (a) plain Ti6Al4V powder (Ti64 powder), (b) graphite flakes (Graphite), (c) one hour (1h), (d) four hours (4h) and (e) eight hours (8h) mixed Ti6Al4V+carbon composite powders.

6.4. SLM Processing

Following the structural analysis, 8h mixed Ti6Al4V-carbon composite powder was processed using SLM parameters listed in Table 6.1, and 14 parts were made in total.

Their relative porosity, hardness and microstructure were examined as parallel to the build direction (YZ plane in Figure 6.1(b)), and both parallel (YZ) and perpendicular (XY plane in Figure 6.1(b)) planes were examined using electron backscatter diffraction (EBSD).

6.4.1. Relative Porosity Change

The relative porosity of *in situ* Ti6Al4V-TiC reinforced composites varied from nearly fully dense (0.008%) to 0.75%. *p*-values of hatch space, laser speed, and quadratic term of laser speed are 0.129, 0.001, 0.010, respectively. 0.129 *p*-value of hatch space means there is no statistical significance of hatch space over porosity change when the confidence interval is set at 95%. Additionally, *p*-values of two-way interaction of hatch space and laser speed and quadratic term of hatch space are above the .05 threshold value for 95% confidence interval, which makes them statistically insignificant over porosity. As a result, only the laser speed and the quadratic term of the laser speed are effective on porosity at a 95% confidence interval. The quadratic term shows that there is a peak or valley value of porosity within the experimental parameter range of this study.

Figure 6.6(a) maps the porosity change for varying hatch space and laser scan speed. There is a substantial increase of Ti6Al4V-TiC porosity at low laser scan speed values. Figure 6.6(c,e,f) shows optical cross-sectional images of samples manufactured with low laser scan speed and resultant high energy density. Pores are spread throughout the whole cross-section. Figure 6.6(b) shows the cross-section of the relatively densest part (sample 12). Only three pores having larger than 5 µm major diameter can be seen in sample 12. Figure 6.6(g) shows the pore structure of the three highly porous parts (samples 1, 2 and 10, low laser scan speed) in a magnified view. Mostly spherical keyhole pores are apparent within all these parts which is a sign of excessive heat input [100], [101]. This type of pores is reported by various researchers studying the SLM of Ti6Al4V alloy process at relatively high energy densities [50], [51], [98], [149].

There is an unusually high porosity while using 960 mm/s laser scan speed and 87 µm hatch space (sample 9, Figure 6.6(a)). This is an unexpected porosity comparing with

similar processing parameters. The optical cross-section of this sample is given in Figure 6.6(d). A large crack on the right side of this sample occurs within the imaged cross-section; however, other regions remain pore and crack free. When this crack is removed from the porosity measurement, porosity drops from 0.51% to 0.01% and the result correlates well with other measurements. Furthermore, if 0.01% porosity is used for statistical analysis, the *p*-value of both laser scan speed and quadratic term of laser scan speed drops to < 0.001, which means their correlation with porosity becomes even more robust.

Figure 6.6(h) shows the change of porosity depending on laser scan speed. The high line represents hatch distances of 80 μm and 87 μm, the medium line represents 64 μm, and the low line represents 41 μm and 48 μm hatch distance in this graph. Porosity reaches the highest levels for medium and low hatch spacings at the lowest laser speed values. There is an exception for this trend for the high hatch spacing line (red line) in this graph. The sample processed with medium laser scan speed (960 mm/s) in this line has the highest porosity among the three samples due to a crack in the analysed cross-section. The reason behind this porosity jump is explained in the previous paragraph. When the crack on the right-hand side is removed from porosity calculation, relative porosity drops to 0.01%. The dotted red line labelled as High – Corrected in Figure 6.6(h) represents the porosity distribution of high hatch spacing samples when this crack is removed from sample 9. This sample again follows the trend seen on the other two curves when the crack is ignored.
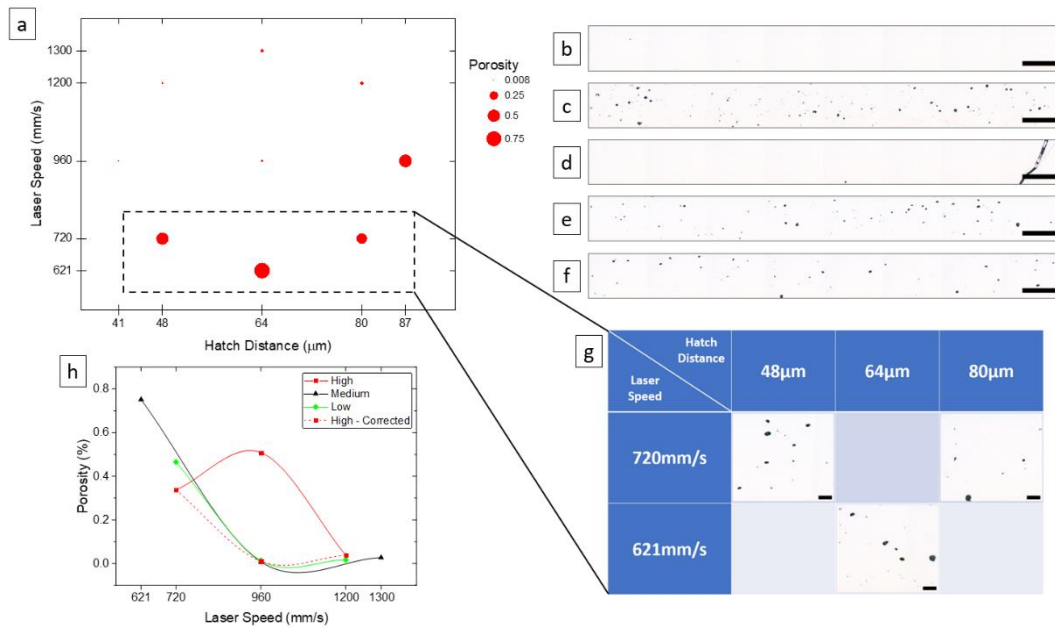
Figure 6.6. (a) porosity of Ti6Al4V-TiC samples depending on laser speed and hatch distance processing parameters, (b-f) large area optical cross-sections of samples (b) 12, (c) 10, (d) 9, (e) 1, and (f) 2. (g) Magnified porosity views of sample 1, 2 and 10. (h) change of porosity depending on laser speed (lines represents High = 80 μm and 87 μm, Medium = 64 μm, Low = 41 μm and 48 μm hatch distances). Scalebars in (b-f) correspond 500 μm, and in (g) correspond 100 μm.

The 960 mm/s laser speed gives the lowest relative porosity of Ti6Al4V-TiC part for all hatch space levels. Below this value, a dramatic increase of porosity is observed due to mostly spherical keyhole pores. The formation mechanism behind keyhole porosity is correlated with material evaporation due to high energy input [101], [103], [160]. Evaporated material right above the melt pool creates a recoil pressure on the molten metal and pushes it downwards [100], [101]. Laser rays cannot reach this pushed down region, and a local reduced temperature due to lack of laser heating results in an increase in surface tension and a decrease in recoil pressure [100]. Recoil pressure cannot overcome surface tension, and a pore is formed [100], [102]. The hydrostatic pressure of liquid metal around the pore results in a spherical pore [100]. Recoil pressure increases exponentially with increasing temperature [102], and this causes larger and more irregular pores with increasing energy input [100].

The exponential increase of recoil pressure with increasing temperature may be the mechanism behind the jump of the porosity to the higher levels for the low laser scan speeds of 720 mm/s and 621 mm/s. This exponential increase also can explain why only a 13% decrease in laser scan speed from 720 mm/s to 621 mm/s resulted in nearly two times more relative porosity in the analysed cross-sections.

Porosity of Ti6Al4V-TiC composites was comparable with plain Ti6Al4V composites examined in Chapter 5. Two processing parameters were identical for plain Ti6Al4V and Ti6Al4V-TiC composites. Sample 1 of unreinforced Ti6Al4V and sample 12 of Ti6Al4V-TiC composites are the couple processed with identical parameters. Relative porosities of these two was measured as 0.005 and 0.008 for unreinforced Ti6Al4V and Ti6Al4V-TiC composite, respectively. For the other two identical parameters, sample 9 for plain Ti6Al4V and sample 4 for Ti6Al4V-TiC composite, porosity was measured as 0.008 for plain Ti6Al4V and 0.038 for Ti6Al4V-TiC composite. The difference between these two samples is quite negligible; however, a minor change is observed for Ti6Al4V-TiC composite when a lower energy density is chosen.

Some TiC particles probably will form in the liquid Ti6Al4V phase [20], [23]. The formation of particles changes the viscosity and surface tension of the liquid [27], [184]. Lower surface tension of the meltpool due to nanoparticles [184] might result in a slightly lower relative density if the energy density is low. This might be the reason behind the slight relative density difference between plain Ti6Al4V and Ti6Al4V-TiC composite; however, the difference is too low to draw a final conclusion from it. A local cold zone and resultant surface tension increase can affect keyhole pore formation [100]. The presence of nanoparticles in the melt pool reduces the surface tension of the liquid [184]. Reduction of molten surface tension can move the keyhole threshold energy input to a higher energy density; hence, energy densities that would result in keyhole formation in Ti6Al4V may produce fully dense parts when nanoparticles are present in the liquid. However, this trend was not observed with the processing parameters of this study.

6.4.2. Surface Structure

The top surface roughness (Sa) of Ti6Al4V-TiC composite samples processed with different SLM parameters varies between 2.7 μm and 9.7 μm. However, roughness measurements from different regions on the same sample vary significantly due to underlying low frequency surface waviness. Therefore, a Gaussian regression filter was applied using 0.2mm short-wavelength cut-off before calculating roughness values.

Figure 6.7 shows sample 12's original scan image, the Gaussian regression filter's waviness profile, and the final image used for roughness calculation. After the filter was applied, roughness of all samples varied between 1 µm and 2.3 µm. No statistical relationship was found between top surface roughness and processing parameters when the confidence interval is set at 95%.
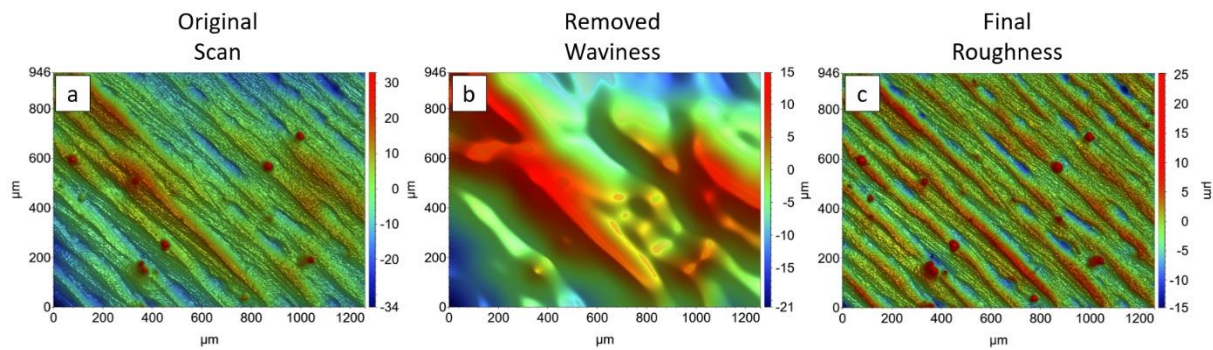
Figure 6.7. (a) initial optical profilometry image, (b) removed low frequency waviness profile and (c) final roughness profile of Ti6Al4V-TiC sample 12.

Figure 6.8(a) and Figure 6.8(b) show optical profilometry images of the top surfaces of Ti6Al4V-TiC sample 8 and sample 9, respectively. Samples 8 and 9 were processed using 41 µm and 87 µm hatch distance, respectively, with laser scan speed was set as 960 mm/s for both. Spatter particles are seen on both samples, and some reach ~80 µm diameter (Figure 6.8(b)). Surface height changes from different laser scans become more distinctive when the larger hatch distance is set (Figure 6.8(b)). On the other hand, height differences between adjacent laser scans become less visible when the hatch distance is set at the lowest value (Figure 6.8(a)). Roughness (Sa) is measured as 1.1 µm for sample 8 (Figure 6.8(a)) and 2.3 µm for sample 9 Figure 6.8(b).

Optical profilometry images of Ti6Al4V-TiC samples 10 and 11 are given in Figure 6.8(c) Figure 6.8(d), respectively. These two samples were processed with the same hatch spacing (64 µm), but different laser scan speeds of 621 mm/s and 1300 mm/s for samples 10 and 11, respectively. The lower laser scan speed (Figure 6.8(c)) causes lower height laser scans than the higher laser scan speed (Figure 6.8(d)). Roughness (Sa) is measured as 1.2 µm and 1.4 µm for samples 10 and 11, respectively with the difference is small comparing with hatch distance variation (Figure 6.8(a) Figure 6.8(b)).

When the hatch distance is reduced, the overlap between adjacent laser scans increases [134], [166], [180], [185]–[187]. The roughness of the top surface decreases due to high overlap when the hatch space is lowered. More overlap creates more total melt pool volume for each layer, and the resultant top surface has a smoother finish [187], [188]. Lower laser scan speed also generates a larger melt pool, and solidification takes longer [161], [163]. Hence, there is more time for the melt pool to flatten [163]. This leads to lower surface roughness; however, the difference is negligible between samples processed using different laser scan speeds in this study. This may be due to high energy density window in this study. Nearly all laser scan speed values were determined to be lower than optimum Ti6Al4V processing parameters. Hatch distance values were also chosen mostly below the optimum processing parameters. Therefore, all parameters give enough time to see the flattening effect and to provide enough overlap. As a result, no significant change is observed between processing parameters.
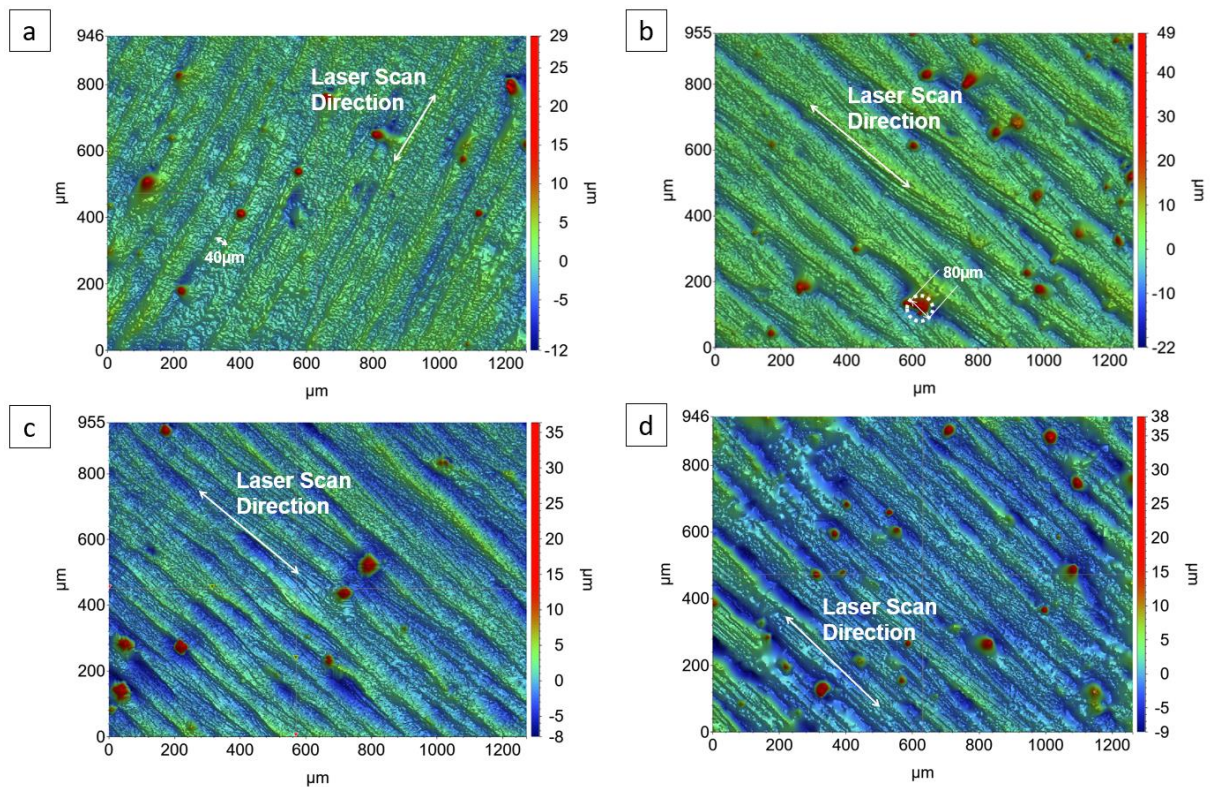
Figure 6.8. Top surface optical profilometry images of Ti6Al4V-TiC (a) sample 8, (b) sample 9, (c) sample 10 and (d) sample 11 after Gaussian regression filter is applied. Extreme spatter particles are highlighted.

Side surface roughness (Sa) of parts varied between 11.9 µm and 17.1 µm, which is considerably higher than the top surface roughness. Like top surface roughness, no

statistically meaningful relationship was found between processing parameters and side surface roughness at a 95% confidence interval. Figure 6.9 shows optical profilometry images of samples with minimum 11.9 μm roughness (sample 6) and maximum side surface roughness 17.1 μm for sample 7. Partially molten particles stuck to the surface can be seen on both samples. No apparent difference was noticed between top and side surface microstructures of plain Ti6Al4V alloy samples and Ti6Al4V-TiC composites.

In order to enhance surface finish and dimensional accuracy of parts manufactured by SLM, contour scanning is often implemented [15], [168]. Here no side surface contour scanning was applied so as not to interfere with analysis of parts' densification behaviour. Hence, no significant relationship between processing parameters and side surface roughness is observed. Powder particles surrounding the melt pool attach to it by being partially molten during laser melting [161], [168] and partially molten particles on side-walls is typical for SLMed parts. Side surface roughness may also be affected by the angle of hatch scans with respect to the side surface, and this may cause lack of correlation of roughness and processing parameters.
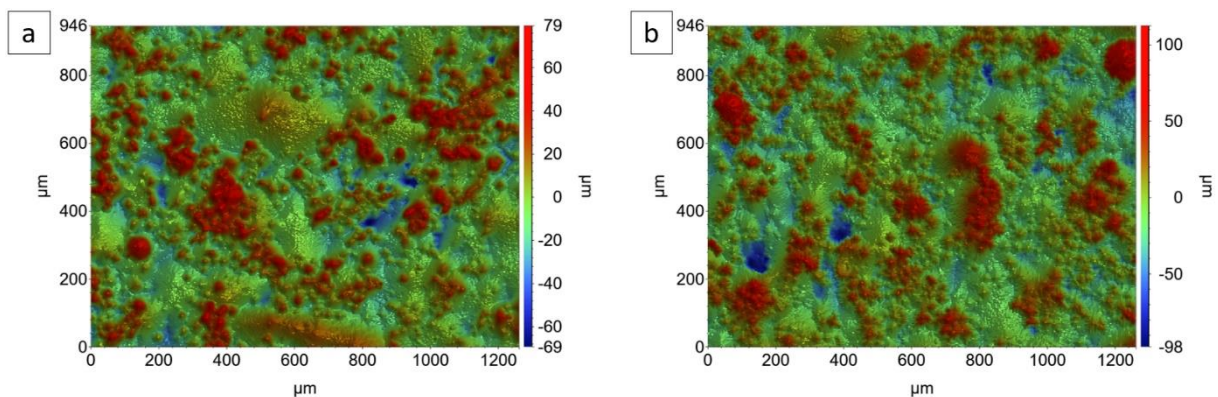
Figure 6.9. Side surface optical profilometry images of Ti6Al4V-TiC (a) sample 6 (Sa = 11.9 μm) and (b) sample 7 (Sa = 17.1 μm). Partially molten adhered particles are clearly visible.

6.4.3. Microstructure

Figure 6.10 shows XRD results of an *in situ* TiC reinforced Ti6Al4V sample, a plain Ti6Al4V sample and the Ti6Al4V pre-alloyed powder. TiC peaks are identified for the TiC reinforced sample confirming *in situ* TiC formation during SLM processing. The TiC XRD peak is detected for all the samples processed in this chapter. TiC can be

formed in a C/Ti compositional ratio range between 0.5-1 [146]; therefore, TiC can be formed within the 4.4-9.9 wt.% range if all carbon is consumed during the reaction [9]. This corresponds to 4.4-9.0 vol.% range considering 4.43g/cm³ density for Ti6Al4V [189] and 4.91g/cm³ density for TiC [146].
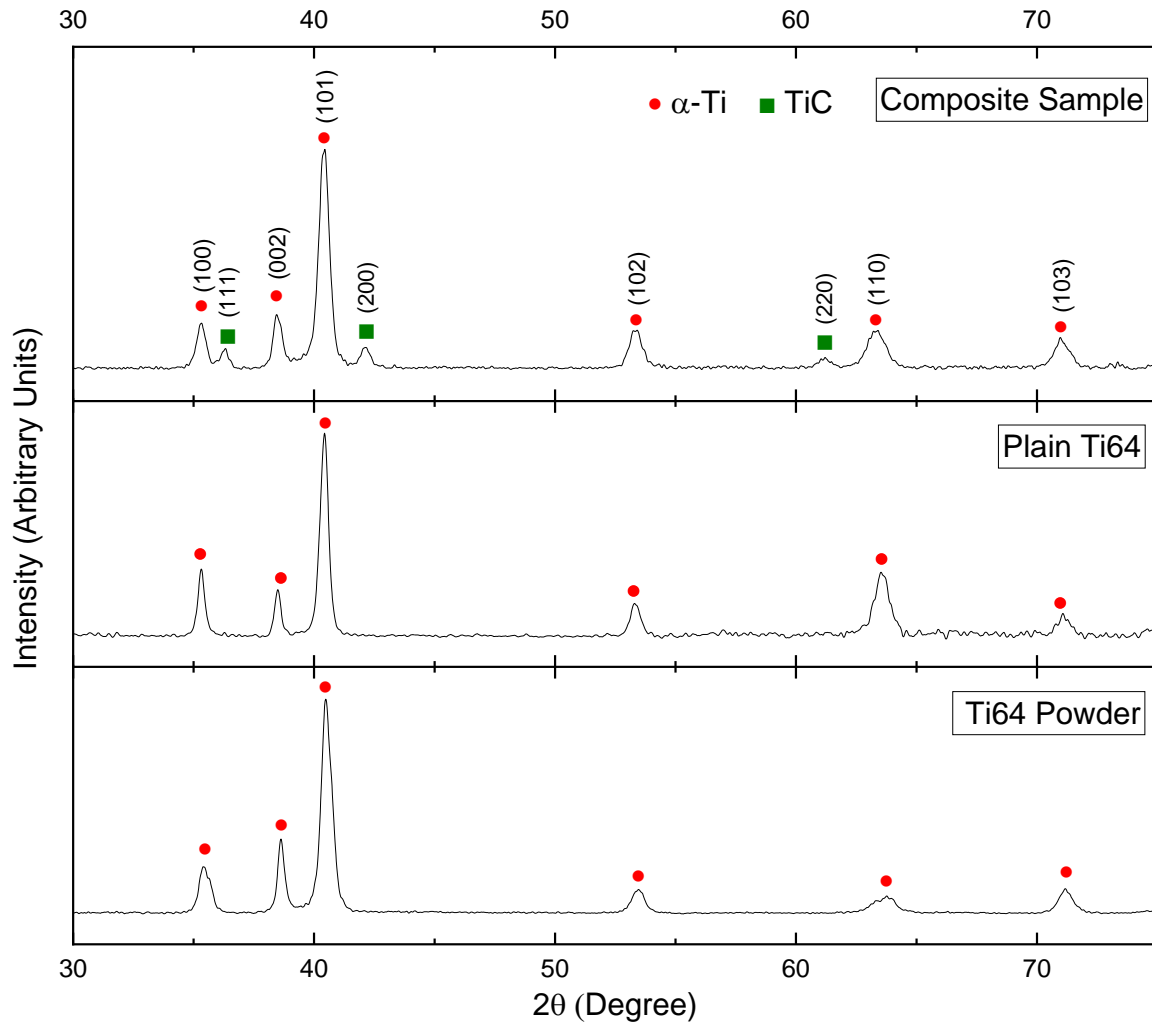
Figure 6.10. XRD profiles of TiC reinforced Ti6Al4V (Composite Sample), unreinforced Ti6Al4V (Plain Ti64) and Ti6Al4V powder used as feedstock (Ti64 Powder).

Optical images of cross-sections through Ti6Al4V-TiC samples 10, 11 and 14 in Table 6.1 are given in Figure 6.11. These samples are produced with different volumetric energy densities (159 J/mm³, 76 J/mm³ and 103 J/mm³, for samples 10, 11 and 14, respectively). Microstructural features with different light scattering (lighter contrast) indicating potential segregation are seen in Figure 6.11((a) (white arrows)). Similar features are not detected with higher energy densities (Figure 6.11(b,c). Melt pools of different processing parameters can be identified in higher magnification images

(Figure 6.11(d,e,f) (dashed lines indicating the boundary of individual melt pools). Overheating (keyhole) pores are spread through the microstructure for the high energy density 159 J/mm³ sample 10 (Figure 6.11(c,f)), whereas similar pores cannot be detected within low and medium energy density parts (Figure 6.11(a,b)).
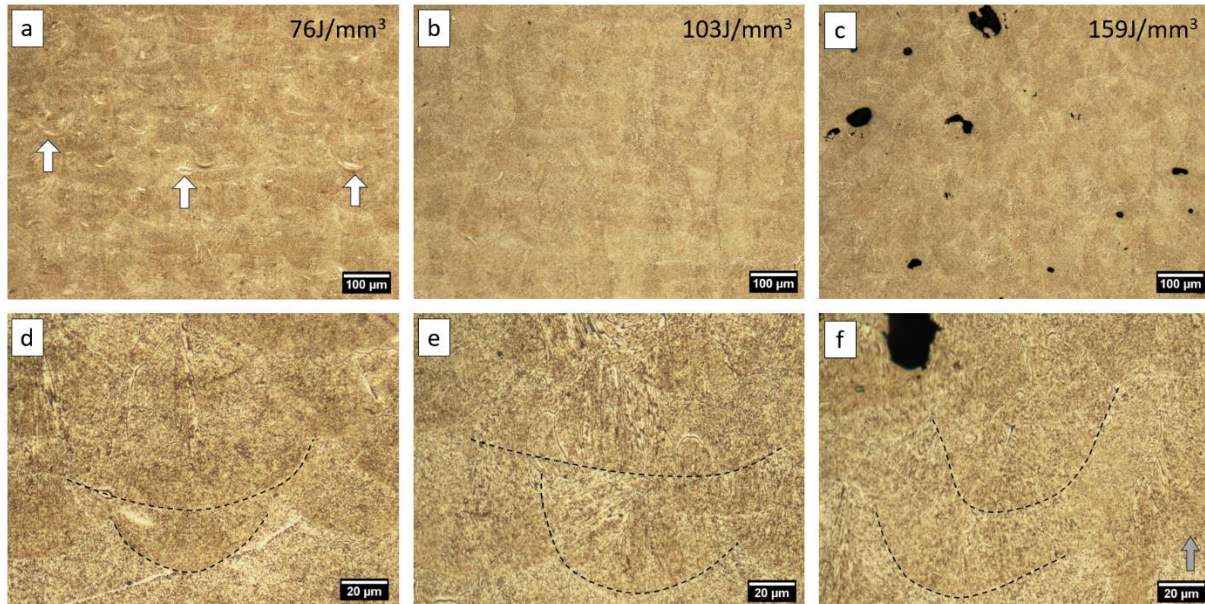
Figure 6.11. Optical images of of cross-sections through Ti6Al4V-TiC (a,d) sample 11 (76 J/mm³), (b,e) sample 14 (103 J/mm³) and (c,f) sample 10 (159 J/mm³) after etching. Top right numbers show SLM volumetric energy densities. Grey arrow (f) shows the SLM build direction for all images.

Secondary electron (SE) SEM images of cross-sections through a low (sample 11, 76 J/mm³), medium (sample 5, 103 J/mm³) and high (sample 1, 183 J/mm³) energy density samples after etching are given in Figure 6.12(a,b,c). TiC particles (high SE emission, bright contrast) have grown *in situ* in the Ti6Al4V matrix for all different SLM energy density levels; however, there are some differences in their distribution. The low energy density sample (sample 11, 76 J/mm³) has some undissolved residual carbon patches within the microstructure (Figure 6.12(a), white arrows) as well as TiC particle deficient zones (Figure 6.12(a), e.g. dashed rectangle). This is the sample processed using the highest laser scan speed on which the features with high light scattering seen with optical microscopy (Figure 6.11(a), white arrows) are likely the undissolved residual carbon or segregations.

Processing with medium and high SLM energy density resulted in a more homogeneous distribution of TiC particles than for low energy density (Figure

6.12(b,c)). As well as randomly distributed TiC orientations, there are also sheets of aligned TiC nanoparticles, which appear as distinct linear lines in the cross-sectional imaging plane. Additionally, undissolved C particles are no longer seen with increasing energy density. Traces of individual laser passes can be seen on medium energy density sample (Figure 6.12(c)). White dashed lines show the borders of different laser scans, which are visible due to a tilt of columnar β grains can be seen from layer to layer. Arrows in Figure 6.12(c) shows the direction of different columns from the different laser passes.
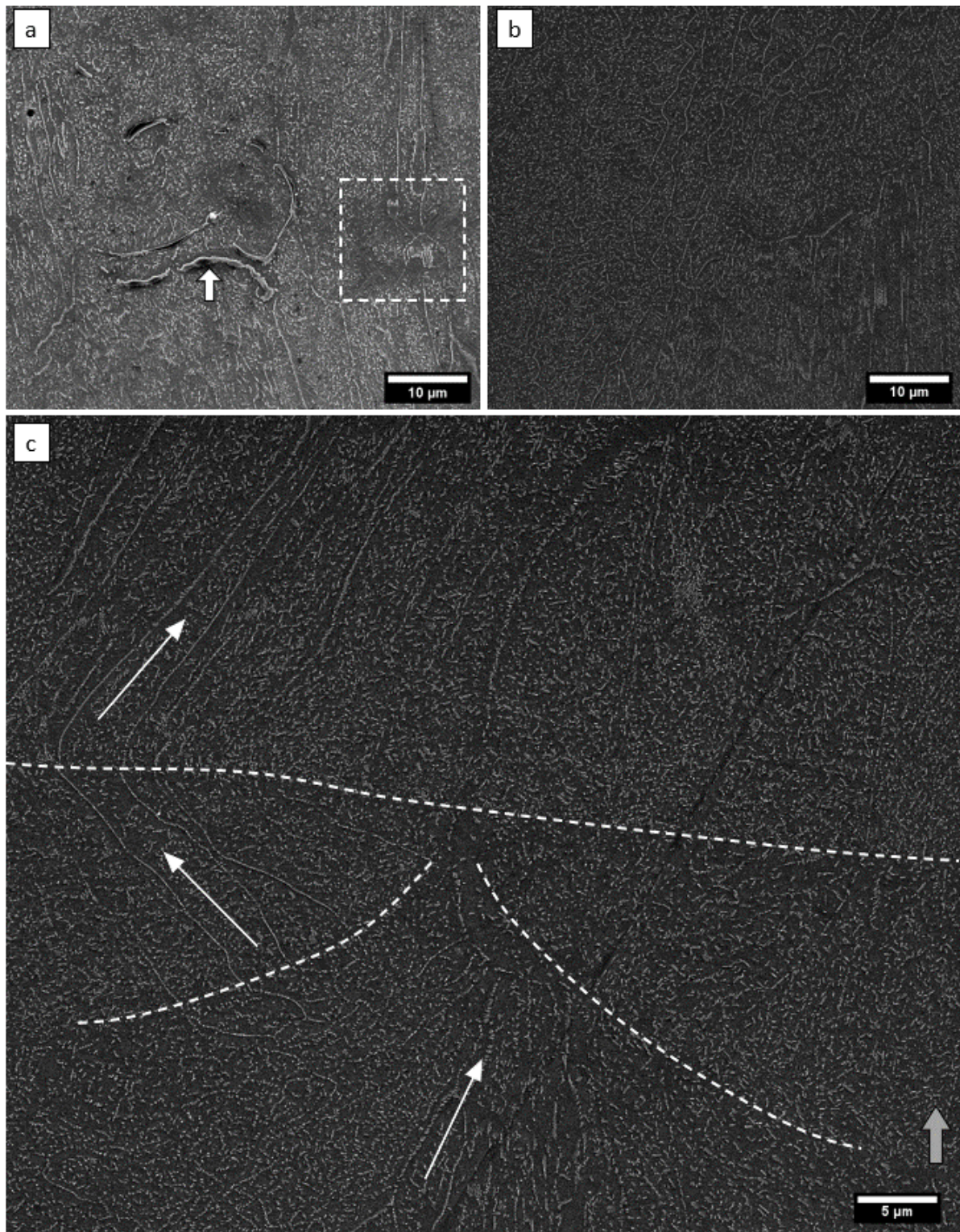
Figure 6.12. Secondary electron SEM images of cross-sections of Ti6Al4V-TiC after etching, with TiC particles (bright contrast) distributed throughout the Ti6Al4V matrix (dark contrast) (a) sample 11 (76 J/mm³) (white dashed square showing a TiC deficient zone), (b) sample 1 (183 J/mm³) and (c) sample 5 (103 J/mm³) after etching. Grey arrow (c) shows the SLMbuild direction for all images.

SE SEM images of Ti6Al4V-TiC samples processed with four different energy densities are given in Figure 6.13. Aligned sheets of TiC particles which intersect the cross-

section plane as lines can be frequently seen in Figure 6.12 and Figure 6.13. In Figure 6.13 the distance between these vertically aligned TiC sheets is approximately 2.5 µm, and they are mostly observed on the right-hand side of the image. Each TiC sheet does not consist of a continuous TiC block, but rather an array of individual TiC nanoplatelets, all aligned parallel to one another. There also is frequently a low-density TiC zone in the immediate vicinity of the TiC sheets.
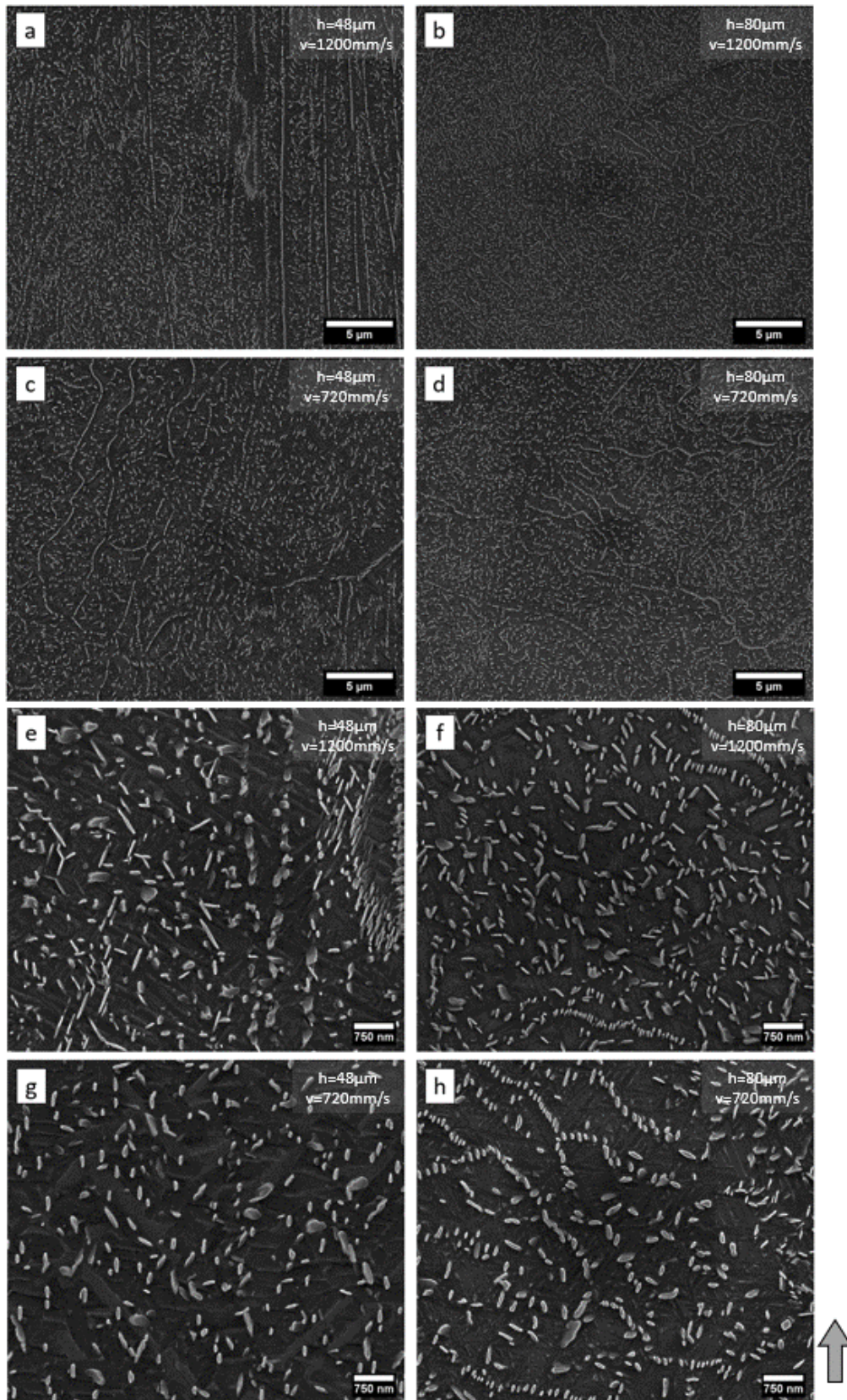
Figure 6.13. Secondary electron SEM images of cross-sections of Ti6Al4V-TiC after etching, with TiC particles (bright contrast) distributed throughout the Ti6Al4V matrix (dark contrast) (a,e) sample 3 (110 J/mm³), (b,f) sample 4 (66 J/mm³), (c,g) sample 1 (183 J/mm³) and (d,h) sample 2 (110 J/mm³) after etching. Lower right arrow shows build direction for all images.

A more homogeneous distribution of TiC particles can be seen for the same laser speed but a larger hatch spacing (Figure 6.13(b)). Despite having lower energy input, particles showed a good distribution. Aligned TiC particle sheets can still be seen and consist of smaller ~100nm particles (Figure 6.13(f)). Samples manufactured with the low laser scan speed also have a regular distribution of TiC particles at both hatch spacing levels without any undissolved carbon regions (Figure 6.13(c,d,g,h)). Again, aligned TiC particle sheets can be seen distributed at the μm level (Figure 6.13(c,d,h)).

TiC particles formed at sub-micron scale for all energy densities, and nearly all of them are below 500nm length (Figure 6.13(e,f,g,h), Figure 6.14). The majority of particles have platelet shapes with a high aspect ratio between platelet width to thickness. Particles seemed slightly thicker/blockier in shape with a smaller aspect ratio when a lower energy density was used (Figure 6.13(f)). Figure 6.14(a,b) shows high magnification SE SEM images of sample 5 (103 J/mm^3) and sample 1 (183 J/mm^3).

SE SEM images of sample 4, which has the highest hatch spacing (80 μm), are given in Figure 6.14(c,d). Similar to the sample processed with the highest laser scan speed (sample 11, 1300 mm/s), some inhomogeneities are noticed. White arrows on Figure 6.14(c) highlight large TiC clusters that are significantly bigger (~1.5 μm length) than the matrix TiC particles (<0.5 μm length). These clusters are consistent with TiC growth around sites of large residual carbon clumps, which have not fully dispersed into the matrix. In Figure 6.14(d) a similar large cuboidal/spherical morphology TiC particle agglomerate is illustrated, and such clusters were only detected in sample 4.

Low magnification SEM images were used to estimate the volume fraction of TiC particles within the samples. These images were converted to black and white images using the Huang thresholding option of the FijiJ software. The ratio of black pixels to white pixels is calculated as TiC areal density, as an approximation for volume density (Figure 6.15(b,c,d,e)). This method neglects any influence of surface roughness due to etching (which may increase the apparent TiC volume), and neglects any TiC particles below the resolution of the ×10 000 magnification SE images (which will decrease the detected TiC volume) Figure 6.15(a) shows TiC particles detected for SLM samples with

different hatch distance and laser scan speed. Increasing energy density tends to decrease TiC areal coverage on the images. According to image analysis, the highest TiC areal fraction of 13.1 vol.% is measured on sample 14 (66 J/mm^3) whereas sample 1 (183 J/mm^3 VED) has the lowest TiC areal fraction of 10.1 vol.%.
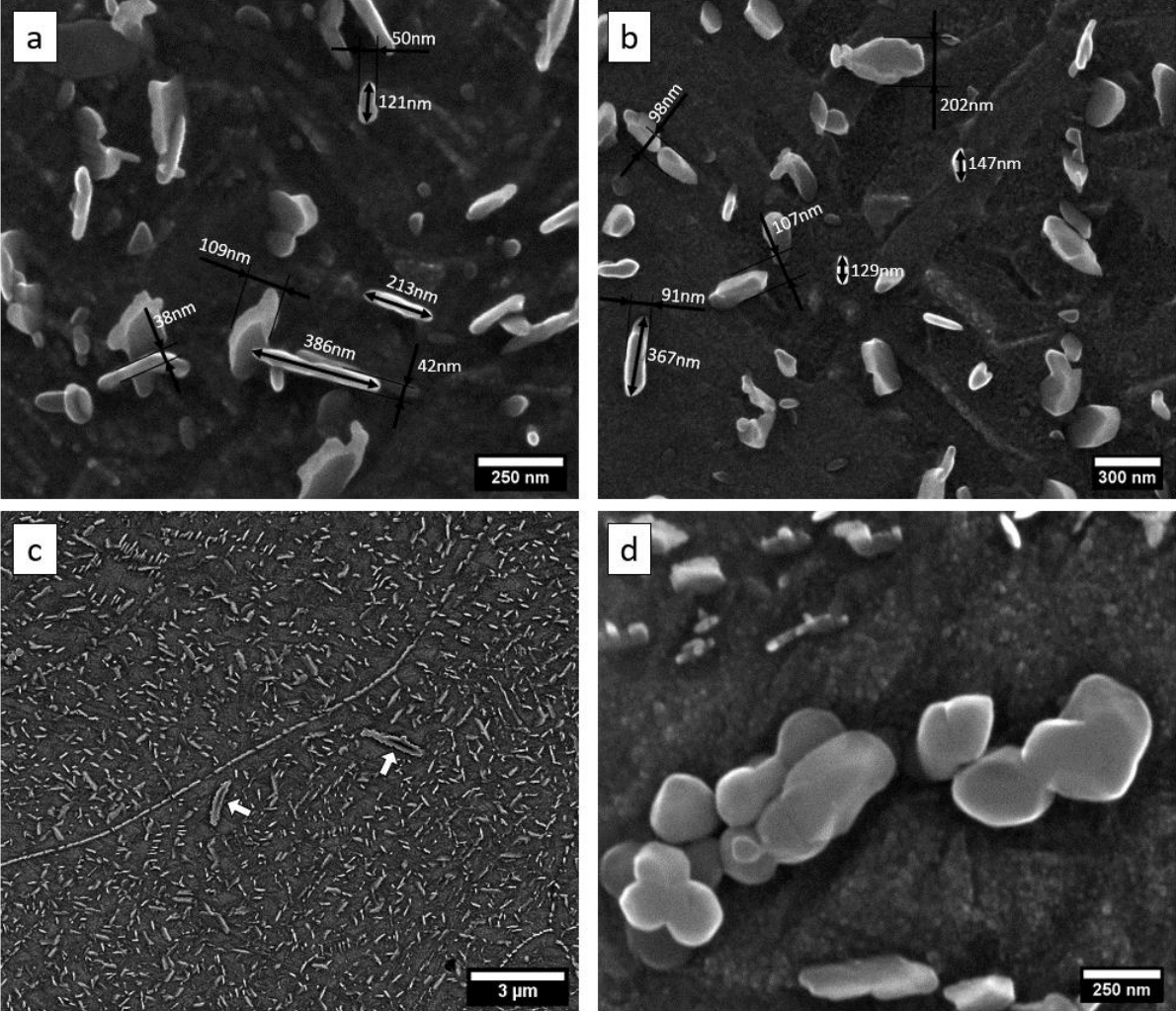
Figure 6.14. Secondary electron SEM images of cross-sections of Ti6Al4V-TiC after etching, with TiC particles (bright contrast) distributed throughout the Ti6Al4V matrix (dark contrast) (a)sample 5 (103 J/mm^3), (b) sample 1 (183 J/mm^3) and (c,d) sample 4 (66 J/mm^3) after etching with large TiC clusters located around residual carbon (white arrows).
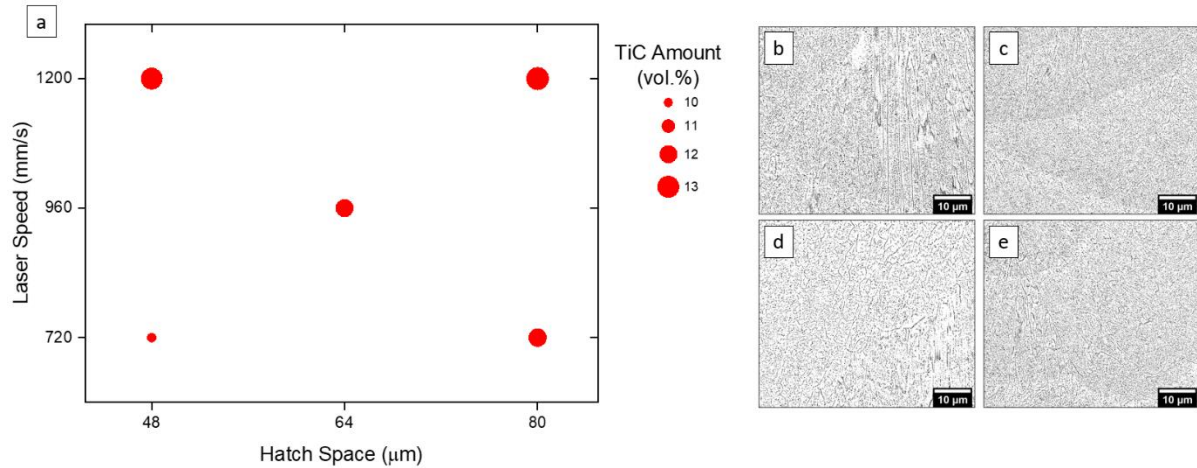
Figure 6.15. (a) TiC particle amount (vol.%) for different SLM processing laser scan speed and hatch distance, (b-e) thresholded SE images used for calculation of (b) sample 3, (c) 4, (d) 1 and (e) 2.

6.4.3.a. Solidification of the Ti6Al4V-TiC microstructure

Solidification of the *in situ* composite Ti6Al4V-TiC microstructure involves a number of microstructural steps (Figure 6.16). The composite powder consisting of up to 53 μm diameter Ti6Al4V parent particles coated in finely dispersed amorphous carbon particles is initially laid down on the substrate (Figure 6.16(a)). When the laser hits the powder particles, it melts the composite powder. The energy density window used to process the mixed powder was selected as higher than the one chosen for plain Ti6Al4V powders (46-103 J/mm³ for plain Ti6Al4V and 66-183 J/mm³ for Ti6Al4V-TiC composite). Therefore, the melt pool temperature could reach over 3500°C due to the chosen high energy density [68]. This is well above the liquidus temperature of 1.1 wt.% C added titanium according to the phase diagram given in Figure 6.17. C particles should dissolve in the liquid titanium alloy considering their advantageous fine nanoparticle size, amorphous nature and micron-level distribution (Figure 6.4). Therefore, ideally a totally liquid Ti alloy matrix and dissolved carbon particles should be achieved, as shown in Figure 6.16(b).

The Ti-C phase diagram shows that 1.1%wt. C containing Ti is a hypereutectic mixture (Figure 6.17, dashed red line). When the liquidus temperature is reached during cooling, dissolved carbon starts to precipitate as primary TiC particles [19], [21], [129]. These particles continue to grow until the eutectic temperature is reached. The SLM process has a different solidification behaviour than conventional manufacturing

routes. The cooling rate could reach up to 10^6-10^8 K/s range during solidification [68], [96]. Therefore, particles have limited time to grow [129], consistent with the nanometre sized TiC observed here. Additionally, the dissolution of the original fine C particles will aid the rapid of a chemically homogeneous liquid solution, promoting many TiC nucleation sites.

Additionally, Marangoni convection plays a significant role in the SLM melt pool. Marangoni convection arises due to high temperature gradient and surface tension within the melt pool during SLM [36], [102], [159]. The convection accelerates homogeneous distribution of fine TiC nanoparticles within the melt pool [20], [190]. The combined effect of rapid solidification and Marangoni convection creates fine TiC particles distributed well within the melt pool before the eutectic solidification (Figure 6.16(c)). When the temperature drops below the eutectic temperature, parent β grains and eutectic TiC at grain boundaries are formed (Figure 6.16(d)). Some TiC within the parent β grains might also be formed through the eutectic transformation. However, the volume fraction of TiC of the eutectic composition is calculated to be relatively low in equilibrium conditions (~0.5%wt. according to Figure 6.17).

Figure 6.16(d) illustrates parent β grains and TiC particles after the eutectic transformation. Further reduction of temperature below the peritectoid temperature results in the formation of the α' phase (Figure 6.16(e)). As a result, the nanoscale TiC reinforced α' matrix is achieved.

Columnar β grains are typical microstructure for SLMed Ti6Al4V [39]. Heat is transferred mainly through conduction in already processed underlying layers due to their higher heat transfer than the surrounding loose powder and atmosphere [68], [90]. Therefore, a columnar solidification throughout the build direction takes place. Traces of these columnar parent β grains are particularly visible in Figure 6.12(c). A semi-circular melt pool boundary is created when using normal and low energy densities [26], [191]. Figure 6.9(c) (dashed lines) shows the borders of different semi-circular laser passes in the cross-section plane examined. Columnar parent β grains skewed depending on the direction of the laser pass and slightly elongated through the

path of laser movement. The laser scan is rotated by 67° for successive layers. Heat gradient change due to alternating laser direction may cause this skewness for different layers [67].

TiC particles can be seen in linear alignments in Figure 6.12 and Figure 6.13. TiC and other ceramic particles located at grain boundaries are typical for MMCs manufactured via SLM [23], [27], [121], [192], [193]. Particles are driven to grain boundaries during solidification; hence they accumulate at grain boundaries [121]. However, here TiC particles are distributed both throughout the β / α' matrices, and also at grain boundaries where TiC particles consist of many small aligned nanoparticles (Figure 6.13(e,f,h). This should be favourable for better mechanical properties because large ceramic particles reduce the crack resistance of composites by providing a path to crack growth [194], and the nanoparticles will be effective in hindering dislocation propagation both within the matrix and at grain boundaries.

Higher laser scan speed results in shorter laser-powder interaction time; hence, the time for carbon dissolution in Ti6Al4V melt is more limited. Additionally, Marangoni convection weakens with decreasing energy input [10], [122]. Therefore, the inhomogeneous TiC particle distribution and large residual carbon clumps seen both on optical images (Figure 6.11(a,d)) and SEM image (Figure 6.12(a)) of the highest laser scan speed sample (1300 mm/s) probably arises due to poor particle carbon-coating mixing, limited carbon dissolution and limited Marangoni flow. TiC formation alongside meltpool boundary can be seen in Figure 6.14(c). This type of formation is observed on the sample processed with the lowest energy density (66 J/mm³). Meltpool boundaries might behave as heterogeneous nucleation sites during solidification. Heterogeneity within the meltpool and lower Marangoni flow might also trigger this sort of solidification around meltpool boundaries when the energy density remains low.
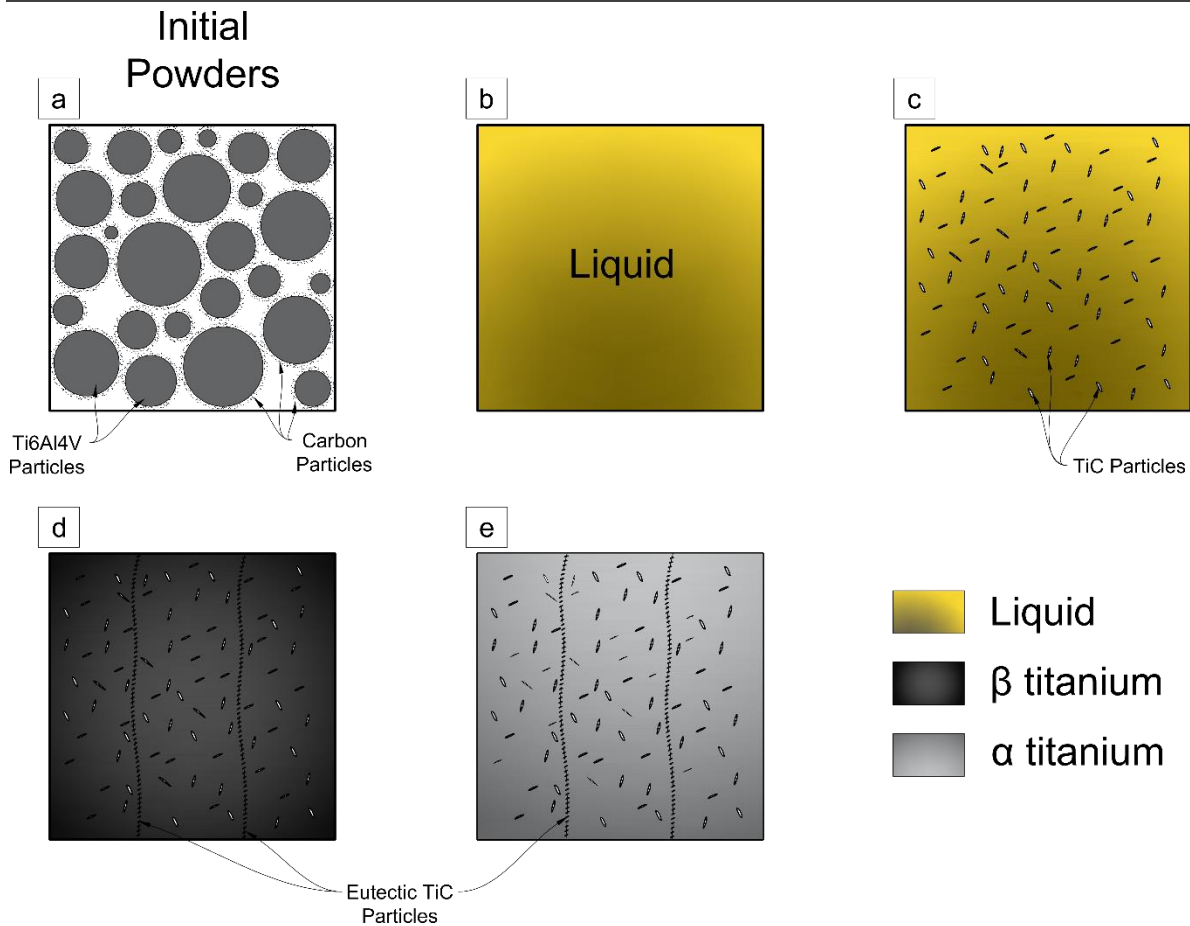
Figure 6.16. The formation process of in situ TiC particles. (a) Parent composite carbon-coated Ti6Al4V particles (b) SLM molten liquid (c) Nucleation of TiC crystals (d) Growth of columnar β-Ti, and (d) β→ α' martensitic phase transformation

Regions of relatively large chunky TiC particles are observed in the highest hatch spacing sample (Figure 6.14(c)), including around the borders of residual carbon agglomerates. Similar to the highest laser scan speed sample, high hatch spacing results in less energy input, resulting in lower melt pool temperature [88]. Carbon dissolves in titanium at high temperatures [153]; however, TiC directly forms by reaction at the carbon surfaces if the melt pool temperature is below 2439°C [23], [153]. The SLM melt pool does not have a homogeneous temperature distribution [155], [156]. The melt pool centre has the highest temperature, and the temperature drops depending on the distance from the centre [156]. When high hatch space is chosen, the overlap between adjacent laser scans' melt pools is reduced. Therefore, more of the molten material reaches a lower peak temperature. The largest hatch space may result in melt pool temperatures below 2439°C. In this case, carbon reacts directly with Ti by combustion rather than dissolving [23], [153]. The large TiC particles are

likely the result of direct TiC formation, as they were observed at the boundaries of residual carbon agglomerates (Figure 6.14(c)).
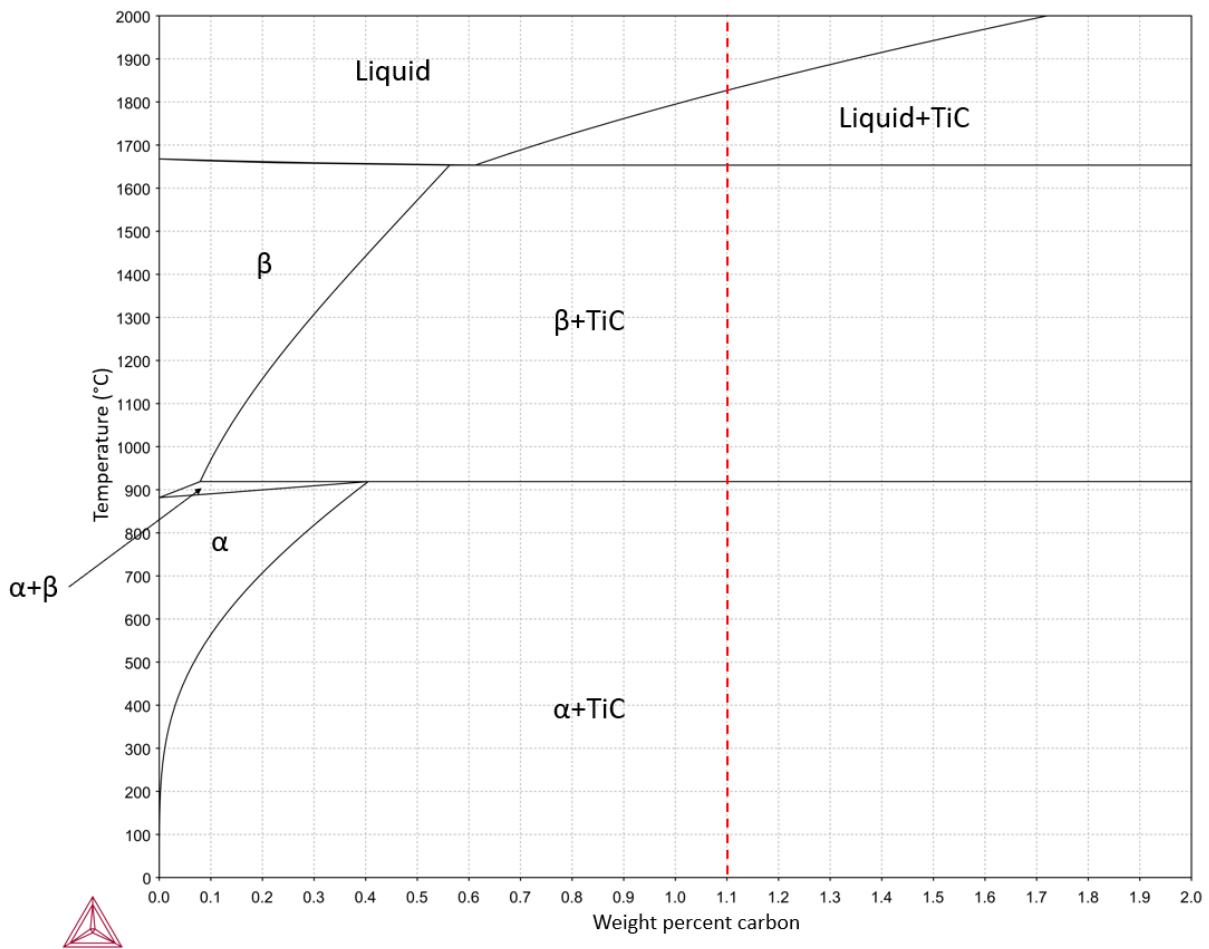
Figure 6.17. Lower carbon content region of the binary Ti-C phase diagram. The diagram was produced using Thermo-Calc software, SSOL4 database.

Lower SLM laser scan speed results in a lower cooling rate [181]. This gives a longer time for TiC particles to grow, and the formation of larger TiC particles and/or more TiC particles is possible. The opposite trend has been observed in this study with parts processed with lower laser scan speed having a lower amount of TiC particles (Figure 6.15). Sequential laser scans on the same layer and adjacent layers create thermal cycles during powder processing [68], [96], which can affect microstructure [96]. When a lower SLM scan speed and small hatch distance are used, thermal cycling can be more significant due to higher melt pool temperature and a consequent larger heat affected zone (HAZ).

The carbon solubility of titanium increases when the temperature reaches near the peritectoid region (Figure 6.17). When a low laser scan speed is chosen, the HAZ of the melt pool enlarges and hits a higher temperature. This high temperature may cause the improved dissolution of carbon into the titanium matrix. Carbon's diffusion in titanium drops significantly with reducing temperature [195], [196]. Rapid cooling may result in a dramatic reduction of carbon diffusion, and dissolved carbon may not be able to form TiC particles due to its limited mobility. As a result, a supersaturated matrix and lower volume of TiC within the Ti6Al4V matrix compared to high laser scan speeds could be achieved (Figure 6.15(a)).

6.4.3.b. Electron backscatter diffraction (EBSD) analysis of Ti6Al4V-TiC composites

The crystallography and grain texture of the Ti6Al4V-TiC composites was characterised using electron backscatter diffraction (EBSD). EBSD images of sample 12 (64 µm, 960 mm/s), are given in Figure 6.18. Similar to the unreinforced Ti6Al4V sample (Figure 5.9(a)), a hierarchical martensitic structure consisting of different α' platelet sizes can be identified. The hierarchical martensite arises due to the cyclic heating regime of the SLM process [68], [95], [96]. For the Ti6Al4V-TiC, the borders of the martensite plates are not as straight as in the unreinforced sample (Figure 5.9(a)), due to the presence of the TiC particles inhibiting growth. Additionally, a significant amount of α' is observed following the parent β grain boundaries in the TiC reinforced Ti6Al4V. This sort of dominant grain boundary α' is not detected within the plain Ti6Al4V sample (Figure 5.9(a)). The grain boundary α' follows the location of the TiC sheets which have adjacent zones deficient in TiC.

EBSD scan was performed using 100nm step size. Most of the TiC particles, on the other hand, has <100nm thickness and <400nm length (Figure 6.14(a,b)). Considering TiC particle thickness of <100nm and 100nm step size, it was not possible to detect TiC particles accurately. Therefore, detected TiC amount was <0.5vol.% for EBSD scans on both planes.

The martensite plate size distribution imaged by EBSD is further analysed using a misorientation limit of 7° set to distinguish different martensite laths. Figure 6.19(a)

shows the maximum Feret diameter distribution for different martensite types, and can be compared to the distribution of different martensites in plain Ti6Al4V (Figure 5.10). In the composite tertiary and quartic martensites are the most dominant martensite types in terms of their number density on the cross-sectional surface, and the 1-2 µm martensite length range of tertiary martensite is most prevalent.

Figure 6.19(b) shows the ratio of covered area and the number of individual martensite plates for different martensite types in Figure 6.18(a). The number of individual martensites is highest for tertiary martensite, followed by quartic martensite. Primary and secondary martensites can be described as rare in terms of their number; however, they still cover a similar total area to quartic martensite. It should be noted that the differences between primary, secondary, and quartic martensite area coverage are small in the analysed region of the Ti6Al4V-TiC composites. Average martensite length (maximum Feret diameter) is measured as 1.45 µm for TiC reinforced sample when EBSD acquisition was performed parallel to the build direction. This compares to 2.16 µm for plain Ti6Al4V samples for the same direction, indicating a grain refinement of α' martensite in the presence of TiC particles.

The inverse pole figure (IPF) image of the reconstructed parent β grains determined from the EBSD α' phase mapping in Figure 6.18(a) is given in Figure 6.18(b). Small β grains elongated along the build direction can be seen from IPF (Figure 6.18(b)), which is a typical microstructure for SLMed Ti6Al4V alloy [39], [67], [88], [177], [178]. Crystallographic texture is developed in the $\langle 100 \rangle_\beta$ direction close to the build direction (Z-axis) on the pole figures of reconstructed β phase (Figure 6.18(d)); however, there is a slight misorientation from the build direction (Z-axis) as for the plain alloy. The grain boundary length of reconstructed β phase per area is measured as 0.144 µm/µm² when the misorientation limit between the grains is set to 7°.
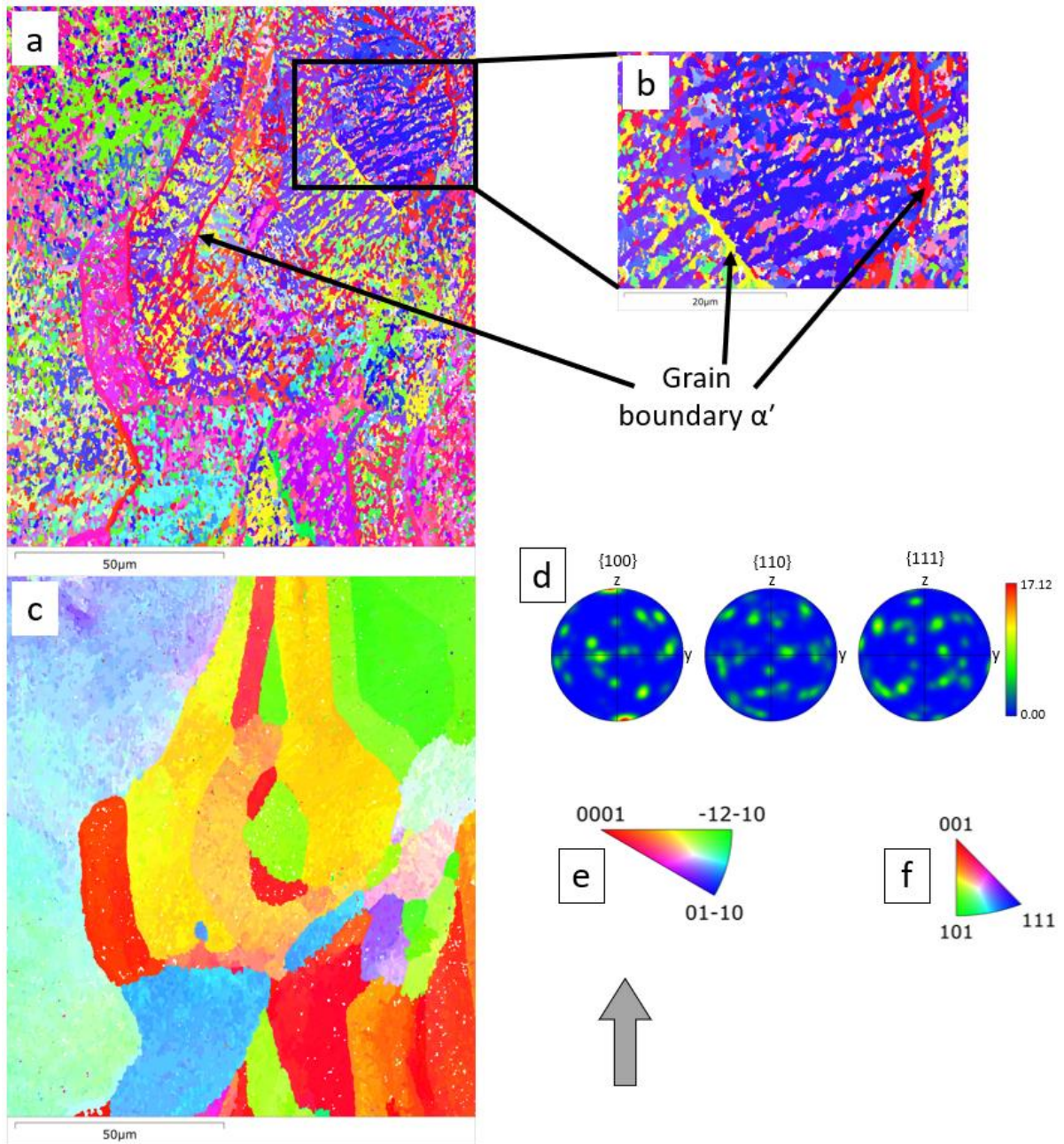
Figure 6.18. Ti6Al4V-TiC sample 12's YZ cross-section plane: (a) EBSD IPF image of α' phase; (b) magnified view of α' phase within the rectangle region in (a); (c) reconstructed parent β phase's IPF map; (d) contour pole figures of {100}, {110} and {111} planes of reconstructed β phase; IPF colour key for (e) α' and (f) β phases. The bottom right arrow indicates the SLM build direction. IPF colours in (a) and (c) represented in the normal direction to image (X-axis).
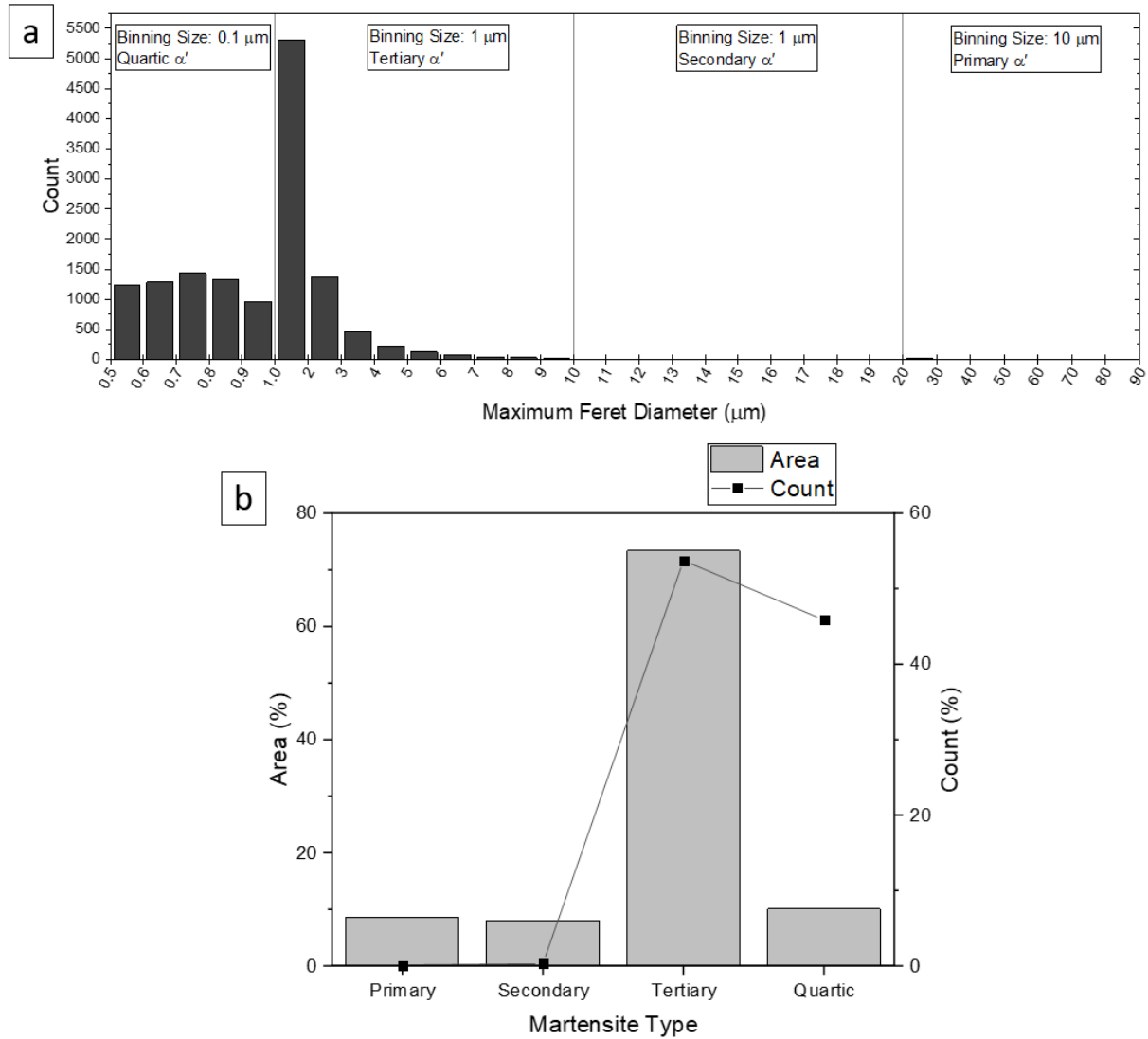
Figure 6.19. α' martensite plate size analysis of Ti6Al4V-TiC Sample 12 EBSD scan in Figure 6.18: (a) Number of identified α' martensite plates evaluated by their maximum Feret diameter distribution and, (b) total area coverage and total count of different martensite types in the EBSD scan. Note different binning sizes for different martensite sizes in (a).

An IPF map of $α'$ phase acquired perpendicular to the SLM build direction (XY plane in Figure 6.1(b)) is given in Figure 6.20(a). This scan was also performed on a sample processed with the exact SLM parameters (64 μm, 960 mm/s) with the plain Ti6Al4V samples used for EBSD scans in Chapter 5 (Figure 5.9, Figure 5.11) and the Ti6Al4V-TiC composite sample used for EBSD scan parallel to the build direction (Figure 6.18).

As in the YZ plane a similar microstructure consisting of hierarchical martensite is observed here. Figure 6.21(a) shows the $α'$ martensite size distribution for primary - quartic martensite types. The martensite size distribution shows a similar trend to the plain Ti6Al4V's martensite size distribution on both XY and YZ planes (Figure 5.10 and

Figure 5.12) and on the YZ plane of TiC reinforced Ti6Al4V (Figure 6.19). Tertiary martensite has the most abundant number of individual martensite plates, followed by quartic martensite (Figure 6.20(b)). The number of primary and secondary martensite laths is extremely low compared with these two. This trend is the same with plain and TiC reinforced Ti6Al4V parts (Figure 5.10, Figure 5.12 and Figure 6.19). However, the area fraction of primary and secondary martensite covers is lower for TiC reinforced samples than plain samples on both planes (Figure 6.19(b) and Figure 6.21(b)). Average martensite length is measured as 1.55 µm for TiC reinforced sample on the XY plane, whereas it is calculated as 2.15 µm for plain Ti6Al4V sample for the same plane.
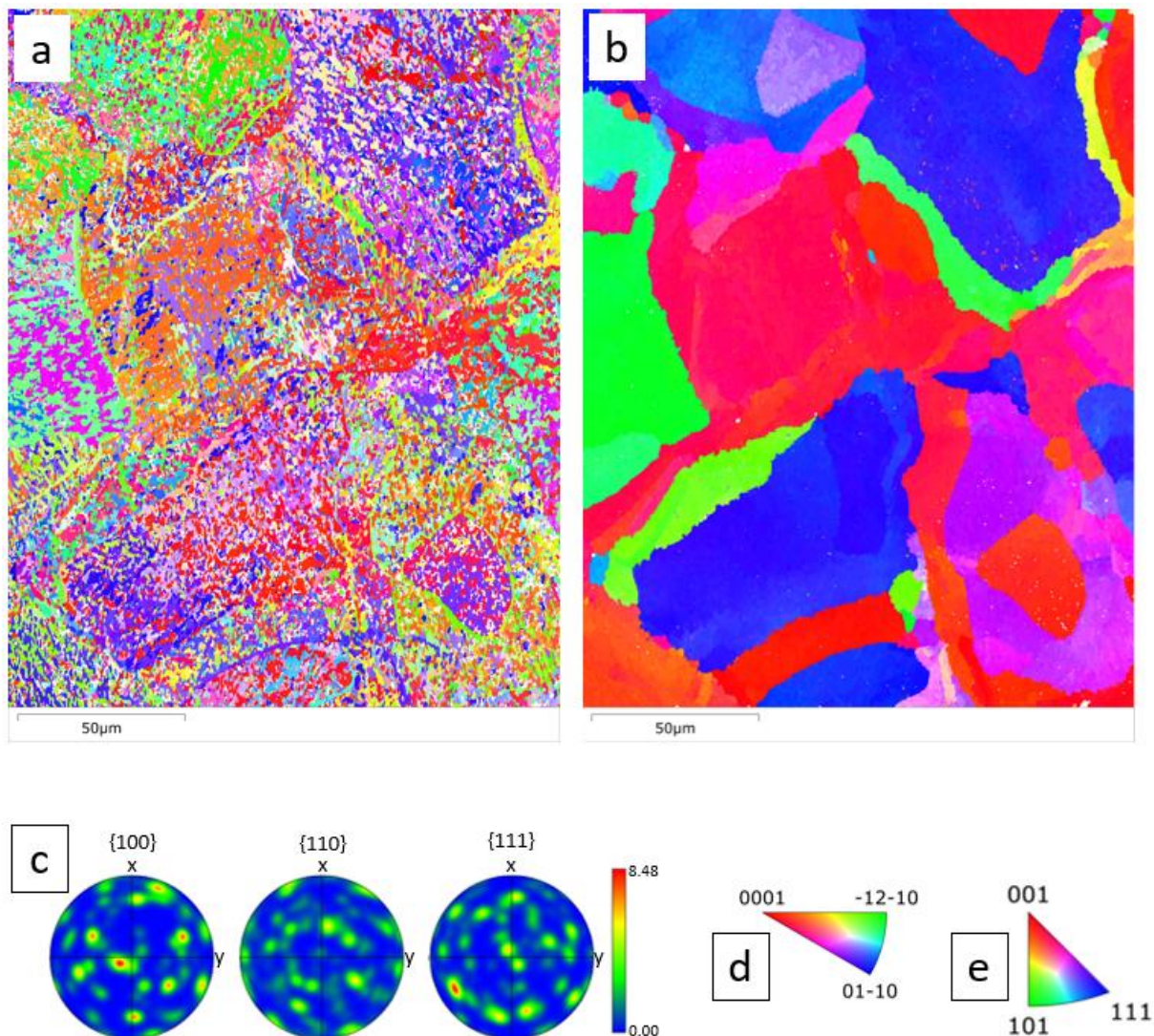
Figure 6.20. Ti6Al4V-TiC sample 5's (a) EBSD IPF image of α' phase, (b) reconstructed parent β phase's IPF map, (c) contour pole figures of {100}, {110} and {111} planes of reconstructed β phase, IPF colour key for (e) α' and (f) β phases. EBSD acquisition performed perpendicular to build direction (XY plane in Figure 6.1(b)). IPF colours in (a) and (b) show orientations with respect to the paper surface normal (Z-axis).

The reconstructed parent β phase grains determined from the EBSD α' phase mapping in Figure 6.20(a) are shown in Figure 6.20(b). Grains are distributed randomly rather than elongated in a direction. A β phase $\langle 100 \rangle_\beta$ direction texture close to the build direction (Z-axis) is observed (Figure 6.20(c)), but with a slight rotation from the $\langle 100 \rangle_\beta$ direction is previously observed. The ratio of total parent β grain boundary to the total scan area when the grain misorientation limit was set to 7° is 0.142 µm/µm².
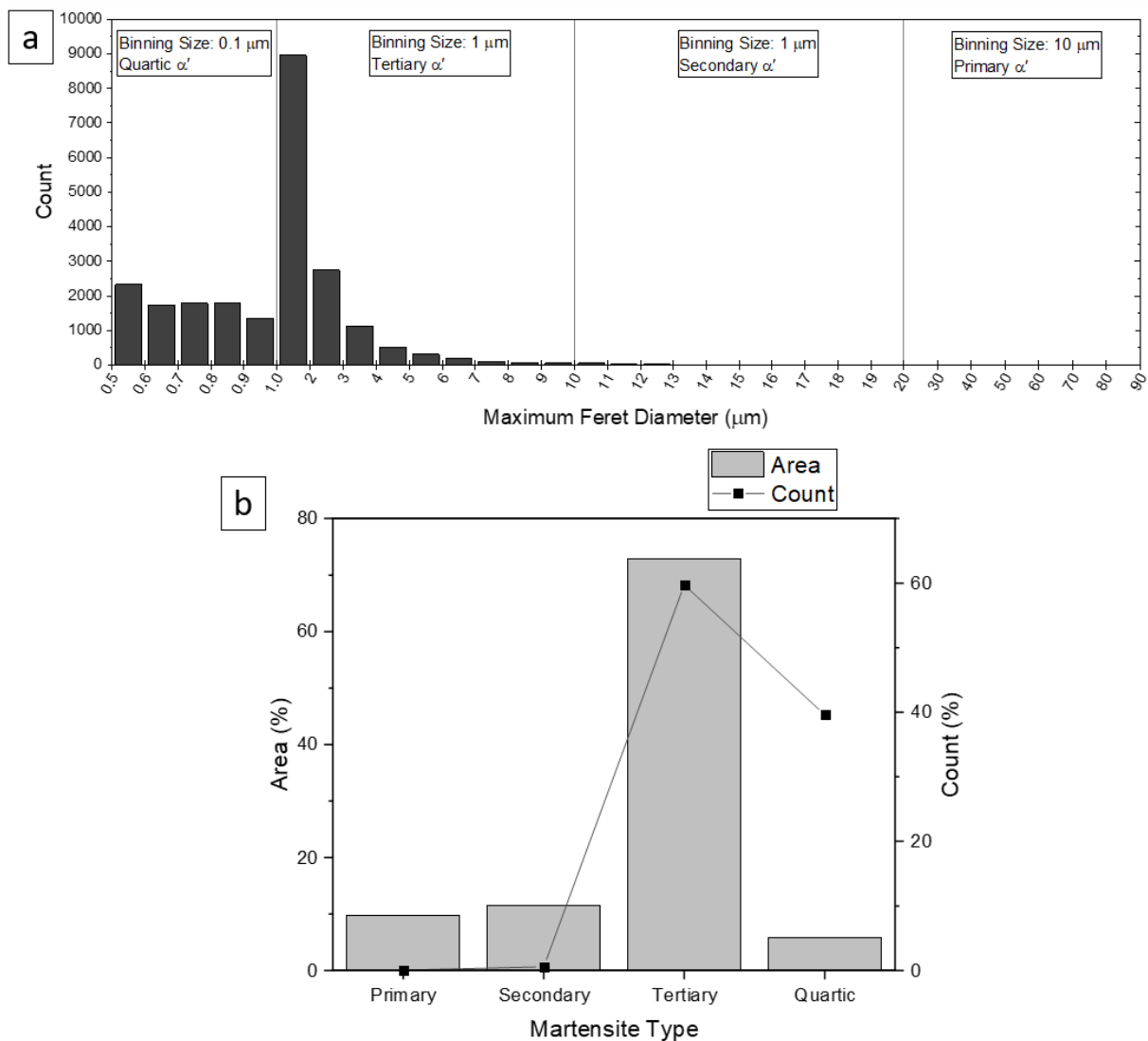
Figure 6.21. α' martensite plate size analysis of Ti6Al4V-TiC sample 5 EBSD scan in Figure 6.20: (a) Number of identified α' martensite plates evaluated by their Maximum Feret diameter distribution and, (b) total area coverage and total count of different martensite types in the EBSD scan. Note different binning sizes for different martensite sizes in (a).

Parent β grain boundary length divided by the total scan area was used to evaluate grain refinement effect of TiC nanoparticles. The aim when dividing the grain boundary length by the area was to be able to compare scans with different scanning area. According to the reconstructed β phase IPF map on the XY plane, total grain boundary length increased more than two times with the presence of TiC nanoparticles (0.059 µm/µm² for plain Ti6Al4V and 0.144 µm/µm² for Ti6Al4V-TiC composite). Analysis on XY plane yielded to a similar increase (0.064 µm/µm² for plain Ti6Al4V and 0.142 µm/µm² for and Ti6Al4V-TiC composite).

Primary TiC solidified before the parent β titanium phase according to the Ti-C phase diagram (Figure 6.16 and Figure 6.17). Nanosized ceramic particles restrict the growth of β grains during solidification, and a more refined grain size is achieved [27], [113]. Additionally, primary TiC particles act as heterogeneous β nucleation sites, which increases the grain refinement effect [197]. The EBSD analysis confirms that α' martensite plate length is reduced ~30% for TiC reinforced sample when compared to the plane Ti6Al4V alloy when the same processing parameters were used (2.16 µm for plain Ti6Al4V and 1.45 µm for Ti6Al4V-TiC composite on YZ plane).

Distinct α' phase grains are identified delineating the original parent β grain boundaries (and therefore the α' domain boundaries) in the examined Ti6Al4V-TiC composites, both on planes parallel and perpendicular to the SLM build direction (Figure 6.18(a) and Figure 6.20(a)). This type of α' domain boundary is not observed with plain Ti6Al4V parts processed with identical parameters (Figure 5.9(a) and Figure 5.11(a)). This type of martensite is noted when Ti6Al4V alloy cooled down slower than typical SLM conditions [89]. All EBSD examined samples were processed using identical parameters; hence, their cooling rate is expected to be the same.

The most significant difference between Ti6Al4V and Ti6Al4V-TiC composite samples is the presence of TiC particles. The presence of nanoparticles in liquid metals reduces thermal conductivity and increases the molten state period [184]. Therefore, the cooling rate is expected to reduce with the presence of nanoparticles. The lower cooling rate of TiC reinforced Ti6Al4V might result in grain boundary martensite.

Of interest is that these α' domain boundaries exhibited a heterogeneous TiC distribution. Sheets of TiC nanoplatelets are identified along the grain boundary. The TiC platelets are oriented at an angle to the boundary plane in parallel arrays, and the nanoparticles are much smaller that the primary TiC. Around the TiC platelets are zones with reduced TiC content. These microstructural features are consistent with these TiC being the last to precipitate at the β grain boundaries.

6.4.4. SLM Ti6Al4V-TiC Composite Hardness

The hardness of Ti6Al4V-TiC reinforced parts varied between 433 HV and 474 HV. *p*-values of hatch distance, laser speed and squared term of laser speed are 0.005, <0.001 and 0.007, respectively with other terms' *p*-values all above 0.05. This shows that both hatch distance and laser scan speed affect the hardness, and laser speed has a more significant effect than hatch distance. Additionally, laser speed has a peak value within the parameter range chosen.

The hardness change differences between TiC reinforced, and unreinforced Ti6Al4V parts is given in Figure 6.22. The lower left region of the graph shows higher energy densities. A reduction of hardness is observed with increasing energy density. The highest hardness is measured on sample 9 (87 μm, 960 mm/s), whereas the lowest hardness is measured on sample 1 (48 μm, 720 mm/s). Two of the used processing parameters were identical for plain, and TiC reinforced Ti6Al4V alloys. When hatch distance and laser scan speed were 80 μm and 1200 mm/s, respectively, hardness is measured as 464 HV for TiC reinforced sample, and 362 HV for plain sample. While for 64 μm hatch distance and 960 mm/s laser scan speed parameter, hardness is measured as 460 HV for TiC reinforced, and 355 HV for plain Ti6Al4V samples, respectively. The harness measurements clearly demonstrate the increased hardness of Ti6Al4V-TiC compared to plain Ti6Al4V with the same parent Ti6Al4V alloy composition.

There are several mechanisms causing the significantly improved strength of the Ti6Al4V-TiC metal matrix composites. A combined effect of grain refinement, presence of hard particles (Orowan strengthening) and increased dislocation density results in

increased strength [27], [115], [120], [121], [151], [152]. Grain boundaries and hard particles within the matrix act as barriers for dislocation movement [27], [113], [190]. Nanosized TiC particles dispersed within the grains can be seen from the SEM images (Figure 6.13 and Figure 6.14). Increased grain boundary length with particle addition is detected through EBSD images (Figure 5.9, Figure 5.11, Figure 6.18 and Figure 6.20). Increased dislocation density is expected due to coefficient of thermal expansion (CTE) and elastic modulus mismatch between TiC and Ti6Al4V matrix.

During the SLM melting of carbon-coated powders, carbon particles dissolved in the Ti6Al4V matrix. Some of this carbon will remain dissolved within the matrix instead of reacting with Ti, and solid solution strengthening acts as an additional strengthening mechanism in this study. The combined effect of all these mechanisms results in an over 100 HV hardness increase when compared to plain Ti6Al4V with the same parent Ti6Al4V alloy composition and using the same SLM processing parameters.

Considering the TiC reinforced Ti6Al4V composites, increasing the SLM energy density lead to a lower hardness although all composites were significantly harder than the plain Ti6Al4V SLM alloy. Increased porosity may result in lower hardness [51], [56], [173], however, this is not likely here due to the low measurement load (500g) of the microhardness measurement which will not encompass significant microporosity. Therefore, a microstructural change is likely to cause hardness variation between different SLM processing parameters.
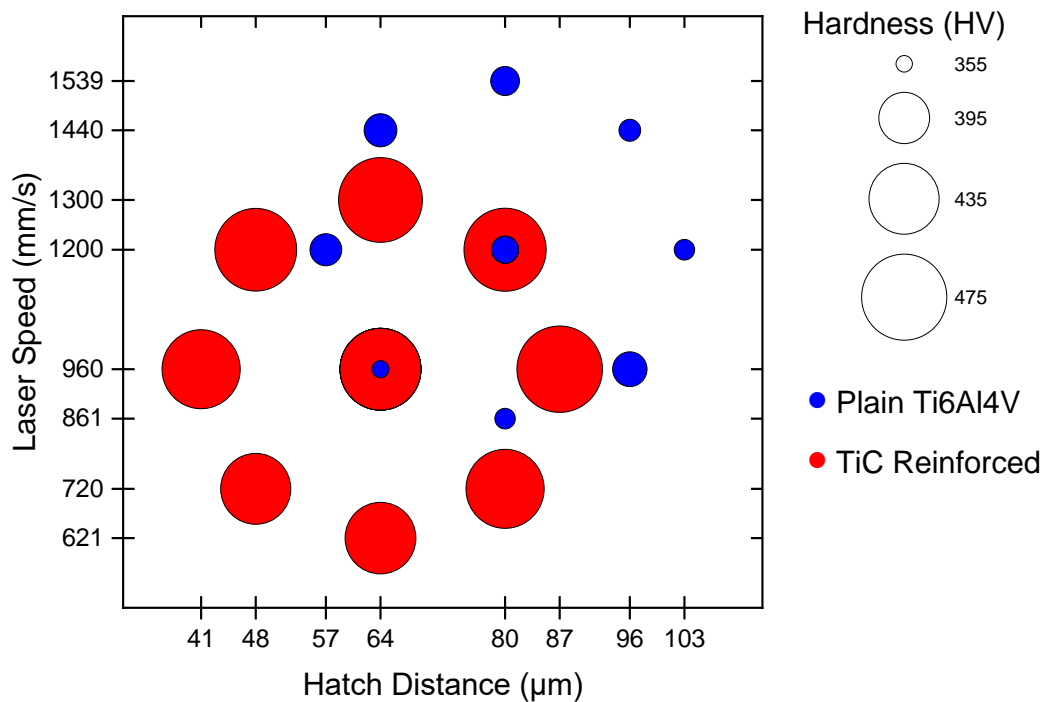
Figure 6.22. Hardness change of plain Ti6Al4V and TiC reinforced composite samples for different processing parameters.

The contribution of different strengthening mechanisms to the hardness is not equal [114], [152], [198]. Wang et al. [114] studied the effects of different strengthening mechanisms on additively manufactured composites' strength. They found that increased dislocation density due to coefficient of thermal expansion (CTE) mismatch has the highest strengthening effect in the as-built state. Additionally, Orowan strengthening, and grain refinement also have significant effects. However, heat treatment reduces the impact of increased dislocation density because heat treatment detracts dislocations arising due to CTE mismatch. Increasing SLM energy density increases the effect of subsequent adjacent laser scans and layer's heat treatment effects due to a larger melt pool and HAZ [199]. Therefore, it is expected that residual dislocation density would be reduced due to increasing SLM energy density, which can be investigated in future work.

A reduction of areal density of TiC particles analysed from SEM images, is detected with increasing SLM energy density (Figure 6.15(a)). The hardness of parts may reduce due to a lower volume of hard particles, depending on how the particles are distributed within the matrix. For a given TiC particle composition, a reduced TiC particle volume would result in higher C concentration within the T6Al4V matrix. Therefore, the

contribution to hardness of solid solution hardening would increase in this case. However, a relatively higher contribution of TiC particles to the strength than dissolved C may result in lower hardness if the TiC volume decreases. Additionally, EBSD measurements revealed that martensite size was reduced ~30%. This also may contribute to the hardness increase of Ti6Al4V-TiC composite parts. As a result, a combination of dislocation density change, TiC particle volume change, martensite plate refinement, and potentially also a TiC particle distribution change, can generate different hardness values for different SLM processing parameters.

6.4.5. Comparison of Low and High Energy Density Ranges

In this study, two different energy density windows were applied using different SLM equipment. In Chapter 4, a low energy density range was employed using a pulsed wave SLM equipment. On the other hand, a higher energy density field was applied in this chapter (Chapter 6) with a continuous wave SLM machine. The main difference between samples manufactured in these two chapters was the type of defects. The lower energy density in Chapter 4 resulted in lack of fusion type defects for all energy densities, and defect size increased with decreasing energy density (Figure 4.6, Figure 4.7 and Figure 4.8). Additionally, increasing energy density resulted in more spherical pores (Figure 4.8(d)); however, sharp-edged lack of fusion type defects was observed at all energy density levels. This type of defects were identified as the most detrimental type due to stress concentrations at sharp crack edges [98], [148]; therefore, these should be avoided whenever possible.

A higher energy density range is used in Chapter 6. The medium energy densities of this chapter provided nearly fully dense parts (Figure 6.6). When energy density increased to the highest range, spherical keyhole pores were formed, but no lack of fusion defects was observed. These results show that a higher energy density range gives better results in terms of relative density.

Another difference between these two chapters was the formation mechanism of TiC. It is claimed by Dadbakhsh et al. that TiC is formed by combustion rather than dissolution precipitation when the temperature stays below 2438 °C [23]. The SLM

meltpool does not have a homogeneous temperature distribution [102], [159]; therefore, most regions of the meltpool could stay below 2438 °C during processing in Chapter 4 due to lower energy density. Additionally, undissolved carbon particles distributed within the matrix are also observed with the optical microscopy examination, indicating a low meltpool temperature (Figure 4.7). SEM images confirm the presence of residual carbon patches covered with TiC as well as fine TiC particles (Figure 4.10). These show that a mixture of direct combustion and dissolution-precipitation mechanisms for TiC formation took place in Chapter 4. Marangoni flow is beneficial for better particle distribution within the matrix [19], [20], [129], [131]. Lower energy input reduced Marangoni flow [10], [122], and particles did not distribute homogeneously within the matrix in Chapter 4.

On the other hand, the higher energy density window used in Chapter 6 resulted in dissolution-precipitation type formation by increasing the meltpool temperature (Figure 6.16). Additionally, Marangoni flow increased due to increased energy input. All of these caused finely dispersed nanosized TiC particles within the matrix (Figure 6.12, Figure 6.13 and Figure 6.14). Considering the microstructure and porosity formation, higher energy density should be favourable for this type of composite.

It is not possible to compare the effects of pulsed and continuous wave systems in this study because different energy inputs were chosen for different equipment. More studies are needed to examine the impact of different laser sources.

6.5. Conclusions

In situ TiC reinforced Ti6Al4V matrix composites were successfully manufactured using a continuous wave laser SLM process. The effect of graphite flake – Ti6Al4V pre-alloyed powder mixing duration is assessed, and homogeneously coated Ti6Al4V particles are prepared as feedstock powder. Ti6Al4V-TiC composites are prepared by SLM using the carbon-coated Ti6Al4V, and part surface roughness, relative porosity, microstructure, and hardness is evaluated using different processing parameters. The relative density of parts improved significantly over the parts processed using the pulsed laser in chapter 4 due to increased energy density. High SLM energy densities

resulted in keyhole pores, whereas medium energy densities led to nearly fully dense parts.

SLM Ti6Al4V-TiC nanocomposites are fabricated by the *in situ* reaction of carbon and Ti. Nanosized TiC particles are spread homogeneously throughout the matrix, with additional sheets of TiC decorating parent β grain boundaries. Grain boundary length increased more than two times comparing with the plain Ti6Al4V parts processed using the same equipment and processing parameters. Microhardness is increased by around 100 HV in the TiC reinforced composites compared to the parent alloy. Hardness is affected by processing parameters, and higher SLM energy input leads to lower hardness. This chapter demonstrates that *in situ* TiC reinforced Ti6Al4V matrix composites can be manufactured by SLM with an advantageous reinforcement distribution and no apparent porosity.

Chapter 7: Friction and Wear Properties of Plain Ti6Al4V Alloy and Ti6Al4V-TiC Composites

7.1. Introduction

The tribological properties of TiC reinforced Ti6Al4V matrix composite, and plain Ti6Al4V alloy is examined in this chapter. TiC reinforced and unreinforced SLM parts, and a conventional Ti6Al4V plate, are used to compare the friction and wear behaviour of different base materials. Bearing steel (AISI 52100), Si_3N_4, and Al_2O_3 balls are used as counterpart materials. Post-mortem analysis of wear tracks are performed utilising optical profilometry and SEM. *In situ* scratch tests are performed to understand and compare the surface mechanical behaviour of TiC reinforced and unreinforced Ti6Al4V SLM samples.

7.2. Experimental

Reciprocating wear tests were performed on TiC reinforced Ti6Al4V composite (referred to as TiC composite), SLMed plain Ti6Al4V (referred to as plain Ti6Al4V) and

a Ti6Al4V grade 23 plate (referred to as Ti6Al4V plate or conventional Ti6Al4V) parts. Plain Ti6Al4V parts and TiC reinforced Ti6Al4V parts were processed using the same processing parameters (Table 7.1). All wear tests were performed under dry sliding conditions, and the following parameters are used: 2.5 mm stroke length, 0.5 N normal load, 1 Hz frequency, 54 m total distance and 3 h total test duration. At least two tests were performed for each test condition on the same material. Three different counterpart balls with a diameter of 4mm are used: bearing steel (AISI 52100), Si_3N_4, and Al_2O_3. The Hertzian contact pressure of different ball materials on Ti6Al4V is calculated as 600 MPa for Al_2O_3, as 557 MPa for Si_3N_4, and 531 MPa for bearing steel when Young's modulus and Poisson's ratios are considered as 110 GPa [94], 0.342 [200] for Ti6Al4V, 380 GPa [201] and 0.23 [201] for Al_2O_3, 255 GPa [202] and 0.23 [202] for Si_3N_4 and 201 GPa [203] and 0.27 [203] for bearing steel, respectively. Volume losses of both ball and base material are measured using optical profilometry, and a spherical shape removal tool is used to flatten the surface of the counterpart ball before the wear rate calculation. Stitched images of the whole wear track are used for volume loss calculations of base materials and balls. Tests of SLM samples were performed parallel to the build direction (YZ plane in Figure 6.1(b)), but one test was performed perpendicular to the build direction using a Si_3N_4 ball (XY plane in Figure 6.1(b)).

In situ scratch tests were performed in an SEM (Alemnis *in situ* SEM indenter) with *in situ* secondary electron imaging to evaluate further the wear mechanism of unreinforced and TiC reinforced Ti6Al4V samples processed using SLM. 25 mN normal force was applied during the SEM scratch tests. Scratch speed was set at 1 µm/s, and the scratch was applied for 100 µm length. All scratch tests were performed on parallel planes to the build direction.

Table 7.1. SLM processing parameters of plain Ti6Al4V and Ti6Al4V-TiC parts used as the base material for wear tests.

Hatch Space (µm)	Laser Speed (mm/s)	Volumetric Energy Density (J/mm³)	Linear Energy Density (J/mm)
64	960	103	0.211

7.3. Wear Test Results

7.3.1. Dry Sliding Wear Test

Wear rates for different base materials (TiC reinforced composite, SLMed Ti6Al4V and Ti6Al4V plate), and counterpart balls (Al_2O_3, Si_3N_4, and bearing steel) are summarised in Figure 7.1. Ti6Al4V-TiC had the highest wear rate for all counterpart materials despite its highest hardness. Alumina balls caused the highest wear rate, whereas steel and Si_3N_4 balls resulted in quite similar values against TiC reinforced composites (Figure 7.1(a)). Wear resistance of the TiC reinforced part is measured as slightly better when testing was performed perpendicular to the build direction (Si_3N_4 - XY plane). Against the Ti6Al4V-TiC, the wear rate of the ball was the highest for the alumina ball (Figure 7.1(b)). On the other hand, steel ball's wear rate was significantly higher against unreinforced Ti6Al4V.
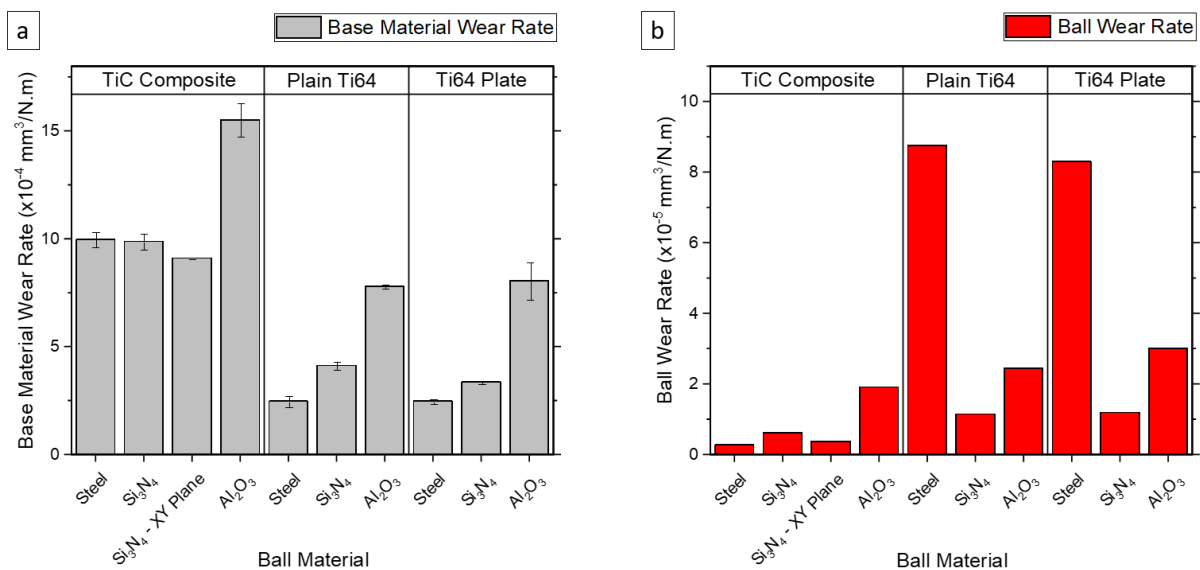
Figure 7.1. Wear of Ti6Al4V-TiC, Ti6Al4V and Ti6Al4V plate against Steel, Si_3N_4 and Al_2O_3 balls. Wear tests used 2.5 mm stroke length, 0.5 N normal load, 1 Hz frequency, 54 m total distance and 3 h total test duration. (a) Base materials' and (b) counterpart balls' wear rates. Error bars (a) shows the standard error of mean.

SLMed plain Ti6Al4V (plain Ti64 in Figure 7.1) and conventional Ti6Al4V (Ti64 plate in Figure 7.1) showed quite similar wear characteristics. The wear rates of both base materials were the lowest when bearing steel was used as counterpart material, and the steel balls showed a very high wear rate (Figure 7.1(b)). Using a Si_3N_4 ball resulted in the second-highest wear rate of Ti6Al4V with conventional Ti6Al4V having slightly lower wear rate than SLMed plain Ti6Al4V. The Si_3N_4 balls themselves had the lowest

wear rate when rubbing against unreinforced SLMed and conventional Ti6Al4V base materials. The Al_2O_3 ball causes the highest base material wear rate for all three materials. The wear rate approximately doubled when using the Al_2O_3 ball compared with the Si_3N_4 ball. Against Ti6Al4V, the wear rate of the alumina ball itself is approximately two times higher than the Si_3N_4 ball but much lower than the steel ball (Figure 7.1(b)).

The wear rates of the base materials and counterpart balls thus vary significantly for different tribological couples. Hence, the tribological behaviour of Ti6Al4V-TiC, Ti6Al4V and Ti6Al4V plate against varying counterpart balls will be examined and characterised in more detail.

7.3.1.a. Sliding wear against steel ball

When Ti6Al4V-TiC composes (TiC composite), SLMed Ti6Al4V (Plain Ti64) and conventional Ti6Al4V plate (Ti64 plate) were rubbed against AISI 52100, base material wear rates were measured as $9.96 \times 10^{-4} mm^3/N.m$, $2.47 \times 10^{-4} mm^3/N.m$, and $2.47 \times 10^{-4} mm^3/N.m$, respectively. Wear rates of the counterpart steel balls measured as $2.68 \times 10^{-6} mm^3/N.m$, $8.76 \times 10^{-5} mm^3/N.m$ and $8.29 \times 10^{-5} mm^3/N.m$, against Ti6Al4V-TiC composes (TiC composite), SLMed Ti6Al4V (Plain Ti64) and conventional Ti6Al4V plate (Ti64 plate) respectively.

The change of coefficient of friction (COF) for Ti6Al4V-TiC composite, SLMed Ti6Al4V and conventional Ti6Al4V plate whilst rubbing against AISI 52100 bearing steel balls is given in Figure 7.2. A distinctively different COF behaviour between unreinforced samples and TiC reinforced composite can be observed. Plain Ti6Al4V alloys, independent being SLMed or not, have a gradual increase in their COF to a plateau followed by a sharp drop. This type of cycle is repeated between COF ~ 0.45 ↔ 0.85 until the end of the tests. In comparison, a more stable COF regime is observed for TiC reinforced sample. Despite the larger amplitude of short-term oscillations, the overall trend is more stable than plain samples with a gradual increase of COF from ~ 0.45 → 0.6. However, increase and drop of COF still can be noticed in smaller amounts.
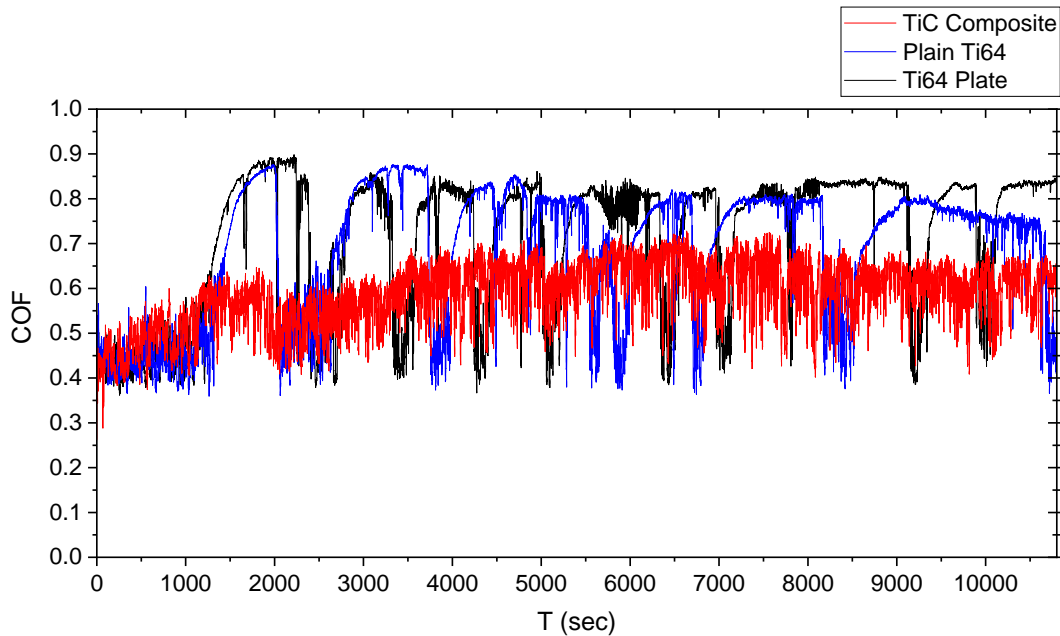
Figure 7.2. Coefficient of friction (COF) of Ti6Al4V-TiC, Ti6Al4V and Ti6Al4V plate rubbing against AISI52100 bearing steel ball. Wear tests used 2.5 mm stroke length, 0.5 N normal load, 1 Hz frequency, 54 m total distance and 3 h total test duration.

Optical profilometry images (stitched) of post-mortem reciprocating wear tracks are given in Figure 7.3. Like the COF curves, a distinctive difference between the TiC reinforced sample and plain Ti6Al4V alloys can be detected from these images. The borders of the composite part's wear track (Figure 7.3(a)) follows an irregular path due to variable depth and significant wear along the wear track. However, both SLMed (Figure 7.3(b)) and conventional Ti6Al4V (Figure 7.3(c)) parts have a wear track with straight borders and low wear depth. Figure 7.3(d) shows transverse linear profiles of the wear tracks extracted from dashed lines in Figure 7.3(a,b,c). The maximum depth of the composite part's wear track ~20 μm is approximately five times deeper than the ~4 μm depth of the plain samples. Additionally, it has a curved shape, due to the shape of the steel ball which undergoes minimal wear (Figure 7.1(b)). In comparison the steel balls undergo significant wear against the plain Ti6Al4V parts (Figure 7.1(b)) resulting in a flatter profile of the final wear tracks (Figure 7.3(b-d)). The difference in the final ball shape is also reflected in the profile of the ends of wear tracks, which have a straight profile for plain Ti6Al4V parts (Figure 7.3(b,c)) compared to curved boundary for the composite sample (Figure 7.3(a)). Small debris patches, which causes increased local height, can be detected on the plain samples (dashed circles in Figure 7.3(b,c)). Such patches are significantly smaller and barely noticeable for composite sample.
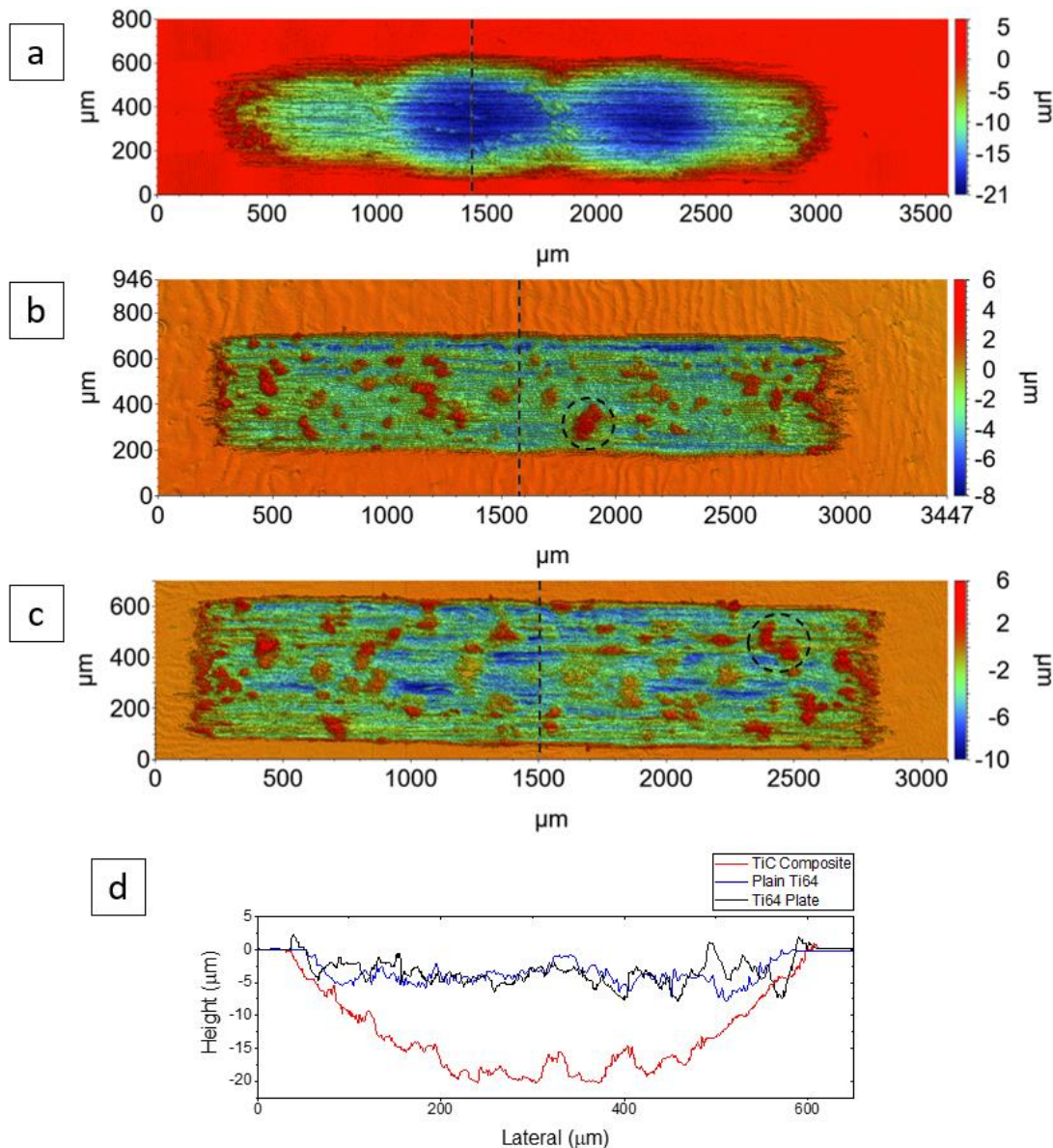
Figure 7.3. Optical profilometry images of reciprocating wear tracks after rubbing against bearing steel balls: (a) Ti6Al4V-TiC composite, (b) plain Ti6Al4V manufactured via SLM, and (c) conventional Ti6Al4V plate. (d) Linear height profiles accross wear tracks from dashed lines on (a,b,c).

Optical profilometry images of the post-wear surfaces of the steel balls rubbed against the Ti6Al4V-TiC, SLMed Ti6Al4V and Ti6Al4V plate materials are given in Figure 7.4(a,b,c). The shape removal function of Vision 64 software (Bruker, USA) is used to remove the original spherical shape of balls from the surface profile to visualise wear profile, and these images are given in Figure 7.4(b,d,f). After 3h of reciprocating rubbing against Ti6Al4V-TiC the steel ball's surface is slightly (Figure 7.4(a,b)), but mostly still preserves its spherical shape and has a ring of debris around the central wear zone (Figure 7.4(b)). In comparison, plain Ti6Al4V parts cause very significant

wear of the balls. Original spherical shape of the balls worn down to flat contact surfaces with parallel reciprocating wear grooves (Figure 7.4(c-f)).

To examine the wear mechanisms in more detail, chemical analysis of the final wear track surfaces was carried out by energy dispersive X-ray spectroscopy (EDS). Coincident secondary electron SEM images and EDS maps of the reciprocating wear tracks of the Ti6Al4V-TiC composite sample and plain Ti6Al4V manufactured via SLM are given in Figure 7.5. The EDS maps confirm the formation of an oxide layer after the tests on both samples (Figure 7.5(e)). For the Ti6Al4V-TiC sample, this oxide layer consists of mostly Ti, rather than Fe (Figure 7.5(a,b,e)). With only relatively small Fe-rich being seen (Figure 7.5(b,e)) consistent with low wear of the steel ball (Figure 7.1(b)). On the other hand, Fe is distributed over the final wear track for the plain Ti6Al4V sample (Figure 7.5(c,d,e). Fe oxide accumulates as larger patches, with coincident strong Fe and O signal in the EDS maps (Figure 7.5(e)) consistent with high wear of the steel ball Figure 7.1(b).

High fluctuations of the COF when the steel ball is rubbing against unreinforced Ti6Al4V (Figure 7.2) indicates the formation of material transformation tribolayer, which periodically gradual grows and then removed from the surface [204]. Large plastic deformation of on the tribolayer/surface occurs when adhesion forces are high enough to resist relative sliding [205]. High fluctuations in the COF curve indicates a cycle of tribofilm formation and removal due to high adhesion and resulting deformation in the tribo-contact zone.

Frictional forces create heat at the interface, and this changes materials' properties during the reciprocating wear tests [206], [207]. Adhesion of the steel ball to the titanium substrate increases friction and adds more heat to the contact zone. AISI 52100 is an oil hardened steel [145] and has higher strength (700-900 HV [145]) than all the Ti6Al4V-based materials. AISI 52100 has a bainitic or martensitic microstructure after the oil quenching [208]. Frictional heat generated by high adhesion between steel ball and base material may stimulate phase transformations in the steel ball including oxidation.

A relatively large mass of base Ti6Al4V material may behave as a heat sink to redistribute frictional heat from the material's surface. On the other hand, the ball material has a relatively small mass, and heat transfer would be more limited. Oxidation of the AISI 52100 steel ball may be accelerated by the temperature arising from the friction. Brittle oxide layers and its poor adhesion to the steel ball may cause fracture and shear of the tribolayer. This mechanism may explain high ball material loss despite its high hardness.

High adhesion of the worn steel ball and Ti6Al4V surfaces results in oxidation and material transfer to the sample surface. Asperities on the wear track of unreinforced parts (Figure 7.3(b,c)) are due to localised wear debris, including transferred from the ball. The high Fe content of oxide regions in the EDS analysis confirms this (Figure 7.5(c,d,e)). High volume loss of the steel ball also corroborates with high adhesion and oxidation of Fe element on the surface (Figure 7.4(c,d,e,f)). The flattened ball creates a wear track with flat ends (Figure 7.3(b,c,d) and Figure 7.4(c,d,e,f)). Additionally, the base of the wear track is quite flat compared with the Ti6Al4V-TiC part (Figure 7.3(d)) where the steel ball undergoes much less wear.

Figure 7.4. Worn surfaces of AISI 52100 bearing steel balls against (a) Ti6Al4V-TiC composite, (c) SLMed Ti6A4V and (e) conventional Ti6Al4V plate. (b,d,f) shows optical profilometry images after the sphericity removing process applied to (a,c,e), respectively.

The Ti6Al4V-TiC part shows an unexpected significantly high wear rate against a steel ball, given its approximately 100 HV higher hardness than the unreinforced Ti6Al4V. Additionally, the wear of the steel ball is extremely low while rubbing against TiC reinforced composite (Figure 7.1(b)). Fluctuation of the COF curve while rubbing

against Ti6Al4V-TiC is less than the COF variations for Ti6Al4V (Figure 7.2). This may be attributed to less adhesion and a reduced amount of transfer layer/tribofilm build-up during the test.

The borders of the wear track do not follow a straight path for the TiC reinforced part (Figure 7.3(a)) due to depth of wear varying along the length of the wear track. This type of wear track is associated with micro and macro adhesions in the wear track of Ti6Al4V while rubbing against WC-Co composite ball [209], [210] with stick-slip movement along the sliding direction [209]. When steel ball rubbed against unreinforced Ti6Al4V parts, it may start to rub on itself due to adhesion and following transfer of the ball material due to explained reasons above. Therefore, plain Ti6Al4V samples may have different flat wear surfaces and wear scar borders.
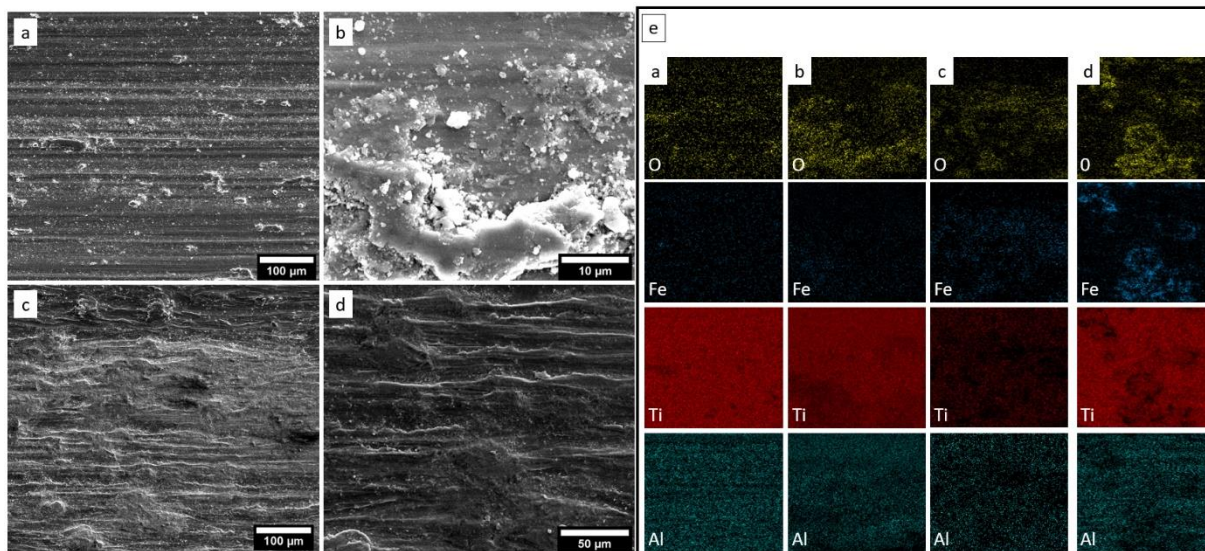
Figure 7.5. Secondary electron SEM images of the reciprocating wear tracks of (a,b) Ti6Al4V-TiC composite sample and (c,d) SLMed plain Ti6Al4V after wear test against bearing steel balls. (e) O, Fe, Ti and Al EDS maps of (a,b,c,d).

The examined Ti6Al4V-TiC, and plain Ti6Al4V were processed using identical SLM parameters but for the composite the incorporation of carbon generates nanosized TiC particles distributed within the Ti6Al4V matrix. These particles are likely the cause of the lower wear rate of the steel ball and higher wear rate of the base part. Both conventional and SLMed Ti6Al4Vs show similar wear and friction behaviour (Figure 7.1 and Figure 7.2). This indicates that the SLM process' characteristics do not create a significant difference.

TiC particles are well distributed within the Ti6Al4V matrix, and will be in contact with the steel ball counterface during the test. When the ball rubs against the base material, it will displace some of the nanosized TiC particles as wear debris. A third-body layer containing TiC debris particles is likely create an abrasive barrier between the steel ball and the base material reducing interfacial adhesion, significantly increasing the wear rate of the Ti6Al4V-TiC surface, and inhibiting the formation of a protective tribo-layer. The reduced COF observed at the interface (Figure 7.2) is consistent with reduced adhesion from the TiC particulates.

Titanium matrix composites generally have lower ductility than the matrix material [107]. Reduced ductility can arise from inhibited dislocation flow, or enhanced fracture at the particle-matrix interfaces. Lower ductility of TiC reinforced composites may result in brittle, less sticky and finer wear debris [211]. This may prevent the formation of a debris layer at the interface and may increase the wear rate of TiC reinforced parts.

7.3.1.b. Sliding wear against S_3N_4 ball

Compared to reciprocating wear tests with steel balls, using a S_3N_4 ball results in similar wear of the Ti6Al4V-TiC ($9.87 \times 10^{-4} mm^3/N.m$), increased (but low) wear of SLMed Ti6Al4V and conventional Ti6Al4V plate ($4.12 \times 10^{-4} mm^3/N.m$, and $3.36 \times 10^{-4} mm^3/N.m$), and low wear rate of the S_3N_4 balls (Figure 7.1). S_3N_4 balls' wear rate measured as $6.10 \times 10^{-6} mm^3/N.m$, $4.12 \times 10^{-4} mm^3/N.m$ and $3.36 \times 10^{-4} mm^3/N.m$ while rubbing against Ti6Al4V-TiC, SLMed Ti6Al4V and conventional Ti6Al4V plate, respectively.

The coefficient of friction (COF) change of for Ti6Al4V-TiC (TiC Composite), SLMed Ti6Al4V (Plain Ti64) and Ti6Al4V plate (Ti64 Plate) materials against S_3N_4 balls is given in Figure 7.6. Different behaviour of all three base materials can be seen from the graph. Plain Ti6Al4V base materials have a periodic gradual increase of COF, and a sudden drop followed this increase. However, a difference between the SLMed part and conventional plate is observed with magnitudes of the periodic COF jumps and drops significantly lower than for the conventional Ti6Al4V plate ($\sim$0.4 $\leftrightarrow$ 0.65 compared to $\sim$0.4 $\leftrightarrow$ 0.8), and with longer stable plateaus. Although the range of COF is lower, the

wear rate of the SLMed part is slightly higher than the conventional Ti6Al4V plate (Figure 7.1(a)). On the other hand, TiC reinforced material's COF curve is quite similar to steel one with a gradual increase of COF from $\sim 0.45 \rightarrow 0.6$.
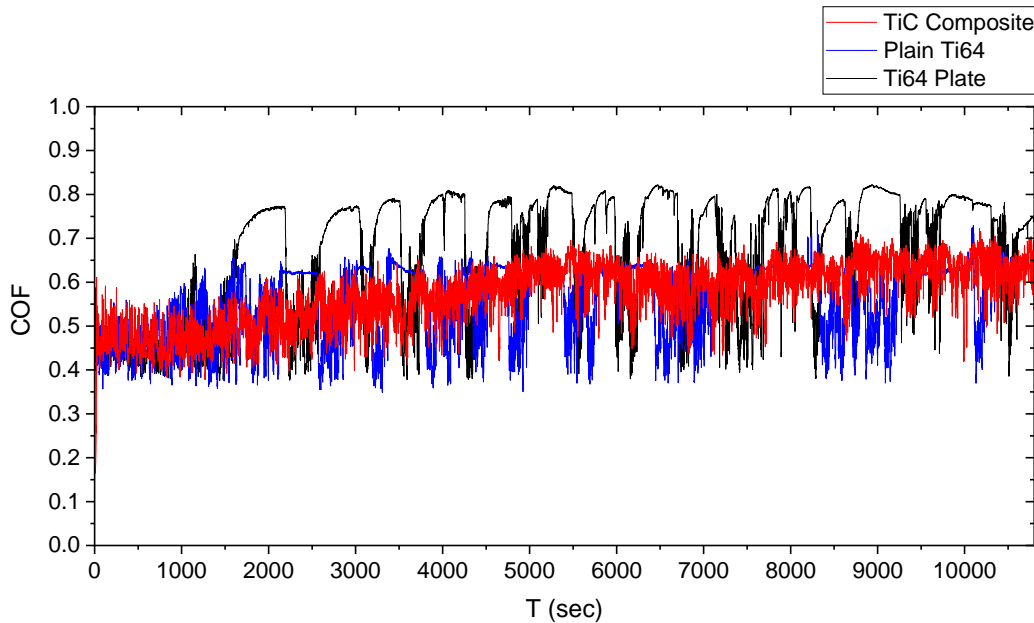
Figure 7.6. Coefficient of friction (COF) change of Ti6Al4V-TiC (TiC Composite), SLMed Ti6Al4V (Plain Ti64) and conventional Ti6Al4V plate (Ti64 Plate) rubbing against Si_3N_4 balls. Wear tests used 2.5 mm stroke length, 0.5 N normal load, 1 Hz frequency, 54 m total distance and 3 h total test duration.

Figure 7.7 shows stitched optical profilometry images of post-mortem reciprocating wear tracks on Ti6Al4V-TiC (YZ and XY planes), SLMed Ti6Al4V and conventional Ti6Al4V plate materials after rubbing against Si_3N_4 balls. An additional TiC reinforced composite sample (XY plane in Figure 6.1(b)) is used to evaluate the effect of the build direction on the wear resistance, with wear testing performed perpendicular to the Z-axis build direction. The wear resistance of Ti6Al4V-TiC composite rubbing against Si_3N_4 balls was measured as $9.10 \times 10^{-4} mm^3/N.m$ when the tests were performed on the XY plane. Si_3N_4 ball's wear rate was measured as $3.75 \times 10^{-6} mm^3/N.m$ when the test were performed on Ti6Al4V-TiC composite's XY plane.

In all tests there was a low wear rate of the S_3N_4 balls (Figure 7.1), so that they retained some of their spherical curvature to the end of the test. The final wear tracks of all parts therefore had a curved shape transverse to the sliding direction and at the ends of the tracks (Figure 7.7(a-d) and Figure 7.7(e)). Additionally, depth variations along the direction of the reciprocating movement are observed for all samples, particularly for

the Ti6Al4V-TiC samples (Figure 7.7(a,b)), which results in irregular wear track width and outer borders. Because of the low of wear of the S_3N_4 balls, the plain Ti6Al4V samples have a curved wear track profile, unlike their profile against the steel ball (Figure 7.3). The maximum wear depth of the wear scars was 25 μm and 21 μm for Ti6Al4V-TiC composites on YZ and XY planes, respectively (Figure 7.7(e)). The maximum wear depth was measured as 11 μm and 9 μm for SLMed Ti6Al4V and conventional Ti6Al4V plate, respectively.
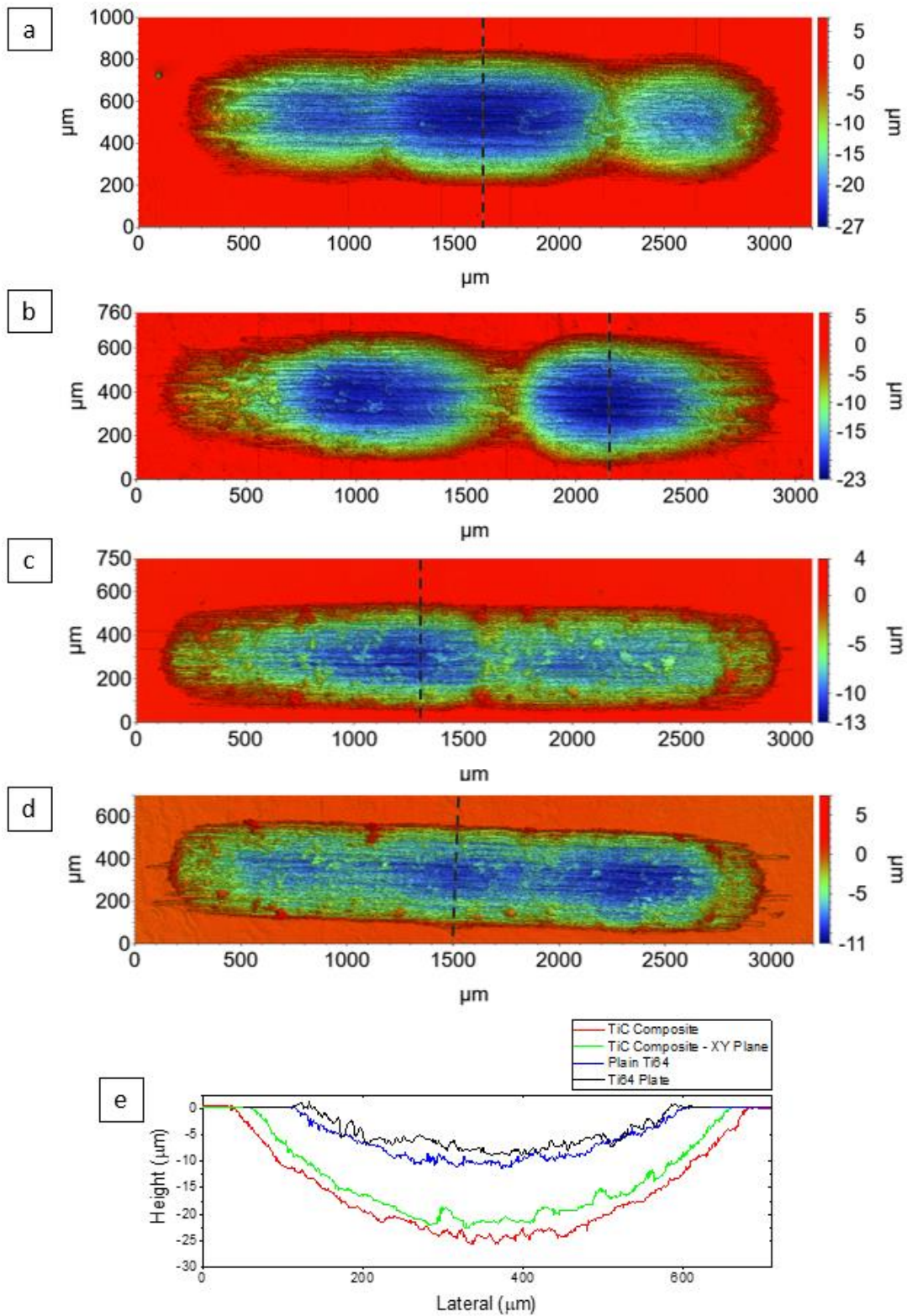
Figure 7.7. Optical profilometry images of reciprocating wear tracks after rubbing against Si₃N₄ balls: (a) Ti6Al4V-TiC composite tested on YZ plane, (b) Ti6Al4V-TiC tested on XY plane, (c) plain Ti6Al4V manufactured via SLM, and (d) Ti6Al4V plate. (e) Linear height profiles across wear tracks from dashed lines on (a,b,c,d).

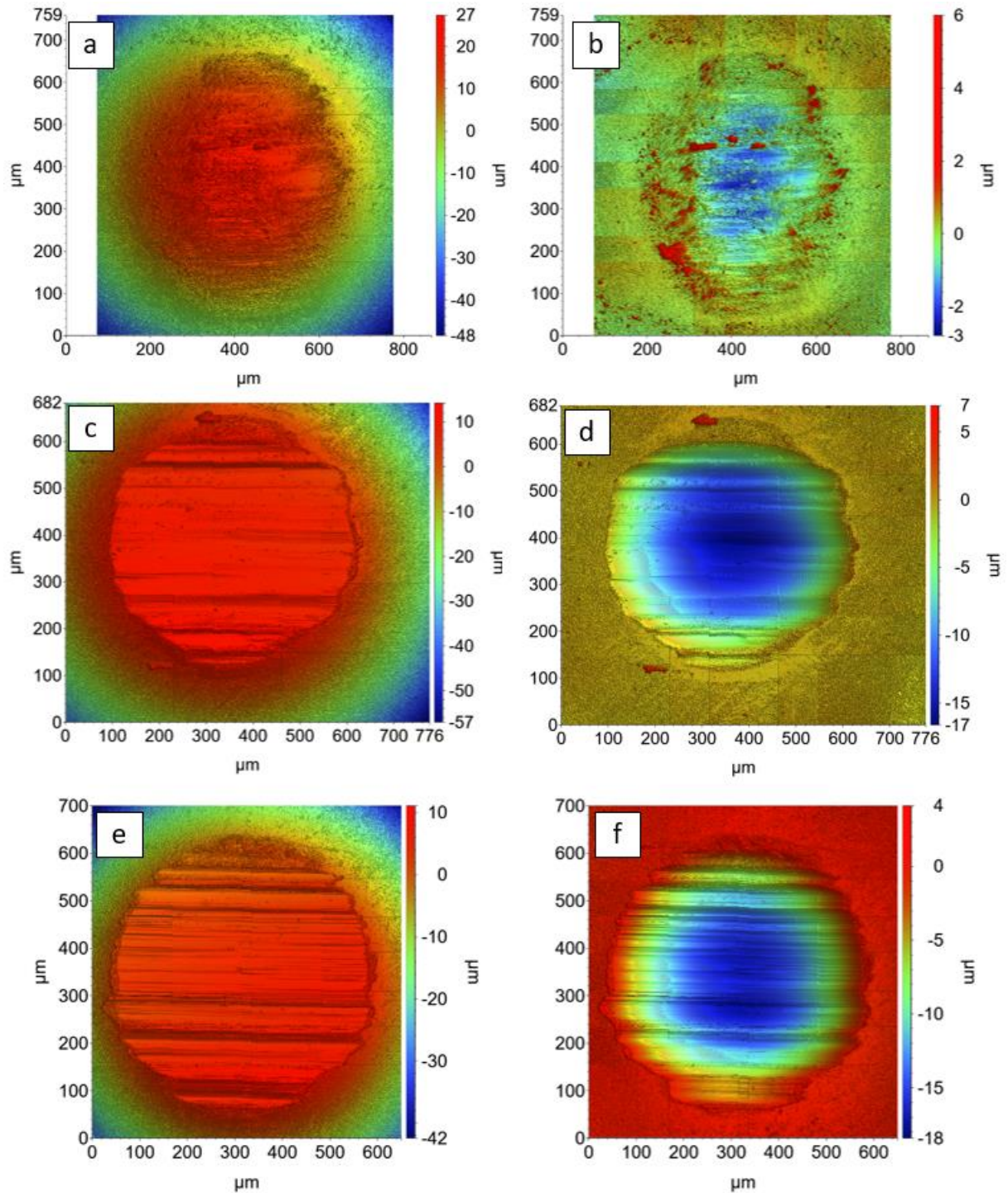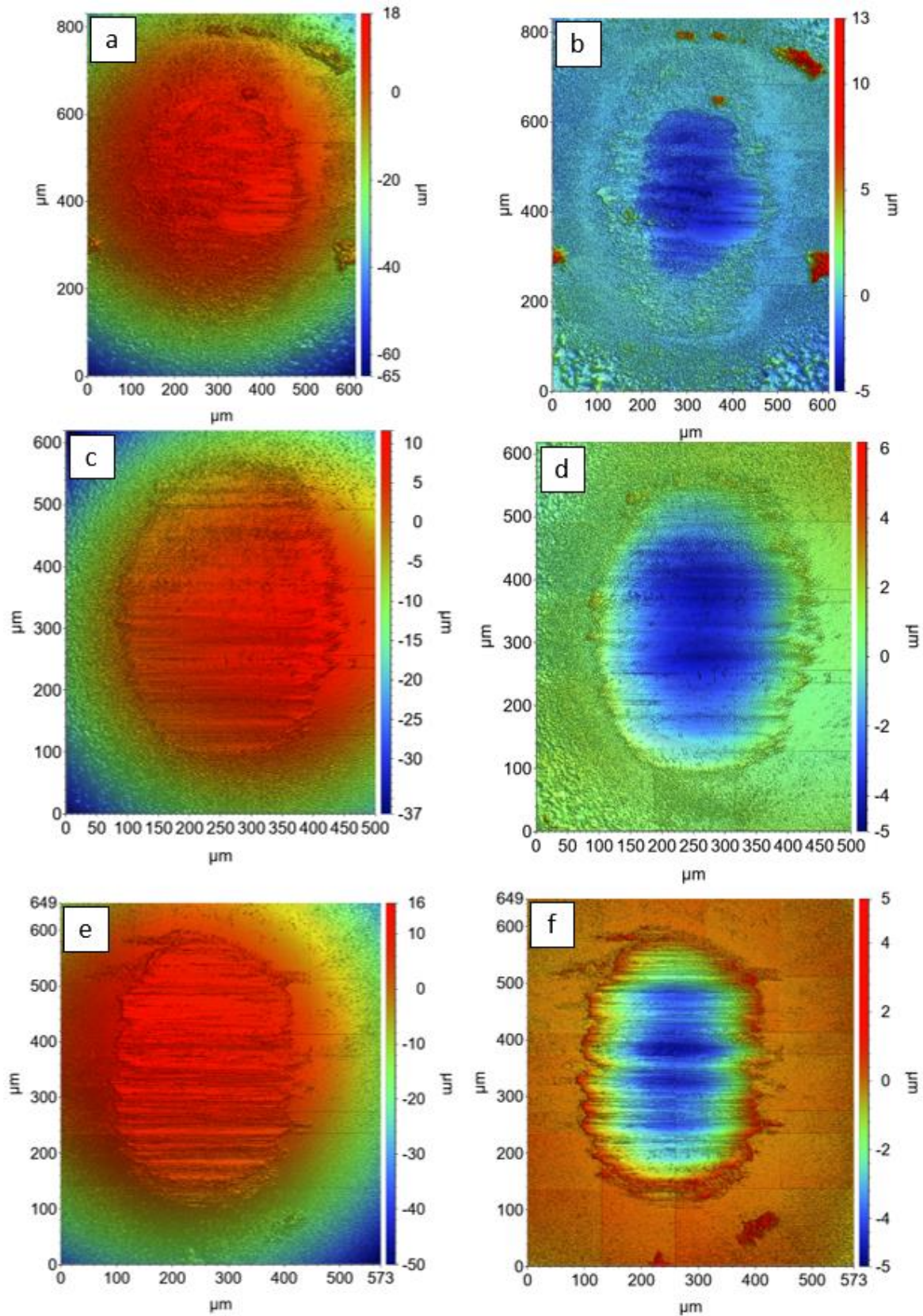*Figure 7.8. Worn surfaces of Si₃N₄ balls against (a) Ti6Al4V-TiC composite, (c) SLMed Ti6A4V and (e) conventional Ti6Al4V. (b,d,f) shows optical profilometry images after the sphericity removing process applied to (a,c,e), respectively . The direction of reciprocating wear is left to right, parallel to the visible scratch tracks.*

Optical profilometry images of the post-wear surfaces of the Si_3N_4 balls after wear tests are given in Figure 7.8. The wear scar of the ball rubbed against the Ti6Al4V-TiC composite is smaller than for the plain Ti6Al4V samples due to lower wear (Figure 7.1(b)). Differences between the wear of the Si_3N_4 balls on Ti6Al4V-TiC, and plain Ti6Al4V is not as dramatic as they are on steel balls due to the wear resistance of the Si_3N_4 on all samples.

Secondary electron SEM images and EDS maps from the central region of the reciprocating wear tracks of the Ti6Al4V-TiC composite sample and plain Ti6Al4V manufactured via SLM are given in Figure 7.9. Significant agglomerates of nanostructured wear debris are visible along the wear tracks. The EDS O-maps confirm the formation of an oxide layer after the tests on both samples (Figure 7.9(e)). The EDS Si signal from the wear surface is relatively weak for the Ti6Al4V-TiC sample (Figure 7.9(a,b,e)), and a stronger Si signal is detected from oxides generated when the ball is rubbed against the plain Ti6Al4V part (Figure 7.9(c,d,e)). This suggests that oxide film is more Si-rich for the plain Ti6Al4V sample, consistent with a higher Si_3N_4 wear rate (Figure 7.1(b)).
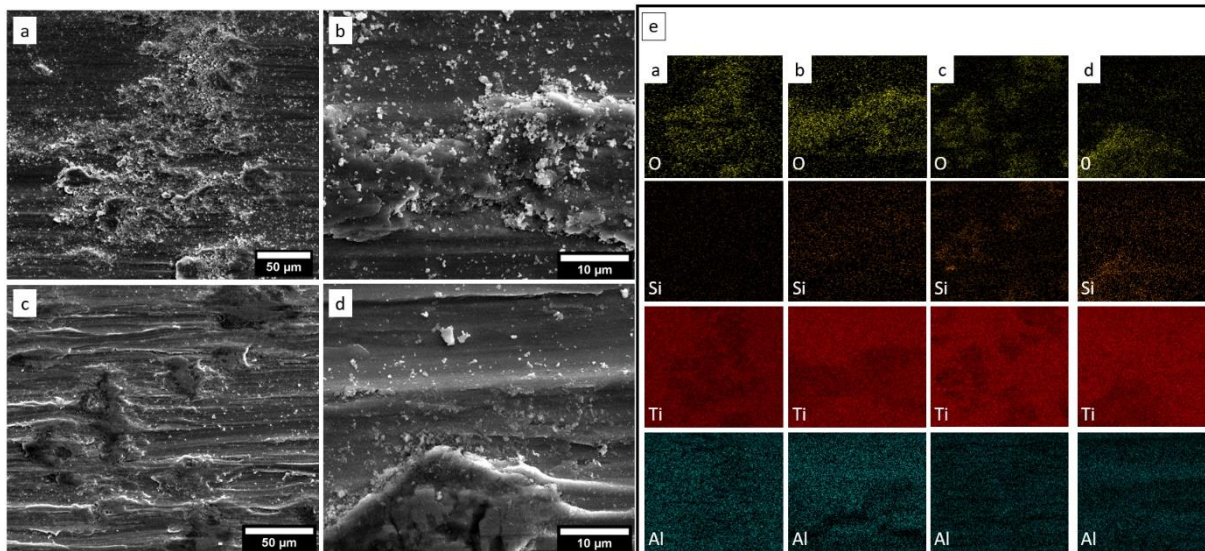
Figure 7.9.Secondary electron SEM images of the reciprocating wear tracks of (a,b) Ti6Al4V-TiC composite sample and (c,d) SLMed plain Ti6Al4V after wear test against Si_3N_4. (e) O, Si, Ti and Al EDS maps of (a,b,c,d).

Against a Si_3N_4 ball, the wear rate of Ti6Al4V-TiC composite is more than two times higher than plain Ti6Al4V samples (Figure 7.1(a)), whilst the wear rate of the Si_3N_4 ball is approximately halved while rubbing against the composite part. The lower wear rate

of the ball results in less Si in oxide debris (Figure 7.9(a,b,e)). The wear mechanism for plain Ti6Al4V and TiC reinforced parts is a combination of abrasive and adhesive mechanisms [9], [212]. The high wear-rate of the Ti6Al4V-TiC composite is similar for both steel and Si_3N_4 balls, and is consistent with substantial 3rd body abrasion due to TiC particles.

The wear rate of the SLMed Ti6Al4V against Si_3N_4 ball is slightly higher than that of the conventional Ti6Al4V plate, although the COF is on average lower. The microstructure of the SLMed Ti6Al4V consists of martensitic α' phase. This microstructure has higher hardness but lower ductility than the equilibrium $\alpha+\beta$ phase which is what conventional Ti6Al4V plate has [45]. Even though high hardness is usually associated with better wear resistance, the low ductility of the SLMed part's martensitic α' may increase its wear rate due to increased fracture of deformed material at the sliding interface [211]. Therefore, less debris sticks to the wear track. The periodic production of new wear debris either by fracture of the surface, or failure of a tribofilm (from deformation, oxidation and/or compacted wear debris) is consistent with the observed periodic COF fluctuations (Figure 7.6). The wear debris may also lower the COF if it reduces local adhesion and acts as a lubricant.

Less debris formation is observed with TiC reinforced parts. The presence of TiC particles may cause less sticky debris and may reduce the wear rate through the same mechanism. Therefore, a combination of 3rd body abrasion and lack of protective tribolayer may be the mechanism behind the deteriorative wear performance.

Bai et al. [9] studied the wear performance of *in situ* Ti6Al4V-TiC composites prepared by spark plasma sintering (SPS) against Si_3N_4 balls. They used the same reciprocating wear test conditions as in this study. Contrary to this study, they have noticed a better wear resistance of TiC reinforced Ti6Al4V than the unreinforced counterpart. The microstructure of the material they prepared differed from here, and consisted of large grain boundary TiC particles arranged in a cellular network. They proposed that the grain boundary TiC network acted as a load-bearing component and resulted in a reduced composite wear rate. In comparison, in this study nanosized TiC particles are

distributed throughout the Ti6Al4V matrix. The dispersion of these TiC nanoparticles in the wear debris, and the ensuing 3rd body abrasion effect of these particles is likely the cause of the significant difference ($9.87 \times 10^{-4} mm^3/N.m$ in this study vs. $2.15 \times 10^{-4} mm^3/N.m$ in [9]) between these two materials.

SLM parts' properties can be dependent on their build direction [72]. This is due to the large thermal gradient through the base plate generating different top surface and side surface microstructures. When wear tests are performed parallel to the build direction, the ball moves through columnar grains. When wear tests are performed on the top surface, however, the ball travels through more equiaxed grain boundaries. A small difference in wear resistance is observed on the YZ and XY planes' wear rates ($9.87 \times 10^{-4} mm^3/N.m$ on YZ plane and $9.10 \times 10^{-4} mm^3/N.m$ on XY plane) (Figure 7.1). The change of martensite and parent β grain size may be the reason behind better performance on the XY plane. More refined grains may result in better wear performance [213]. When the ball rubs perpendicular to the build direction, it passes through columnar parent β grains which means more grain boundaries were passed in a transverse direction. On the other hand, it travels through equiaxed cross-sections of the grains when the tests were performed on XY plane. Grain boundary direction will be more random in this case. This may be the reason behind slightly better performance when the test is done on the XY plane.

7.3.1.c. Sliding wear against Al₂O₃ ball

Compared to reciprocating wear tests with steel and S_3N_4 balls, using Al₂O₃ balls results in the maximum observed wear of the Ti6Al4V-TiC ($1.55 \times 10^{-3} mm^3/N.m$), Ti6Al4V ($7.79 \times 10^{-4} mm^3/N.m$) and Ti6Al4V plate ($8.04 \times 10^{-4} mm^3/N.m$), and the Al₂O₃ ball wear rate is more than S_3N_4 balls (Fig 7.1), but less than steel for the plain alloy (Fig 7.1). The use of Al₂O₃ balls introduces significant amounts of oxygen into the wear zone.

The coefficient of friction (COF) changes for Ti6Al4V-TiC, Ti6Al4V and Ti6Al4V plate materials against Al₂O₃ balls is given in Figure 7.10. Unlike for steel and Si_3N_4 counterpart balls, all three materials' showed quite similar COF behaviour, with a

gradual increase from ~0.45 ↔ 0.6-0.7. These COF values are similar in magnitude and evolution to the COF of Ti6Al4V-TiC against steel (Figure 7.2) and Si_3N_4 (Figure 7.6). Even though there is some COF modulation during the tests, these changes are small in magnitude, and periodic modulation and sharp COF decreases are not observed.

Stitched optical profilometry images of post-mortem reciprocating wear tracks on Ti6Al4V-TiC, Ti6Al4V and Ti6Al4V plate materials after rubbing against Al_2O_3 balls are given in Figure 7.11. All three base materials' wear track have marked depth variations alongside the sliding direction, and the wear track widths correspondingly vary due to the variable penetration of the counterface ball. These depth variations are more noticeable on the Ti6Al4V-TiC part, and are similar to the scratch tracks by S_3N_4 balls (Figure 7.7). For all three materials the wear scar depths, and widths are reduced at both ends of the reciprocating wear tracks (Figure 7.11(a)) (Figure 7.11(b,c), which is observed to a lesser degree for the S_3N_4 tests (Figure 7.7).

Linear depth profiles extracted perpendicular to the scratch tracks (dashed lines in Figure 7.11(a,b,c)) are given in Figure 7.11(d). All materials have a curved residual wear track profile due to the curved nature of the counterface Al_2O_3 balls. The maximum depths are 25 μm for Ti6Al4V-TiC and 15 μm for Ti6Al4V, consistent with the higher wear rate of the composite (Figure 7.1(a)). Grooves that are parallel to the sliding direction can be observed within the wear scars, together with raised debris particles on the Ti6Al4V wear surfaces (Figure 7.11(b,c)).
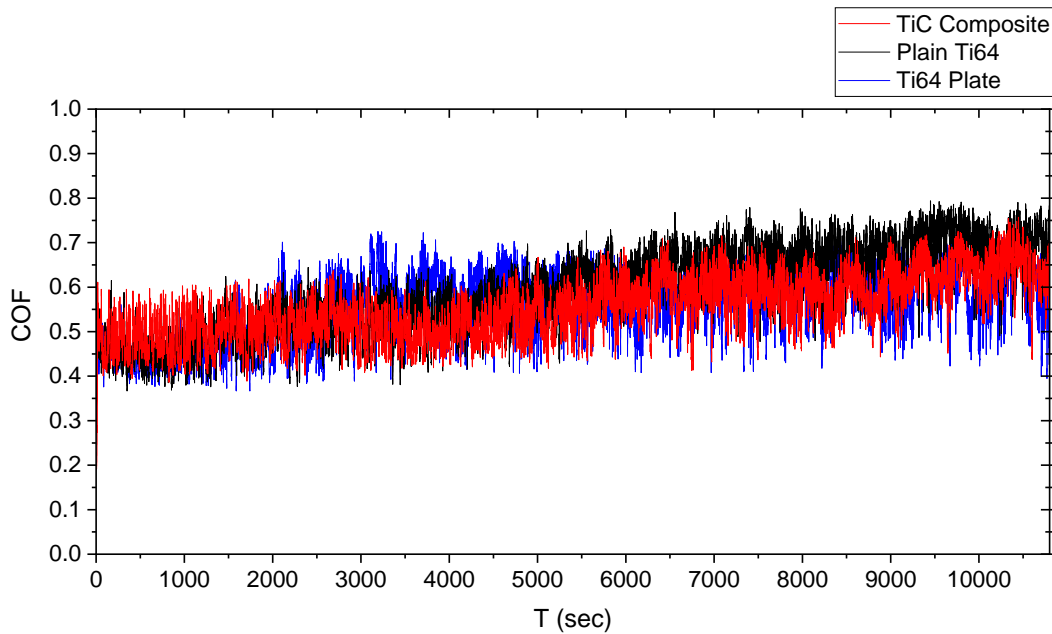
Figure 7.10. Coefficient of friction (COF) change of different base plates rubbing against Al₂O₃ ball. Wear tests used 2.5 mm stroke length, 0.5 N normal load, 1 Hz frequency, 54 m total distance and 3 h total test duration.

Optical profilometry images of the post-wear surfaces of the counterpart Al_2O_3 balls after the wear tests are given in Figure 7.12. Parallel grooves can be seen on the ball rubbed against the Ti6Al4V-TiC part (Figure 7.12(b)). However the balls rubbed against plain Ti6Al4V are covered in substantial amounts of debris (Figure 7.12(d,f)), as are the Ti6Al4V residual scratch tracks (Figure 7.11(b,c)). The wear scar of the Al_2O_3 ball rubbed against the Ti6Al4V-TiC composite is smaller than for the plain Ti6Al4V samples due to lower wear (Figure 7.1 (b)), but bigger than the scars on the Si_3N_4 balls (Figure 7.8) due to the lower wear resistance of the Al_2O_3.

Figure 7.13 gives secondary electron SEM images and EDS maps of the residual reciprocating wear tracks' central region of the Ti6Al4V-TiC composite sample (Figure 7.13(a,b,e)) and plain Ti6Al4V sample (Figure 7.13(c,d,e)) processed via SLM. Significant agglomerates of nanostructured wear debris are visible along the wear tracks (Figure 7.13 (a-d)). Larger agglomerates of debris were observed on the scratch tracks of the Ti6Al4V samples, consistent with the debris observed by profilometry (Figure 7.11 and Figure 7.12). The EDS O-maps confirm the formation of a significant oxide layer after the tests on both samples (Figure 7.13 (e)). Al signal alongside the O indicates that debris contains particles of Al_2O_3 ball. In the examined areas the EDS Ti signal is stronger on the oxide particles for the Ti6Al4V-TiC part, either due to more Ti

presence in the debris or thinner debris transmitting more Ti signal from the underlying base material. The use of Al_2O_3 balls results in the maximum observed wear of the Ti6Al4V-TiC ($1.55 \times 10^{-3} mm^3/N.m$), SLMed Ti6Al4V ($7.79 \times 10^{-4} mm^3/N.m$), and Ti6Al4V plate ($8.04 \times 10^{-4} mm^3/N.m$), (Fig 7.1(a).

Similar COF behaviour of all three materials is only noticed against the Al_2O_3 ball (Figure 7.10). Small fluctuations of COF during the test are correlated with stick-slip movement, adhesion of counter bodies, formation of localised wear debris during the wear test and differences between static and dynamic COFs [9], [209]. The similar COF is probably due to 3rd body particle driven friction for all three materials. It is likely that, a combination of TiC particulate 3rd body abrasive wear and high oxidation combination caused the very worst wear resistance of Ti6Al4V-TiC composites. The wear resistance of the plain Ti6Al4V was also the worst against Al_2O_3 ball. This also probably arises due to the enhanced oxidation and leading to faster abrasion.

Reduced depth of the wear track at both tails on all base materials may be attributed to the presence of debris. Debris is pushed in front of the ball and to the outside of the wear track due to the movement of the reciprocating ball. Therefore, more debris is accumulated at the end of wear tracks. Debris stuck to the wear surface may behave as a protective layer and could reduce the wear rate [212]. Therefore, an accumulated pile debris at both ends of the wear tracks may reduce the wear rate at tails.
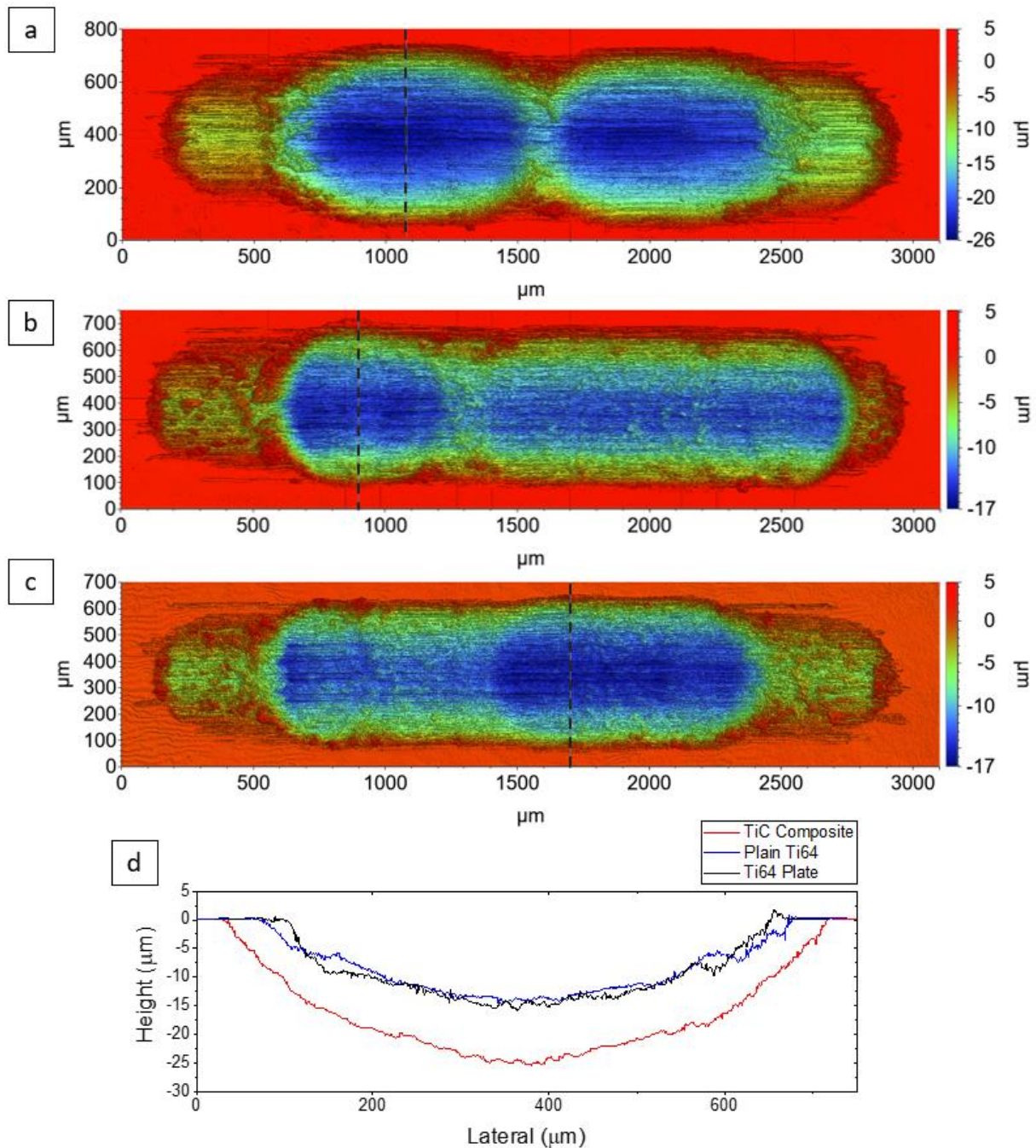
Figure 7.11. Optical profilometry images of reciprocating wear tracks after rubbing against Al₂O₃ balls: (a) Ti6Al4V-TiC composite, (b) plain Ti6Al4V manufactured via SLM, and (c) Ti6Al4V plate. (d) Linear height profiles across wear tracks from dashed lines on (a,b,c).

This mechanism also may help to explain the mechanism behind the highest wear rate of TiC reinforced composites against all counterpart balls. The lower ductility of the debris generated by Ti6Al4V-TiC reinforced parts may lead less adhesion of the debris on the interface [211]. This may lead lack of protective tribolayer and more abrasive particles on the wear interface. Lack of protective debris could lead more sticking and

resultant stick-slip behaviour which leads more height variation alongside the wear track due to material breakages [209].
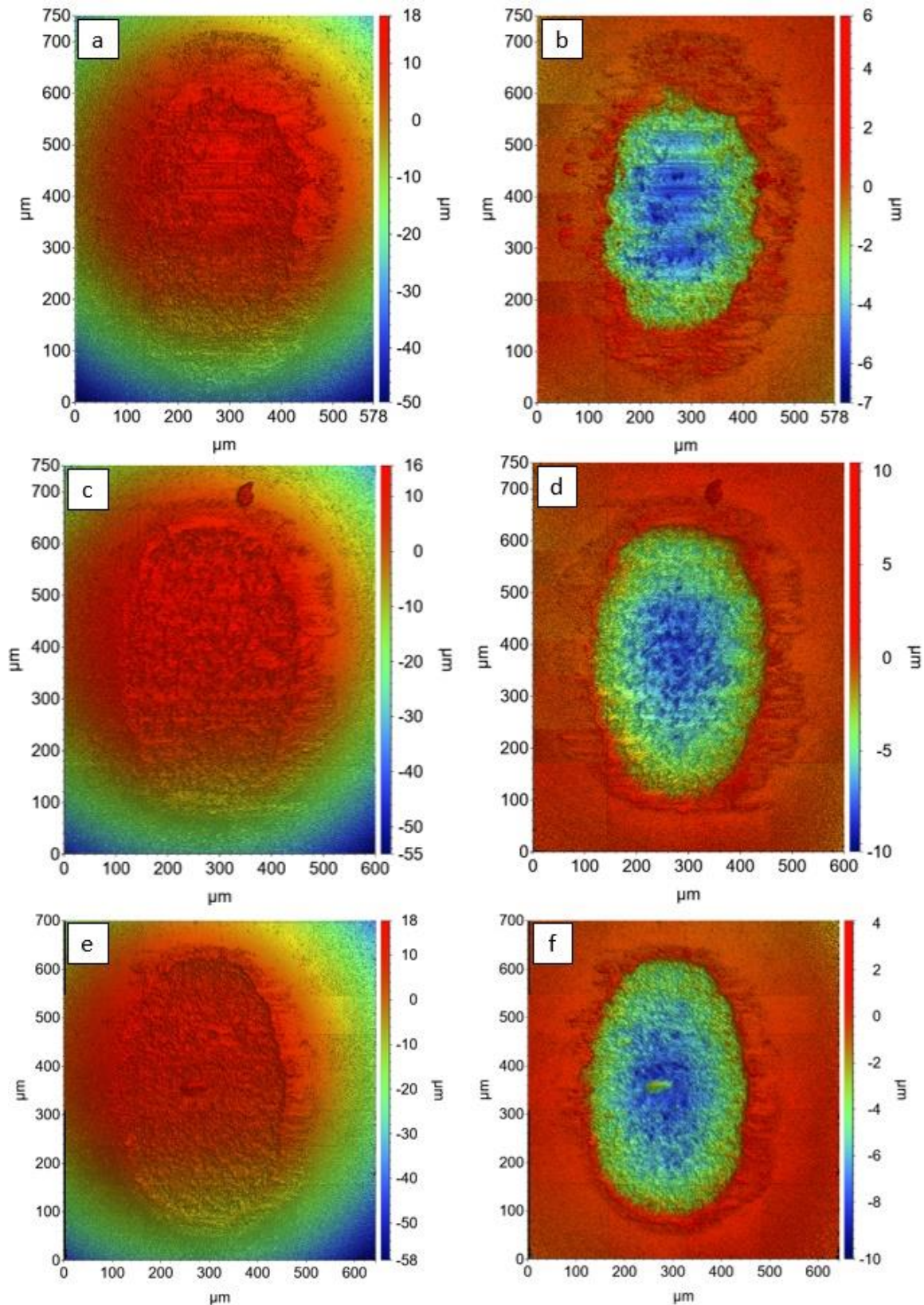
Figure 7.12. Worn surfaces of Al₂O₃ balls against (a) Ti6Al4V-TiC reinforced composite, (c) SLMed Ti6A4V and (e) conventional Ti6Al4V. (b,d,f) shows optical profilometry images after the sphericity removing process applied to (a,c,e), respectively. The direction of reciprocating wear is left to right, parallel to the visible scratch tracks on (a).
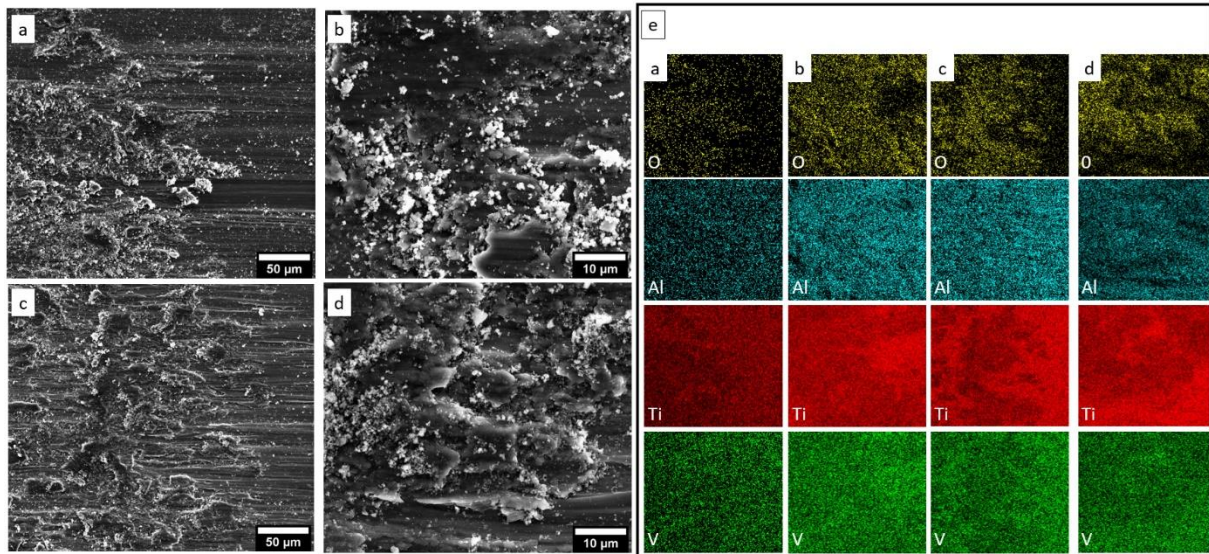
Figure 7.13. Secondary electron SEM images of the reciprocating wear tracks of (a,b) Ti6Al4V-TiC composite sample and (c,d) SLMed plain Ti6Al4V after wear tests against Al₂O₃ ball. (e)) O, Al, Ti and V EDS maps of (a,b,c,d).

More agglomerations of debris on the final wear tracks of plain Ti6Al4V parts compared to Ti6Al4V-TiC wear tracks can be observed for all counterpart balls (Figure 7.3, Figure 7.7, and Figure 7.11). Lack of a protective debris layer may be the reason behind the low wear resistance of TiC composites. A combination of active 3rd body abrasion from TiC particles, formation of less ductile, more fragile, and less sticky debris due to the presence of TiC particles, and presence of less stick debris on the contact zone would be the reason behind the low resistance of TiC reinforced parts. Closer examination of the debris distribution and tribolayers would be beneficial future work.

7.3.2. *In situ* SEM Scratch Tests

In situ dynamical scratch tests inside SEM have been performed to understand further the difference of friction and wear mechanisms between Ti6Al4V-TiC and SLMed plain Ti6Al4V parts. Tests were carried out using an Alemnis SEM nanoindenter, with a conical diamond tip having 0.7 µm radius. 25 mN normal load, 5mN/s ramp-up speed, 1 µm/s scratch speed and 100 µm scratch length were tests parameters.

Figure 7.14 shows normal force, lateral force, and coefficient of friction (COF) changes during these single stroke lateral scratch tests. COF curves are plotted by dividing lateral load to normal load presented in Figure 7.14(a,c). The COF shows some variations on both samples due to local microstructure, stick-slip mechanisms and resultant debris formation. When the test was performed on the Ti6Al4V-TiC sample, the COF variation showed a more consistent behaviour than the plain Ti6Al4V sample (Figure 7.14(b,d)), which exhibited fluctuations similar to the stick-slip behaviour against steel and Si_3N_4 balls (Figure 7.2 and Figure 7.6). The COF measured were Ti6Al4V-TiC COF=0-8-0.9, and plain Ti6Al4V COF=0.6-0.9. The COF range of the Ti6Al4V-TiC measured with a nanoscale diamond tip and single stroke is higher than that measured at the macroscale in reciprocating wear mode (Figure 7.2, Figure 7.6 and Figure 7.10). However, the COF range of the Ti6Al4V measured with a nanoscale diamond tip and single stroke is similar to the reciprocating wear using steel and Si_3N_4 balls (Figure 7.2 and Figure 7.6).

Examples of sequential *in situ* secondary electron (SE) SEM images obtained during single stroke scratch testing of TiC reinforced composite are given in Figure 7.15. The formation of a ductile chip can be seen to grow ahead of the tip as the scratch progresses during the test (black arrows in Figure 7.15(b,c,d)). The scratch scars have smooth edges, and no cracks were observed during the tests. A similar chip formation is detected when the test is performed on plain Ti6Al4V sample (Figure 7.16). Again, a wear scar having smooth edges is observed. Formed swarf of both materials have a smooth surface on the surface in contact with the diamond tip, whereas the outer surfaces are rough due to the periodic deformation and displacement mechanism. This periodic material deformation and shear also explains the small variations of COF during the scratch tests.
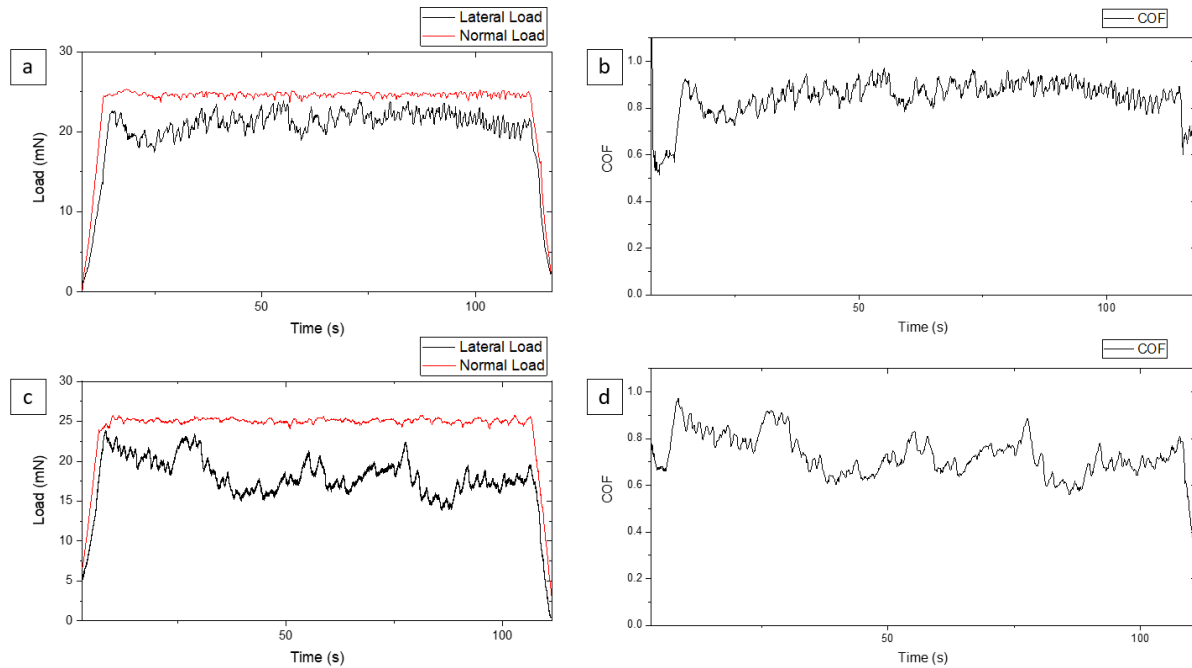
Figure 7.14. Change of lateral and normal force during in situ SEM scratch testing using a diamond tip, 25 mN normal load, 1 µm/s scratch speed and 100 µm length. (a) Ti6Al4V-TiC sample and (c) SLMed plain Ti6Al4V during the scratch test. Coefficient of friction (COF) change during scratch tests of (b) Ti6Al4V-TiC and (d) SLMed plain Ti6Al4V samples.
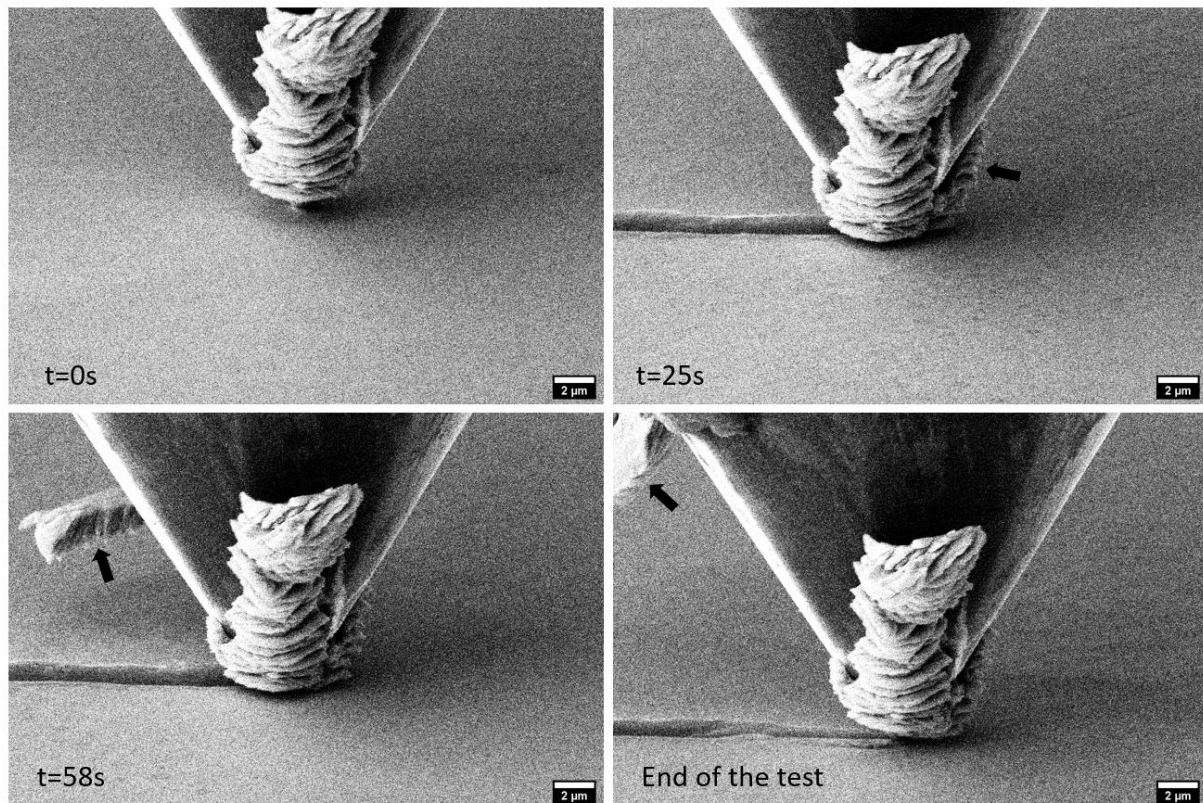
Figure 7.15. Secondary electron (SE) SEM images of Ti6Al4V-TiC taken at different time points during the scratch duration. Values on the bottom left of the images show the scratch time for the image in seconds. The sample is moving to the left with respect to the scratch tip.
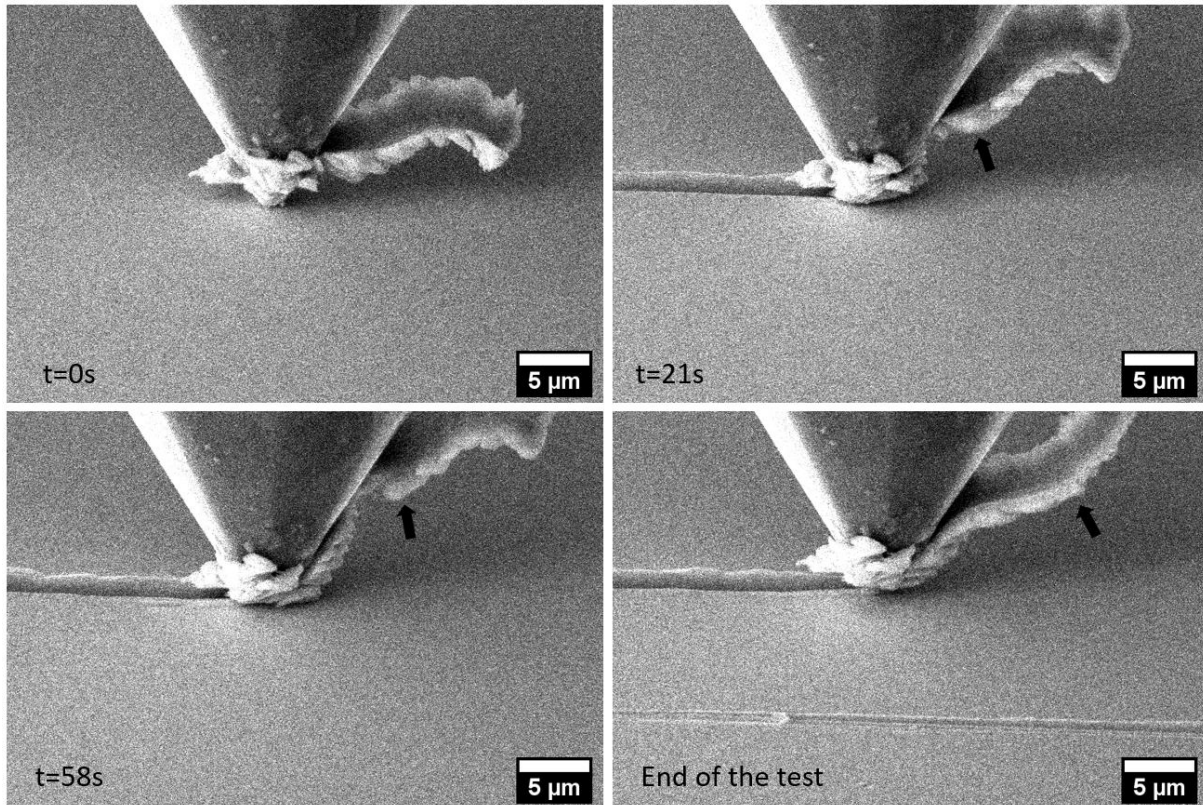
Figure 7.16. Secondary electron (SE) SEM images of unreinforced Ti6Al4V sample taken at different time points during the scratch duration. Values on the bottom left of the images show scratch time for the image in seconds. The sample is moving to the left with respect to the scratch tip.

Post-mortem examinations were performed to further examine the nature of the scratch tracks after the *in situ* SEM scratch tests. Figure 7.17 shows Ti6Al4V-TiC reinforced part's (Figure 7.17(a,b)) and the plain Ti6Al4V part's (Figure 7.17(c,d)) scratch track after the test. Small holes along the internal surface of the wear track are detected after the scratch test of the Ti6Al4V-TiC reinforced part (red circles in Figure 7.17(a)). These small holes have similar dimensions to the *in situ* formed TiC particles examined in the previous chapter. Two of these holes are shown in more detail in Figure 7.17(b). The 83 nm and 128 nm length of these holes, and their relatively high aspect ratio, correlates well with the size and shape of the TiC particles. In addition to particles, groves are detected inside the scratch scar (black arrows in Figure 7.17(b)). Both the holes and grooves are consistent with the displacement of TiC particles from the Ti6Al4V matrix during the impact with the indenter tip, and the movement of TiC particles trapped in the contact zone contributing to 3rd body wear.

The plain Ti6Al4V's scratch track has a smoother surface (Figure 7.17(c,d)). Only some minor grooves can be seen (black arrows in Figure 7.17(d)). Additionally, the holes detected on the Ti6Al4V-TiC scratch track are not observed on the plain sample's scratch scar. Both Ti6Al4V-TiC, and unreinforced samples' scratch tracks have pile-up ridges of plastically deformed and displaced material either side of the scratch tracks. The displaced material is non-uniform at the nanometer level, with ripples due to non-uniform shear of the martensite matrix. Some of the displaced material will also be removed by the lateral formation of swarf, as visible in Figure 7.17. This heterogeneous deformation will also contribute to local variations in the COF during the scratch test.

TiC reinforced parts have a higher wear rate than plain Ti6Al4V against all counterface balls (Figure 7.1(a)). Removal of TiC particles from the matrix during the *in situ* scratch test shows that 3rd body abrasion should be a significant factor in the high wear rate of these composites. Removal of nanoparticles from the matrix may cause a high wear rate and provide a 3rd body layer that may reduce the ball material's adhesion. This also may be the mechanism behind the lower wear rate of the counterpart balls (Figure 7.1(b)).

Swarf formed during *in situ* scratch tests of TiC-Ti6Al4V and Ti6Al4V. Both tests resulted in long ductile swarf formation. Surface of swarf in contact with the diamond tip was smooth whereas the opposite surface had ripples alongside its length. Both TiC-Ti6Al4V composites and unreinforced Ti6Al4V samples has martensitic microstructure. Different martensite plates, grain boundaries may be the reason behind this ripple formation in the nanoscale. TiC-Ti6Al4V composites had the finer microstructure according to the examinations in Chapter 6. Additionally, homogeneously dispersed TiC particles were present. Finer microstructure of TiC-Ti6Al4V may lead more homogeneous deformation and less variations on the COF curve. Homogeneous distribution of TiC particles may be contributing to this smoother behaviour.

During the macro wear tests, oxidation took place, which is prevented due to the vacuum environment of the SEM. Additionally, COF variations happens over many 1

Hz cycles due to the reciprocating movement. Oxidised wear debris containing 3rd body TiC particles is present at the base material-counterpart ball contact zone. This tribolayer is responsible for the COF variations during the macro wear tests.
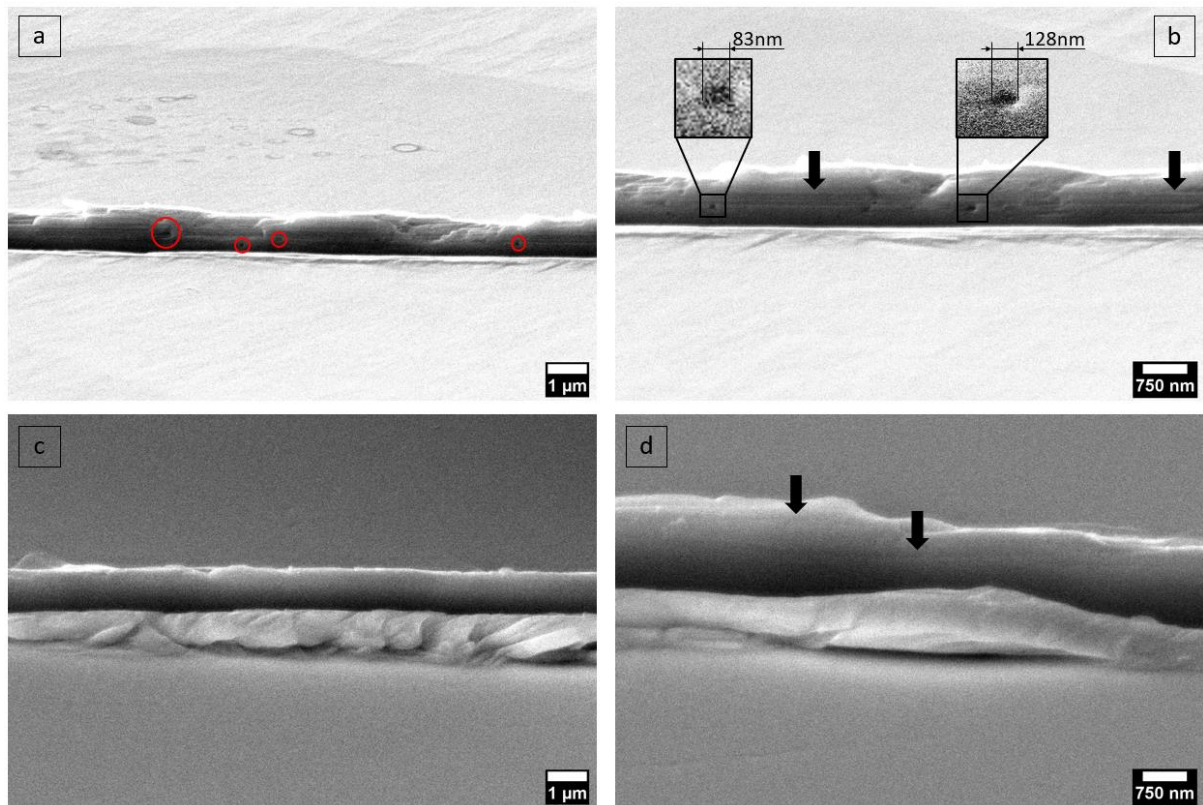
Figure 7.17. Secondary electron (SE) SEM images of residual scratch surfaces tracks after the in situ single stroke scratch test. (a,b) Ti6Al4V-TiC reinforced sample, with pores identified along the internal edges of the wear track. (c,d) plain Ti6Al4V. Black arrows show grooves formed during the scratch test.

7.4. Conclusions

In this chapter, friction, and wear resistance of *in situ* Ti6Al4V-TiC reinforced composites, unreinforced SLMed Ti6Al4V and conventional Ti6Al4V plates are evaluated through a dry sliding reciprocating wear and *in situ* SEM scratch tests. The three base materials were tested against steel, Si_3N_4 and Al_2O_3 balls. Surprisingly, TiC reinforced composites had the highest wear rate (lowest wear resistance) against all counterpart balls in the selected test conditions. This is consistent with a high rate of 3rd body wear from abraded TiC particles. SLMed Ti6Al4V and conventional Ti6Al4V's

wear rates were quite similar to each other and significantly lower than the Ti6Al4V-TiC.

The Ti6Al4V-TiC, SLMed Ti6Al4V and conventional Ti6Al4V all exhibited more wear against Al_2O_3 balls compared to steel and Si_3N_4 balls, consistent with a higher rate of oxidation. When the tests were performed against bearing steel (AISI 52100), excessive wear of the steel balls against unreinforced Ti6Al4V was observed, whereas TiC reinforced part caused limited damage to the steel balls. The Ti6Al4V-TiC composite had relatively stable COF curves than SLMed Ti6Al4V and conventional Ti6Al4V all conditions, likely due to the TiC-rich 3rd body interlayer. The SLMed Ti6Al4V and conventional Ti6Al4V had significant periodic fluctuations in the COF against steel and Si3N4 balls, due to stick-slip behaviour, however more stable COF against the oxidative Al_2O_3 balls.

In situ SEM scratch tests revealed that nanosized TiC particles are displaced from the matrix when subjected to frictional forces during scratch testing. It is believed that removed TiC particles cause 3rd body abrasion during the macroscale wear tests and this leads higher wear rate of Ti6Al4V-TiC composites.

Chapter 8: Conclusions and Future Work

8.1. Conclusions

This work aimed manufacture of *in situ* Ti6Al4V-TiC nanoparticle reinforced composites using undeformed near-spherical composite powder feedstock via selective laser melting (SLM) and characterisation of manufactured parts. Titanium matrix composites (TMCs) have the potential to replace high-performance metallic materials. However, their manufacture is expensive and complex due to hard reinforcement particles in the matrix and problems with the titanium's machining. Various researchers have employed SLM to overcome manufacturing issues thanks to its near-net-shape nature, but the preparation of powder feedstocks is a barrier to their widespread use. Composite powder feedstocks must bring acceptable flowability, homogeneous particle distribution and cost-effectiveness together. However, current direct mixing and ball milling methods fail to meet all these criteria simultaneously. This need was provided the motivation behind this study.

There were certain reasons behind the selection of manufacturing method, matrix material, reinforcement particle, powder mixing technique and carbon source in this study. First, SLM was chosen due to its ability to control processing parameters and its finest feature size among metal additive manufacturing methods. Second, Ti6Al4V alloy was selected due to its high strength, low density, and extensive literature on its processing via SLM. Third, TiC reinforcement was chosen due to its excellent coherence with the Ti6Al4V matrix. Fourth, direct mixing was selected to ensure undeformed particles and acceptable flowability. Lastly, graphite flake was chosen to provide a cheap carbon solution to the composite feedstock.

The first experimental chapter investigated the applicability of direct mixing to provide SLM powder feedstocks with acceptable quality. It was found that direct mixing of pre-alloyed Ti6Al4V powders with graphite flakes provides near-spherical, homogeneously carbon-coated composite powder feedstock. When this powder feedstock was processed by a pulsed wave laser SLM system, TiC formation within the Ti6Al4V matrix was provided. Samples with a maximum %99.5 relative density were successfully manufactured. However, lack of fusion defects was detected within all samples after the X-ray computer tomography and optical microscopy examinations. Increasing energy density led to higher relative density parts.

The following chapter examined the manufacture of plain Ti6Al4V materials using a continuous wave laser SLM system by varying hatch distance and laser scan speed parameters of the SLM process. The unreinforced parts' microstructure was examined using optical microscopy, XRD, SEM, and large area EBSD mapping. Surface topography is examined using optical profilometry, and mechanical properties are evaluated using microhardness. Martensite lath size distribution and parent β titanium grains are analysed using the EBSD. A fully martensitic microstructure was confirmed by XRD, SEM and EBSD analyses. The hardness of SLM parts was found to be dependant on the processing parameters. A hierarchical martensitic structure consisting of primary, secondary, tertiary, and quartic martensite laths was identified by means of SEM and EBSD. Tertiary martensite (1 μm<lath length<10 μm) was found as the most abundant type in terms of the count of individual laths and total area

coverage. Results from this chapter provided a baseline for TiC-Ti6Al4V composite properties.

The manufacture of *in situ* TiC-Ti6Al4V composites was examined in the succeeding chapter. The powder mixing method, proven as applicable to SLM in Chapter 4, was investigated in more detail. Composite Ti6Al4V-carbon feedstock was processed with a continuous wave SLM system. A higher energy density window than the one used with the pulsed laser system trial was used. The microstructure of the composites was examined using XRD, SEM, and EBSD. Mechanical properties were investigated using hardness.

Increasing powder mixing duration resulted in more homogeneously carbon-coated Ti6Al4V particles. Nearly fully dense composites with homogeneously dispersed nanosized TiC reinforcements were successfully manufactured using composite powder feedstock. The rapid cooling nature of the SLM process and Marangoni convection within the melt pool led to homogeneously dispersed fine TiC particles below 500 nm size. Primary TiC particles spread within the parent β grains, whereas some linearly aligned eutectic TiC particles consisting of many nanosized small particles were present at the grain boundaries. Low SLM energy density led to undissolved residual carbon and microstructural segregations, whereas high energy densities created keyhole pores. The presence of TiC particles refined parent β grains by increasing the grains boundary length more than two times. Additionally, TiC particles refined the martensite laths by reducing the average martensite lath length by ~30%. The hardness of TiC-Ti6Al4V composites were ~100 HV higher than unreinforced Ti6Al4V parts processed with identical parameters. Strength increase was provided by the presence of nanosized TiC particles, Orowan strengthening and thermal expansion coefficient mismatch. Increasing energy density led to lower hardness due to intrinsic heat treatment effects of adjacent laser scans and SLM layers.

In the last experimental chapter, the wear performance of plain Ti6Al4V alloy and Ti6Al4V-TiC composites were investigated. Conventionally processed Ti6Al4V, SLMed Ti6Al4V and Ti6Al4V-TiC composites' wear and friction behaviours were compared

using a dry reciprocating wear test. Additionally, *in situ* scratch tests were performed to evaluate the friction and wear behaviour of Ti6Al4V-TiC composites. Three different counterpart ball materials, AISI 52100 bearing steel, Si_3N_4 and Al_2O_3 balls, are used as the counterpart material. Surprisingly, the wear rate of the Ti6Al4V-TiC composite was highest against all AISI 52100 bearing steel, Si_3N_4 and Al_2O_3 counterpart balls despite its significantly higher hardness. *In situ* SEM scratch tests revealed the removal of TiC particles from the Ti6Al4V matrix under frictional forces. Only a minor difference between conventional Ti6Al4V and SLMed Ti6Al4V was observed after rubbing against the Si3N4 ball. This showed that microstructural differences between conventionally processed and SLMed Ti6Al4V did not cause a significant difference. It is believed that third body abrasion arising from TiC particles in the tribolayer caused lower hardness of Ti6Al4V-TiC composites.

8.2. Future Work

The manufacture of nearly fully dense parts was successfully performed in this work. However, there are points to be examined further to understand mechanisms. These are listed below:

- Homogeneous distribution of nanosized TiC particles within the Ti6Al4V was provided in this study. However, the orientation relationship between the α' martensite phase and TiC particles remained unclear. Therefore, further transmission electron microscopy studies may be performed to reveal this relationship.

- A formation mechanism for *in situ* TiC nanoparticles was proposed in this study. However, presence of repeated heating and cooling cycles due to subsequent laser scans and layers, rapid cooling nature of the SLM process create a complex thermal history for composite parts. Further single track laser scans, higher resolution EBSD imaging and TEM investigation may help to better understand the formation process of these composites.

- The strengthening mechanisms of Ti6Al4V-TiC composites needs further investigation. Although mechanisms behind strength increase are known, their contribution to this particular material is unclear.

- The reasons behind the hardness change of unreinforced Ti6Al4V parts with varying processing parameters have not been fully understood. Therefore, a systematic study including crystallographic characterisation techniques, such as EBSD, may be performed to reveal microstructural and mechanical changes for different SLM energy inputs.

- A composite powder feedstock with 1 wt.% graphite addition to Ti6Al4V particles was examined in this study. However, lower and higher additions of carbon could provide better properties for different applications. For example, higher carbon addition may lead better wear resistance, whereas lower carbon addition may increase the strength without sacrificing the ductility.

- Different matrix materials could be produced using the same powder mixing method to produce *in situ* carbides as reinforcement materials. This would be particularly useful for commercially pure titanium because the strength of Ti6Al4V could be achieved with the formation of nanoparticles without cytotoxic vanadium.

- The wear performance and wear mechanisms of TiC-Ti6Al4V composites and unreinforced Ti6Al4V alloy is assessed using dry reciprocating wear tests and *in situ* SEM scratch tests. However, further studies are needed to reveal the structure of the tribofilm for a better understanding of the wear mechanisms of *in situ* Ti6Al4V-TiC composites.

References

[1]   K. U. Kainer, "Basics of Metal Matrix Composites," in *Metal Matrix Composites*, 2006, pp. 1–54. doi: doi:10.1002/3527608117.ch1.

[2]   D. K. Sharma, D. Mahant, and G. Upadhyay, "Manufacturing of metal matrix composites: A state of review," *Mater. Today Proc.*, vol. 26, pp. 506–519, 2019, doi: 10.1016/j.matpr.2019.12.128.

[3]   W. Zhou, X. Sun, K. Kikuchi, N. Nomura, K. Yoshimi, and A. Kawasaki, "In situ synthesized TiC/Mo-based composites via laser powder bed fusion," *Mater. Des.*, vol. 146, pp. 116–124, 2018, doi: 10.1016/j.matdes.2018.03.001.

[4]   S. Li, "Powder metallurgy Ti – TiC metal matrix composites prepared by in situ reactive processing of Ti-VGCFs system," *Carbon N. Y.*, vol. 61, pp. 216–228, 2013, doi: 10.1016/j.carbon.2013.04.088.

[5]   S. Dadbakhsh, R. Mertens, L. Hao, J. Van Humbeeck, and J. Kruth, "Selective Laser Melting to Manufacture 'In Situ' Metal Matrix Composites: A Review," *Adv. Eng. Mater.*, vol. 21, no. 3, p. 1801244, Mar. 2019, doi: 10.1002/adem.201801244.

[6]   F. Ma, J. Zhou, P. Liu, W. Li, X. Liu, D. Pan, W. Lu, D. Zhang, L. Wu, and X. Wei, "Strengthening effects of TiC particles and microstructure refinement in in situ TiC-reinforced Ti matrix composites," *Mater. Charact.*, vol. 127, pp. 27–34, 2017, doi: 10.1016/j.matchar.2017.02.004.

[7]   I. Y. Kim, B. J. Choi, Y. J. Kim, and Y. Z. Lee, "Friction and wear behavior of titanium matrix (TiB+TiC) composites," *Wear*, vol. 271, no. 9–10, pp. 1962–

1965, Jul. 2011, doi: 10.1016/j.wear.2010.12.072.

[8] L. J. Huang, L. Geng, and H. X. Peng, "In situ TiBw/Ti composites with a novel quasi-continuous network reinforcement architecture," *ICCM Int. Conf. Compos. Mater.*, pp. 1–5, 2011.

[9] M. Bai, R. Namus, Y. Xu, D. Guan, M. W. Rainforth, and B. J. Inkson, "In-situ Ti-6Al-4V/TiC composites synthesized by reactive spark plasma sintering: processing, microstructure, and dry sliding wear behaviour," *Wear*, vol. 432–433, p. 202944, Aug. 2019, doi: 10.1016/j.wear.2019.202944.

[10] P. Yuan, D. Gu, and D. Dai, "Particulate migration behavior and its mechanism during selective laser melting of TiC reinforced Al matrix nanocomposites," *Mater. Des.*, vol. 82, pp. 46–55, 2015, doi: 10.1016/j.matdes.2015.05.041.

[11] J. Liu, J. Li, and C. Xu, "Interaction of the cutting tools and the ceramic-reinforced metal matrix composites during micro-machining: A review," *CIRP Journal of Manufacturing Science and Technology*, vol. 7, no. 2. CIRP, pp. 55–70, 2014. doi: 10.1016/j.cirpj.2014.01.003.

[12] M. Peters and C. Leyens, "Fabrication of Titanium Alloys," in *Titanium and Titanium Alloys*, Weinheim, FRG: Wiley-VCH Verlag GmbH & Co. KGaA, 2005, pp. 245–261. doi: 10.1002/3527602119.ch8.

[13] M. J. Donachie, "Machining," in *Titanium: A Technical Guide*, Second., Ohio: ASM International, 2000, pp. 79–84. doi: 10.1361/tatg2000p079.

[14] T. Childerhouse and M. Jackson, "Near net shape manufacture of titanium alloy components from powder and wire: A review of state-of-the-art process routes," *Metals (Basel).*, vol. 9, no. 6, 2019, doi: 10.3390/met9060689.

[15] I. Gibson, D. Rosen, and B. Stucker, "Powder Bed Fusion Processes," in *Additive Manufacturing Technologies*, Second., New York, NY: Springer New York, 2015, pp. 107–145. doi: 10.1007/978-1-4939-2113-3_5.

[16] W. J. Sames, F. A. List, S. Pannala, R. R. Dehoff, and S. S. Babu, "The metallurgy and processing science of metal additive manufacturing," *Int. Mater. Rev.*, vol. 61, no. 5, pp. 315–360, 2016, doi: 10.1080/09506608.2015.1116649.

[17] B. He, W. Wu, L. Zhang, L. Lu, Q. Yang, Q. Long, and K. Chang, "Microstructural characteristic and mechanical property of Ti6Al4V alloy fabricated by selective laser melting," *Vacuum*, vol. 150, pp. 79–83, Apr. 2018, doi: 10.1016/j.vacuum.2018.01.026.

[18] S. Gorsse, C. Hutchinson, M. Gouné, and R. Banerjee, "Additive manufacturing of metals: a brief review of the characteristic microstructures and properties of steels, Ti-6Al-4V and high-entropy alloys," *Sci. Technol. Adv. Mater.*, vol. 18, no. 1, pp. 584–610, 2017, doi: 10.1080/14686996.2017.1361305.

[19] D. Gu, H. Wang, and G. Zhang, "Selective laser melting additive manufacturing of Ti-based nanocomposites: The role of nanopowder," *Metall. Mater. Trans. A Phys. Metall. Mater. Sci.*, vol. 45, no. 1, pp. 464–476, 2014, doi: 10.1007/s11661-013-1968-4.

[20] D. Gu, Y. C. Hagedorn, W. Meiners, K. Wissenbach, and R. Poprawe, "Nanocrystalline TiC reinforced Ti matrix bulk-form nanocomposites by Selective Laser Melting (SLM): Densification, growth mechanism and wear behavior," *Compos. Sci. Technol.*, vol. 71, no. 13, pp. 1612–1620, 2011, doi: 10.1016/j.compscitech.2011.07.010.

[21] D. Gu, Y. Shen, and G. Meng, "Growth morphologies and mechanisms of TiC grains during Selective Laser Melting of Ti-Al-C composite powder," *Mater. Lett.*, vol. 63, no. 29, pp. 2536–2538, Dec. 2009, doi: 10.1016/j.matlet.2009.08.043.

[22] D. Gu, Y. C. Hagedorn, W. Meiners, K. Wissenbach, and R. Poprawe, "Selective Laser Melting of in-situ TiC/Ti5Si3 composites with novel reinforcement architecture and elevated performance," *Surf. Coatings Technol.*, vol. 205, no. 10, pp. 3285–3292, 2011, doi: 10.1016/j.surfcoat.2010.11.051.

[23] S. Dadbakhsh, R. Mertens, K. Vanmeensel, G. Ji, and J. P. Kruth, "In situ transformations during SLM of an ultra-strong TiC reinforced Ti composite," *Sci. Rep.*, vol. 10, no. 1, pp. 1–12, 2020, doi: 10.1038/s41598-020-67434-3.

[24] H. Attar, M. Bönisch, M. Calin, L. C. Zhang, K. Zhuravleva, A. Funk, S. Scudino, C. Yang, and J. Eckert, "Comparative study of microstructures and mechanical properties of in situ Ti-TiB composites produced by selective laser melting, powder metallurgy, and casting technologies," *J. Mater. Res.*, vol. 29, no. 17, pp. 1941–1950, 2014, doi: 10.1557/jmr.2014.122.

[25] H. Attar, M. Bönisch, M. Calin, L.-C. C. Zhang, S. Scudino, and J. Eckert, "Selective laser melting of in situ titanium-titanium boride composites: Processing, microstructure and mechanical properties," *Acta Mater.*, vol. 76, pp. 13–22, Sep. 2014, doi: 10.1016/j.actamat.2014.05.022.

[26] Y. He, C. Montgomery, J. Beuth, and B. Webler, "Melt pool geometry and microstructure of Ti6Al4V with B additions processed by selective laser melting additive manufacturing," *Mater. Des.*, vol. 183, p. 108126, 2019, doi: 10.1016/j.matdes.2019.108126.

[27] W. H. Yu, S. L. Sing, C. K. Chua, C. N. Kuo, and X. L. Tian, "Particle-reinforced metal matrix nanocomposites fabricated by selective laser melting: A state of the art review," *Prog. Mater. Sci.*, vol. 104, pp. 330–379, Jul. 2019, doi: 10.1016/j.pmatsci.2019.04.006.

[28] D. L. Bourell and T. Wohlers, "Introduction to Additive Manufacturing," in *Additive Manufacturing Processes*, ASM International, 2020, pp. 3–10. doi: 10.31399/asm.hb.v24.a0006555.

[29] C. K. Chua, C. H. Wong, and W. Y. Yeong, *Standards, quality control, and measurement sciences in 3D printing and additive manufacturing*.

[30] I. Gibson, D. Rosen, and B. Stucker, "Introduction and Basic Principles," in *Additive Manufacturing Technologies*, Second., New York, NY: Springer New York, 2015, pp. 1–18. doi: 10.1007/978-1-4939-2113-3_1.

[31] I. Gibson, D. Rosen, and B. Stucker, "Development of Additive Manufacturing Technology," in *Additive Manufacturing Technologies*, New York, NY: Springer New York, 2015, pp. 19–42. doi: 10.1007/978-1-4939-2113-3_2.

[32] D. D. Gu, W. Meiners, K. Wissenbach, and R. Poprawe, "Laser additive manufacturing of metallic components: materials, processes and mechanisms," *Int. Mater. Rev.*, vol. 57, no. 3, pp. 133–164, 2012, doi: 10.1179/1743280411Y.0000000014.

[33] S. Sun, M. Brandt, and M. Easton, "2 – Powder bed fusion processes: An overview," in *Laser Additive Manufacturing*, 2017, pp. 55–77. doi: 10.1016/B978-0-08-100433-3.00002-6.

[34] R. Hague, "Unlocking the Design Potential of Rapid Manufacturing," *Rapid Manufacturing*. pp. 5–18, Nov. 11, 2005. doi: https://doi.org/10.1002/0470033991.ch2.

[35] R. Liu, Z. Wang, T. Sparks, F. Liou, and J. Newkirk, "13 - Aerospace applications of laser additive manufacturing," in *Laser Additive Manufacturing*, Elsevier, 2017, pp. 351–371. doi: 10.1016/B978-0-08-100433-3.00013-0.

[36] T. DebRoy, H. L. Wei, J. S. Zuback, T. Mukherjee, J. W. Elmer, J. O. Milewski, A. M. Beese, A. Wilson-Heid, A. De, and W. Zhang, "Additive manufacturing of metallic components – Process, structure and properties," *Prog. Mater. Sci.*, vol. 92, pp. 112–224, Mar. 2018, doi: 10.1016/j.pmatsci.2017.10.001.

[37] E. Herderick, "Additive Manufacturing of Metals: A Review," *Mater. Sci. Technol.*, vol. 2, pp. 1413–1425, 2011.

[38] H. K. Rafi, N. V. Karthik, H. Gong, T. L. Starr, and B. E. Stucker, "Microstructures and mechanical properties of Ti6Al4V parts fabricated by selective laser melting and electron beam melting," *J. Mater. Eng. Perform.*, vol. 22, no. 12, pp. 3872–3883, 2013, doi: 10.1007/s11665-013-0658-0.

[39] S. Liu and Y. C. Shin, "Additive manufacturing of Ti6Al4V alloy: A review," *Mater. Des.*, vol. 164, p. 107552, Feb. 2019, doi: 10.1016/j.matdes.2018.107552.

[40] S. Ghods, E. Schultz, C. Wisdom, R. Schur, R. Pahuja, A. Montelione, D. Arola, and M. Ramulu, "Electron beam additive manufacturing of Ti6Al4V: Evolution of powder morphology and part microstructure with powder reuse," *Materialia*, vol. 9, p. 100631, Mar. 2020, doi: 10.1016/j.mtla.2020.100631.

[41]   S. L. Sing, J. An, W. Y. Yeong, and F. E. Wiria, "Laser and electron-beam powder-bed additive manufacturing of metallic implants: A review on processes, materials and designs," *Journal of Orthopaedic Research*. 2016. doi: 10.1002/jor.23075.

[42]   Y. J. Liu, S. J. Li, H. L. Wang, W. T. Hou, Y. L. Hao, R. Yang, T. B. Sercombe, and L. C. Zhang, "Microstructure, defects and mechanical behavior of beta-type titanium porous structures manufactured by electron beam melting and selective laser melting," *Acta Mater.*, vol. 113, pp. 56–67, 2016, doi: 10.1016/j.actamat.2016.04.029.

[43]   H. Ali, L. Ma, H. Ghadbeigi, and K. Mumtaz, "In-situ residual stress reduction, martensitic decomposition and mechanical properties enhancement through high temperature powder bed pre-heating of Selective Laser Melted Ti6Al4V," *Mater. Sci. Eng. A*, vol. 695, pp. 211–220, May 2017, doi: 10.1016/j.msea.2017.04.033.

[44]   S. Beretta and S. Romano, "A comparison of fatigue strength sensitivity to defects for materials manufactured by AM or traditional processes," *Int. J. Fatigue*, vol. 94, pp. 178–191, 2017, doi: 10.1016/j.ijfatigue.2016.06.020.

[45]   L. Facchini, E. Magalini, P. Robotti, A. Molinari, S. Höges, and K. Wissenbach, "Ductility of a Ti-6Al-4V alloy produced by selective laser melting of prealloyed powders," *Rapid Prototyp. J.*, vol. 16, no. 6, pp. 450–459, 2010, doi: 10.1108/13552541011083371.

[46]   B. Liu, R. Wildman, C. Tuck, I. Ashcroft, and R. Hague, "Investigation the effect of particle size distribution on processing parameters optimisation in selective laser melting process," *Int. solid Free. Fabr. Symp. an Addit. Manuf. Conf.*, no. mm, pp. 227–238, 2011, doi: 10.1017/CBO9781107415324.004.

[47]   C. D. Boley, S. A. Khairallah, and A. M. Rubenchik, "Calculation of laser absorption by metal powders in additive manufacturing," *Addit. Manuf. Handb. Prod. Dev. Def. Ind.*, vol. 54, no. 9, pp. 507–517, 2017, doi: 10.1201/9781315119106.

[48]   P. O'Regan, P. Prickett, R. Setchi, G. Hankins, and N. Jones, "Metal Based Additive Layer Manufacturing: Variations, Correlations and Process Control," *Procedia Comput. Sci.*, vol. 96, pp. 216–224, 2016, doi: 10.1016/j.procs.2016.08.134.

[49]   D. K. Do and P. Li, "The effect of laser energy input on the microstructure, physical and mechanical properties of Ti-6Al-4V alloys by selective laser melting," *Virtual Phys. Prototyp.*, vol. 11, no. 1, pp. 41–47, 2016, doi: 10.1080/17452759.2016.1142215.

[50]   H. Shipley, D. McDonnell, M. Culleton, R. Coull, R. Lupoi, G. O'Donnell, and D. Trimble, "Optimisation of process parameters to address fundamental challenges during selective laser melting of Ti-6Al-4V: A review," *Int. J. Mach.*

Tools Manuf., vol. 128, pp. 1–20, May 2018, doi: 10.1016/j.ijmachtools.2018.01.003.

[51] T. Majumdar, T. Bazin, E. M. C. Ribeiro, J. E. Frith, and N. Birbilis, "Understanding the effects of PBF process parameter interplay on Ti-6Al-4V surface properties," *PLoS One*, vol. 14, no. 8, pp. 1–24, 2019, doi: 10.1371/journal.pone.0221198.

[52] N. Singh, P. Hameed, R. Ummethala, G. Manivasagam, K. G. Prashanth, and J. Eckert, "Selective laser manufacturing of Ti-based alloys and composites: impact of process parameters, application trends, and future prospects," *Mater. Today Adv.*, vol. 8, p. 100097, Dec. 2020, doi: 10.1016/j.mtadv.2020.100097.

[53] L. C. Zhang and H. Attar, "Selective Laser Melting of Titanium Alloys and Titanium Matrix Composites for Biomedical Applications: A Review," *Adv. Eng. Mater.*, vol. 18, no. 4, pp. 463–475, 2016, doi: 10.1002/adem.201500419.

[54] S. K. Everton, M. Hirsch, P. Stravroulakis, R. K. Leach, and A. T. Clare, "Review of in-situ process monitoring and in-situ metrology for metal additive manufacturing," *Mater. Des.*, vol. 95, pp. 431–445, Apr. 2016, doi: 10.1016/j.matdes.2016.01.099.

[55] B. Zhang, Y. Li, and Q. Bai, "Defect Formation Mechanisms in Selective Laser Melting: A Review," *Chinese J. Mech. Eng. (English Ed.*, vol. 30, no. 3, pp. 515–527, 2017, doi: 10.1007/s10033-017-0121-5.

[56] H. R. Javidrad, M. Ghanbari, and F. Javidrad, "Effect of scanning pattern and volumetric energy density on the properties of selective laser melting Ti-6Al-4V specimens," *J. Mater. Res. Technol.*, vol. 12, pp. 989–998, 2021, doi: 10.1016/j.jmrt.2021.03.044.

[57] D. Wang, W. Dou, and Y. Yang, "Research on selective laser melting of Ti6Al4V: Surface morphologies, optimized processing zone, and ductility improvement mechanism," *Metals (Basel).*, vol. 8, no. 7, 2018, doi: 10.3390/met8070471.

[58] K. G. Prashanth, S. Scudino, T. Maity, J. Das, and J. Eckert, "Is the energy density a reliable parameter for materials synthesis by selective laser melting?," *Mater. Res. Lett.*, vol. 5, no. 6, pp. 386–390, 2017, doi: 10.1080/21663831.2017.1299808.

[59] U. Scipioni Bertoli, A. J. Wolfer, M. J. Matthews, J. P. R. Delplanque, and J. M. Schoenung, "On the limitations of Volumetric Energy Density as a design parameter for Selective Laser Melting," *Mater. Des.*, vol. 113, pp. 331–340, Jan. 2017, doi: 10.1016/j.matdes.2016.10.037.

[60] A. G. Demir, P. Colombo, and B. Previtali, "From pulsed to continuous wave emission in SLM with contemporary fiber laser sources: effect of temporal and spatial pulse overlap in part quality," *Int. J. Adv. Manuf. Technol.*, vol. 91, no. 5–8, pp. 2701–2714, 2017, doi: 10.1007/s00170-016-9948-7.

[61] F. Freeman, "Structuring Difference The Additive Manufacture of Spatially & Functionally Differentiated Microstructures," The University of Sheffield, 2018.

[62] A. Y. Alfaify, J. Hughes, and K. Ridgway, "Critical evaluation of the pulsed selective laser melting process when fabricating Ti64 parts using a range of particle size distributions," *Addit. Manuf.*, vol. 19, pp. 197–204, Jan. 2018, doi: 10.1016/j.addma.2017.12.003.

[63] J. A. Cherry, H. M. Davies, S. Mehmood, N. P. Lavery, S. G. R. Brown, and J. Sienz, "Investigation into the effect of process parameters on microstructural and physical properties of 316L stainless steel parts by selective laser melting," *Int. J. Adv. Manuf. Technol.*, vol. 76, no. 5–8, pp. 869–879, 2014, doi: 10.1007/s00170-014-6297-2.

[64] N. J. Harrison, I. Todd, and K. Mumtaz, "Reduction of micro-cracking in nickel superalloys processed by Selective Laser Melting: A fundamental alloy design approach," *Acta Mater.*, vol. 94, pp. 59–68, Aug. 2015, doi: 10.1016/J.ACTAMAT.2015.04.035.

[65] Y. (Morris) Wang, C. Kamath, T. Voisin, and Z. Li, "A processing diagram for high-density Ti-6Al-4V by selective laser melting," *Rapid Prototyp. J.*, vol. 24, no. 9, pp. 1469–1478, 2018, doi: 10.1108/RPJ-11-2017-0228.

[66] Z. Xiang, M. Yin, G. Dong, X. Mei, and G. Yin, "Modeling of the thermal physical process and study on the reliability of linear energy density for selective laser melting," *Results Phys.*, vol. 9, pp. 939–946, Jun. 2018, doi: 10.1016/j.rinp.2018.03.047.

[67] M. Simonelli, Y. Y. Tse, and C. Tuck, "On the texture formation of selective laser melted Ti-6Al-4V," *Metall. Mater. Trans. A Phys. Metall. Mater. Sci.*, vol. 45, no. 6, pp. 2863–2872, 2014, doi: 10.1007/s11661-014-2218-0.

[68] M. V. Pantawane, Y. H. Ho, S. S. Joshi, and N. B. Dahotre, "Computational Assessment of Thermokinetics and Associated Microstructural Evolution in Laser Powder Bed Fusion Manufacturing of Ti6Al4V Alloy," *Sci. Rep.*, vol. 10, no. 1, pp. 1–14, 2020, doi: 10.1038/s41598-020-63281-4.

[69] I. Todd, "Printing steels," *Nat. Mater.*, vol. 17, no. 1, pp. 13–14, Jan. 2018, doi: 10.1038/nmat5042.

[70] M. Losertová and V. Kubeš, "Microstructure and mechanical properties of selective laser melted Ti6Al4V alloy," *IOP Conf. Ser. Mater. Sci. Eng.*, vol. 266, no. 1, 2017, doi: 10.1088/1757-899X/266/1/012009.

[71] M. Simonelli, C. Tuck, N. T. Aboulkhair, I. Maskery, I. Ashcroft, R. D. Wildman, and R. Hague, "A Study on the Laser Spatter and the Oxidation Reactions During Selective Laser Melting of 316L Stainless Steel, Al-Si10-Mg, and Ti-6Al-4V," *Metall. Mater. Trans. A Phys. Metall. Mater. Sci.*, vol. 46, no. 9, pp. 3842–3851, 2015, doi: 10.1007/s11661-015-2882-8.

[72] M. Simonelli, Y. Y. Tse, and C. Tuck, "Effect of the build orientation on the mechanical properties and fracture modes of SLM Ti-6Al-4V," *Mater. Sci. Eng. A*, vol. 616, pp. 1–11, Oct. 2014, doi: 10.1016/j.msea.2014.07.086.

[73] W. E. Frazier, "Metal additive manufacturing: A review," *J. Mater. Eng. Perform.*, vol. 23, no. 6, pp. 1917–1928, 2014, doi: 10.1007/s11665-014-0958-z.

[74] W. S. W. Harun, M. S. I. N. Kamariah, N. Muhamad, S. A. C. Ghani, F. Ahmad, and Z. Mohamed, "A review of powder additive manufacturing processes for metallic biomaterials," *Powder Technology*, vol. 327. pp. 128–151, 2018. doi: 10.1016/j.powtec.2017.12.058.

[75] D. Zhang, S. Sun, D. Qiu, M. A. Gibson, M. S. Dargusch, M. Brandt, M. Qian, and M. Easton, "Metal Alloys for Fusion-Based Additive Manufacturing," *Adv. Eng. Mater.*, vol. 1700952, p. 1700952, 2018, doi: 10.1002/adem.201700952.

[76] C. Y. Yap, C. K. Chua, Z. L. Dong, Z. H. Liu, D. Q. Zhang, L. E. Loh, and S. L. Sing, "Review of selective laser melting: Materials and applications," *Appl. Phys. Rev.*, vol. 2, no. 4, p. 041101, Dec. 2015, doi: 10.1063/1.4935926.

[77] M. J. Donachie, "Introduction to Selection of Titanium Alloys," in *Titanium: A Technical Guide*, Second., Ohio: ASM International, 2000, pp. 5–11. doi: 10.1361/tatg2000p005.

[78] M. Peters, J. Hemptenmacher, J. Kumpfert, and C. Leyens, "Structure and Properties of Titanium and Titanium Alloys," in *Titanium and Titanium Alloys*, Weinheim, FRG: Wiley-VCH Verlag GmbH & Co. KGaA, 2005, pp. 1–36. doi: 10.1002/3527602119.ch1.

[79] M. J. Donachie, "A Primer on Titanium and Its Alloys," in *Titanium: A Technical Guide*, Second., Ohio: ASM International, 2000, pp. 1–3. doi: 10.1361/tatg2000p001.

[80] A. P. B. T.-I. to A. M. Mouritz, Ed., "Titanium alloys for aerospace structures and engines," in *Introduction to Aerospace Materials*, Elsevier, 2012, pp. 202–223. doi: 10.1533/9780857095152.202.

[81] D. F. Williams, "Titanium for Medical Applications," in *Titanium in Medicine: Material Science, Surface Science, Engineering, Biological Responses and Medical Applications*, Berlin, Heidelberg: Springer Berlin Heidelberg, 2001, pp. 13–24. doi: 10.1007/978-3-642-56486-4_2.

[82] J. Breme, E. Eisenbarth, and V. Biehl, "Titanium and its Alloys for Medical Applications," *Titanium and Titanium Alloys*. Jan. 28, 2005. doi: doi:10.1002/3527602119.ch16.

[83] M. J. Donachie, "Understanding the Metallurgy of Titanium," in *Titanium: A Technical Guide*, Second., Ohio: ASM International, 2000, pp. 12–24. doi: 10.1361/tatg2000p013.

[84] M. J. Donachie, "Heat Treating," in *Titanium: A Technical Guide*, Second., Ohio: ASM International, 2000, pp. 55–63. doi: 10.1361/tatg2000p055.

[85] M. J. Donachie, "Forging and Forming," in *Titanium: A Technical Guide*, Second., Ohio: ASM International, 2000, pp. 33–38. doi: 10.1361/tatg2000p033.

[86] G. Terlinde and G. Fischer, "Beta Titanium Alloys," in *Titanium and Titanium Alloys*, Wiley-Blackwell, 2005, pp. 37–57. doi: 10.1002/3527602119.ch2.

[87] ASTM International, "Standard Specification for Titanium-6Aluminum-4Vanadium Alloy Castings for Surgical Implants (UNS R56406)," 2010 doi: 10.1520/F1108-04R09.2.

[88] L. Thijs, F. Verhaeghe, T. Craeghs, J. Van Humbeeck, and J. P. Kruth, "A study of the microstructural evolution during selective laser melting of Ti-6Al-4V," *Acta Mater.*, vol. 58, no. 9, pp. 3303–3312, 2010, doi: 10.1016/j.actamat.2010.02.004.

[89] B. Vrancken, L. Thijs, J. P. Kruth, and J. Van Humbeeck, "Heat treatment of Ti6Al4V produced by Selective Laser Melting: Microstructure and mechanical properties," *J. Alloys Compd.*, vol. 541, pp. 177–185, Nov. 2012, doi: 10.1016/j.jallcom.2012.07.022.

[90] J. Yang, H. Yu, H. Yang, F. Li, Z. Wang, and X. Zeng, "Prediction of microstructure in selective laser melted Ti−6Al−4V alloy by cellular automaton," *J. Alloys Compd.*, vol. 748, pp. 281–290, 2018, doi: 10.1016/j.jallcom.2018.03.116.

[91] J. Tong, C. R. Bowen, J. Persson, and A. Plummer, "Mechanical properties of titanium-based Ti−6Al−4V alloys manufactured by powder bed additive manufacture," *Mater. Sci. Technol. (United Kingdom)*, vol. 33, no. 2, pp. 138–148, 2017, doi: 10.1080/02670836.2016.1172787.

[92] H. Ali, H. Ghadbeigi, and K. Mumtaz, "Effect of scanning strategies on residual stress and mechanical properties of Selective Laser Melted Ti6Al4V," *Mater. Sci. Eng. A*, vol. 712, pp. 175–187, Jan. 2018, doi: 10.1016/j.msea.2017.11.103.

[93] B. Dutta and F. H. (Sam. Froes, "The Additive Manufacturing (AM) of titanium alloys," *Met. Powder Rep.*, vol. 72, no. 2, pp. 96–106, 2017, doi: 10.1016/j.mprp.2016.12.062.

[94] G. Kasperovich and J. Hausmann, "Improvement of fatigue resistance and ductility of TiAl6V4 processed by selective laser melting," *J. Mater. Process. Technol.*, vol. 220, pp. 202–214, 2015, doi: 10.1016/j.jmatprotec.2015.01.025.

[95] M. V. Pantawane, S. Sharma, A. Sharma, S. Dasari, S. Banerjee, R. Banerjee, and N. B. Dahotre, "Coarsening of martensite with multiple generations of twins in laser additively manufactured Ti6Al4V," *Acta Mater.*, vol. 213, p. 116954, 2021,

doi: 10.1016/j.actamat.2021.116954.

[96] J. Yang, H. Yu, J. Yin, M. Gao, Z. Wang, and X. Zeng, "Formation and control of martensite in Ti-6Al-4V alloy produced by selective laser melting," *Mater. Des.*, vol. 108, pp. 308–318, Oct. 2016, doi: 10.1016/j.matdes.2016.06.117.

[97] H. Gong, K. Rafi, H. Gu, T. Starr, and B. Stucker, "Analysis of defect generation in Ti-6Al-4V parts made using powder bed fusion additive manufacturing processes," *Addit. Manuf.*, vol. 1, pp. 87–98, 2014, doi: 10.1016/j.addma.2014.08.002.

[98] G. Kasperovich, J. Haubrich, J. Gussone, and G. Requena, "Correlation between porosity and processing parameters in TiAl6V4 produced by selective laser melting," *Mater. Des.*, vol. 105, pp. 160–170, Sep. 2016, doi: 10.1016/j.matdes.2016.05.070.

[99] W. E. King, H. D. Barth, V. M. Castillo, G. F. Gallegos, J. W. Gibbs, D. E. Hahn, C. Kamath, and A. M. Rubenchik, "Observation of keyhole-mode laser melting in laser powder-bed fusion additive manufacturing," *J. Mater. Process. Technol.*, vol. 214, no. 12, pp. 2915–2925, Dec. 2014, doi: 10.1016/j.jmatprotec.2014.06.005.

[100] M. Bayat, A. Thanki, S. Mohanty, A. Witvrouw, S. Yang, J. Thorborg, N. S. Tiedje, and J. H. Hattel, "Keyhole-induced porosities in Laser-based Powder Bed Fusion (L-PBF) of Ti6Al4V: High-fidelity modelling and experimental validation," *Addit. Manuf.*, vol. 30, p. 100835, Dec. 2019, doi: 10.1016/j.addma.2019.100835.

[101] R. Cunningham, C. Zhao, N. Parab, C. Kantzos, J. Pauza, K. Fezzaa, T. Sun, and A. D. Rollett, "Keyhole threshold and morphology in laser melting revealed by ultrahigh-speed x-ray imaging," *Science*, vol. 363, no. 6429. pp. 849–852, 2019. doi: 10.1126/science.aav4687.

[102] S. A. Khairallah, A. T. Anderson, A. Rubenchik, and W. E. King, "Laser powder-bed fusion additive manufacturing: Physics of complex melt flow and formation mechanisms of pores, spatter, and denudation zones," *Acta Mater.*, vol. 108, pp. 36–45, 2016, doi: 10.1016/j.actamat.2016.02.014.

[103] S. M. H. Hojjatzadeh, N. D. Parab, Q. Guo, M. Qu, L. Xiong, C. Zhao, L. I. Escano, K. Fezzaa, W. Everhart, T. Sun, and L. Chen, "Direct observation of pore formation mechanisms during LPBF additive manufacturing process and high energy density laser welding," *Int. J. Mach. Tools Manuf.*, vol. 153, no. November 2019, p. 103555, 2020, doi: 10.1016/j.ijmachtools.2020.103555.

[104] K. K. Chawla, "Introduction," in *Composite Materials*, New York, NY: Springer New York, 2012, pp. 3–6. doi: 10.1007/978-0-387-74365-3_1.

[105] K. K. Chawla, "Reinforcements," in *Composite Materials*, New York, NY: Springer New York, 2012, pp. 7–71. doi: 10.1007/978-0-387-74365-3_2.

[106] K. K. Chawla, "Metal Matrix Composites," in *Composite Materials: Science and Engineering*, New York, NY: Springer New York, 2012, pp. 197–248. doi: 10.1007/978-0-387-74365-3_6.

[107] M. D. Hayat, H. Singh, Z. He, and P. Cao, "Titanium metal matrix composites: An overview," *Composites Part A: Applied Science and Manufacturing*, vol. 121, no. March. pp. 418–438, 2019. doi: 10.1016/j.compositesa.2019.04.005.

[108] Y. Jiao, L. Huang, and L. Geng, "Progress on discontinuously reinforced titanium matrix composites," *J. Alloys Compd.*, vol. 767, pp. 1196–1215, 2018, doi: 10.1016/j.jallcom.2018.07.100.

[109] S. C. Tjong and Y. W. Mai, "Processing-structure-property aspects of particulate- and whisker-reinforced titanium matrix composites," *Compos. Sci. Technol.*, vol. 68, no. 3–4, pp. 583–601, 2008, doi: 10.1016/j.compscitech.2007.07.016.

[110] K. K. Chawla, "Metal Matrix Composites," in *Composite Materials*, New York, NY: Springer New York, 2012, pp. 197–248. doi: 10.1007/978-0-387-74365-3_6.

[111] H. Dieringa and K. U. Kainer, "Particles, Fibers and Short Fibers for the Reinforcement of Metal Materials," in *Metal Matrix Composites*, John Wiley & Sons, Ltd, 2006, pp. 55–76. doi: https://doi.org/10.1002/3527608117.ch2.

[112] B. Gülenç, Y. Kaya, A. Durgutlu, I. T. Gülenç, M. S. Yildirim, and N. Kahraman, "Production of wire reinforced composite materials through explosive welding," *Arch. Civ. Mech. Eng.*, vol. 16, no. 1, pp. 1–8, 2016, doi: 10.1016/j.acme.2015.09.006.

[113] R. Casati and M. Vedani, "Metal matrix composites reinforced by Nano-Particles—A review," *Metals (Basel).*, vol. 4, no. 1, pp. 65–83, 2014, doi: 10.3390/met4010065.

[114] Y. Wang, J. Shi, X. Deng, and S. Lu, "Contribution of different strengthening effects in particulatereinforced metal matrix nanocomposites prepared by additive manufacturing," *ASME Int. Mech. Eng. Congr. Expo. Proc.*, vol. 2, pp. 1–7, 2016, doi: 10.1115/IMECE201667312.

[115] S. Pan, X. Zhou, K. Chen, M. Yang, Y. Cao, X. Chen, and Z. Wang, "In-situ nanoparticles: A new strengthening method for metallic structural material," *Appl. Sci.*, vol. 8, no. 12, 2018, doi: 10.3390/app8122479.

[116] H. Attar, S. Ehtemam-Haghighi, D. Kent, and M. S. Dargusch, "Recent developments and opportunities in additive manufacturing of titanium-based matrix composites: A review," *Int. J. Mach. Tools Manuf.*, vol. 133, no. June, pp. 85–102, 2018, doi: 10.1016/j.ijmachtools.2018.06.003.

[117] J. Wang, L. Li, P. Lin, and J. Wang, "Effect of TiC particle size on the microstructure and tensile properties of TiCp/Ti6Al4V composites fabricated by

laser melting deposition," *Opt. Laser Technol.*, vol. 105, pp. 195–206, Sep. 2018, doi: 10.1016/j.optlastec.2018.03.009.

[118] X. Sun, Y. Han, S. Cao, P. Qiu, and W. Lu, "Rapid in-situ reaction synthesis of novel TiC and carbon nanotubes reinforced titanium matrix composites," *J. Mater. Sci. Technol.*, vol. 33, no. 10, pp. 1165–1171, 2017, doi: 10.1016/j.jmst.2017.07.005.

[119] M. Y. Koo, J. S. Park, M. K. Park, K. T. Kim, and S. H. Hong, "Effect of aspect ratios of in situ formed TiB whiskers on the mechanical properties of TiB w/Ti-6Al-4V composites," *Scr. Mater.*, vol. 66, no. 7, pp. 487–490, 2012, doi: 10.1016/j.scriptamat.2011.12.024.

[120] W.-H. Wei, Z.-N. Shao, J. Shen, and X.-M. Duan, "Microstructure and mechanical properties of in situ formed TiC-reinforced Ti–6Al–4V matrix composites," *Mater. Sci. Technol.*, vol. 0836, pp. 1–8, 2017, doi: 10.1080/02670836.2017.1366737.

[121] B. AlMangour, D. Grzesiak, and J. M. Yang, "In-situ formation of novel TiC-particle-reinforced 316L stainless steel bulk-form composites by selective laser melting," *J. Alloys Compd.*, vol. 706, pp. 409–418, Jun. 2017, doi: 10.1016/j.jallcom.2017.01.149.

[122] Y. Hu, W. Cong, X. Wang, Y. Li, F. Ning, and H. Wang, "Laser deposition-additive manufacturing of TiB-Ti composites with novel three-dimensional quasi-continuous network microstructure: Effects on strengthening and toughening," *Compos. Part B Eng.*, vol. 133, pp. 91–100, 2018, doi: 10.1016/j.compositesb.2017.09.019.

[123] K. Zhang, X. Tian, M. Bermingham, J. Rao, Q. Jia, Y. Zhu, X. Wu, S. Cao, and A. Huang, "Effects of boron addition on microstructures and mechanical properties of Ti-6Al-4V manufactured by direct laser deposition," *Mater. Des.*, vol. 184, 2019, doi: 10.1016/j.matdes.2019.108191.

[124] M. J. Bermingham, S. D. McDonald, and M. S. Dargusch, "Effect of trace lanthanum hexaboride and boron additions on microstructure, tensile properties and anisotropy of Ti-6Al-4V produced by additive manufacturing," *Mater. Sci. Eng. A*, vol. 719, no. December 2017, pp. 1–11, 2018, doi: 10.1016/j.msea.2018.02.012.

[125] D. Gu, Z. Wang, Y. Shen, Q. Li, and Y. Li, "In-situ TiC particle reinforced Ti-Al matrix composites: Powder preparation by mechanical alloying and Selective Laser Melting behavior," *Appl. Surf. Sci.*, vol. 255, no. 22, pp. 9230–9240, Aug. 2009, doi: 10.1016/j.apsusc.2009.07.008.

[126] B. Vrancken, S. Dadbakhsh, R. Mertens, K. Vanmeensel, J. Vleugels, S. Yang, and J. P. Kruth, "Selective Laser Melting process optimization of Ti–Mo–TiC metal matrix composites," *CIRP Ann.*, vol. 68, no. 1, pp. 221–224, 2019, doi: 10.1016/j.cirp.2019.04.120.

[127] A. S. Patil, V. D. Hiwarkar, P. K. Verma, and R. K. Khatirkar, "Effect of TiB2 addition on the microstructure and wear resistance of Ti-6Al-4V alloy fabricated through direct metal laser sintering (DMLS)," *J. Alloys Compd.*, vol. 777, pp. 165–173, 2019, doi: 10.1016/j.jallcom.2018.10.308.

[128] T. Kühnle and K. Partes, "In-Situ Formation of Titanium Boride and Titanium Carbide by Selective Laser Melting," *Phys. Procedia*, vol. 39, pp. 432–438, 2012, doi: 10.1016/j.phpro.2012.10.058.

[129] D. Gu, G. Meng, C. Li, W. Meiners, and R. Poprawe, "Selective laser melting of TiC/Ti bulk nanocomposites: Influence of nanoscale reinforcement," *Scr. Mater.*, vol. 67, no. 2, pp. 185–188, 2012, doi: 10.1016/j.scriptamat.2012.04.013.

[130] C. Ma, D. Gu, D. Dai, G. Yu, M. Xia, and H. Chen, "Thermodynamic behaviour and formation mechanism of novel titanium carbide dendritic crystals within a molten pool of selective laser melting TiC/Ti-Ni composites," *CrystEngComm*, vol. 19, no. 7, pp. 1089–1099, 2017, doi: 10.1039/c6ce02284g.

[131] C. Kun, H. Beibei, W. Wenheng, and Z. Cailin, "The formation mechanism of TiC reinforcement and improved tensile strength in additive manufactured Ti matrix nanocomposite," *Vacuum*, vol. 143, pp. 23–27, Sep. 2017, doi: 10.1016/j.vacuum.2017.05.029.

[132] J. Wang, L. Li, C. Tan, H. Liu, and P. Lin, "Microstructure and tensile properties of TiCp/Ti6Al4V titanium matrix composites manufactured by laser melting deposition," *J. Mater. Process. Technol.*, vol. 252, no. September 2017, pp. 524–536, 2018, doi: 10.1016/j.jmatprotec.2017.10.005.

[133] B. Fotovvati, S. F. Wayne, G. Lewis, and E. Asadi, "A Review on Melt-Pool Characteristics in Laser Welding of Metals," *Adv. Mater. Sci. Eng.*, vol. 2018, 2018, doi: 10.1155/2018/4920718.

[134] A. Maamoun, Y. Xue, M. Elbestawi, and S. Veldhuis, "Effect of Selective Laser Melting Process Parameters on the Quality of Al Alloy Parts: Powder Characterization, Density, Surface Roughness, and Dimensional Accuracy," *Materials (Basel).*, vol. 11, no. 12, p. 2343, Nov. 2018, doi: 10.3390/ma11122343.

[135] A. B. Spierings, M. Voegtlin, T. Bauer, and K. Wegener, "Powder flowability characterisation methodology for powder-bed-based metal additive manufacturing," *Prog. Addit. Manuf.*, vol. 1, no. 1–2, pp. 9–20, 2016, doi: 10.1007/s40964-015-0001-4.

[136] L. C. Ardila, F. Garciandia, J. B. González-Díaz, P. Álvarez, A. Echeverria, M. M. Petite, R. Deffley, and J. Ochoa, "Effect of IN718 recycled powder reuse on properties of parts manufactured by means of Selective Laser Melting," *Phys. Procedia*, vol. 56, no. C, pp. 99–107, 2014, doi: 10.1016/j.phpro.2014.08.152.

[137] M. N. Ahsan, A. J. Pinkerton, R. J. Moat, and J. Shackleton, "A comparative study of laser direct metal deposition characteristics using gas and plasma-

atomized Ti-6Al-4V powders," *Mater. Sci. Eng. A*, vol. 528, no. 25–26, pp. 7648–7657, Sep. 2011, doi: 10.1016/j.msea.2011.06.074.

[138] "Owner's Manual for Aconity Mini."

[139] D. C. Montgomery, "Response Surface Methods and Designs," in *Design and analysis of experiments*, 9th ed., John Wiley & Sons, Inc., 2017, pp. 489–568.

[140] K. Dunn, "Design and Analysis of Experiments," in *Process Improvement Using Data*, 2021, pp. 231–314.

[141] M. Schneider, R. Eggenberger, and a. B. Spierings, "Comparison of density measurement techniques for additive manufactured metallic parts," *Rapid Prototyping Journal*, vol. 17, no. 5. pp. 380–386, 2011. doi: 10.1108/13552541111156504.

[142] J. Schindelin, I. Arganda-Carreras, E. Frise, V. Kaynig, M. Longair, T. Pietzsch, S. Preibisch, C. Rueden, S. Saalfeld, B. Schmid, J.-Y. Tinevez, D. J. White, V. Hartenstein, K. Eliceiri, P. Tomancak, and A. Cardona, "Fiji: an open-source platform for biological-image analysis," *Nat. Methods*, vol. 9, no. 7, pp. 676–682, 2012, doi: 10.1038/nmeth.2019.

[143] ASTM International, "Standard Test Method for Microindentation Hardness of Materials," 2017 doi: 10.1520/E0384-17.

[144] ASTM International, "Standard Test Method for Linearly Reciprocating Ball-on-Flat Sliding Wear," 2016 doi: 10.1520/G0133-05R16.

[145] "AISI 52100 Chrome Steel Data Sheet." Simply Bearings Ltd.

[146] E. K. B. T.-R. M. Storms, Ed., "I - The Titanium–Titanium Carbide System," in *The Refractory Carbides*, vol. 2, Elsevier, 1967, pp. 1–17. doi: https://doi.org/10.1016/B978-1-4832-3070-2.50006-9.

[147] T. Vilaro, C. Colin, and J. D. Bartout, "As-fabricated and heat-treated microstructures of the Ti-6Al-4V alloy processed by selective laser melting," *Metall. Mater. Trans. A Phys. Metall. Mater. Sci.*, vol. 42, no. 10, pp. 3190–3199, 2011, doi: 10.1007/s11661-011-0731-y.

[148] J. Günther, D. Krewerth, T. Lippmann, S. Leuders, T. Tröster, A. Weidner, H. Biermann, and T. Niendorf, "Fatigue life of additively manufactured Ti–6Al–4V in the very high cycle fatigue regime," *Int. J. Fatigue*, vol. 94, pp. 236–245, 2017, doi: 10.1016/j.ijfatigue.2016.05.018.

[149] H. Gong, D. Christiansen, J. Beuth, and J. J. Lewandowski, "Melt Pool Characterization for Selective Laser Melting of Ti-6Al-4V Pre-alloyed Powder," *Solid Free. Fabr. Symp.*, pp. 256–267, 2014.

[150] S. Liu and Y. C. Shin, "The influences of melting degree of TiC reinforcements on microstructure and mechanical properties of laser direct deposited Ti6Al4V-TiC

composites," *Mater. Des.*, vol. 136, pp. 185–195, 2017, doi: 10.1016/j.matdes.2017.09.063.

[151] B. AlMangour, M. S. Baek, D. Grzesiak, and K. A. Lee, "Strengthening of stainless steel by titanium carbide addition and grain refinement during selective laser melting," *Mater. Sci. Eng. A*, vol. 712, pp. 812–818, Jan. 2018, doi: 10.1016/j.msea.2017.11.126.

[152] J. B. Ferguson, B. F. Schultz, D. Venugopalan, H. F. Lopez, P. K. Rohatgi, K. Cho, and C. S. Kim, "On the superposition of strengthening mechanisms in dispersion strengthened alloys and metal-matrix nanocomposites: Considerations of stress and energy," *Met. Mater. Int.*, vol. 20, no. 2, pp. 375–388, 2014, doi: 10.1007/s12540-014-2017-6.

[153] S. D. Dunmead, D. W. Readey, C. E. Semler, and J. B. Hol, "Kinetics of Combustion Synthesis in the Ti-C and Ti-C-Ni Systems," *J. Am. Ceram. Soc.*, vol. 72, no. 12, pp. 2318–2324, Dec. 1989, doi: 10.1111/j.1151-2916.1989.tb06083.x.

[154] H. Ali, H. Ghadbeigi, and K. Mumtaz, "Residual stress development in selective laser-melted Ti6Al4V: a parametric thermal modelling approach," *Int. J. Adv. Manuf. Technol.*, vol. 97, no. 5–8, pp. 2621–2633, 2018, doi: 10.1007/s00170-018-2104-9.

[155] P. A. Hooper, "Melt pool temperature and cooling rates in laser powder bed fusion," *Addit. Manuf.*, vol. 22, no. May, pp. 548–559, 2018, doi: 10.1016/j.addma.2018.05.032.

[156] V. Manvatkar, A. De, and T. DebRoy, "Spatial variation of melt pool geometry, peak temperature and solidification parameters during laser assisted additive manufacturing process," *Mater. Sci. Technol. (United Kingdom)*, vol. 31, no. 8, pp. 924–930, 2015, doi: 10.1179/1743284714Y.0000000701.

[157] A. Bin Anwar and Q. C. Pham, "Selective laser melting of AlSi10Mg: Effects of scan direction, part placement and inert gas flow velocity on tensile strength," *Journal of Materials Processing Technology*, vol. 240. pp. 388–396, 2017. doi: 10.1016/j.jmatprotec.2016.10.015.

[158] A. Ladewig, G. Schlick, M. Fisser, V. Schulze, and U. Glatzel, "Influence of the shielding gas flow on the removal of process by-products in the selective laser melting process," *Addit. Manuf.*, vol. 10, pp. 1–9, 2016, doi: 10.1016/j.addma.2016.01.004.

[159] C. Qiu, C. Panwisawas, M. Ward, H. C. Basoalto, J. W. Brooks, and M. M. Attallah, "On the role of melt flow into the surface structure and porosity development during selective laser melting," *Acta Mater.*, vol. 96, pp. 72–79, Sep. 2015, doi: 10.1016/j.actamat.2015.06.004.

[160] Q. Han, Y. Geng, R. Setchi, F. Lacan, D. Gu, and S. L. Evans, "Macro and nanoscale wear behaviour of Al-Al2O3 nanocomposites fabricated by selective

laser melting," *Compos. Part B Eng.*, vol. 127, pp. 26–35, Oct. 2017, doi: 10.1016/j.compositesb.2017.06.026.

[161] S. Pal, G. Lojen, R. Hudak, V. Rajtukova, T. Brajlih, V. Kokol, and I. Drstvenšek, "As-fabricated surface morphologies of Ti-6Al-4V samples fabricated by different laser processing parameters in selective laser melting," *Addit. Manuf.*, vol. 33, no. January, p. 101147, 2020, doi: 10.1016/j.addma.2020.101147.

[162] K. Mumtaz and N. Hopkinson, "Top surface and side roughness of Inconel 625 parts processed using selective laser melting," *Rapid Prototyp. J.*, vol. 15, no. 2, pp. 96–103, 2009, doi: 10.1108/13552540910943397.

[163] F. Calignano, D. Manfredi, E. P. Ambrosio, L. Iuliano, and P. Fino, "Influence of process parameters on surface roughness of aluminum parts produced by DMLS," *Int. J. Adv. Manuf. Technol.*, vol. 67, no. 9–12, pp. 2743–2751, 2013, doi: 10.1007/s00170-012-4688-9.

[164] R. Li, J. Liu, Y. Shi, L. Wang, and W. Jiang, "Balling behavior of stainless steel and nickel powder during selective laser melting process," *International Journal of Advanced Manufacturing Technology*, vol. 59, no. 9–12. pp. 1025–1035, 2012. doi: 10.1007/s00170-011-3566-1.

[165] J. P. Kruth, L. Froyen, J. Van Vaerenbergh, P. Mercelis, M. Rombouts, and B. Lauwers, "Selective laser melting of iron-based powder," *J. Mater. Process. Technol.*, vol. 149, no. 1–3, pp. 616–622, Jun. 2004, doi: 10.1016/j.jmatprotec.2003.11.051.

[166] E. Yasa, J. Deckers, and J. Kruth, "The investigation of the influence of laser re-melting on density, surface quality and microstructure of selective laser melting parts," *Rapid Prototyp. J.*, vol. 17, no. 5, pp. 312–327, 2011, doi: 10.1108/13552541111156450.

[167] D. Ye, K. Zhu, J. Y. H. Fuh, Y. Zhang, and H. G. Soon, "The investigation of plume and spatter signatures on melted states in selective laser melting," *Opt. Laser Technol.*, vol. 111, pp. 395–406, Apr. 2019, doi: 10.1016/j.optlastec.2018.10.019.

[168] Z. Chen, X. Wu, D. Tomus, and C. H. J. Davies, "Surface roughness of Selective Laser Melted Ti-6Al-4V alloy components," *Addit. Manuf.*, vol. 21, pp. 91–103, May 2018, doi: 10.1016/j.addma.2018.02.009.

[169] G. Pyka, G. Kerckhofs, I. Papantoniou, M. Speirs, J. Schrooten, and M. Wevers, "Surface roughness and morphology customization of additive manufactured open porous Ti6Al4V structures," *Materials (Basel).*, vol. 6, no. 10, pp. 4737–4757, 2013, doi: 10.3390/ma6104737.

[170] C. Kenel, D. Grolimund, X. Li, E. Panepucci, V. A. Samson, D. F. Sanchez, F. Marone, and C. Leinenbach, "In situ investigation of phase transformations in Ti-6Al-4V under additive manufacturing conditions combining laser melting and high-speed micro-X-ray diffraction," *Sci. Rep.*, vol. 7, no. 1, pp. 1–10, 2017,

doi: 10.1038/s41598-017-16760-0.

[171] J. Han, J. Yang, H. Yu, J. Yin, M. Gao, Z. Wang, and X. Zeng, "Microstructure and mechanical property of selective laser melted Ti6Al4V dependence on laser energy density," *Rapid Prototyp. J.*, vol. 23, no. 2, pp. 217–226, 2017, doi: 10.1108/RPJ-12-2015-0193.

[172] N. Kazantseva, P. Krakhmalev, M. Thuvander, I. Yadroitsev, N. Vinogradova, and I. Ezhov, "Martensitic transformations in Ti-6Al-4V (ELI) alloy manufactured by 3D Printing," *Mater. Charact.*, vol. 146, no. September, pp. 101–112, 2018, doi: 10.1016/j.matchar.2018.09.042.

[173] S. Pal, G. Lojen, N. Gubeljak, V. Kokol, and I. Drstvensek, "Melting, fusion and solidification behaviors of Ti-6Al-4V alloy in selective laser melting at different scanning speeds," *Rapid Prototyp. J.*, vol. 26, no. 7, pp. 1209–1215, 2020, doi: 10.1108/RPJ-07-2019-0206.

[174] G. M. Ter Haar and T. H. Becker, "Selective laser melting produced Ti-6Al-4V: Post-process heat treatments to achieve superior tensile properties," *Materials (Basel).*, vol. 11, no. 1, 2018, doi: 10.3390/ma11010146.

[175] J. Yang, J. Han, H. Yu, J. Yin, M. Gao, Z. Wang, and X. Zeng, "Role of molten pool mode on formability, microstructure and mechanical properties of selective laser melted Ti-6Al-4V alloy," *Mater. Des.*, vol. 110, pp. 558–570, Nov. 2016, doi: 10.1016/j.matdes.2016.08.036.

[176] X. Zhao, S. Li, M. Zhang, Y. Liu, T. B. Sercombe, S. Wang, Y. Hao, R. Yang, and L. E. Murr, "Comparison of the microstructures and mechanical properties of Ti-6Al-4V fabricated by selective laser melting and electron beam melting," *Mater. Des.*, vol. 95, pp. 21–31, Apr. 2016, doi: 10.1016/j.matdes.2015.12.135.

[177] M. Simonelli, Y. Y. Tse, and C. Tuck, "Further Undestanding of Ti-6Al-4V Selective Saser Melting Using Texture Analysis," *23rd Annu. Int. Solid Free. Fabr. Symp. - An Addit. Manuf. Conf. SFF 2012*, pp. 480–491, 2012, doi: http://dx.doi.org/10.26153/tsw/15367.

[178] J. Cho, "Characterization of the α'-Martensite phase and its decomposition in Ti-6Al-4V additively manufactured by selective laser melting," RMIT University, 2018.

[179] S. S. Al-Bermani, M. L. Blackmore, W. Zhang, and I. Todd, "The origin of microstructural diversity, texture, and mechanical properties in electron beam melted Ti-6Al-4V," *Metall. Mater. Trans. A Phys. Metall. Mater. Sci.*, vol. 41, no. 13, pp. 3422–3434, 2010, doi: 10.1007/s11661-010-0397-x.

[180] A. M. Khorasani, I. Gibson, U. S. Awan, and A. Ghaderi, "The effect of SLM process parameters on density, hardness, tensile strength and surface quality of Ti-6Al-4V," *Addit. Manuf.*, vol. 25, no. August 2018, pp. 176–186, 2019, doi: 10.1016/j.addma.2018.09.002.

[181] U. Scipioni Bertoli, G. Guss, S. Wu, M. J. Matthews, and J. M. Schoenung, "In-situ characterization of laser-powder interaction and cooling rates through high-speed imaging of powder bed fusion additive manufacturing," *Materials and Design*, vol. 135. pp. 385–396, 2017. doi: 10.1016/j.matdes.2017.09.044.

[182] Y. Liao, C. Ye, B. J. Kim, S. Suslov, E. A. Stach, and G. J. Cheng, "Nucleation of highly dense nanoscale precipitates based on warm laser shock peening," *J. Appl. Phys.*, vol. 108, no. 6, 2010, doi: 10.1063/1.3481858.

[183] D. Gu, W. Meiners, Y. Hagedorn, K. Wissenbach, and R. Poprawe, "Structural evolution and formation mechanisms of TiC/Ti nanocomposites prepared by high-energy mechanical alloying," *J. Phys. D. Appl. Phys.*, vol. 43, no. 13, p. 135402, Apr. 2010, doi: 10.1088/0022-3727/43/13/135402.

[184] C. Ma, J. Zhao, C. Cao, T.-C. Lin, and X. Li, "Fundamental Study on Laser Interactions With Nanoparticles-Reinforced Metals—Part II: Effect of Nanoparticles on Surface Tension, Viscosity, and Laser Melting," *J. Manuf. Sci. Eng.*, vol. 138, no. 12, pp. 2–7, Dec. 2016, doi: 10.1115/1.4033446.

[185] I. Yadroitsev and I. Smurov, "Surface morphology in selective laser melting of metal powders," *Phys. Procedia*, vol. 12, no. PART 1, pp. 264–270, 2011, doi: 10.1016/j.phpro.2011.03.034.

[186] F. Cabanettes, A. Joubert, G. Chardon, V. Dumas, J. Rech, C. Grosjean, and Z. Dimkovski, "Topography of as built surfaces generated in metal additive manufacturing: A multi scale analysis from form to roughness," *Precis. Eng.*, vol. 52, pp. 249–265, Apr. 2018, doi: 10.1016/j.precisioneng.2018.01.002.

[187] M. F. Sadali, M. Z. Hassan, N. H. Ahmad, H. Yahya, and A. F. M. Nor, "Effect of hatching distance on surface morphology and surface roughness of the TI6AL4V for biomedical implant using SLM process," *Malaysian J. Microsc.*, vol. 15, no. 1, pp. 72–82, 2019.

[188] S. J. Foster, K. Carver, R. B. Dinwiddie, F. List, K. A. Unocic, A. Chaudhary, and S. S. Babu, "Process-Defect-Structure-Property Correlations During Laser Powder Bed Fusion of Alloy 718: Role of In Situ and Ex Situ Characterizations," *Metall. Mater. Trans. A Phys. Metall. Mater. Sci.*, vol. 49, no. 11, pp. 5775–5798, 2018, doi: 10.1007/s11661-018-4870-2.

[189] M. J. Donachie, "Relationships among Structures, Processing, and Properties," in *Titanium: A Technical Guide*, Second., Ohio: ASM International, 2000, pp. 95–121. doi: 10.1361/tatg2000p095.

[190] W. Wei, Q. Zhang, W. Wu, H. Cao, J. Shen, S. Fan, and X. Duan, "Agglomeration-free nanoscale TiC reinforced titanium matrix composites achieved by in-situ laser additive manufacturing," *Scr. Mater.*, vol. 187, pp. 310–316, 2020, doi: 10.1016/j.scriptamat.2020.06.057.

[191] T. Zhang, H. Li, S. Liu, S. Shen, H. Xie, W. Shi, G. Zhang, B. Shen, L. Chen, B.

Xiao, and M. Wei, "Evolution of molten pool during selective laser melting of Ti-6Al-4V," *J. Phys. D. Appl. Phys.*, vol. 52, no. 5, 2019, doi: 10.1088/1361-6463/aaee04.

[192] B. AlMangour, D. Grzesiak, T. Borkar, and J. M. Yang, "Densification behavior, microstructural evolution, and mechanical properties of TiC/316L stainless steel nanocomposites fabricated by selective laser melting," *Mater. Des.*, vol. 138, pp. 119–128, Jan. 2018, doi: 10.1016/j.matdes.2017.10.039.

[193] M. Tang, L. Zhang, and N. Zhang, "Microstructural evolution, mechanical and tribological properties of TiC/Ti6Al4V composites with unique microstructure prepared by SLM," *Mater. Sci. Eng. A*, vol. 814, no. March, p. 141187, 2021, doi: 10.1016/j.msea.2021.141187.

[194] J. Zhang, Y. Zhang, W. Li, S. Karnati, F. Liou, and J. W. Newkirk, "Microstructure and properties of functionally graded materials Ti6Al4V/TiC fabricated by direct laser deposition," *Rapid Prototyp. J.*, vol. 24, no. 4, pp. 677–687, 2018, doi: 10.1108/RPJ-12-2016-0215.

[195] M. I. De Barros, D. Rats, L. Vandenbulcke, and G. Farges, "Influence of internal diffusion barriers on carbon diffusion in pure titanium and Ti-6Al-4V during diamond deposition," *Diam. Relat. Mater.*, vol. 8, no. 6, pp. 1022–1032, 1999, doi: 10.1016/s0925-9635(98)00439-7.

[196] L. Scotti and A. Mottura, "Interstitial diffusion of O, N, and C in α-Ti from first-principles: Analytical model and kinetic Monte Carlo simulations," *Journal of Chemical Physics*, vol. 144, no. 8. 2016. doi: 10.1063/1.4942030.

[197] E. Fereiduni, A. Ghasemi, and M. Elbestawi, "Selective laser melting of aluminum and titanium matrix composites: Recent progress and potential applications in the aerospace industry," *Aerospace*, vol. 7, no. 6, 2020, doi: 10.3390/AEROSPACE7060077.

[198] Z. Zhang and D. L. Chen, "Contribution of Orowan strengthening effect in particulate-reinforced metal matrix nanocomposites," *Mater. Sci. Eng. A*, vol. 483–484, no. 1-2 C, pp. 148–152, 2008, doi: 10.1016/j.msea.2006.10.184.

[199] J. Haubrich, J. Gussone, P. Barriobero-Vila, P. Kürnsteiner, E. A. Jägle, D. Raabe, N. Schell, and G. Requena, "The role of lattice defects, element partitioning and intrinsic heat effects on the microstructure in selective laser melted Ti-6Al-4V," *Acta Mater.*, vol. 167, pp. 136–148, Apr. 2019, doi: 10.1016/j.actamat.2019.01.039.

[200] S. Lampman, "Wrought Titanium and Titanium Alloys," in *Properties and Selection: Nonferrous Alloys and Special-Purpose Materials*, vol. 2, ASM International, 1990, pp. 592–633. doi: 10.31399/asm.hb.v02.a0001081.

[201] M. Asmani, C. Kermel, A. Leriche, and M. Ourak, "Influence of porosity on Youngs modulus and poisson's ratio in alumina ceramics," *J. Eur. Ceram. Soc.*,

vol. 21, no. 8, pp. 1081–1086, 2001, doi: 10.1016/S0955-2219(00)00314-9.

[202] R. L. Edwards, G. Coles, and W. N. Sharpe, "Comparison of Tensile and Bulge Tests for Thin-Film Silicon Nitride," *Exp. Mech.*, vol. 44, no. 1, pp. 49–54, 2004, doi: 10.1177/0014485104039749.

[203] A. Chavan and V. Sargade, "Surface integrity of AISI 52100 steel during hard turning in different near-dry environments," *Adv. Mater. Sci. Eng.*, vol. 2020, 2020, doi: 10.1155/2020/4256308.

[204] B. Attard, A. Matthews, A. Leyland, and G. Cassar, "Enhanced surface performance of Ti-6Al-4V alloy using a novel duplex process combining PVD-Al coating and triode plasma oxidation," *Surf. Coatings Technol.*, vol. 257, pp. 154–164, 2014, doi: 10.1016/j.surfcoat.2014.07.083.

[205] K. Kato and K. Adachi, "Wear Mechanisms," in *Modern Tribology Handbook, Two Volume Set*, Ohio: CRC Press, 2000, pp. 273–299. doi: 10.1201/9780849377877.

[206] M. O. Alam and A. S. M. A. Haseeb, "Response of Ti-6Al-4V and Ti-24Al-11Nb alloys to dry sliding wear against hardened steel," *Tribol. Int.*, vol. 35, no. 6, pp. 357–362, Jun. 2002, doi: 10.1016/S0301-679X(02)00015-4.

[207] N. W. Khun, W. Q. Toh, X. P. Tan, E. Liu, and S. B. Tor, "Tribological Properties of Three-Dimensionally Printed Ti–6Al–4V Material Via Electron Beam Melting Process Tested Against 100Cr6 Steel Without and With Hank's Solution," *J. Tribol.*, vol. 140, no. 6, p. 061606, May 2018, doi: 10.1115/1.4040158.

[208] R. J. Kar, R. M. Horn, and V. F. Zackay, "The effect of heat treatment on microstructure and mechanical properties in 52100 steel," *Metall. Trans. A*, vol. 10, no. 11, pp. 1711–1717, 1979, doi: 10.1007/BF02811705.

[209] G. Cassar, J. C. A. B. Wilson, S. Banfield, J. Housden, A. Matthews, and A. Leyland, "A study of the reciprocating-sliding wear performance of plasma surface treated titanium alloy," *Wear*, vol. 269, no. 1–2, pp. 60–70, 2010, doi: 10.1016/j.wear.2010.03.008.

[210] Q. L. Niu, X. H. Zheng, W. W. Ming, and M. Chen, "Friction and Wear Performance of Titanium Alloys against Tungsten Carbide under Dry Sliding and Water Lubrication," *Tribol. Trans.*, vol. 56, no. 1, pp. 101–108, 2013, doi: 10.1080/10402004.2012.729296.

[211] H. Li, M. Ramezani, and Z. W. Chen, "Dry sliding wear performance and behaviour of powder bed fusion processed Ti–6Al–4V alloy," *Wear*, vol. 440–441, no. July, 2019, doi: 10.1016/j.wear.2019.203103.

[212] Z. Doni, A. C. Alves, F. Toptan, J. R. Gomes, A. Ramalho, M. Buciumeanu, L. Palaghian, and F. S. Silva, "Dry sliding and tribocorrosion behaviour of hot pressed CoCrMo biomedical alloy as compared with the cast CoCrMo and

Ti6Al4V alloys," *Mater. Des.*, vol. 52, pp. 47–57, 2013, doi: 10.1016/j.matdes.2013.05.032.

[213] C. T. Wang, N. Gao, M. G. Gee, R. J. K. Wood, and T. G. Langdon, "Effect of grain size on the micro-tribological behavior of pure titanium processed by high-pressure torsion," *Wear*, vol. 280–281, pp. 28–35, Mar. 2012, doi: 10.1016/J.WEAR.2012.01.012.